UNIVERSITY OF CALIFORNIA
RIVERSIDE

Photodissociation Dynamics of Free Radicals Using High-*n* Rydberg Atom Time-of-Flight Spectroscopy

A Dissertation submitted in partial satisfaction
of the requirements for the degree of

Doctor of Philosophy

in

Chemistry

by

Ge Sun

March 2020

Dissertation Committee:
Dr. Jingsong Zhang, Chairperson
Dr. Christopher Bardeen
Dr. Quan Jason Cheng

The Dissertation of Ge Sun is approved:

Committee Chairperson

University of California, Riverside

Acknowledgements

First, I would like to express my gratitude to my advisor Professor Jingsong Zhang, without the help and support from him this work could not be completed. During my work, he taught me so much from the basic experimental techniques to the dissociation dynamics with his patience and guidance, which allows me finally to achieve this milestone. I am also impressed by his profound knowledge of chemistry and science during these years. What's more, he supported me and helped me to attend many conferences where I met so many great scientists and broaden my horizon of science.

I would also thank the whole Zhang research group members, previous members and the visitors Dr. Michael Lucas, Dr. Mixtli Campos-Pineda, Lydia Plett, Paul Jones, Kuanliang Shao, Lei Yang, Yuan Qin, Min Chen, Jian Chen, and Xinghua Liu for their input and observations during these years.

I also want to thank Professor Christopher Bardeen and Professor Quan Jason Cheng for participating in my oral exam and final defense as committee members, helping me to polish this dissertation.

I still remember the old time in University of Science and Technology of China (USTC). Professor Shuiming Hu and Professor Anwen Liu allowed me and provided me a good opportunity to start the researching under their supervision. Without the help from them, I will never start to walk my way on the research as a chemist. Also, I will say thank you to my old friends from USTC, Zitan Zhang, Jia Song, Yijie Tang, Minxiang Zeng, and other people.

I would like to appreciate the help and support form the staffs in the Department of Chemistry, from the enrollment, reserving the conference room, processing the purchase order, and everything else. Their professional works release me from other works and allow me focusing on the study and research.

I want to say thank you to my friends at UC Riverside, Yufei Ni, Ji Feng, Tongxin Han, Tianyi Yu, Zihao Wang, and many others. Thank you all for your support when I have troubles in my research, or I am depressed. No matter what is going on, you guys are away there.

Last part, I would like to thank the people out of UC Riverside. Qian Wang, Bin Zhao, Minyu Li and others all over the world. It was a great time to share the great researches and the funny stories from you.

Dedication

To my parents

Junmei Wang and Yan Sun

for their love and support over the Pacific Ocean

Copyright Acknowledgement

The works in chapter 3 is submitted to Chinese Journal of Chemical Physics.

The works in chapter 6 is published in the Chinese Journal of Chemical Physics (DOI: 10.1063/1674-0068/31/cjcp1805103).

The works in chapter 7 is published in the Journal of Physical Chemistry A (DOI: 10.1021/acs.jpca.9b07797).

The works in chapter 9 is published in the Journal of Physical Chemistry A (DOI: 10.1021/acs.jpca.9b01791)

ABSTRACT OF THE DISSERTATION

Photodissociation Dynamics of Free Radicals
Using High-*n* Rydberg Atom Time of Flight Spectroscopy

by

Ge Sun

Doctor of Philosophy, Graduate Program in Chemistry
University of California, Riverside, March 2020
Dr. Jingsong Zhang, Chairperson

Free radicals are open-shell systems that have one or more unpaired valence electrons, and are thus short-lived and highly reactive. Free radicals can be found as important reactive intermediates in a wide range of chemical environments, for example, combustion, atmospheric chemistry, plasma, and interstellar chemistry. The photodissociation studies of free radicals can provide spectroscopic and electronic excited state information of free radicals, probe excited-state potential energy surfaces (PESs), their interactions, and their influence on reaction dynamics, and provide benchmarks for theoretical studies of the open-shell systems. The photodissociation dynamics of free radicals were studied using the high-*n* Rydberg H-atom time-of-flight technique. Several systems were investigated in the dissertation. The hydroxyl radical (OH), which is a prototypical diatomic radical, has been examined via several rovibrational levels in the $A^2\Sigma^+$ state. The H + O(^3P_J) product branching ratios and angular distributions from the $A^2\Sigma^+$ state were obtained. Sequential two-photon excitations to the $2^2\Pi$ and $B^2\Sigma^+$ repulsive

states were observed, leading to the H + O(^{1}D) and H + O(^{1}S) products, respectively. Ultraviolet (UV) photodissociation of a series of alkyl radicals, ethyl (C_2H_5), *n*-butyl (*n*-C_4H_9), *i*-butyl (*i*-C_4H_9), *t*-butyl (*t*-C_4H_9), and 1-pentyl (1-C_5H_{11}), via their Rydberg states were observed to have two main dissociation channels: (i) direct dissociation from the electronic excited state, and (ii) unimolecular dissociation after internal conversion from the electronic excited state to the ground state. 2-Propenyl radical (CH_2CCH_3), in the alkenyl category, undergoes unimolecular dissociation on the ground electronic state following the UV photoexcitation and internal conversion from the excited state. Vinoxy radical (CH_2CHO) is a prototypical unsaturated alkoxy radical. After photoexcitation to the $\widetilde{B}^2A''$ state, the vinoxy radical undergoes unimolecular dissociation following internal conversion to the ground state ($\widetilde{X}^2A''$) and the first excited state ($\widetilde{A}^2A'$). The UV photodissociation of thiomethoxyl radical (CH_3S), a sulfur system, is similar to that of the ethyl radical and has two main channels: (i) direct dissociation on the repulsive PES, and (ii) unimolecular dissociation after internal conversion from the electronic excited state to the ground electronic state.

Table of Contents

List of Figures

List of Tables

Chapter 1

Introduction

1.1 Free Radical

Free radicals are atoms, molecules, or ions that have one or more unpaired valence electrons. These unpaired electrons make free radicals short-lived and highly-reactive transient species. As a result, it is very difficult to detect them and investigate their chemical reactions. Free radicals are commonly seen in a wide range of chemical reaction processes. They play roles as important intermediates in combustion, atmospheric chemistry, plasma chemistry, interstellar chemistry, and many other chemical processes. Experimentally, it is difficult to investigate the chemical behaviors of the free radicals due to the difficulty in the preparation of clean and intense source, and the sensitive detection of radicals and their products. For theories, it is challenges to obtain accurate potential energy surfaces (PESs) of the excited states of the open-shell systems and characterized their interactions.

1.2 Photodissociation Dynamics

One of the aspects of physical chemistry is to investigate the chemical compound on the microscopic scale. During a chemical reaction process, the bond breaking and formation, energy transfer, reaction kinetics and dynamics, and the motion of the atoms are all of the interests for physical chemists. Chemical dynamics aims at the energies and their influences on motions at the molecular level. The dynamics of a dissociation reaction of a molecule or a radical depend on the PESs which contain the energy information with all the relevant reaction coordinates.

In the photodissociation process, a molecule or a radical absorbs one or more photons, and the chemical compound is excited to an excited state. When the energy absorbed by the chemical compound is larger than the dissociation threshold, the compound could break into fragments and the extra energy will be distributed into the different degrees of freedom of the products. Photodissociation dynamics focuses on this process to reveal the transition states of the chemical compounds, the dissociation pathways, and the PESs of the excited electronic states and their couplings. It is also possible to investigate the state-to-state dynamics of the dissociation of a molecule or a radical after the excitation to a specific energy level with a photon from the laser radiation. In the atmosphere, the molecule or the radical absorbs the photons from the sunlight, and the energies of the photons could be high enough for them to dissociate into many kinds of fragments which have further reactions. In the combustion process, the compounds, such

as hydrocarbon radicals, are highly vibrationally and rotationally excited and can have the chemical bond cleavage to form small radicals or molecules. The photodissociation experiments are a good way to simulate the atmospheric chemistry process as the photon from the laser radiation has enough energy to break the chemical bond, and many molecules and free radicals in their electronic excited states could undergo internal conversion to the electronic ground state with high vibrational and rotational excitations, which could reproduce the combustion processes in the laboratory. In addition, the spectroscopy study on the chemical compounds will help the identification of the compositions and their abundance in the interstellar clouds.

In conclusion, the experimental study on photodissociation dynamics of the free radicals can reveal the spectroscopic and electronic excited state information of the free radicals, probe the PESs and their influence on reaction dynamics, and provide benchmark for theoretical studies of the open-shell species.

1.3 Types of Photodissociation

A general photodissociation reaction can be illustrated as $AB + h\upsilon \rightarrow (AB)^* \rightarrow A + B$, in which the molecule AB absorbs a photon and is excited to an excited state, then the excited molecule dissociates into the products A + B. The photodissociation mechanisms to generate the fragments can be summarized into direct and indirect dissociation mechanisms which are shown in Figure 1.1. Direct dissociation mechanism is presented in

Types of Photodissociation

$$AB + h\upsilon \rightarrow (AB)^* \rightarrow A + B$$

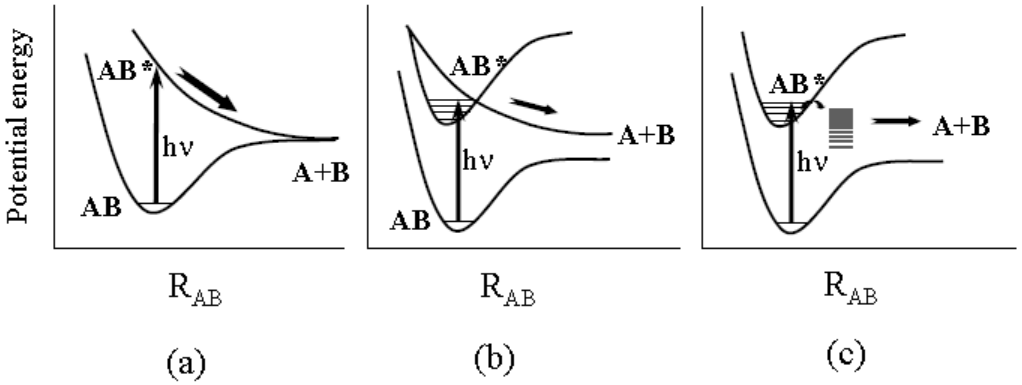

Figure 1.1 Three types of photodissociation mechanisms: (a) direct dissociation; (b) indirect dissociation: predissociation by coupling between a bound electronic state with a repulsive electronic state; (c) indirect dissociation: unimolecular dissociation of the internally (vibrationally and rotationally) excited AB in the ground electronic state after the internal conversion (IC) from the electronic excited state.

Figure 1.1(a). When the molecule or radical AB is excited by a photon with the energy of $h\upsilon$ to an excited state, which is unbound and repulsive, the excited AB* can directly dissociate along the potential energy surface toward to the product of A + B. In this case, the dissociation occurs very fast and most of the excess energy is distributed into the translational energy of the products instead of the energies in the internal degrees of freedom (vibrational and rotational energy of the products), making the energy distribution non-statistical. Indirect dissociation mechanisms are illustrated in Figure 1.1(b) and (c). When AB is excited to a bound electronic excited state, the excited state can relax to the ground electronic state via a radiative decay (*i.e.* fluorescence) or nonradiative decay. The bound excited state can be coupled to another repulsive and AB* finally decays through the repulsive state to the photofragments A + B, as shown in Figure 1.1(b). The dissociation rate of AB depends on the extent of the coupling between these two electronic states. The other circumstance of indirect dissociation is internal conversion (IC) followed by unimolecular dissociation mechanism as presented in Figure 1.1(c). After pumped to a bound excited state, the AB* excited molecule or radical can undergo internal conversion (IC) to highly vibrationally and rotationally excited (internal hot) levels in the ground electronic state. The internally excited energy levels are above the dissociation threshold of the lower or ground electronic state, and the AB* can dissociate in the lower or ground electronic state to the products. Typically, this mechanism has a longer dissociation time scale than that of the direct dissociation. The excess energy can be randomized to all the degrees of freedom to make a statistical energy distribution, with less translational energy in the photofragments.

1.4 Experimental Approach of Photodissociation Dynamics

Thanks to the advancement of the laser and molecular beam techniques in the past decades, the photodissociation dynamics of molecules and free radicals have been studies extensively. The experimental methods used to study photodissociation dynamics can be put into two categories according to the information acquired in the experiments. These two approaches are time-resolved experiments and energy-resolved experiments.

Time-resolved methods investigate the time evolution in a chemical reaction. The reaction rate and transition lifetime can be obtained from these measurements. Different motions in the photodissociation dynamics and the time scales of them are presented in Table 1.1. Zewail, known as the father of femtochemistry, and co-workers investigated the dissociation of ICN molecule.[1] The ICN was excited by a femtosecond laser radiation (photolysis pulse), and then the CN fragment was detected by observing the laser induced fluorescence with the excitation of another femtosecond laser radiation (probe laser). The amount of CN photofragment was monitored as a function of the photolysis-probe delay time and the dissociation time of ICN was obtained. These experiments provided a direct view of the process of a chemical bond breaking. Pioneered by this work and with the advancement of ultrafast techniques, researchers could investigate the photodissociation dynamics all the way down to the femtosecond time scale. However, this method does not have the energy resolution according to the uncertainty principle with the short time (~ fs) of the laser pulse.

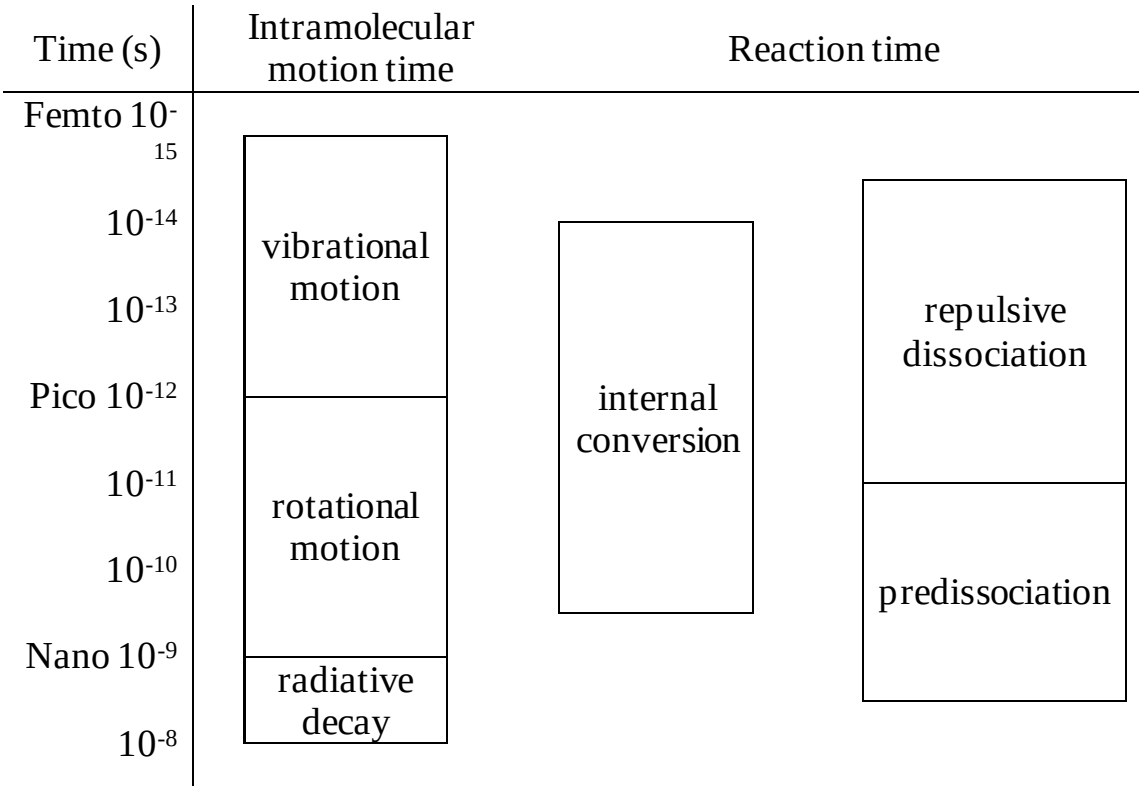

Table 1.1 Time scales of different motions in the photodissociation dynamics. The time scale is presented from femtosecond to nanosecond. The different types of intramolecular motions and dissociation mechanisms are shown.

Energy-resolved experiments record the energy partitioning and angular distributions information of the fragments. In these experiments, the reactant is typically prepared in a specific vibronic state in a molecular beam and by laser excitation. The products from the dissociation reaction are detected and analyzed with different experimental techniques. The experimental methods can be separated into two main categories, direct and indirect measurements, as shown in Figure 1.2. Absorption spectroscopy (*i.e.* Raman spectroscopy and infrared absorption spectroscopy), laser induced fluorescence (LIF), and multiphoton ionization (MPI) techniques are optical-based direct measurement methods. These experimental techniques can accurately provide information by probing the quantum states of the products with high resolution. However, these methods are usually restricted in the electronic and vibrational transitions which are optically accessible. Moreover, the background interference could also limit the applications of these optical-based methods. Finally, it is time-consuming to obtain the complete product distributions as these techniques need probe a large collection of specific states.

The product state distributions can be acquired indirectly by deriving product translational energy distribution and angular distributions using photofragment translational spectroscopy. Photofragment velocity experimental techniques include Doppler spectroscopy, photofragment imaging, and time-of-flight (TOF) spectroscopy, with the advantage of universal detection. Pioneered by Welge and co-workers, the high-*n* H-atom Rydberg time-of-flight (HRTOF) can provide great resolution and sensitivity in the measurements.[2-4] This technique provides very high resolution in the translational

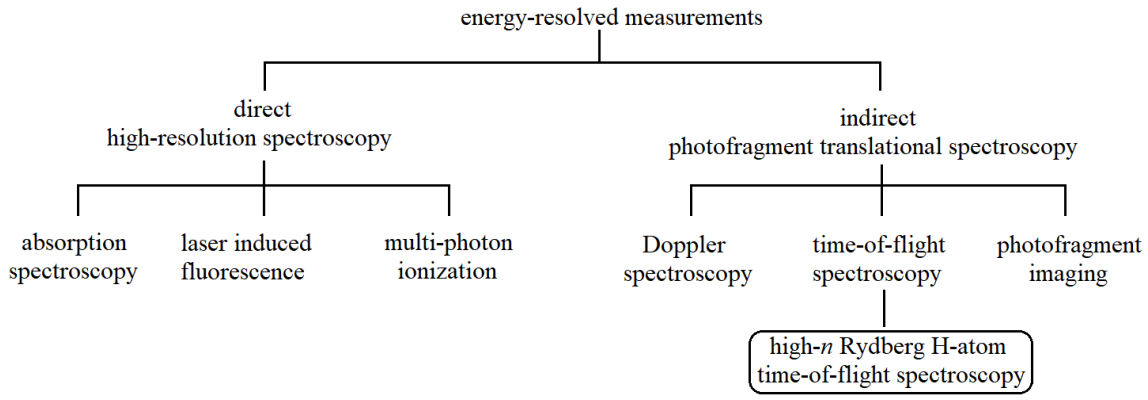

Figure 1.2 The energy-resolved experimental methods for photodissociation dynamics and the HRTOF technique.

energy distribution ($\Delta E/E \sim 0.3$-0.6%), and the rotational state distribution of the counterfragment can be observed.[2] The HRTOF technique is restricted to the molecules or radicals that contain H atoms and it can only study the dissociation dynamics of the H-atom product channels. In this dissertation, the HRTOF technique is employed to investigate the photodissociation dynamics of several free radicals.

1.5 High-*n* Rydberg H-atom Time-of-Flight Technique

1.5.1 High-*n* Rydberg H-atom

In the HRTOF technique, the TOF of the nascent H-atom product is measured. The more precise in the TOF measurement, the higher energy resolution can be achieved. The ideal case is to place a detector on the path of the flight at a certain distance and count the number of the H atoms as a function of the flight time. For the detector to count the number of atoms, the best way is to ionize the atoms and collect the electric signals. In the HRTOF experiment, all the H-atom products from the dissociation are in the ground electronic state ($1^2S_{1/2}$), due to the very high first excited state of the H atom (10.2 eV = 235.22 kcal/mol). The ionization of the H atom can be achieved on or in front of the detector, or in the reaction region, but it would be impossible to ionize the H atom in its ground electronic state on the detector because of the high ionization potential of the ground state of the H atom (13.6 eV = 313.62 Kcal/mol). The H atom produced in the reaction region can be ionized by laser radiations or electron impact, but most of the species (precursors for the radicals, radicals

of interest, and the photofragments) would be ionized as well, as they have lower ionization energies than that of H atom. The ions of other chemical species would introduce interferences on the H-atom signal measurement and the number counting of the H atoms will be inaccurate. Furthermore, the electric field utilized for extracting the ionized H atoms could change the nascent velocity of the H-atom product and the dynamic information would be lost. The way to solve this dilemma is to probe the H atoms immediately after the photodissociation with laser radiations that excite them to a high-*n* Rydberg state.

The high-*n* Rydberg H atom is the H-atom in the electronic excited Rydberg state with a very large principle quantum number. The H atoms are neutral, but with very high electronic energy so that they can be easily ionized be an electron field in front of the detector. As shown in Figure 1.3, the H atom produced from photodissociation is excited by a two-color resonant excitation. The first photon pumps the H atom from the ground state $1^2S_{1/2}$ to the excited state 2^2P via the Lyman-α transition with a photon at 121.6 nm, then the second photon at ~ 366 nm excites the H atom to a high-*n* Rydberg state. The lifetime of the 2^2P state H atom is ~ 10 ns, which is long enough for the second photon excitation. A small fraction of the high-*n* Rydberg H atoms fly towards the detector with their nascent velocities, then are field ionized in front of the detector and detected. The lifetime of Rydberg state H atom is in the order of millisecond (ms) scale,[4] longer than the time of flight of the H atom (in the tens of microseconds (μs) scale). Thus, the high-*n* Rydberg state H atom survives the flight path and can be detected with nearly 100% efficiency. The detection of the neutral metastable H atom can avoid the interference from

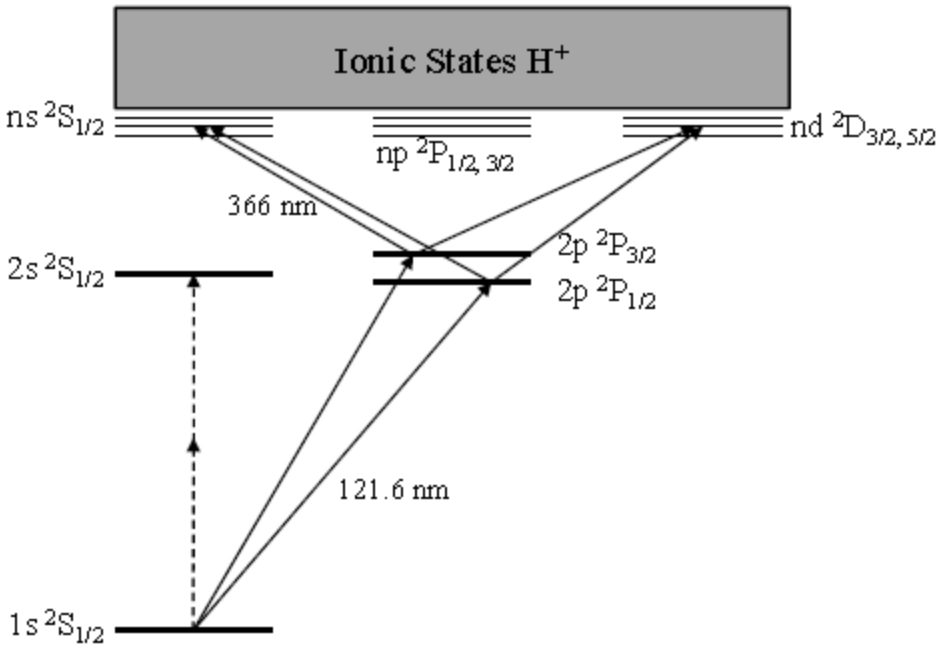

Figure 1.3 Energy diagram of the H atom and the two-color resonance excitation process of the H atom from ground state to high-*n* Rydberg state.

other species and make the HRTOF technique a powerful tool to investigate the photodissociation dynamics of molecules and radicals with high resolution and sensitivity.

1.5.2 High-*n* Rydberg H-atom Time-of-Flight Spectroscopy

The HRTOF technique is limited to the detection of the H-atoms. The H-atom photodissociation channel of a H-atom containing chemical compound can be written as:

$$\mathrm{HR}\ (v'',\ j'') + h\upsilon \rightarrow \mathrm{H} + \mathrm{R}\ (v',\ j') \tag{1.1}$$

The conservation of energy in the center-of-mass (CM) frame can be written as:

$$E_{int}^{HR} + E_{h\upsilon} = D_0(H\text{-}R) + E_{trans}^{H} + E_{trans}^{R} + E_{int}^{H} + E_{int}^{R} \tag{1.2}$$

in which E_{int}^{X} is the internal energy of species X, $E_{h\upsilon}$ is the energy of photon, $D_0(H\text{-}R)$ is the bond dissociation energy, and E_{trans}^{X} is the translational energy of species X. If the experiment is performed with the chemical compound in the molecular beam, it can be assumed that the compound is in the ground vibrational and rotational level, and the E_{int}^{HR} term is negligible. The H-atom product is in the ground state, therefore $E_{int}^{H} = 0$. The equation (1.2) can be written as:

$$E_{avail} = E_{trans}^{H} + E_{trans}^{R} + E_{int}^{R} \tag{1.3}$$

$$E_{avail} = E_{h\upsilon} - D_0(H\text{-}R) \tag{1.4}$$

In equation (1.4), the $E_{h\upsilon}$ and $D_0(H\text{-}R)$ are already known or fixed for a photodissociation at a photolysis wavelength, then this equation presents a one-to-one correspondence

between translational energy and the product internal (vibrational and rotational) energy. The internal energy distribution of the R product can be converted, and this information is helpful for determination of the dissociation mechanism.

In equation (1.3), the E_{trans}^{H} and E_{trans}^{R} are the translational energies in the center-of-mass (CM) frame and can be derived from the TOF of the H-atom form the reaction region. According to the conservation of momentum, the total translation energy of the H and R products can be expressed as:

$$E_{trans}^{H,R} = E_{trans}^{H} + E_{trans}^{R} = (1 + \frac{m_H}{m_R})E_{trans}^{H} \quad (1.5)$$

In the HRTOF experimental setup, the flight axis of the H-atom is orthogonal to the molecular beam, as shown in Figure 1.4. Figure 1.4 also present the relationship between the CM frame velocities and the laboratory frame velocities. The E_{trans}^{H} can be converted from the TOF measurement in the laboratory frame. Equation (1.5) can be rewrite into the product CM translational energy format:

$$E_{trans}^{H,R} = \left(1 + \frac{m_H}{m_R}\right) E_{trans}^{H,Lab} + \frac{m_H}{m_R} E_{trans}^{HR,Lab} = \frac{1}{2} m_H \left(1 + \frac{m_H}{m_R}\right) \left(\frac{L}{t_H}\right)^2 + \frac{m_H}{m_R} E_{trans}^{HR,Lab} \quad (1.6)$$

in which $E_{trans}^{H,R}$ is the CM translational energy of the products, $E_{trans}^{H,Lab}$ and $E_{trans}^{HR,Lab}$ are the laboratory translational energy of the H-atom product and the HR parent, L is the length of the flight path, and t_H is the TOF of the H-atom product. The second term, $\frac{m_H}{m_R} E_{trans}^{HR,Lab}$, is due to the motion of the HR parent in the molecular beam (V_{CM}) which is orthogonal to the

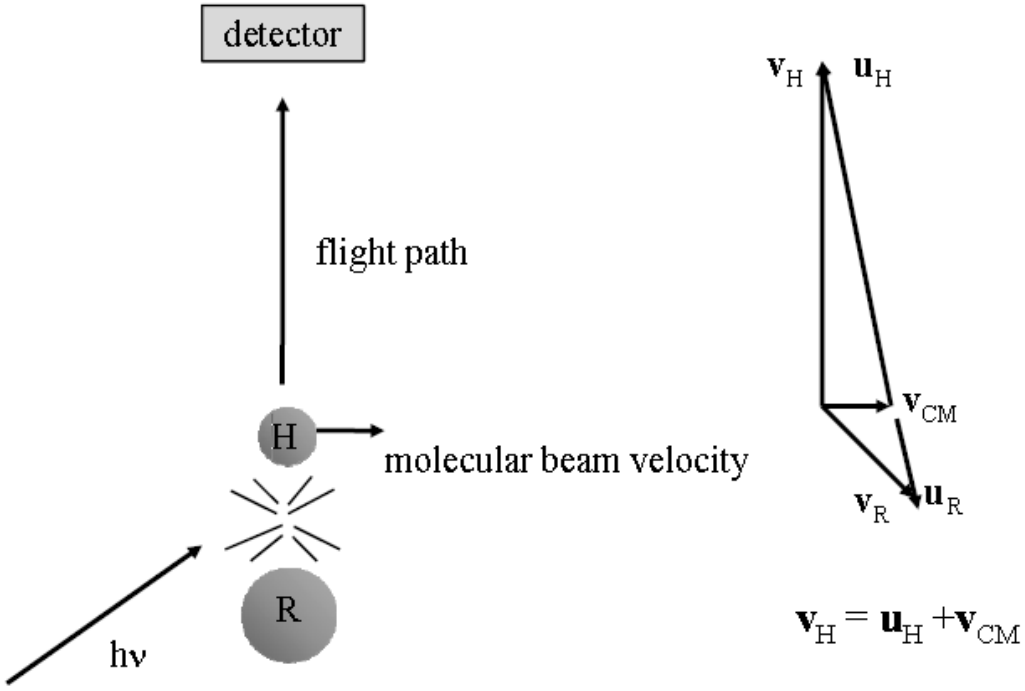

Figure 1.4 Left: The schematics of the directions of the molecular beam and flight path of the H-atom product. Right: Newton diagram of the relationship between the center-of-mass frame and the laboratory frame. The $\mathbf{v}_{CM}$ is the velocity of the center-of-mass (CM). The $\mathbf{v}_H$, $\mathbf{v}_R$ and $\mathbf{u}_H$, $\mathbf{u}_R$ are the velocities of the H-atom product and the co-fragment in the laboratory frame and CM frame, respectively.

flight path, and this term is very small compared to the first term and can be neglected. The product translational energy and internal energy can often be written as following:

$$E_{trans}^{H,R} = \frac{1}{2} m_H \left(1 + \frac{m_H}{m_R}\right) \left(\frac{L}{t_H}\right)^2 \quad (1.7)$$

$$E_{int}^{R} = E_{avail} - E_{trans}^{H,R} = E_{hv} - D_0(H\text{-}R) - \frac{1}{2} m_H \left(1 + \frac{m_H}{m_R}\right) \left(\frac{L}{t_H}\right)^2 \quad (1.8)$$

The flight path distance L is calibrated by the photodissociation of HBr with the well-studied bond dissociation energy and the spin-orbit energy splitting of the Br($^2P_{3/2}$) and Br($^2P_{1/2}$) products. The product energy distributions can be derived from the H-atom TOF spectra with equations (1.7) and (1.8) which will be used to describe the dissociation mechanism and the characteristics of the excited electronic states.

After the breaking of the H-R bond during the dissociation process, the excess energy distributes into the E_{int}^{R} and $E_{trans}^{H,R}$. The dissociation energy can be expressed as:

$$D_0(H\text{-}R) = hv - E_{trans}^{H,R} - E_{int}^{R} \quad (1.9)$$

In the extreme case, when the internal energy of the fragment R, E_{int}^{R} = 0, all the excess energy is distributed into the $E_{trans}^{H,R}$. Then by finding the largest translational energy of the products, the upper limit of the bond dissociation can be obtained:

$$D_0(H\text{-}R) \leq hv - E_{trans}^{H,R}(Max) \quad (1.10)$$

This equation can be used to facilitate the determination of the dissociation pathway since different pathways have different dissociation energies. As the bond dissociation energy can be found in several data base, the maximum translational energy of the single photon

process can be obtained and the transitional energy of the products can also be used to determine if multiphoton absorption occurs during the reaction process.

The product translational energy distribution could provide information on the dissociation pathway and its mechanism, as well as the characteristics of the excited electronic state in the photodissociation process. In the meantime, the product angular distribution could also be obtained and used to analysis the dissociation mechanism.

The angular distribution studies the recoil of the products after the dissociation. In the molecular beam, the parent HR radicals or molecules are randomly oriented initially. The linearly polarized photolysis radiation will preferentially excite the parent HR whose transition dipole moment, $\boldsymbol{\mu}$, is parallel to the electric field vector, $\boldsymbol{E}$, of the linearly polarized radiation with the absorption probability:

$$P = |\boldsymbol{\mu} \cdot \boldsymbol{E}|^2 \tag{1.11}$$

After the absorption of the photons, the transition dipole moment of the excited HR will align with the $\boldsymbol{E}$ according to the probability in equation (1.11). If the dissociation time scale is shorter than the HR rotational period, the parent HR will not have time to rotate and will dissociate along the breaking bond, giving rise anisotropic angular distribution. On the other hand, if the dissociation time scale is longer than the rotational period, the orientation of the parent HR will be randomized in space and the product recoil will be isotropic. The lifetime (or the dissociation time) information can be inferred from the product angular distribution. The photofragment angular distribution is described as:[5]

$$I(\theta) = [1 + \beta P_2(\cos\theta)]/4\pi \tag{1.12}$$

in which θ is the angle between the electric vector $\boldsymbol{E}$ and the recoil velocity vector $\mathbf{v}$ in the laboratory frame, $P_2(\cos\theta) = \frac{1}{2}(3\cos^2\theta - 1)$ is the second Legendre polynomial, and $\beta = 2P_2(\cos\chi)$ is the anisotropy parameter with χ is the angle between the transition dipole moment $\boldsymbol{\mu}$ and the recoil velocity $\mathbf{v}$ in the molecular frame. In a prompt dissociation, when $\beta = 2$, $\cos\chi = 1$ and $\boldsymbol{\mu}$ is parallel with $\mathbf{v}$, indicating a parallel transition. When $\beta = -1$, $\cos\chi = 0$ and $\boldsymbol{\mu}$ is perpendicular with $\mathbf{v}$, indicating a perpendicular transition. When $\beta = 0$, $I(\theta) = \frac{1}{4\pi}$ is independent of θ angle and corresponds to an isotropic product angular distribution. The different cases of the product angular distributions are summarized and shown in Figure 1.5. The β parameter can be calculated with the following equation:

$$\beta = \frac{I(\theta=0°)/I(\theta=90°)-1}{1+0.5[I(\theta=0°)/I(\theta=90°)]} \tag{1.13}$$

where $I(\theta = 90°)$ and $I(\theta = 0°)$ are the angular distributions with the electric vector $\boldsymbol{E}$ is perpendicular and parallel to the recoil velocity $\boldsymbol{v}$, which is same as the TOF axis. The anisotropic product angular distribution indicates that dissociation time scale is shorter than the rotational period of the parent HR which is about on the picosecond (*ps*) scale. The isotropic product angular distribution suggests that the dissociation time scale is longer than one rotational period of the parent. Note that for some cases when θ is at the magic angle ($\theta = 54.7°$), the product angular distribution is isotropic, but the dissociation time scale can be shorter than the rotational period of the parent. Sometime, the β parameter varies as a function of the product translational energy, suggesting multiple different dissociation pathways for the parent.

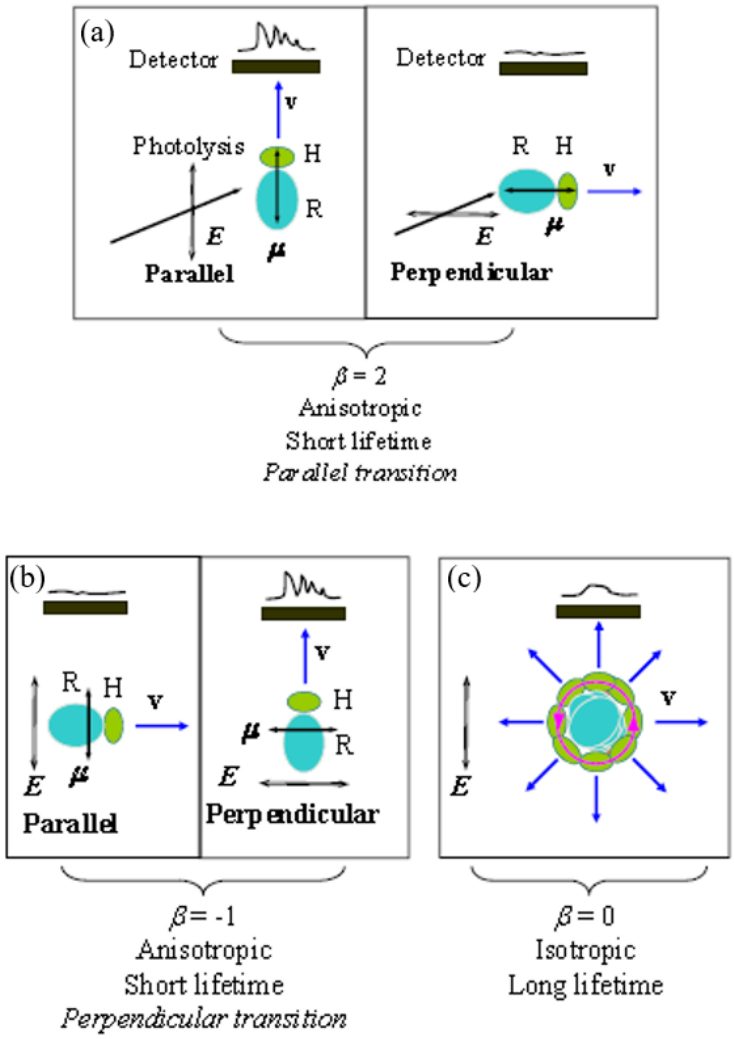

Figure 1.5 Angular distributions of the photofragments after the absorption of linearly polarized photolysis radiation with electric vector $\boldsymbol{E}$. $\boldsymbol{\mu}$ is the transition dipole moment and **v** is the recoil velocity vector. β is the anisotropy parameter. (a), (b), (c) present the different cases for anisotropic distributions with $\beta = 2$, anisotropic distributions $\beta = -1$ and isotropic distribution with $\beta = 0$, respectively.

1.6 High-*n* Rydberg H-atom Time-of-Flight Experimental Apparatus

The experimental setup for the HRTOF spectra is presented in Figure 1.6. The precursors for the radicals are mixed with the carrier gas He or Ar at a concentration of ~1-10% at a total stagnation pressure of 1.05-1.25 atm before entering the source chamber. A pulse valve is used to create a pulsed molecular beam and this beam is crossed in front of the pulse nozzle by a 193 nm laser radiation to generate the radicals of interest. The radical beam formed from the photolysis is collimated by a 1 mm diameter skimmer which is placed ~2.8 cm away from the nozzle before the beam enters the high vacuum reaction chamber (~10^7 torr). In this process, which is called supersonic expansion, the radicals undergo many collisions with the carrier gas and are cooled down both vibrationally (~ 50 K) and rotationally (~ 15 K). At 4.6 cm downstream in the high vacuum reaction chamber, the radical beam is crossed with a tunable, linearly polarized ultraviolet (UV) laser radiation that photodissociates the radicals. The wavelength of the photolysis laser radiation is monitored by a wavemeter (Burleigh WA-4500). The polarization can be changed by a Fresnel rhomb achromatic $\lambda/2$ plate for the product angular distribution measurements study. The H-atom product form the photodissociation is probed by a two-color excitation (121.6 + 366.3 nm), i.e., from 1^2S to 2^2P via the H-atom Lyman-α transition and then further to a metastable high-*n* Rydberg state (n ~ 50-90). The Rydberg H atoms fly away from the interaction region with their nascent velocities. A small portion of them reach a microchannel plate (MCP) detector positioned perpendicular to the molecular beam, and are field-ionized in front of the detector then detected. The timings of

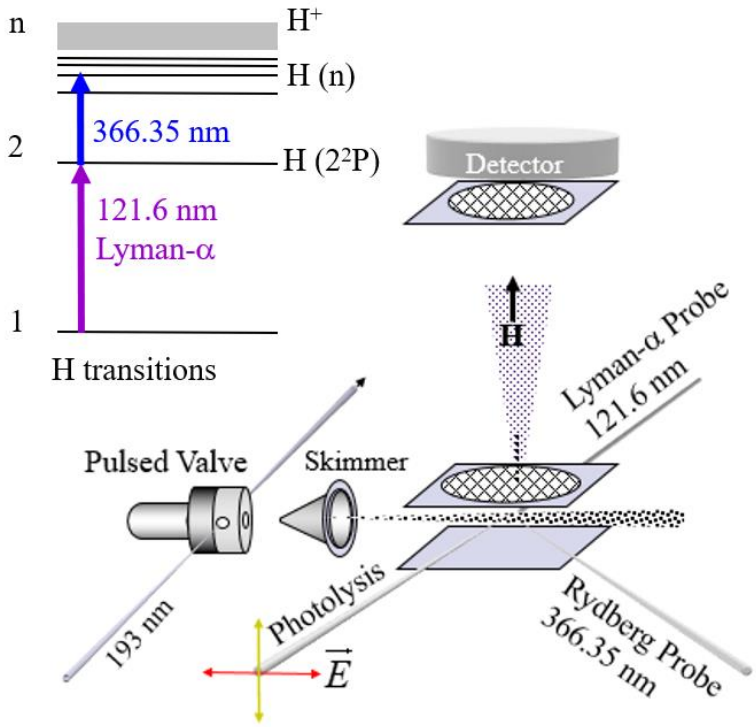

Figure 1.6 Experimental apparatus for HRTOF measurements. The insert indicates the excitation scheme of the H-tom product from the ground state to the high-*n* Rydberg state.

the pulsed molecular beam, laser radiations, and the time zero of the detector are controlled by digital delay generators (SRS DG 535). The length of the flight path is calibrated by the photodissociation of HBr with the well-studied HBr bond dissociation energy and spin-orbit energy splitting of the $Br(^2P_{3/2})$ and $Br(^2P_{1/2})$ products. The ion signals are amplified by a fast preamplifier and averaged by a multichannel scaler. Usually, the H-atom TOF spectra are acquired with 50-300k laser shots each spectrum.

Compared to other photodissociation dynamics experimental methods, the HRTOF technique can have a large reduction of the background. The voltage setup for the electric grid in the main chamber is presented in Figure 1.7. In the HRTOF measurement, interaction region of the molecular beam and the laser radiations is at the center of the repeller and the first grid. The first and second grids are ground while the repeller has a small negative voltage. In the interaction region, some of the cations can be created by the 121.6 nm and UV multiphoton ionization of any compounds in the molecular beam, and these cations will be removed by the negative voltage on the repeller to prevent them from flying to the MCP detector. Furthermore, one of the MCP front grids has a small positive bias and it can further prevent any cations from reaching to the MCP detector. These charged grids could prevent the cations going into the detector, however, some negatively charged particles, such as electrons, will be accelerated by them and move toward the detector. A -3kV voltage is applied in front of the detector and the negative charged particles will be attracted and stopped from entering the detector. The neutral Rydberg H-atoms will not be affected by the space charge and stray field interferences in the main

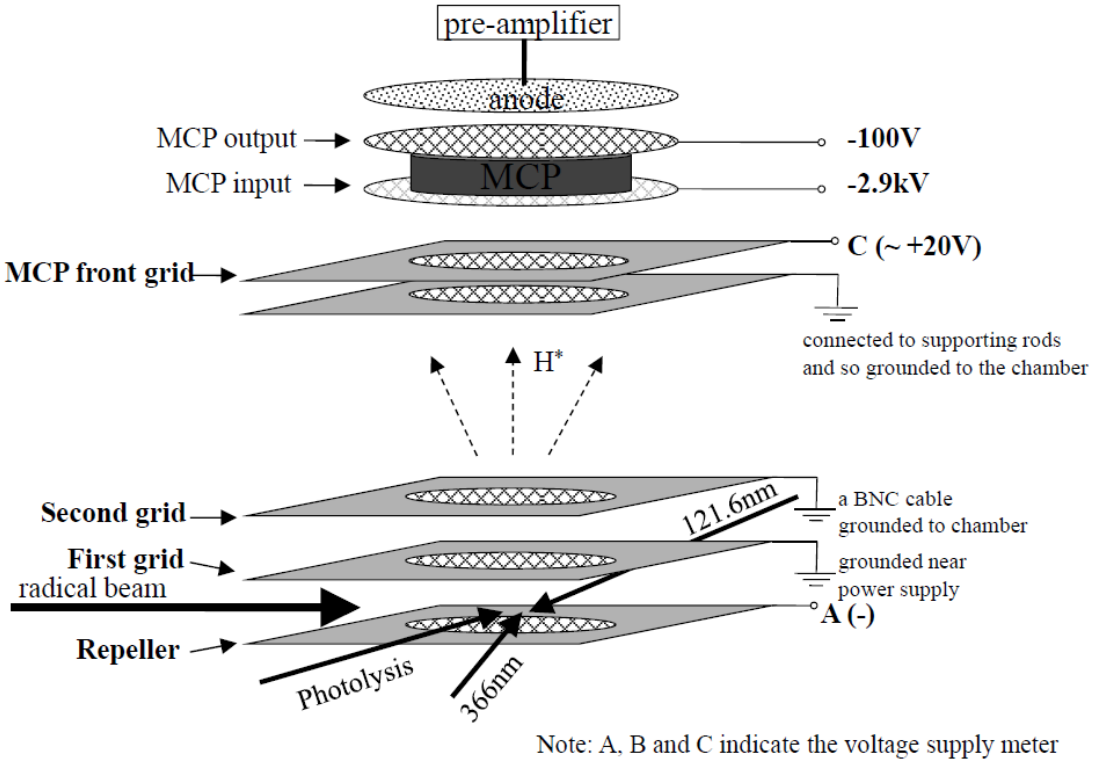

Figure 1.7 Schematic of the voltage setup for the electric grids in the main chamber for the high-*n* Rydberg H-atom detection in the HRTOF technique.

chamber, and the nascent velocity information of the H-atoms will be kept. A much better resolution and sensitivity can be achieved with the HRTOF technique.

1.7 REMPI and TOFMS Experimental Setup

This experimental apparatus can be applied for resonance-enhanced multiphoton ionization (REMPI) and TOF mass spectroscopy (TOFMS) experiments by setting different voltages of the girds in the main chamber, as shown in Figure 1.8. The molecular beam and laser beams alignments for these two experimental setups are the same as the HRTOF technique, but the wavelengths of some laser radiations and the voltage of repeller and grids are different. The repeller and the first grid are applied with positive charges of +765V and +596V, respectively, while the MCP front grid is set to ground for the REMPI and TOFMS experiments. The ions formed in these experiments are accelerated by the repeller and first gird then enter the MCP detector. The arrival time of the ions is related to its mass-to-charge ratio (m/z) and expressed with the equation below:

$$(t - t_0)^2 \times C = \frac{m}{z} \quad (1.14)$$

where t_0 is the absolute time zero when the ions are generated, and C is a constant. In the mass spectrum, the H-atom peak and the precursor peak are readily assigned as they are the two most intense peaks and the H-atom peak has the smallest m/z value. With the

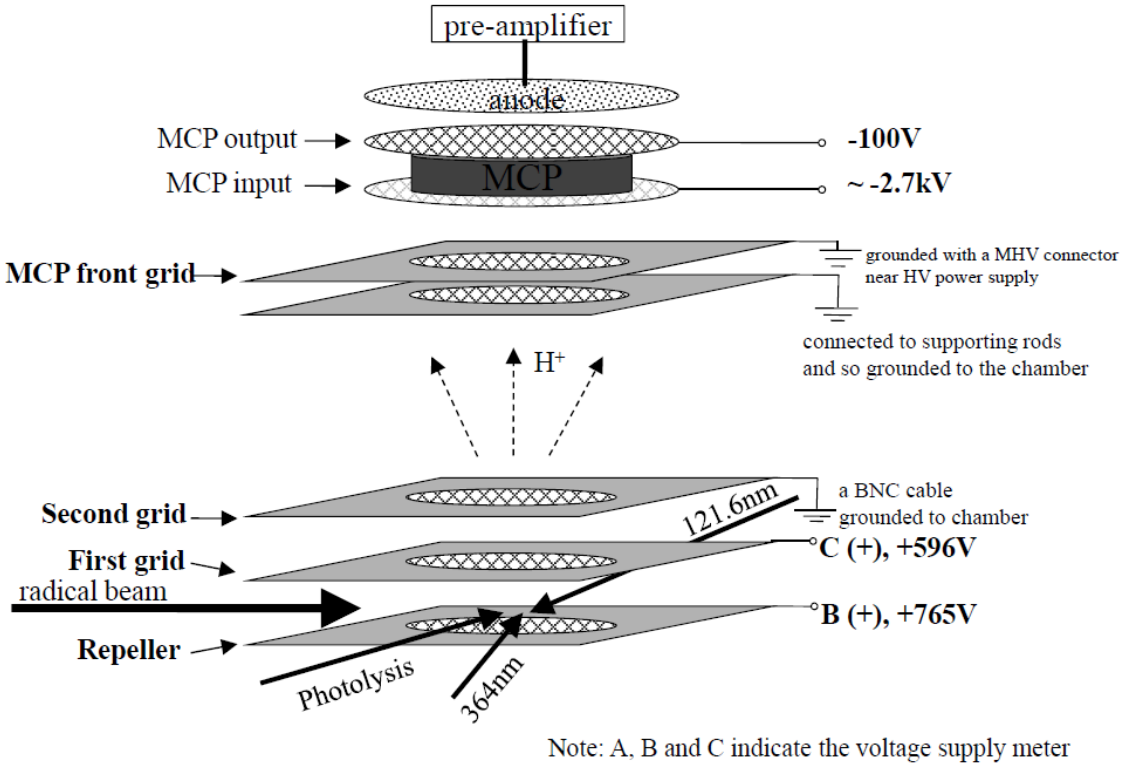

Figure 1.8 Schematic of the voltage setup for the electric grids in the main chamber for the H^+ and R^+ detection in the REMPI and TOFMS techniques.

information above, the constant C and t_0 value can be solved and calibrated and all the peaks in the TOFMS can be identified, after the time to mass conversion.

The VUV photoionization mass spectroscopy is used to identify and characterize the species in the molecular beam. In the mode, the 193 nm radiation and 121.6 nm radiation are on, while the UV photolysis radiation and the Rydberg probe laser radiation are not used. The TOF mass spectra are saved by a digital oscilloscope and the mass peaks are characterized after the time-to-mass conversion. In the measurement, two types of TOFMS spectra were taken: (1) full spectrum with the 193 nm radiation on for the radical production and the 121.6 nm radiation on to ionize the species in the molecular beam; (2) background spectrum with the 193 nm radiation off but the 121.6 nm radiation on. The net mass spectrum is obtained by subtracting the background spectrum from the full spectrum.

The REMPI spectrum of radical R can be applied to investigate the spectroscopy of the free radicals. In the setup, the 193 nm radiation is on to generate the radical from the precursor and the UV REMPI radiation is scanned to hit a resonance state of the radical and a second photon of the UV radiation ionizes the radical to product R^+ using a 1 + 1 REMPI scheme. The probe laser radiations (121.6 nm radiation and the Rydberg probe) are not used in this measurement. The ion signals for the radical is monitored by digital oscilloscope and integrated as a function of the ionization wavelength using a Boxcar averager. Boxcar averager consists of a gate generator and gated integrator and a specific portion of the mass spectrum (in a TOF window) is selected then integrated and averaged. The averaged signal is sent to the data acquisition system and the REMPI spectrum is obtained.

In this dissertation, the photodissociation dynamics of several free radicals are investigated by the HRTOF technique. Chapters 2 and 3 discuss the photodissociation of hydroxy radical. Hydroxy radical is an important intermediate in combustion and atmospheric chemistry, and it is a prototypic open-shell diatomic system for the investigation of the photodissociation dynamics with multiple potential energy curves and nonadiabatic interactions. Chapter 4, Chapter 5, and Chapter 6 investigate the UV photodissociation dynamics of ethyl, butyls (*n*-butyl, *s*-butyl, and *t*-butyl), and 1-pentyl radicals. These are expanding works for the photodissociation of alkyl radicals, and the different dynamics in the dissociation of primary, secondary, and tertiary alkyl radicals are studied. Chapter 7 discusses the photodissociation dynamics of 2-propenyl radical. This is the third isomer in the alkenyl C_3H_5 series, which provide a good system to investigate the *isomer-specific* photochemistry. Chapter 8 studies the near-UV photodissociation dynamic of the vinoxy radical. The vinoxy radical is a prototype of the unsaturated alkoxy radical, and it can be produced from the reactions of small organic compounds with oxygen atom or hydroxy radical. It is an important radical in combustion and atmospheric chemistry. Chapter 9 investigated the UV photodissociation dynamics of the thiomethoxy radical. Thiomethoxy radical belongs to the sulfur system and it is an important intermediate in atmospheric oxidation processes of sulfur compounds.

Reference

1. N. F. Scherer, J. L. Knee, D. D. Smith, and A. H. Zewail, *J. Phys. Chem*. **89**, 5141 (1985).

2. L. Schnieder, W. Meier, K. H. Welge, M. N. R. Ashfold, and C. M. Western, *J. Chem*. *Phys.* **92**, 7027 (1990).

3. L. Schnieder, K. Seekamp-Rahn, J. Borkowski, E. Wrede, K. H. Welge, F. J. Aoiz, L. Bañiares, M. J. Mello, V. J. Herrero, V. S. Rábanos, and R. E. Wyatt, *Science* **269**, 207 (1995).

4. L. Schnieder, K. Seekamp-Rahn, F. Liedeker, H. Steuwe, and K. H. Welge, *Faraday Discuss. Chem*. *Soc.* **91**, 259 (1991).

5. R. N. Zare, *Mol. Photochem*. **4**, 1 (1972).

Chapter 2

State-to-State Predissociation Dynamics of Hydroxyl Radical via the $A^2\Sigma^+$ State

Abstract

Photo-predissociation dynamics of the jet-cooled hydroxyl radical (OH) via several rovibrational levels (v' = 2, 3, and 4, N' = 0, 1, and 2) in the $A^2\Sigma^+$ state are studied by using the high-n Rydberg-atom time-of-flight (HRTOF) technique. Spin-orbit branching fractions and angular distributions of the H + $O(^3P_{J=2,1,0})$ product channels are measured. The $A^2\Sigma^+$, v' = 2 and 3 states of OH predissociate predominantly via the single $1^4\Sigma^-$ repulsive state, while at the $A^2\Sigma^+$, v' = 4 state dissociates via the $1^4\Sigma^-$, $1^2\Sigma^-$, and $1^4\Pi$ repulsive states and interferences among these dissociation channels play an important role in the $O(^3P_{J=2,1,0})$ product distributions. The experimental $O(^3P_{J=2,1,0})$ product fine-structure branching ratios are in excellent agreement with the full quantum calculation results. The product angular distributions strongly depend on the different rotational levels. The measured anisotropy parameters are in a reasonable agreement with the simulation. Using dissociation lifetime, excitation frequency, rotational level, and rotational constant [Kim *et al.* J. Chem. Phys. 2006, 125, 133316]. The predissociation time scales of the OH radical are measured to be 130 ± 30 ns and ~14 ps for $A^2\Sigma^+$(v' = 2, N' = 2, F_1) and $A^2\Sigma^+$(v' = 4, N' = 0, F_1) states, respectively.

2.1 Introduction

The hydroxy radical (OH) plays a key role in combustion and atmospheric chemistry processes. In the atmosphere, the hydroxy radicals are produced from a sequence of photochemical reactions (e.g., $O_3 + h\nu \rightarrow O(^1D) + O_2$ and $O(^1D) + H_2O \rightarrow OH + OH$)[1] and from decomposition of the Criegee intermediates formed in the ozonolysis of alkenes.[1-3] The OH radicals react with a large number of volatile organic compounds in the atmosphere, such as alkanes, alkenes, ketone, alkyne, and ethers, etc..[4-6] The hydroxy radical is also a prototypic open-shell diatomic system for photodissociation study, which involves multiple potential energy curves (PECs) and their nonadiabatic interactions.

The ground electronic and lower electronically excited states of the OH radical are well investigated with experimental[7-15] and theorical works.[14,16-36] As shown in Figure 2.1, the ground-electronic state, $X^2\Pi$, correlates with the ground state products $O(^3P_J) + H(^2S)$. The $A^2\Sigma^+$ state correlates with the excited-state products $O(^1D) + H(^2S)$, and this state is crossed by three repulsive states, $1^4\Sigma^-$, $1^2\Sigma^-$, and $1^4\Pi$, which correlate with the $O(^3P_J) + H(^2S)$ products. The spectroscopy of the $A^2\Sigma^+ - X^2\Pi$ band system, and the vibrational and rotational constants of the $A^2\Sigma^+$ state of OH are well characterized.[16,18,21,23,24,28-30,33,35-37] The lifetime and the predissociation dynamics of several vibrational levels in the $A^2\Sigma^+$ state are determined, with $\tau < 150$ ns for $v' = 2$, ~300 ps for $v' = 3$, and ~20 ps for $v' = 4$, respectively.[13,33]

The fine-structure branching ratios of the $H + O(^3P_{J=2,1,0})$ products from predissociation of the OH $A^2\Sigma^+$ state have been investigated experimentally[38,39] and

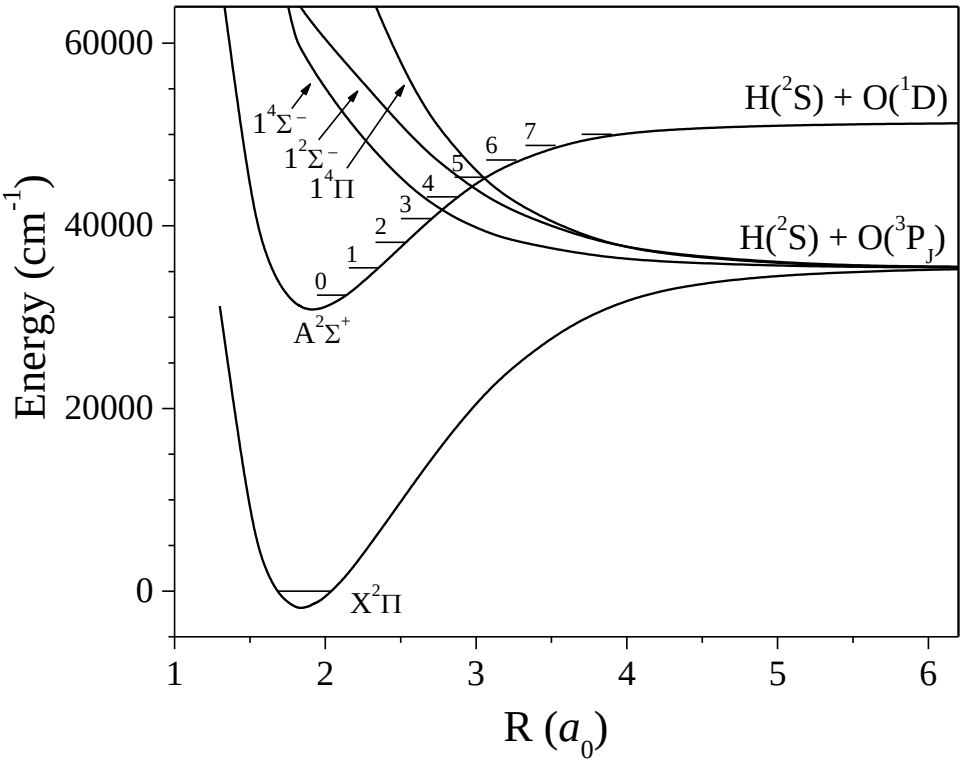

Figure 2.1. Potential energy curves of the OH electronic states. The vibrational levels of the $A^2\Sigma^+$ state are labeled. The information is from Ref. 10 and 13.

theoretically.[13] Yarkony and coworker examined the state-specific predissociation of OH at $A^2\Sigma^+$ state using multichannel scattering theory, spin-orbit couplings, and Coriolis couplings.[13] For v' = 2 and 3 (J' = 0.5), the energy levels are below the crossing of $A^2\Sigma^+$ and $1^4\Sigma^-$, and the decays would be predominantly via the single state ($1^4\Sigma^-$). While the v' = 4 (J' = 0.5) state lies between the crossing points of $1^4\Sigma^-$ and $1^2\Sigma^-$, all the three repulsive states contribute to the predissociation. In the sudden (diabatic) limit, the $O(^3P_J)$ branching fractions are determined by the projection of the molecular wavefunctions to the atomic product basis sets, and are given as $O(^3P_{J=2,\,1,\,0})$ = 0.611:0.167:0.222; 0.556:0.333:0.111; 0.306:0.250:0.444 for the $1^4\Sigma^-$, $1^2\Sigma^-$, and $1^4\Pi$ repulsive states, respectively. From the multichannel scattering calculations including all the nonadiabatic interactions from the Franck-Condon (FC) region to the asymptotic region, the branching ratios are determined to be $O(^3P_{J=2,1,0})$ = 0.676:0.135:0.189; 0.675:0.141:0.184; 0.888:0.091:0.021 for v' = 2, 3, and 4 (N' = 0), respectively.

Zhang and coworkers studied the fine-structure distributions of the H + $O(^3P_J)$ product from the dissociation of the OH via the $A^2\Sigma^+$ (v' = 3, and 4; J' = 0.5) state experimentally.[38] For v' =3, J' = 0.5, the spin-orbit branching ratios $O(^3P_{J=2,1,0})$ = 0.676 ± 0.010: 0.138 ± 0.013:0.186 ± 0.017,[38] in excellent agreement with the full quantum calculation, 0.675:0.141:0.184.[13] This indicates that $1^4\Sigma^-$ dominates in the predissociation of v' = 3, $A^2\Sigma^+$ state of OH, with spin-orbit and Coriolis interactions in the recoupling zone being not significant. For v' = 4, the spin-orbit branching ratios $O(^3P_{J=2,1,0})$ = 0.873 ± 0.026:0.102 ± 0.028:0.025 ± 0.005, also in good agreement with the full-quantum calculation values of 0.888:0.091:0.021.[13] The predissociation of OH on $A^2\Sigma^+$ state, v' = 4,

is confirmed to be via multiple repulsive states ($1^4\Sigma^-$, $1^2\Sigma^-$, and $1^4\Pi$), and revealing the quantum interferences among these repulsive states without significant spin-orbit and Coriolis interactions in the recoupling zone. The spin-orbit branching ratio measurements agreed well with the full-quantum multichannel scattering calculation including all the nonadiabatic interactions from the FC region to asymptotic region, as shown in the predissociation processes. Parker and coworkers studied the predissociation of the $A^2\Sigma^+$ (v' = 3) state of the OH radical.[39] The spin-orbit product branching ratios was obtained with $O(^3P_{J=2,1,0})$: 0.58:0.20:0.22 $\pm$ 0.07, with the same order as the experimental result of Zhang[38] and the theory from Yarknony.[13]

In this chapter, we report our recent work which extends our previous study on the spin-orbit branching fractions of the $O(^3P_{J=2,1,0})$ product from the predissociation of OH *via* several rovibrational levels in the $A^2\Sigma^+$ state. The $O(^3P_{J=2,1,0})$ product branching ratios and H-atom product angular distributions are measured. Dissociation lifetimes of the OH radical on the $A^2\Sigma^+$ (v' = 2 and 4) state are investigated.

2.2 Experimental

The high-*n* Rydberg-atom time-of-flight (HRTOF) technique was applied in this study, and the details of this technique and the experimental apparatus have been reported in previous publications.[38,40-42] HNO_3 ($\geq$ 99.5%, Fluka) was used as the precursor, and the OH molecular beam was formed by photolysis the precursor in Ar (~ 5%, total pressure ~ 1.2 atm) in front of a pulsed nozzle with a 193 nm radiation from an ArF excimer laser.

The OH radical beam created from the photolyzing was subsequently cooled by supersonic expansion and then collimated downstream by a skimmer into a high-vacuum chamber. In the photolysis region, the OH radical was photodissociated by a tunable, linearly polarized UV laser radiation (230 to 264 nm, 2 to 6 mJ/pulse, linewidth ~ 0.2 cm^{-1}). A wavemeter (Burleigh WA-4500) was used to monitor the photolysis wavelength. The polarization of the photolysis radiation can be shifted by a Fresnel-Rhomb achromatic λ/2 plate for the product angular distribution measurements. The effective rotational temperature of the OH radical in the beam was estimated to be ~ 50 K based on the relative singlet intensities from several initial rotational levels, with the ground state ($X^2\Pi_{3/2}$, v = 0, J = 1.5, F_1) being predominantly populated.[38,43,44] By tuning the photolysis laser wavelength precisely to the resonant wavelengths of the well-known OH transitions [$A^2\Sigma^+$ (v' = 2, 3, or 4, N', J', F_1) ← $X^2\Pi$ (v'' = 0, N'', J'', F_1)], specific rovibrational levels of the OH radical on the $A^2\Sigma^+$ state can be reached. The H-atom products from the photodissociation of OH were excited by two-color resonant excitation (121.6 nm + 366.2 nm), i.e., from 1^2S to 2^2P via the Lyman-α transition and then to a high-n Rydberg state. A small fraction of the metastable H atoms drifted with their nascent velocities to a microchannel plate (MCP) detector that was positioned perpendicular to the molecular beam and were field ionized in front of the detector and detected. The nominal flight distance was 37.24 cm, which was calibrated by photodissociation of HBr with the well-studied HBr bond dissociation energy and the spin-orbit energy splitting of the Br ($^2P_{3/2}$) and Br ($^2P_{1/2}$) products. The H-atom TOF spectra were typically acquired with ~ 100 k laser firings for each spectrum.

2.3 Results

The H-atom TOF spectra of the photodissociation of OH via the $A^2\Sigma^+$ (v' = 2, 3, or 4) ← $X^2\Pi$ (v'' = 0) transition resonances display several sharp peaks and a weak broad background. When the photolysis laser frequency was off the transition resonances (by ~ 1 cm^{-1}), the sharp peaks disappeared and only the weak broad background was present. By integrating the sharp peaks in the TOF spectra with different photolysis wavelengths near the transition resonances, the H-atom photofragment yield (PFY) spectra can be acquired. The PFY spectra reproduce the OH $A^2\Sigma^+ \leftarrow X^2\Pi$ transition absorption lines. The lines positions are in a good agreement with the literature, and the linewidths are consistent with the predissociation lifetimes of the OH radical.[13] This observation confirms that the sharp peaks in the H-atom TOF spectra were due to the predissociation of the OH radical via the $A^2\Sigma^+$ state.

The center-of-mass (CM) $H(^2S) + O(^3P_J)$ product translational energy distributions, $P(E_T)$, can be calculated from the H-atom TOF spectra with the following equation:

$$E_T = \left(1 + \frac{m_H}{m_O}\right) E_H + \frac{m_H}{m_O} E_{OH} = \frac{1}{2} m_H \left(1 + \frac{m_H}{m_O}\right) \left(\frac{L}{t_H}\right)^2 + \frac{m_H}{m_O} E_{OH}$$

in which E_H and E_{OH} are the laboratory translational energy of the H-atom product and the parent hydroxy radical, L is the length of the TOF path, and t_H is the H-atom product flight time. The second term is due to the motion of the parent hydroxy radical in the molecular beam which is perpendicular to the TOF path, and this term is estimated to be around 23 cm^{-1} (based on the beam velocity of ~ 700 m/s for the OH/Ar gas mixture). The CM product

translational energy and angular distributions can be described as $P(E_T, \theta) = \frac{1}{4\pi} P(E_T)$ [1 + $\beta(E_T)$ $P_2(\cos\theta)$], where β is the anisotropy parameter ($-1 \leq \beta \leq 2$), θ is the angle between the electronic vector of the linearly polarized photolysis radiation and the nascent velocity vector of the H-atom product (i.e., the direction of the TOF axis), $P(E_T)$ is the angle integrated product translational energy distribution, and $P_2(\cos\theta)$ is the second Legendre polynomial.[45] The translational energy dependent anisotropy, $\beta(E_T)$, can be calculated as $\beta(E_T) = 2\,[P_{\parallel}(E_T) - P_{\perp}(E_T)]/\,[P_{\parallel}(E_T) + 2P_{\perp}(E_T)]$. At the magic angle $\theta_m = 54.7^o$, the $P_m(E_T)$ is proportional to the angle integrated distribution $P(E_T)$, then it is usually used to calculated the average translational energy release and the branching ratios of different dissociation channels. $P_m(E_T)$ can be derived from the experimental measurements of $P_{\parallel}(E_T)$ and $P_{\perp}(E_T)$.

2.3.1 v' = 2 Vibronic Transitions

Figure 2.2 (a) and (c) show the $P(E_T)$ distributions of the photodissociation of the OH radical with the linearly polarized photolysis radiation parallel and perpendicular to the TOF axis via the $A^2\Sigma^+$ (v' = 2, J' = 0.5, F_1) ← $X^2\Pi$ (v'' = 0, J'' = 1.5, F_1) transition[$P_1(1.5)$], and Figure 2.2 (b) is the $P_m(E_T)$ distribution calculated from (a) and (c). The three peaks correspond to the three spin-orbit product channels $O(^3P_{J=2,1,0}) + H(^2S)$, and they are deconvoluted with asymmetric double Gaussian line shape. The line shape of the peaks is well established by fitting the ground state $O(^3P_2)$ peak which is well separated and has the strongest intensity, then the $O(^3P_1)$ and $O(^3P_0)$ peaks are deconvoluted by using the same line shape with different peak heights, and the relative positions of the three peaks

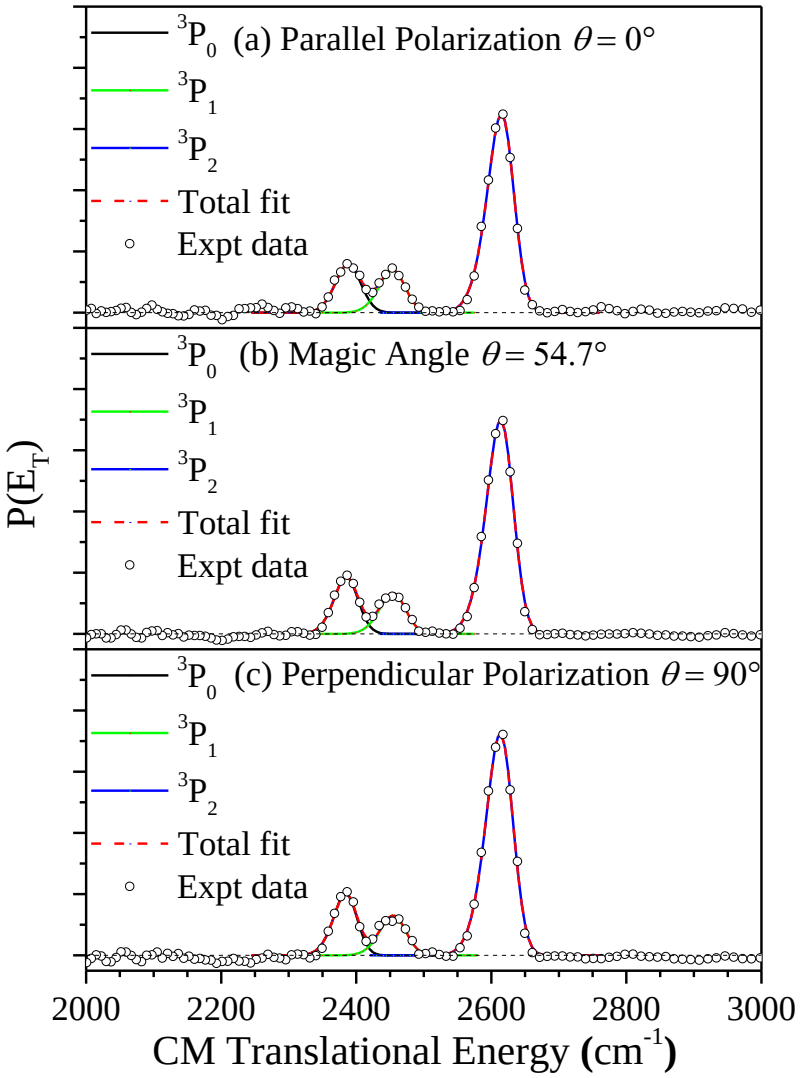

Figure 2.2. Center-of-mass translational energy distributions, P(E_T)'s of the H(^{2}S) + O(^3P_J) products from the predissociation of the OH ($A^2\Sigma^+$, $v' = 2$, $N' = 0$, $J' = 0.5$, F_1) radical via the $P_1(1.5)$ transition. The P(E_T) distributions are converted from the TOF spectra with the linearly polarized photolysis radiation parallel and perpendicular to the TOF path, and the one at magic angle is calculated from the parallel and perpendicular distributions. The spin-orbit splitting of the O($^3P_{J=2,1,0}$) sublevels are deconvoluted using Gaussian functions. See text for more details.

are fixed using the spin-orbit splitting energies of the $O(^3P_{J=2,1,0})$ components.[46] The relative peak areas in the best fit from the $P_m(E_T)$ distributions provided the spin-orbit branching ratios of the $O(^3P_{J=2,1,0})$ product from OH ($A^2\Sigma^+$, $v' = 2$, $J' = 0.5$) to be 0.705 ± 0.025: 0.135 ± 0.026: 0.160 ± 0.036, and the error bars represent the 95% confidence limit. Note that the HRTOF technique, as based on detection of the H-atom fragment, has a same detection sensitivity for the $O(^3P_J)$ sublevel product channels. The branching fractions via the $Q_1(1.5)$ and $R_1(1.5)$ transitions of ($A^2\Sigma^+$, $v' = 2$) have the values close to those via the $P_1(1.5)$ transition. The anisotropy parameters for the different $O(^3P_{J=2,1,0})$ branches are calculated from the deconvoluted peak areas in the $P(E_T)$ distributions at the parallel and perpendicular polarizations. The anisotropy β parameters for the three $O(^3P_{J=2,1,0})$ branches via the $P_1(1.5)$ transition are -0.10 ± 0.14, 0.06 ± 0.22, and -0.12 ± 0.10 for $O(^3P_2)$, $O(^3P_1)$, and $O(^3P_0)$, respectively, similar within the error limit. The weighted average of β for $P_1(1.5)$ is -0.09 ± 0.11. The same measurements for $Q_1(1.5)$ and $R_1(1.5)$ transitions were taken to study the predissociation of OH via different rovibrational levels ($J' = 1.5$ and2.5) of $A^2\Sigma^+$ ($v' = 2$), and the result of the branching ratios and anisotropy parameters of the H + $O(^3P_{J=2,1,0})$ channels are shown in Table 2.1 and Table 2.2. The $O(^3P_{J=2,1,0})$ spin-orbit branching ratios vary slightly with different J'. The anisotropy parameters for $Q_1(1.5)$ transitions are negative and similar for the different $O(^3P_{J=2,1,0})$ product channels, with a weighted average of -0.12 ± 0.09. Those of the $R_1(1.5)$ transitions are positive and also similar for the different $O(^3P_{J=2,1,0})$, with and weighted average of 0.37 ± 0.12. All the branching ratio and anisotropy parameter results via the $P_1(1.5)$, $Q_1(1.5)$, and $R_1(1.5)$ transitions are summarized in Table 2.1 and Table 2.2.

Table 2.1. Experimental fine structure branching ratios (BR) of the O($^3P_{J=2,1,0}$) fragments from the predissociation of the OH $A^2\Sigma^+$ (v' = 2, 3, and 4) states with the theoretical predictions. The error is 95% confidence limit.

				$BR_{expt.}$			BR_{theo}[b]		
		N'	J'	$^3P_2$	$^3P_1$	$^3P_0$	$^3P_2$	$^3P_1$	$^3P_0$
v'=2	$P_1(1.5)$	0	0.5	0.705±0.025	0.135±0.026	0.160±0.036	0.676	0.135	0.189
	$Q_1(1.5)$	1	1.5	0.673±0.024	0.129±0.034	0.198±0.019			
	$R_1(1.5)$	2	2.5	0.650±0.040	0.148±0.031	0.202±0.018			
v'=3	$P_1(1.5)$[a]	0	0.5	0.676±0.010	0.138±0.013	0.186±0.017	0.675	0.141	0.184
	$Q_1(1.5)$	1	1.5	0.662±0.005	0.144±0.011	0.194±0.013			
	$R_1(1.5)$	2	2.5	0.667±0.035	0.138±0.011	0.195±0.025			
v'=4	$P_1(1.5)$[a]	0	0.5	0.873±0.026	0.102±0.028	0.025±0.005	0.888	0.091	0.021
	$Q_1(1.5)$	1	1.5	0.874±0.019	0.092±0.015	0.034±0.014			
	$R_1(1.5)$	2	2.5	0.866±0.042	0.101±0.022	0.033±0.020			

[a] Ref. 38. W. Zhou, Y. Yuan, and J. Zhang, *J. Chem. Phys.* **119**, 9989 (2003).
[b] Ref. 13. G. Parlant and D. R. Yarkony, *J. Chem. Phys.* **110**, 363 (1999).

Table 2.2. Experimental measurements of the anisotropy parameter β of predissociation of the OH $A^2\Sigma^+$ (v' = 2, 3, and 4) states with the predicted β values. The error is 95% confidence limit.

				β_{exp}				β_{cal}
		N'	J'	$^3P_2$	$^3P_1$	$^3P_0$	Weighted Average	
v'=2	$P_1(1.5)$	0	0.5	-0.10±0.14	0.06±0.22	-0.12±0.10	-0.09±0.11	0.00
	$Q_1(1.5)$	1	1.5	-0.13±0.11	-0.10±0.11	-0.11±0.20	-0.12±0.09	-0.60
	$R_1(1.5)$	2	2.5	0.41±0.13	0.32±0.45	0.30±0.25	0.37±0.12	0.38
v'=3	$P_1(1.5)$	0	0.5	0.00±0.03	-0.01±0.12	0.02±0.09	0.00±0.03	0.00
	$Q_1(1.5)$, $^QP_{21}(1.5)$	1	1.5	-0.39±0.30	-0.38±0.24	-0.32±0.21	-0.37±0.21	-0.60
	$R_1(1.5)$, $^RQ_{21}(1.5)$	2	2.5	0.47±0.05	0.42±0.17	0.45±0.14	0.46±0.05	0.38
v'=4	$P_1(1.5)$	0	0.5	-0.02±0.07	0.04±0.16	0.11±0.51	-0.01±0.07	0.00
	$Q_1(1.5)$, $^QP_{21}(1.5)$	1	1.5	-0.69±0.11	-0.67±0.24	-0.72±0.29	-0.69±0.10	-0.72
	$R_1(1.5)$, $^RQ_{21}(1.5)$	2	2.5	0.36±0.16	0.30±0.21	0.31±0.25	0.35±0.14	0.41

2.3.2 v' = 3 Vibronic Transitions

The predissociation dynamics of the OH radical ($A^2\Sigma^+$, v' = 3, J' = 1.5 and 2.5, F_1) are studied via the $Q_1(1.5)$ and $R_1(1.5)$ transitions. Figure 2.3 (a) and (c) present the P(E_T) distributions with the polarization of the photolysis radiation parallel and perpendicular to the TOF path via the $Q_1(1.5)$ transitions. The P(E_T) distributions at the magic angle is calculated from those at the parallel and perpendicular polarizations and shown in Figure 2.3 (b). The branching fractions and the anisotropy parameters for the $O(^3P_{J=2,1,0})$ spin-orbit product channels from the predissociation of OH via the $Q_1(1.5)$ transition are obtained based on the deconvoluted peak areas. The relative peak areas give $O(^3P_{J=2,1,0})$ = 0.662 ± 0.005: 0.144 ± 0.011: 0.194 ± 0.013 for the $Q_1(1.5)$ transition. The branching fractions via the $R_1(1.5)$ transition have a similar result (0.667 ± 0.035, 0.138 ± 0.011, and 0.195 ± 0.025 for $O(^3P_2)$, $O(^3P_1)$, and $O(^3P_0)$, respectively). The spin-orbit product branching factions via the $Q_1(1.5)$ and $R_1(1.5)$ transitions are almost identical to those via the $P_1(1.5)$ transition, which were investigated by experimental and theoretical work previously.[13,38] The anisotropy β parameter for each $O(^3P_{J=2,1,0})$ spin-orbit product are negative for the $Q_1(1.5)$ transition (-0.39 ± 0.30, -0.38 ± 0.24, and -0.32 ± 0.21 for $O(^3P_2)$, $O(^3P_1)$, and $O(^3P_0)$, respectively, with a weighted average of -0.37 ± 0.21), about 0 for the $P_1(1.5)$ transition (0.00 ± 0.03, -0.01 ± 0.12, and 0.02 ± 0.09 for $O(^3P_2)$, $O(^3P_1)$, and $O(^3P_0)$, respectively, with a weighted average of 0.00 ± 0.03), and positive for the $R_1(1.5)$ transition (0.47 ± 0.05, 0.42 ± 0.17, and 0.45 ± 0.14 for $O(^3P_2)$, $O(^3P_1)$, and $O(^3P_0)$, respectively, with a weighted average of 0.46 ± 0.05).

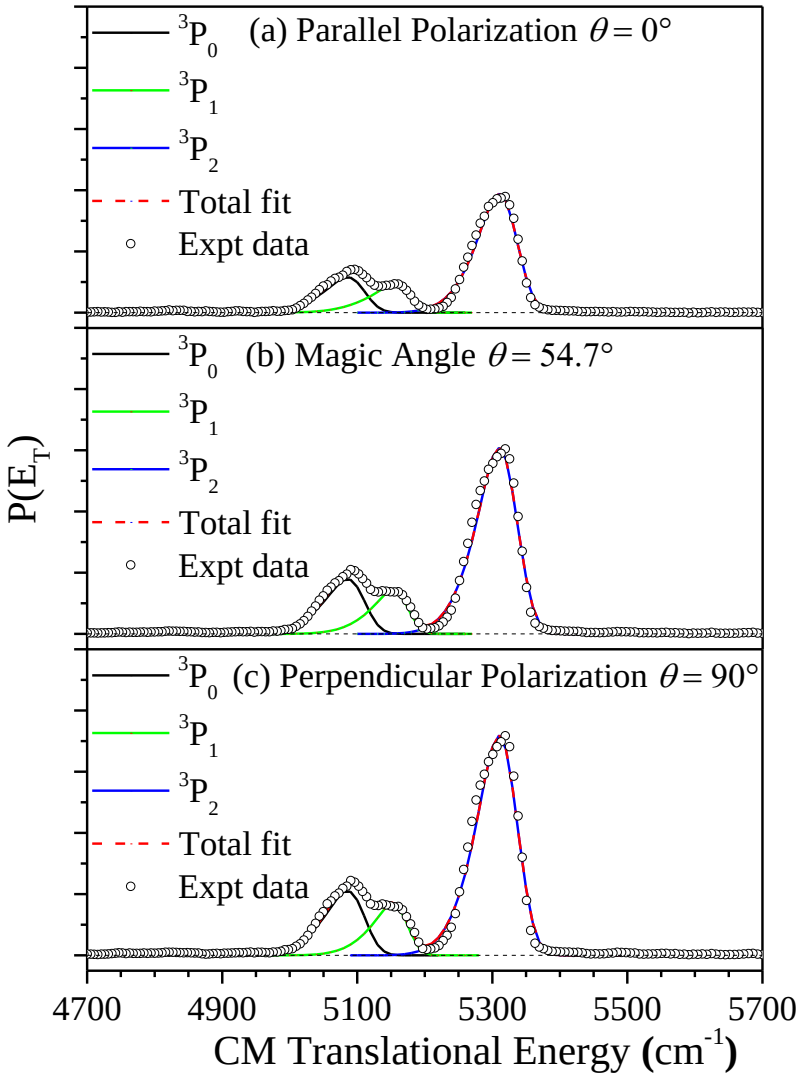

Figure 2.3. P(E_T) distributions of the H(^{2}S) + O(^3P_J) products from the predissociation of the OH ($A^2\Sigma^+$, v' = 3, N' = 1, J' = 1.5, F_1) radical via the Q_1(1.5) transition. The P(E_T) distributions are converted from the TOF spectra with the polarized photolysis radiation parallel and perpendicular to the TOF path, and the one at magic angle is calculated from the parallel and perpendicular distributions. The spin-orbit splitting of the O($^3P_{J=2,1,0}$) sublevels are deconvoluted using asymmetric Gaussian functions. See text for more details.

2.3.3 v' = 4 Vibronic Transitions

The P(E_T) distributions of the predissociation of OH ($A^2\Sigma^+$, v' = 4, J' = 2.5, F_1) with the parallel and perpendicular photolysis polarization via the $R_1(1.5)$ transition shown in Figure 2.4 (a) and (c), and the one at the magic angle is acquired by combining the parallel and perpendicular P(E_T) distributions and presented in Figure 2.4 (b). The spin-orbit O(^3P_J) product branching ratios and anisotropy parameters are calculated based on the deconvoluted peak areas. The branching fractions for O($^3P_{J = 2,1,0}$) 0.866 ± 0.042: 0.101 ± 0.022: 0.033 ± 0.020 for the $R_1(1.5)$ transition [from Figure 2.4 (b)], and 0.873 ± 0.026: 0.102 ± 0.028: 0.025 ± 0.005 for $P_1(1.5)$ transition,[38] 0.866 ± 0.042: 0.101 ± 0.022: 0.033 ± 0.020 for the $Q_1(1.5)$ transition. The branching factions stay almost the same as those from the predissociation via the $P_1(1.5)$ transition.[13,38] The anisotropy β parameters for the $R_1(1.5)$ transition are 0.36 ± 0.16, 0.30 ± 0.21, and 0.31 ± 0.25 for O($^3P_2$), O($^3P_1$), and O($^3P_0$), respectively, with a weighted average of 0.35 ± 0.14. Those for the $P_1(1.5)$ transition are $-0.02 \pm 0.04 \pm 0.16$ and 0.11 ± 0.51 (weighted average -0.01 ± 0.07), and -0.69 ± 0.11, -0.67 ± 0.24, and -0.72 ± 0.29 (weighted average -0.69 ± 0.10) for the $Q_1(1.5)$ transition.

2.3.4 Simulation of β parameters

A simulation program was used to predict the recoil photofragment angular distributions as a function of the transition energy, rotational level, rotation constant, and dissociation time scale.[47] The P_1, Q_1, and R_1 branches of the $A^2\Sigma^+$ (v' = 2-4, J' = 0.5-2.5, F_1) $\leftarrow$ $X^2\Pi$ (v'' = 0, J'' = 1.5, F_1) transitions are simulated. In Figure 2.5, the black curve

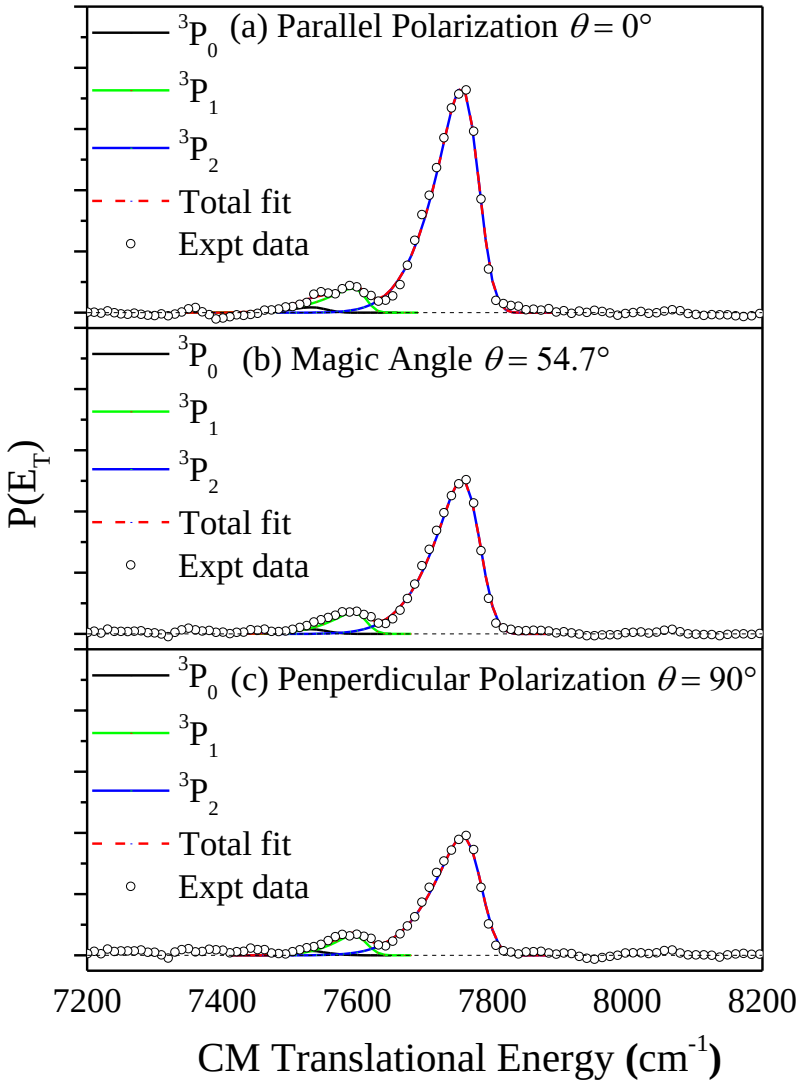

Figure 2.4. P(E_T) distributions of the H(^{2}S) + O(^3P_J) products channel from the predissociation of the OH ($A^2\Sigma^+$, $v' = 4$, $N' = 2$, $J' = 2.5$, F_1) radical via the $R_1(1.5)$ transition. The spin-orbit splitting of the O($^3P_{J=2,1,0}$) sublevels are deconvoluted using asymmetric Gaussian functions. See text for more details.

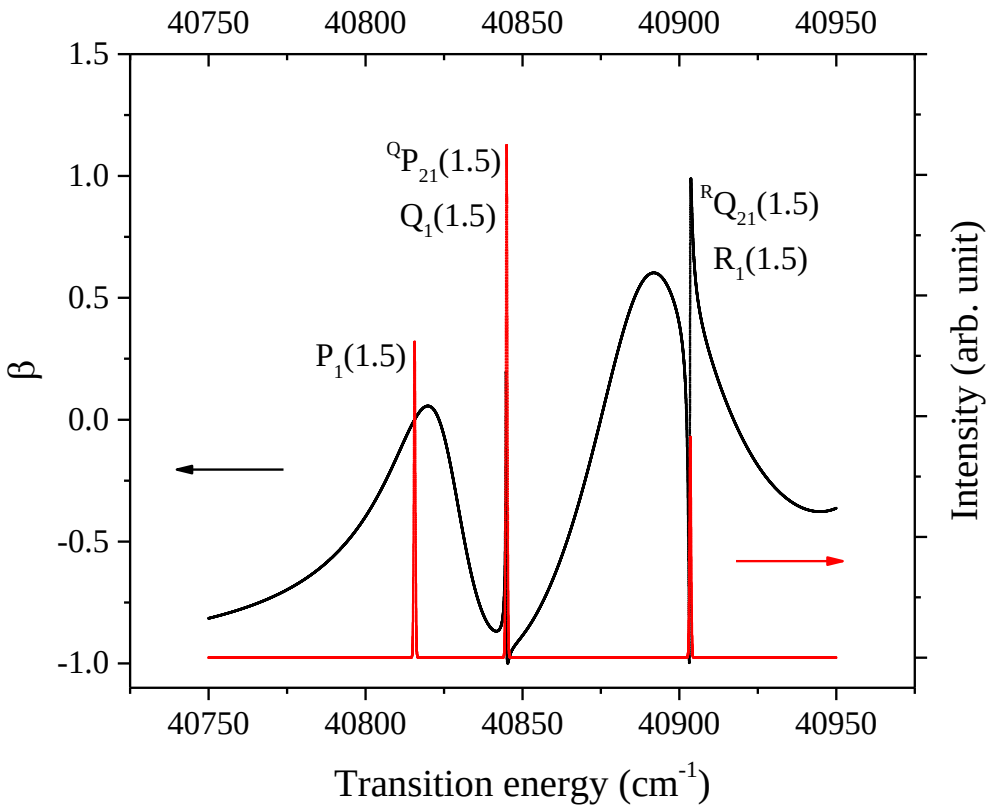

Figure 2.5. Simulated absorption spectrum (red) and anisotropy parameter (black) of the predissociation of the OH radical via the $A^2\Sigma^+(v' = 3)$ state. The OH radical is assumed to be populated at the lowest rotational level $N'' = 1$ of the $X^2\Pi_{3/2}$ electronic ground state. The β parameter can be measured where the absorption is significant (i.e., on the transition resonances). See text for more details.

presents the predicted β parameter as a function of the transition energy for the v' = 3 transitions and the red curve is the reproduced absorption spectrum at the experimental condition (~ 0.6 cm^{-1} laser bandwidth). The parameters such as the rotational constant, spin-orbit splitting, excited state lifetime can be obtained from *LIFBASE*[48] and *NIST Chemistry Webbook*.[49] The simulated β parameter has a strong interference effect due to the excitation of the satellite transitions, $^{Q}P_{21}(1.5)$ and $^{R}Q_{21}(1.5)$, which are very close to the main transitions branches, $Q_1(1.5)$ and $R_1(1.5)$, respectively. The absorption spectrum is also reproduced with this program. The laser bandwidth (~ 0.6 cm^{-1}) in this experimental study is comparable or larger than the separation of the main branches and satellite branches. The β parameters for the main transitions are predicted by calculating the average value of β for the region that covering two times the full width at half maximum of the absorption peaks (~ 1.2 cm^{-1}) with the Gaussian laser line shape as the weighting factor. For the *v'=3* transitions, the β parameters are obtained as $\beta(P_1(1.5))$ = 0.00, $\beta(Q_1(1.5), {}^{Q}P_{21}(1.5))$ = - 0.60, and $\beta(R_1(1.5), {}^{R}Q_{21}(1.5))$ = 0.38. The predicted anisotropy parameters are in a reasonable agreement with our experimental measurements. The β parameters for the v' = 2 and 4 transition bands are simulated as well, and all the results are listed in Table 2.2.

2.3.5 Determination of Dissociation Time

The dissociation time scale of the OH radical was studied. Figure 2.6 presents the integrated the $O(^3P_J)$ product channel signals of the HRTOF spectra with different pump-probe delay time after the OH radical was excited to the $A\,^2\Sigma^+(v' = 2, J' = 2.5, F_1)$ state via

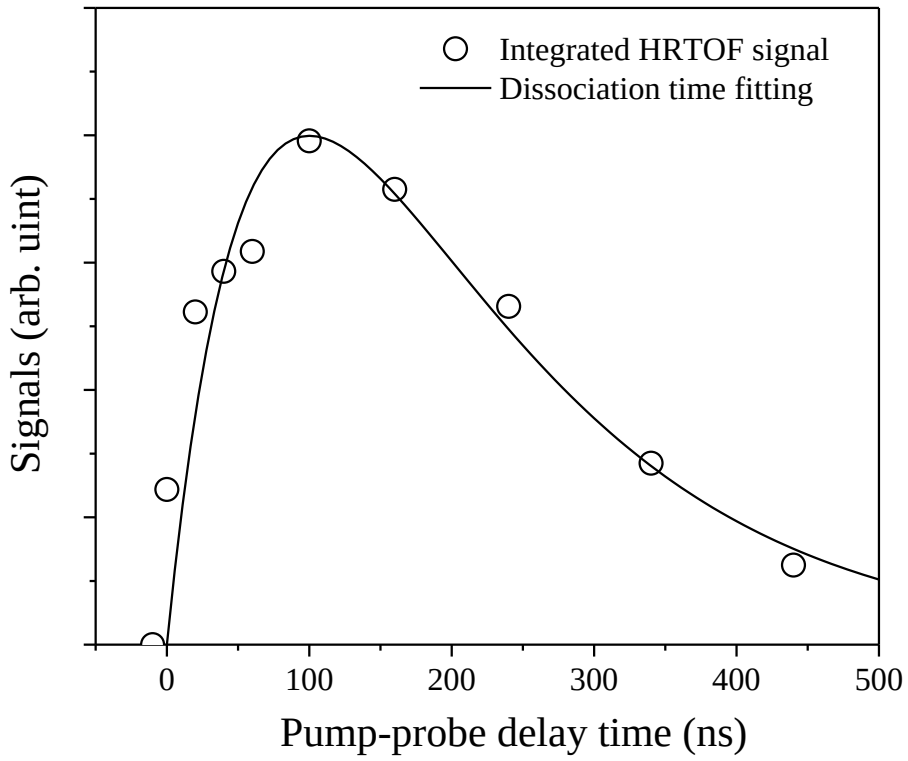

Figure 2.6. H-atom product signals from predissociation of OH ($A^2\Sigma^+$, $v' = 2$, $N' = 2$, $J' = 2.5$, F_1) as a function of photolysis and probe radiation delay time. The signals were obtained by integrating the $H(^2S) + O(^3P_J)$ products peaks from the HRTOF spectra of the predissociation of OH via $R_1(1.5)$ transition at various photolysis pump-probe delay times. The solid line is the fitting result of the H-atom product time profile that can give the dissociation time scale. See text for details.

the $R_1(1.5)$ transition. The rise of the signals in the pump-probe delay time region of 0 to 100 ns indicates the formation of the H atom from the dissociation of the OH radical, and the decay of the signals after the peak at ~ 100 ns is due to the H atom flight out of the interaction region of the photolysis and probe laser beams. The time profile of the H-atom signals, $S_H(t)$, can be described by the following equation:[50]

$$S_H(t) = N[1 - \exp(-k_H t)] \cdot [\frac{1}{\exp[(t-a)/b] + 1}]$$

where k_H is the unimolecular dissociation rate constant of the OH radical, and a and b are the constants to describe the width of the plateau region and the decay of the signals. The solid line in Figure 2.6 provides a dissociation rate constant $k_H \sim 7.7 \times 10^6$ s^{-1} for the predissociation of the OH radical. Our experimental measurement shows that the dissociation time scale of the OH radical via the $A^2\Sigma^+(v' = 2, J' = 2.5, F_1)$ state is 130 ± 30 ns, and this result is in a good agreement with the theoretical predication of 114 ns by the full quantum treatment.[13]

Similarly, the pump-probe delay time profile of the H-atom signal from the predissociation of the OH radical at $A^2\Sigma^+(v' = 4, J' = 0.5, F_1)$ via the $P_1(1.5)$ transition is obtained and plotted in Figure 2.7. The fitting indicates that the dissociation rate constant, k_H, is $\sim 9.3 \times 10^7$ s^{-1} with a dissociation time of 11 ns. The 10 ns time resolution of the pump and probe laser radiations limits the H-atom product appearance time resolution, and therefore the observed 11 ns predissociation time gives the upper limit of the actual dissociation time scale. In the meantime, the H-atom signals were measured as a function of the photolysis wavelength by integrating the $H(^2S) + O(^3P_J)$ products channel regions

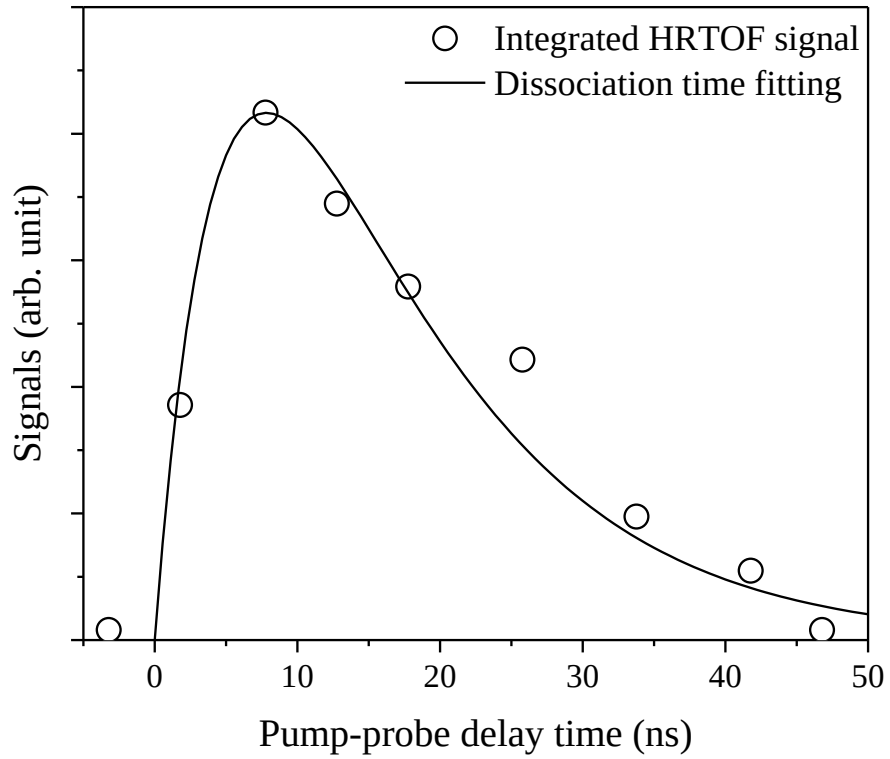

Figure 2.7. H-atom product signals from predissociation of OH ($A^2\Sigma^+$, $v' = 4$, $N' = 0$, $J' = 0.5$, F_1) as a function of photolysis and probe radiation delay time. The signals were obtained by integrating the $H(^2S) + O(^3P_J)$ products channel regions from the HRTOF spectra of OH via $P_1(1.5)$ transition at various photolysis pump probe delay times. The solid line is the fitting result of the H-atom product time profile. See text for details.

from the HRTOF spectra of the predissociation of OH ($A^2\Sigma^+$, v' = 4, J' = 0.5, F_1) via the $P_1(1.5)$ transition with the slightly shifting the frequency of the photolysis off the resonance. Figure 2.8 presents the linewidth profile with the Voigt function fitting (solid line), which is the convolution of the Gaussian function that describes the line shape of the photolysis radiation (FWHM = 0.20 cm^{-1}) and the Lorentzian function (FWHM = 0.38 cm^{-1}) that has the predissociation lifetime information. The Doppler broadening is estimated to be ~ 0.06 cm^{-1} (based on the ~ 50 K molecular beam temperature) and can be neglected. The lower limit of the predissociation time is obtained with 14 ps, and our experimental result is consistent with the full quantum treatment of 18 ps by Yarkony with coworkers[13] and the 22 $\pm$ 3 ps value from linewidth measurement by Lester with coworkers.[33]

2.4 Discussions

The photo-predissociation dynamics of the OH radical are investigated via the $A^2\Sigma^+$ (v' = 2-4, J' = 0.5-2.5, F_1) states in this study. The branching fractions and anisotropy parameters of the $O(^3P_{J=2,1,0})$ product channels are obtained and summarized in Table 2.1 and Table 2.2. The experimental branching ratios are in excellent agreement with the full quantum calculation, in which the multichannel scattering calculations including all the nonadiabatic interactions from the FC region to the asymptotic region ($O(^3P_{J=2,1,0})$ = 0.676:0.135:0.189 for v' = 2, $O(^3P_{J=2,1,0})$ = 0.675:0.141:0.0.184 for v' = 3, $O(^3P_{J=2,1,0})$ = 0.888:0.091:0.021 for v' = 4. Respectively).[13] For the predissociation of OH on $A^2\Sigma^+$ v' = 2 and 3, the $^4\Sigma^-$ state dominates. The spin-orbit and Coriolis interactions in the recoupling

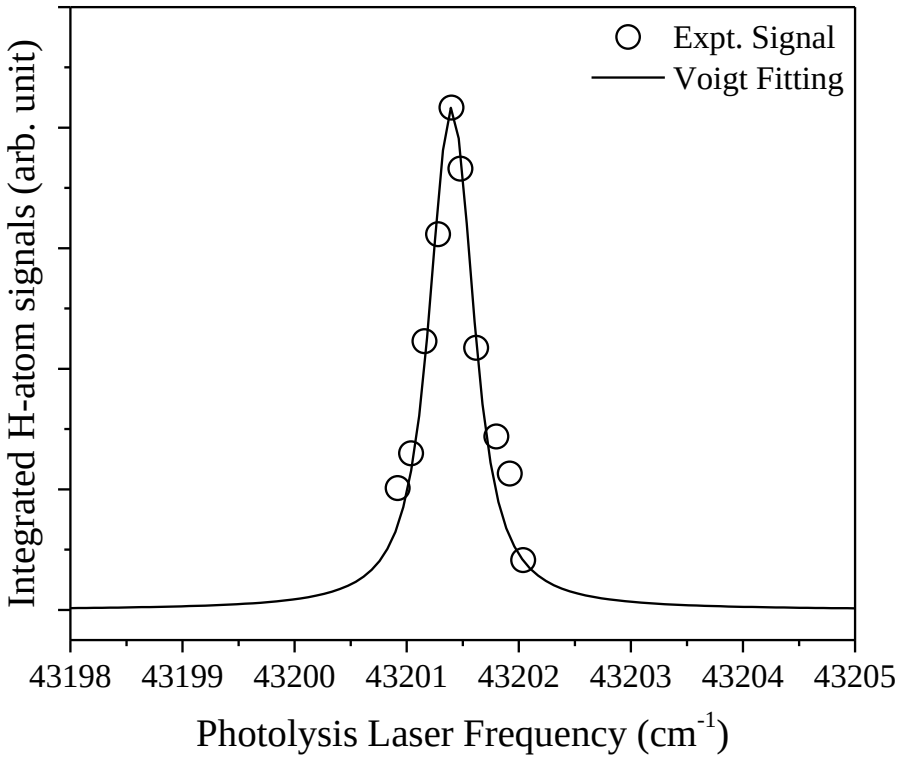

Figure 2.8. H-atom signals from predissociation of OH ($A^2\Sigma^+$, $v' = 4$, $N' = 0$, F_1) as a function of the photolysis laser frequency. The signals were obtained by integrating the $H(^2S) + O(^3P_J)$ product peaks from the HRTOF spectra of the OH near $P_1(1.5)$ transition. The solid line is the fitting result with the Voigt function and the dissociation time can be obtained from the peak linewidth parameters. See text for details.

region can be observed but not significant, but the asymptotic spin-orbit interactions play an important role in the $O(^3P_{J=2,1,0})$ fine-structure distributions. As $A^2\Sigma^+$ $v' = 4$ lies higher than $v' = 2$ and 3, and between the crossing points of $^2\Sigma^-$ and $^4\Sigma^-$, the predissociation on $A^2\Sigma^+$ $v' = 4$ involves all three repulsive states. The predissociation dynamics of $A^2\Sigma^+$ $v' = 4$ would be the predissociation via these three repulsive states. In the recoupling region the spin-orbit with the Coriolis interactions are not significant, while the quantum interferences among these three repulsive states are important in the determining of the $O(^3P_{J=2,1,0})$ product branching ratios. Moreover, the J' values (between 0.5-2.5) do not change the branching ratios significantly as the relative energy levels are close to each other.

The anisotropy parameters are measured in the experiment, and they show a strong dependence on the transitions. As shown from Table 2.2, the β parameters are close to 0 for the $P_1(1.5)$ transitions, negative for the $Q_1(1.5)$ transitions, and positive for the $R_1(1.5)$ transitions. Zare applied the rigid rotor model to characterize the alignment parameters for the different transitions with the absorption of plane polarized radiation.[51] The P and R branches are predicted with this model, and P branches have the alignment parameter starting with 0 and increasing with rotational quantum number, while R branches start with 2 and decreasing with the rotational quantum number. Both branches approach the same limit 0.5 at high rotational quantum number. The values of Q branches are predicted by a symmetric top model in which the alignment parameters are negative. During the excitation of the OH radical, the same model can be applied and the measured β parameters have the same signs as the prediction from Zare. As the dissociation time of the different vibrational levels are different (detail is present in the following part), the angular anisotropy is

depolarized due to the slow predissociation, and the β parameter will be reduced toward close to 0, especially for $v' = 2$, which the dissociation time scale is determined to be about 130 ns. During the initial excitation, the OH radials are aligned by the linearly polarized photolysis with the total rotational quantum number J', which is the sum of the molecular rotational quantum number N', and the spin of the unpaired electron S'. The initial alignment of the OH radical will be lose due to the precession of the axis of rotation of OH, which would result in the reducing of the β parameters toward to 0.

The $O(^3P_{J=2,1,0})$ branching fractions stay almost the same with different J' in the same vibrational state; while the H-atom product angular distributions via the $P_1(1.5)$, $Q_1(1.5)$, and $R_1(1.5)$ transitions are different with ~0 values for $P_1(1.5)$, negative values for $Q_1(1.5)$, and positive values for $R_1(1.5)$ transition.

The predissociation time scales are determined by using the pump-probe decay and linewidth measurement. The lifetime for $v' = 2$ is determined to be 130 ± 30 ns. This vibrational level lies below the crossing of $A^2\Sigma^+$ and $1^4\Sigma^-$, and the tunneling effect would be the dominate predissociation channel. As this process is slow, it caused the long dissociation time. While for $v' = 4$, a lower limit predissociation time of 14 ps is obtained by measuring the linewidth of H-atom PFY spectrum. This vibrational level lies higher and it is between the crossing of $A^2\Sigma^+$ and $1^2\Sigma^-$, $1^4\Pi$. Compared to the tunneling process, the direct surface hopping would be easier and will make the predissociation on this vibrational level occur on have a shorter dissociation time scale. Other effect such as power broadening also has contribution to the width of the peak, our experiment measurement could only

provide a lower limit of the predissociation time scale. Both dissociation times measured are in good agreement with the previous theorical and experimental studies.[13,33]

2.5 Conclusion

Photodissociation dynamics of the OH radical is studied via several rovibrational levels in the $A^2\Sigma^+$ (v' = 2-4, J' = 0.5-2.5, F_1) state via the $P_1(1.5)$, $Q_1(1.5)$, and $R_1(1.5)$ transitions. The spin-orbit $O(^3P_{J=2,1,0})$ product branching ratios from the predissociation of OH are determined experimentally. The branching ratios stay nearly constant for the same vibrational quantum number, with only a small change with the rotational quantum number (J' = 0.5-2.5), and the results are in excellent agreement with the previous theory. The product angular distributions for the H + $O(^3P_{J=2,1,0})$ product channels via the $P_1(1.5)$, $Q_1(1.5)$, and $R_1(1.5)$ transitions are investigated experimentally and theoretically, and the β parameters are about 0 for $P_1(1.5)$, negative for $Q_1(1.5)$, and positive for $R_1(1.5)$ transitions. The predissociation time is determined to be 130 $\pm$ 30 ns for the $A^2\Sigma^+$(v' = 2, J' = 2.5, F_1) state and $\geq$ 14 ps for the $A^2\Sigma^+$(v' = 4, J' = 0.5, F_1) state.

Reference

1. C. A. Taatjes, D. E. Shallcross, and C. J. Percival, *Phys. Chem. Chem. Phys.* **16**, 1704 (2014).

2. M. Campos-Pineda and J. Zhang, *Chem. Phys. Lett.* **683**, 647 (2017).

3. Z. Zhao, Q. Xu, X. Yang, and H. Zhang, *ACS Earth Space Chem.* **3**, 344 (2019).

4. K. Lorenz and R. Zellner, *Ber. Bunsenges, Phys. Chem.* **88**, 1228 (1984).

5. V. Schmidt, G. Y. Zhu, K. H. Becker, and E. H. Fink, *Ber. Bunsenges, Phys. Chem.* **89**, 321 (1985).

6. T. J. Wallington, R. Liu, P. Dagaut, and M. J. Kurylo, *Int. J. Chem. Kinet.* **20**, 41 (1988).

7. M. L. Sink, A. D. Bandrauk, and R. Lefebvre, *J. Chem. Phys.* **73**, 4451 (1980).

8. E. F. van Dishoeck and A. Dalgarno, *J. Chem. Phys.* **79**, 873 (1983).

9. S. Lee and K. F. Freed, *J. Chem. Phys.* **87**, 5772 (1987).

10. D. R. Yarkony, *J. Chem. Phys.* **97**, 1838 (1992).

11. C. Kalyanaraman and N. Sathyamurthy, *Chem. Phys.* **187**, 219 (1994).

12. S. Lee, *J. Chem. Phys.* **103**, 3501 (1995).

13. G. Parlant and D. R. Yarkony, *J. Chem. Phys.* **110**, 363 (1999).

14. M. P. J. van der Loo and G. C. Groenenboom, *J. Chem. Phys.* **123**, 074310 (2005).

15. B. S. D. R. Vamhindi and M. Nsangou, *Mol. Phys.* **114**, 2204 (2016).

16. G. H. Dieke and H. M. Crosswhite, *J. Quant. Spectrosc. Radiat. Transfer* **2**, 97 (1962).

17. C. Carlone and F. W. Dalby, *Can. J. Phys.* **47**, 1945 (1969).

18. E. A. Moore and W. G. Richards, *Phys. Scr.* **3**, 223 (1971).

19. K. R. German, *J. Chem. Phys.* **63**, 5252 (1975).

20. T. Bergeman, P. Erman, and M. Larsson, *Chem. Phys.* **54**, 55 (1980).

21. J. A. Coxon, *Can. J. Phys.* **58**, 933 (1980).

22. J. B. Nee and L. C. Lee, *J. Chem. Phys.* **81**, 31 (1984).

23. R. A. Copeland, J. B. Jeffries, and D. R. Crosley, *J. Mol. Spectrosc.* **143**, 183 (1990).

24. R. J. Cody, C. Moralejo, and J. E. Allen, *J. Chem. Phys.* **95**, 2491 (1991).

25. M. Collard, P. Kerwin, and A. Hodgson, *Chem. Phys. Lett.* **179**, 422 (1991).

26. J. A. Coxon, A. D. Sappey, and R. A. Copeland, *J. Mol. Spectrosc.* **145**, 41 (1991).

27. E. de Beer, M. P. Koopmans, C. A. de Lange, Y. Wang, and W. A. Chupka, *J. Chem. Phys.* **94**, 7634 (1991).

28. J. A. Gray and R. L. Farrow, *J. Chem. Phys.* **95**, 7054 (1991).

29. D. E. Heard, D. R. Crosley, J. B. Jeffries, G. P. Smith, and A. Hirano, *J. Chem. Phys.* **96**, 4366 (1992).

30. J. J. L. Spaanjaars, J. J. ter Meulen, and G. Meijer, *J. Chem. Phys.* **107**, 2242 (1997).

31. E. S. Hwang, J. B. Lipson, R. W. Field, and J. A. Dodd, *J. Phys. Chem. A* **105**, 6030 (2001).

32. C. McRaven, J. Alnis, B. Furneaux, and N. Shafer-Ray, *J. Phys. Chem. A* **107**, 7138 (2003).

33. E. L. Derro, I. B. Pollack, L. P. Dempsey, M. E. Greenslade, Y. Lei, D. Č. Radenović, and M. I. Lester, *J. Chem. Phys.* **122**, 244313 (2005).

34. M. E. Greenslade, M. I. Lester, D. Č. Radenović, A. J. A. van Roij, and D. H. Parker, *J. Chem. Phys.* **123**, 074309 (2005).

35. Q. Xiong, A. Y. Nikiforov, L. Li, P. Vanraes, N. Britun, R. Snyders, X. P. Lu, and C. Leys, *Eur. Phys, J. D.* **66**, 281 (2012).

36. A. Fast, J. E. Furneaux, and S. A. Meek, *Phys. Rev. A* **98**, 052511 (2018).

37. J. Brzozowski, P. Erman, and M. Lyyra, *Phys. Scr.* **17**, 507 (1978).

38. W. Zhou, Y. Yuan, and J. Zhang, *J. Chem. Phys.* **119**, 9989 (2003).

39. D. Č. Radenović, A. J. A. van Roij, S.-M. Wu, J. J. ter Meulen, D. H. Parker, M. P. J. van der Loo, and G. C. Groenenboom, *Phys. Chem. Chem. Phys.* **11**, 4754 (2009).

40. G. Amaral, K. Xu, and J. Zhang, *J. Chem. Phys.* **114**, 5164 (2001).

41. W. Zhou, Y. Yuan, S. Chen, and J. Zhang, *J. Chem. Phys.* **123**, 054330 (2005).

42. X. Zheng, J. Wu, Y. Song, and J. Zhang, *Phys. Chem. Chem. Phys.* **11**, 4761 (2009).

43. P. Andresen, N. Aristov, V. Beushausen, D. Häusler, and H. W. Lülf, *J. Chem. Phys.* **95**, 5763 (1991).

44. D. M. Sonnenfroh, R. G. Macdonald, and K. Liu, *J. Chem. Phys.* **94**, 6508 (1991).

45. R. N. Zare, *Mol. Photochem.* **4**, 1 (1972).

46. A. Kramida, Y. Ralchenko, J. Reader,(2019), NIST Atmoic Spectra Database (ver 5.7.2). https://doi.org/10.18434/T4W30F.

47. H. Kim, K. S. Dooley, S. W. North, G. E. Hall, and P. L. Houston, *J. Chem. Phys.* **125**, 133316 (2006).

48. J. Luque and D. R. Crosley, *SRI International Report MP 99-009* (1999).

49. E. W. Lemmon, M. O. McLinden, and D. G. Friend, in *NIST Standard Reference Database Number 69*, edited by p. J. Linstrom and M. W. G. (National Institute of Standards and Technology, Gaithersburg, MD, 2018).

50. T. Gilbert, T. L. Grebner, I. Fischer, and P. Chen, *J. Chem. Phys.* **110**, 5485 (1999).

51. R. N. Zare, *Ber. Bunsenges, Phys. Chem.* **86**, 422 (1982).

Chapter 3

Two-photon Dissociation Dynamics of the Hydroxyl Radical

Abstract

Two-photon dissociation dynamics of the OH radical is studied using the high-*n* Rydberg atom time-of-flight (HRTOF) technique. The $H(^2S) + O(^1D)$ and $H(^2S) + O(^1S)$ product channels are observed in the dissociation of the OH radical on the $2\,^2\Pi$ and $B^2\Sigma^+$ repulsive states, respectively, from sequential two-photon excitation via the $A^2\Sigma^+$ ($v' = 2$, $J' = 0.5$-2.5) state. Both H + O product channels have anisotropic angular distributions, with $\beta = -0.97$ for $H(^2S) + O(^1D)$ and 1.97 for $H(^2S) + O(^1S)$. The anisotropic angular distributions are consistent with a mechanism of OH direct dissociation on the repulsive potential energy curves (PECs) leading to the H + O products. The OH bond dissociation energy D_0(O-H) is determined to be 35580 ± 15 cm^{-1}.

3.1 Introduction

The hydroxyl radical (OH) is a prototype open-shell diatomic system. It is also an important intermediate in combustion processes, atmospheric chemistry, and astrophysics. Multiple potential energy curves (PECs) and non-adiabatic interactions are known to be involved in the photodissociation processes of the OH radical. The photolysis of OH can also serve as a benchmark for theoretical studies of open-shell species.

The electronic structure and spectroscopy of the OH radical have been well studied by both theory[1-9] and experiment.[8,10-30]. Figure 3.1 shows the PECs of the lowest electronic states of OH. The ground electronic state, $X^2\Pi$, correlates asymptotically to the $H(^2S)$ + $O(^3P_J)$ products. The first excited state, $A^2\Sigma^+$, correlates to the excited-state products $H(^2S)$ + $O(^1D)$ and is crossed by three repulsive states $1^4\Sigma^-$, $1^2\Sigma^-$, and $1^4\Pi$, which correlate with the ground-state products $H(^2S)$ + $O(^3P_J)$. Two other high-energy states, $1^2\Delta$ and $2^2\Pi$, correlate adiabatically to $H(^2S)$ + $O(^1D)$, whereas another state, $B^2\Sigma^+$, crosses with $2^2\Pi$ and correlates asymptotically to $H(^2S)$ + $O(^1S)$. The $D^2\Sigma^-$ state (at higher energy, not shown in Figure 3.1) is the lowest-energy Rydberg state of OH and is crossed with $1^2\Delta$, $2^2\Pi$, and $B^2\Sigma^+$.

The spectroscopy of the $A^2\Sigma^+$-$X^2\Pi$ band system has been well characterized.[10,12,15,17,18,22-24,27,29-31] The predissociation dynamics of the OH $A^2\Sigma^+$ state has also been investigated theoretically[1,3,5-7,32] and experimentally.[7,22-24,27,31-35] The predissociation lifetimes of different vibrational levels of the $A^2\Sigma^+$ state are determined to be $\tau \sim 150$ ns for $v' = 2$, ~ 300 ps for $v' = 3$, and ~ 20 ps for $v' = 4$, respectively.[7,27] The $A^2\Sigma^+$

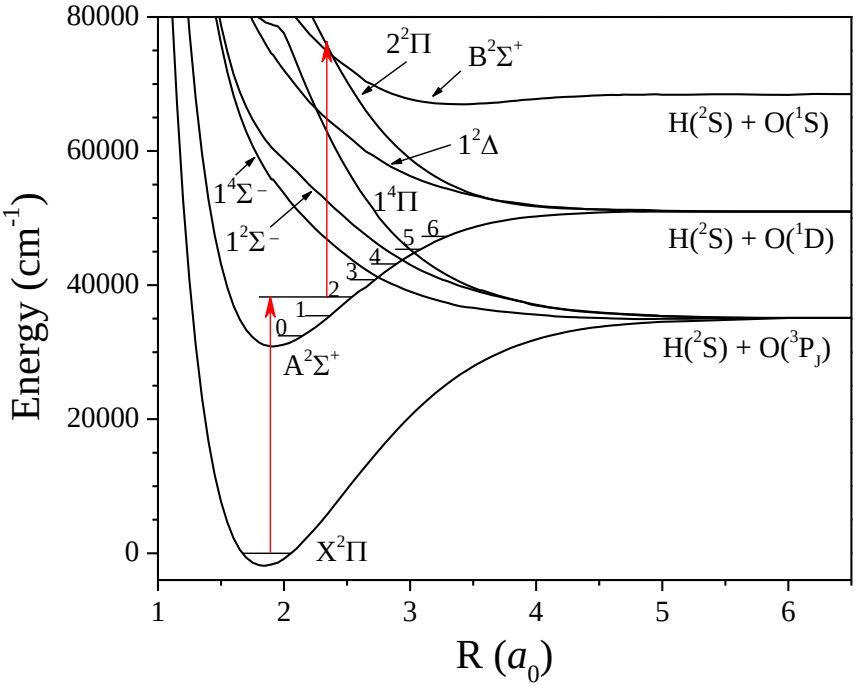

Figure 3.1. Potential energy curves of the OH system. The vibrational levels $v' = 0$–6 of the $A^2\Sigma^+$ state are shown and labeled. Details of the calculation of the PECs are in the text.

state is crossed by three repulsive states $1^4\Sigma^-$, $1^2\Sigma^-$, and $1^4\Pi$, which lead to the $H(^2S)$ + $O(^3P_J)$ products. The predissociations of the $A^2\Sigma^+$ state at vibrational levels $v' = 0$ ($N' \geq 24$), 1 ($N' \geq 15$), 2, and 3 proceed mainly via the $1^4\Sigma^-$ state [1,4,5,7,22-24,31,33,35], while that of $v' = 4$ involves three states, $1^4\Sigma^-$, $1^2\Sigma^-$, and $1^4\Pi$ states.[4,5,7,17,33,35] The experimental fine-structure branching ratios of the $O(^3P_{J=0,1,2})$ products from the predissociation of OH $A^2\Sigma^+$ are in excellent agreement with the theoretical calculations.[7,32,33,35]. The product angular distributions from the predissociation of OH at different rovibational levels of the $A^2\Sigma^+$ state were measured,[32,33,35] and the anisotropy parameter β is found to be strongly dependent on the different rotational transitions.

Lee and coworkers obtained the absorption spectrum of OH in the region of 115-183 nm.[16] The observed continuum in the longer wavelength region could be due to transitions to the repulsive states ($1^2\Sigma^-$ and $1^2\Delta$), whereas the sharp discrete transition at 122 nm is likely due to the $D^2\Sigma^-$ state.[16] The peak observed at 124.5 nm could be due to a transition to the avoided crossing region of the $2^2\Pi$ state. The second continuum near 120 nm may result from the superposition of absorptions into several different excited states, such as $B^2\Sigma^+$ and $1^2\Delta$. The experimental and theoretical information avaiable on the photodissociation of OH via higher electronic states is limited. The photodissociation of OH at 157 nm via the repulsive $1^2\Sigma^-$ state was examined by Cody et al.[18] The H-atom product, presumably arising from the $H(^2S) + O(^3P_J)$ product channel, was detected with a quantum yield of 1.10 ± 0.28. The photodissociation of vibrationally excited OH/OD via the repulsive $1^2\Sigma^-$ state was investigated by Parker and coworkers.[34] A pure perpendicular dissociation was observed, which is consistent with the $1^2\Sigma^- \leftarrow X^2\Pi$ transition. The

measured $O(^3P_J)$ product branching ratios were found to be constant with a ~5:3:1 ratio, as predicted theoretically for a sudden limit diabatic dissociation process; the measured product angular distributions are thus consistent with the sudden-limit theoretical treatment and a prompt, repulsive dissociation. Dodd and coworkers obtained the OH $B^2\Sigma^+$-$X^2\Pi$ rovibronic spectra using the laser-induced fluorescence (LIF) technique.[25] The lifetimes of the rotational levels were determined and displayed a rapid decrease with increasing value of *J'*, indicting predissociation of the OH $B^2\Sigma^+$ state.[25] The predissociation is induced by the $2^2\Pi$- $B^2\Sigma^+$ state crossing through the combination of spin-orbit and gyroscopic interactions, whereby the predissociation rate depends on the rotational state and increases with increasing *J'* values. Carlone *et. al.* examined the $B^2\Sigma^+ \rightarrow A^2\Sigma^+$ and $C^2\Sigma^+ \rightarrow A^2\Sigma^+$ emission systems of OH,[11] which are weaker than the $A^2\Sigma^+ \rightarrow X^2\Pi$ emission system.

In this chapter, we report an investigation on the $H(^2S) + O(^1D)$ and $H(^2S) + O(^1S)$ product channels in the photodissociation of the OH radical from higher excited electronic states following two-photon excitation *via* the intermediate $A^2\Sigma^+$ state. The $H(^2S) + O(^1D)$ and $H(^2S) + O(^1S)$ product channels are both directly observed in the H-atom product time-of-flight (TOF) spectra and the product anisotropic parameters are measured. The nature of the electronic excited states involved and the dissociation dynamics of OH are characterized. An accurate OH bond dissociation energy D_0(O-H) is also determined.

3.2 Experimental and Calculation

The high-*n* Rydberg time-of-flight (HRTOF) technique was utilized in this study, and the details were reported in previous publications.[33,36-39] The OH radical beam was generated by photolyzing a ~ 5% mixture of HNO_3 ($\geq$ 99.5%, Fluka) in Ar (total pressure ~ 1.2 atm) with a 193 nm laser radiation. The OH radicals formed from the photolysis were cooled down by supersonic expansion and entrained in the molecular beam. The rotational temperature of the OH radical was estimated to be ~ 50 K. Downstream in a high vacuum chamber, the OH radicals were photolyzed by a tunable UV laser beam (around 261 nm, ~ 2 mJ/pulse, linewidth $\leq$ 0.3 cm^{-1}). The photolysis wavelengths were tuned to the $A^2\Sigma^+$ (v' = 2, J'' = 0.5-2.5, F_1) $\leftarrow$ $X^2\Pi$ (v'' = 0, J'' = 1.5, F_1) transitions [$P_1(1.5)$, $Q_1(1.5)$, and $R_1(1.5)$, at 38222.25, 38252.86, and 38314.10 cm^{-1}, respectively]. A wavemeter (Burleigh WA-4500) was used to monitor the wavelengths. The polarization of the photolysis radiation can be rotated by a Fresnel-Rhomb $\lambda/2$ plate for product angular distribution measurements. The H atoms produced from the dissociation of the OH radicals were excited by two-color resonance excitation (121.6 nm + 366.3 nm), i.e. from 1^2S to 2^2P via the Lyman-α transition and then to a high-*n* Rydberg state. A small portion of the Rydberg H atoms flew away from the interaction region with their nascent velocity to a microchannel plate (MCP) detector and were then field-ionized in front of the detector and detected. The flight distance was calibrated to be 37.24 cm by using photodissociation of HBr and the well-known spin-orbit splitting energy between $Br(^2P_{3/2})$ and $Br(^2P_{1/2})$. The flight distance calibration was further refined by the energetics of the $H(^2S) + O(^1S)$, $O(^1D)$,

and $O(^3P_J)$ product channels, which will be discussed later. The H-atom TOF spectra were typically accumulated with ~ 100 k laser shots.

The *ab initio* Λ-*S* electronic structure calculations of OH were carried out with the self-consistent field (SCF) multireference single and double excitation configuration interaction (MRD-CI) package developed previously.[40-42] The cc-pV4Z basis set[43], augmented with 11 diffuse (Rydberg) functions was used for the O-atom, whereas for the H-atom the same extended basis set used earlier was employed.[44] In total, there were 25 shells for O-atom basis and 14 shells for H-atom basis, respectively. In all CI calculations, the OH 1σ ($1a_1$) molecular orbital, which corresponds essentially to the 1s orbital of the oxygen atom, was kept doubly-occupied, frozen. Also, the uppermost virtual molecular orbital (MO) of a_1 symmetry was discarded. The SCF MOs of the OH^- system were employed as basis for the CI calculations of all computed electronic states of OH. This choice ensured an equivalent treatment of the two components, $1\pi x$ and $1\pi y$, of the 1π MO. A threshold of 1 μH was chosen to select the configurations to be included in the reference spaces. The CI treatments were carried out employing spaces of a few hundred configurations (depending on irreducible representation, multiplicity, and internuclear distance), from which all possible single and double excitations were generated. The actual dimensions of the matrices which were diagonalized directly were 100 000–300 000. All calculations were carried out in C_{2v} symmetry, a subgroup of the $C_{\infty v}$ group to which the heteronuclear linear OH system belongs. The PECs of the lowest-lying doublet and quartet states of OH, up to about 10 eV, were calculated and are depicted in Figure 3.1.

3.3 Results and Discussions

Figure 3.2 presents the H-atom TOF spectra on and off the OH $A^2\Sigma^+$ (v' = 2, N' = 1, J' = 1.5, F_1) ← $X^2\Pi$ (v'' = 0, N'' = 1, J'' = 1.5, F_1) transition resonance [the $Q_1(1.5)$ line], with the photolysis radiation polarization (a) perpendicular (⊥, θ = 90°) and (b) parallel (∥, θ = 0°) to the TOF path. The TOF spectra display several peaks at ~16, 29, and 50 μs when on resonance, and these peaks disappeared when the photolysis wavelength was off the resonance (shifted by ~ 1 cm^{-1}). All spectra were scaled to the same number of photolysis laser shots and power. The H-atom peak signals around 50 μs had a linear dependence on the photolysis laser power, while those around 16 and 29 μs showed nonlinear power dependence indicating multi-photon processes. The peaks at ~ 50 μs are slightly stronger at the perpendicular polarization (Figure 3.2). The intensities of the peaks around 16 and 29 μs present strong dependences on the photolysis polarizations. The peak around 16 μs has an intense signal in the perpendicular TOF spectrum and a negligible signal at the parallel polarization. On the other hand, the peak at ~ 29 μs has a strong signal in the parallel TOF spectrum and a very small intensity at the perpendicular polarization (Figure 3.2). Similar observations were found in the H-atom TOF spectra of the OH radical with the photolysis wavelengths on the $P_1(1.5)$ and $R_1(1.5)$ transition resonances. As discussed later, the peaks at ~50 μs are assigned to the $H(^2S)$ + $O(^3P_J)$ product channel from one-photon dissociation via the $A^2\Sigma^+$ state, while the peaks at 16 and 29 μs are due to two-photon dissociation to the $H(^2S)$ + $O(^1D)$ and $H(^2S)$ + $O(^1S)$ products, respectively. The disappearance of the signals at ~ 50 μs when the photolysis wavelengths were off the

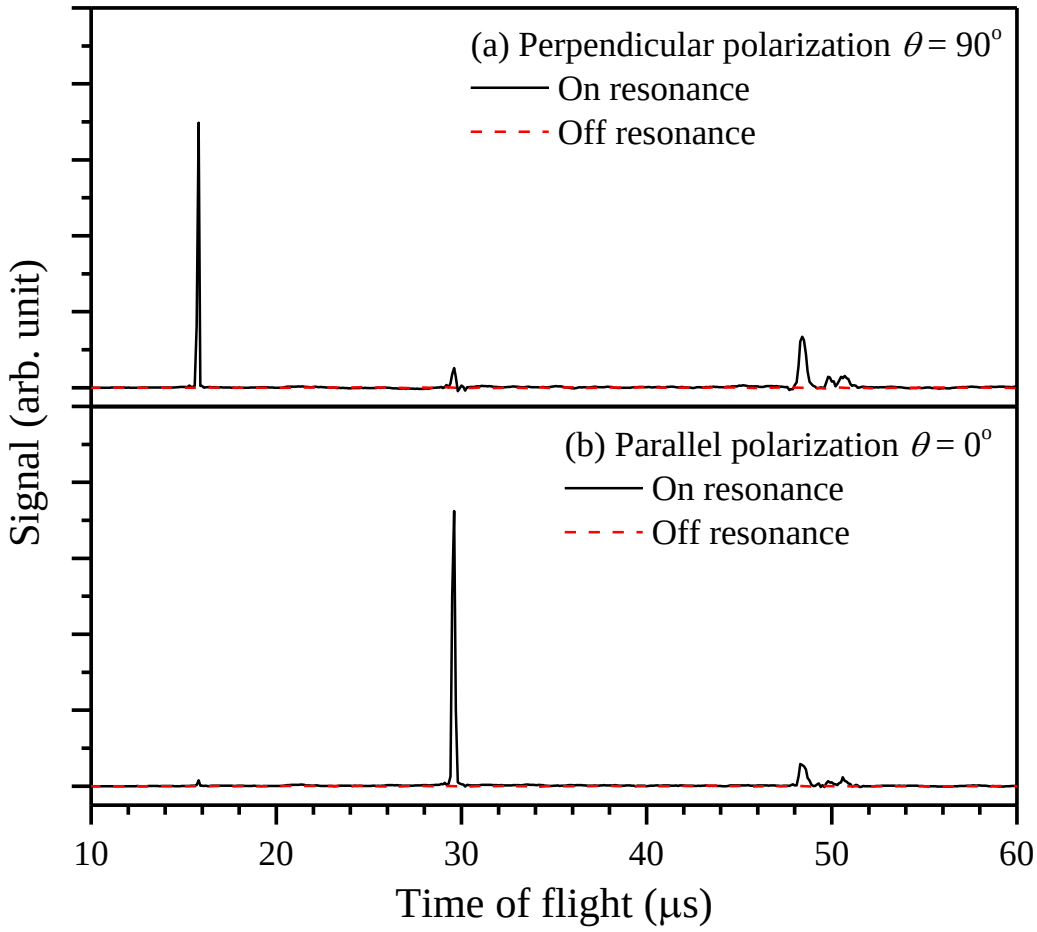

Figure 3.2. H-atom TOF spectra of the photodissociation of OH radical via the $A\,^2\Sigma^+$ (v' = 2, N' = 1, J' = 1.5, F_1) ← $X^2\Pi$ (v'' = 0, N'' = 1, J'' = 1.5, F_1) transition (the $Q_1(1.5)$ transition), with the polarization of the photolysis radiation (a) perpendicular and (b) parallel to the TOF path. The spectra are scaled to the same number of photolysis laser shots and laser power. See the text for details.

$P_1(1.5)$, $Q_1(1.5)$, and $R_1(1.5)$ transition resonances confirmed the photodissociation via the $A^2\Sigma^+$ state. The disappearance of the signals at ~16 and 29 μs when off resonances indicated a sequential absorption of two photons via the $A^2\Sigma^+$ intermediate state, from which the second photon starts sequentially, instead of a concerted two-photon process.

The H + O product center-of-mass (c.m.) frame translational energy distribution, $P(E_T)$, can be directly converted from the H-atom TOF spectra using the following equation:

$$E_T = \left(1 + \frac{m_H}{m_O}\right) E_H + \frac{m_H}{m_O} E_{OH} = \frac{1}{2} m_H \left(1 + \frac{m_H}{m_O}\right) \left(\frac{L}{t_H}\right)^2 + \frac{m_H}{m_O} E_{OH}$$

in which E_H and E_{OH} are the laboratory frame translational energies of the H-atom product and the parent OH radical, L is the length of the flight path, and t_H is the H-atom flight time. The second term is due to the motion of the parent OH radical in the molecular beam, which is perpendicular to the TOF path and is about 23 cm^{-1} based on the estimation of the ~700 m/s OH radical beam velocity. Figure 3.3 shows the $P(E_T, \theta)$ distributions of the H + O product channels resulting from the photodissociation of the OH radical via the $Q_1(1.5)$ transition, at the perpendicular and parallel photolysis polarization, which are retrieved from the TOF spectra in Figure 3.2. The $P(E_T, \theta)$ distributions at both polarizations present three peaks in the range of 2400 to 2700 cm^{-1} (the TOF peaks at ~ 50 μs), with the perpendicular ones having a slightly higher intensity. These peaks are assigned to the $H(^2S)$ + $O(^3P_J)$ product channel from the predissociation of the OH radical via the $A^2\Sigma^+$ ($v' = 2$, $N' = 1$, $J' = 1.5$, F_1) state [the $Q_1(1.5)$ transition] following one-photon excitation. Similar observations are found in the $P(E_T, \theta)$ distributions for predissociation via [$A^2\Sigma^+$ ($v' = 2$,

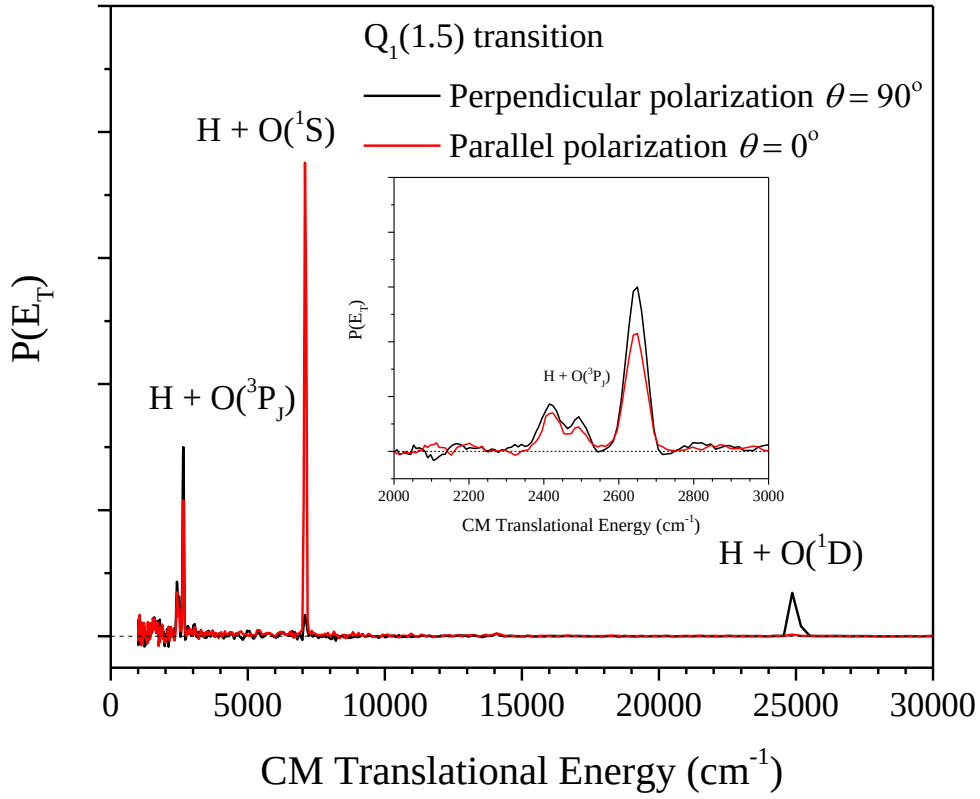

Figure 3.3. Center-of-mass product channel translational energy distribution from the photodissociation of OH via the $A^2\Sigma^+$ (v' = 2, N' = 1, J' = 1.5, F_1) ← $X^2\Pi$ (v'' = 0, N'' = 1, J'' = 1.5, F_1) transition $Q_1(1.5)$, with the linearly polarized photolysis radiation perpendicular (black curve) and parallel (red curve) to the TOF axis. The inserted figure is the enlarged region in the 2000 to 3000 cm^{-1} product translational energy. Different O-atom product channels are indicated in the figure. See the text for more details.

N' = 0 and 2, J' = 0.5 and 2.5, F_1)] states [the $P_1(1.5)$ and $R_1(1.5)$ transitions], but with different product angular distributions. In a one-photon dissociation process, the c.m. translational energy and angular distributions of the products can be described with the following equation:[45]

$$P(E_T, \theta) = \left(\frac{1}{4\pi}\right) P(E_T)[1 + \beta P_2(cos\theta)]$$

in which, $P(E_T)$ is the angle-integrated product translational energy distribution, β is the anisotropy parameter ($-1 < \beta < 2$), θ is the angle between the electric vector of the linearly polarized photolysis radiation and the recoiling velocity vector of the H-atom product, and $P_2(cos\theta)$ is the second Legendre polynomial. The anisotropic parameter of the $H(^2S)$ + $O(^3P_J)$ product channel from the dissociation of OH via the $P_1(1.5)$ transition is ~ 0, while that via the $Q_1(1.5)$ transition is slightly negative and that via the $R_1(1.5)$ transition is slightly positive.[33,35] The predissociation dynamics of the $A^2\Sigma^+$ (v' = 2, N' = 0-2, J' = 0.5-2.5) state will be discussed in a separate publication.[35]

The two peaks at ~25000 and 7000 cm^{-1} in the $P(E_T)$ distributions correspond to the peaks at ~16 and 29 μs in the H-atom TOF spectra. The high kinetic energies of these two channels confirm the two-photon dissociation processes. The relative positions of the peaks around 25000 and 7000 cm^{-1} with respect to the three peaks from the $H(^2S)$ + $O(^3P_J)$ product channel in the $P(E_T, \theta)$ distributions match excellently with the differences between the photon energy minus the electronic energies of the O atom [$O(^1D)$ at 15867.862 cm^{-1} and $O(^1S)$ 33792.583 cm^{-1} with respective to $O(^3P_2)$ at 0 cm^{-1}].[46] The two peaks at ~ 25000 and 7000 cm^{-1} are therefore assigned to the dissociation of the OH radical to the $H(^2S)$ + $O(^1D)$ and $H(^2S)$ + $O(^1S)$ product channels, respectively, following the two-photon excitations.

The $H(^2S) + O(^1D)$ peak at ~25000 cm^{-1} has a strong signal at the perpendicular polarization and a negligible signal at the parallel polarization, while the $H(^2S) + O(^1S)$ peak around 7000 cm^{-1} is strong at the parallel polarization and very weak at the perpendicular polarization. The first photon excites the OH radical to the $A^2\Sigma^+$ (v' = 2, N' = 0-2, J' = 0.5-2.5, F_1) state and partially aligns the OH radical, with an isotropic spatial distribution in N' = 0 following the $P_1(1.5)$ transition and slightly anisotropic distributions in N' = 1 and 2 following the $Q_1(1.5)$ and $R_1(1.5)$ transitions. The second photon sequentially excites the OH ($A^2\Sigma^+$) radical to higher states. In the sequential excitation, the second step can be considered as a one-photon process initiated from the partially aligned OH radical in the $A^2\Sigma^+$ (v' = 2, N' = 0-2, J' = 0.5-2.5) state. The best way to estimate the β parameters of the second step in the two H + O dissociation channels is to use the angular distributions via the $P_1(1.5)$ transition, in which the OH radical in the $A^2\Sigma^+$ (v' = 2, N' = 0, J' = 0.5) state is isotropically aligned in space. For the two-photon dissociation via the $P_1(1.5)$ transition resonance, the β value for the $H(^2S) + O(^1D)$ product channel is estimated to be -0.97, indicating a pure perpendicular transition in the second-photon excitation for this product channel, while the β value for the $H(^2S) + O(^1S)$ product channel is 1.97, showing a pure parallel transition in the second-photon excitation. The possible spin-allowed doublet electronic excited states of OH energetically accessible from the $A^2\Sigma^+$ state by the second photon excitation are $1^2\Sigma^-$, $1^2\Delta$, and $B^2\Sigma^+$. The $D^2\Sigma^-$ state has a higher energy than the two photons and is not accessible in this study. As the one-photon $1^2\Delta - A^2\Sigma^+$ excitation is forbidden, the only allowed accessible final states of OH in the two-photon excitation in this work are $2^2\Pi$ and $B^2\Sigma^+$ (Figure 3.1). The transition dipole moment of the

$2^2\Pi \leftarrow A^2\Sigma^+$ excitation is perpendicular to the OH bond, while that of the $B^2\Sigma^+ \leftarrow A^2\Sigma^+$ transition is parallel to the OH bond. During the dissociation of the OH radical, the nascent velocity of the H-atom should be along the OH bond in a prompt dissociation; the direct dissociation on the repulsive $2^2\Pi$ state to the $H(^2S) + O(^1D)$ product channel has a limiting β parameter of -1 and the prompt dissociation on the $B^2\Sigma^+$ state to $H(^2S) + O(^1S)$ has a limiting β of 2. The observed anisotropy parameters are consistent with the PECs that correlate to the different H + O product channels and that the $H(^2S) + O(^1D)$ and $H(^2S) + O(^1S)$ product channels are from dissociations on the $2^2\Pi$ and $B^2\Sigma^+$ states, respectively. An inspection of the PECs (Figure 3.1) indicates that both $2^2\Pi$ and $B^2\Sigma^+$ can be reached from the $A^2\Sigma^+ (v' = 2)$ state by the second photon excitation with comparable probabilities. While the $2^2\Pi$ state is purely repulsive [thus implying prompt, repulsive dissociation to $H(^2S) + O(^1D)$], the repulsive part of the $B^2\Sigma^+$ state is reached in the two-photon excitation process and the dissociation to $H(^2S) + O(^1S)$ is also repulsive (despite the shallow well of the $B^2\Sigma^+$ state at the longer internuclear distance).

The angle-integrated product translational energy distribution $P(E_T)$ can be derived from the $P(E_T, \theta)$ distributions at the perpendicular and parallel photolysis polarizations. The branching ratios of different product channels can be obtained from the $P(E_T)$ distribution. The branching ratio of the $H(^2S) + O(^1D)$ and $H(^2S) + O(^1S)$ product channels is calculated from the integrated peak intensities and is estimated to be ~ 3:4. As shown in Figure 3.1, in the Franck-Condon (FC) region the second photon reaches near the crossing points of the $2^2\Pi$ and $B^2\Sigma^+$ states; this fact supports that both PECs are involved

comparably during the dissociation processes, thus yielding likewise comparable $H(^2S)$ + $O(^1D)$ and $H(^2S)$ + $O(^1S)$ productions.

In the case of a slower, non-prompt dissociation or if the dissociation process crosses between the $2^2\Pi$ and $B^2\Sigma^+$ states, the observed anisotropy in the product channels would be reduced (i.e., the anisotropy parameter is not close to the limiting value of 2 or -1 for these two product channels). However, the anisotropy parameters of these two channels are both near the extreme cases, which suggests that the crossing between these two PECs is not significant during the prompt, repulsive dissociation processes. The anisotropic product angular distributions of these two product channels also reveal that the OH radical dissociates on repulsive states in a very short dissociation time (significantly shorter than a rotational period of the OH radical). The mechanism and dynamics of the $H(^2S)$ + $O(^1D)$ and $H(^2S)$ + $O(^1S)$ product channels would thus be direct dissociation of the OH radical on the repulsive potential energy curves ($2^2\Pi$ and $B^2\Sigma^+$) following the sequential two-photon excitation.

Based on conservation of energy and the electronic energies of the O atom and H atom,

$$E_{h\upsilon} + E_{int}(OH) - D_0(O\text{-}H) = E_T + E_{elec}(O)$$

$$= \frac{1}{2} m_H \left(1 + \frac{m_H}{m_O}\right)\left(\frac{L}{t_H}\right)^2 + \frac{m_H}{m_O} E_{OH} + E_{elec}(O)$$

in which $E_{h\upsilon}$ is the photon(s) energy, $E_{int}(OH)$ the initial internal energy of OH, $D_0(O\text{-}H)$ the bond dissociation energy of OH (from the ground-state level $X^2\Pi$ (v'' = 0, N'' = 1, J'' = 1.5, F_1), and $E_{elec}(O)$ the electronic energy of the O-atom product. As the $P_1(1.5)$, $Q_1(1.5)$,

and $R_1(1.5)$ transitions are all from the same OH ground state ($E_{int}(OH) = 0$), the equation can be rewritten as

$$E_{h\upsilon} - E_{elec}(O) = \frac{1}{2} m_H \left(1 + \frac{m_H}{m_O}\right) \left(\frac{L}{t_H}\right)^2 + D_0(O\text{-}H) + \frac{m_H}{m_O} E_{OH}$$

By using a linear regression of $E_{h\upsilon} - E_{elec}(O)$ versus $\left(\frac{1}{t_H}\right)^2$, along with the TOF peak positions of the two-photon products $H(^2S) + O(^1D)$ and $H(^2S) + O(^1S)$ and the one-photon prodcuts $H(^2S) + O(^3P_J)$ [from $A^2\Sigma^+$ (v' = 2 and 3, J' = 0.5-2.5, F_1)] (v' = 3 information was from our other work [33,35]) and the well-known electronic energy levels of the O atom, the y-intercept gives $D_0(O\text{-}H) + \frac{m_H}{m_O} E_{OH}$, and the refined calibration of L can be obtained from the slope. More than 30 TOF peak positions were included in the linear regression to achieve a high precision. As $\frac{m_H}{m_O} E_{OH}$ is determined to be ~23 cm^{-1}, an accurate O-H bond dissociation energy $D_0(O\text{-}H) = 35580 \pm 15$ cm^{-1} was obtained. This experimental value is in excellent agreement with the recent value (35580 ± 3 cm^{-1}) reported in the Active Thermochemical Tables (ATcT) database.[47]

3.4 Conclusions

The photodissociation of the OH radical is investigated whereby the photolysis energy is on the $P_1(1.5)$, $Q_1(1.5)$, and $R_1(1.5)$ transition resonances [$A^2\Sigma^+$ (v' = 2, J' = 0.5-2.5, F_1) $\leftarrow X^2\Pi$ (v'' = 0, J'' = 1.5, F_1)]. The $H(^2S) + O(^1D)$ and $H(^2S) + O(^1S)$ product channels are observed which are due to the dissociation of the OH radical on the $2^2\Pi$ and $B^2\Sigma^+$ PECs, respectively, following sequential two photon excitations via the $A^2\Sigma^+$

intermediate state. The product angular distribution of these two channels are anisotropic, with β = -0.97 for H(^{2}S) + O(^{1}D) and β = 1.97 for H(^{2}S) + O(^{1}S). The branching ratios of the H(^{2}S) + O(^{1}D) and H(^{2}S) + O(^{1}S) channels is estimated to be ~ 3:4. The dynamics of these electronic excited O-atom product channels would be the direct dissociation of the OH radical on the repulsive electronic states ($2^2\Pi$ and $B^2\Sigma^+$). The bond dissociation energy of OH is determined to be D_0(O-H) = 35580 $\pm$ 15 cm^{-1}, in excellent agreement with the value from the Active Thermochemical Tables (ATcT) database.

Reference

1. M. L. Sink, A. D. Bandrauk, and R. Lefebvre, *J. Chem. Phys.* **73**, 4451 (1980).

2. E. F. van Dishoeck and A. Dalgarno, *J. Chem. Phys.* **79**, 873 (1983).

3. S. Lee and K. F. Freed, *J. Chem. Phys.* **87**, 5772 (1987).

4. D. R. Yarkony, *J. Chem. Phys.* **97**, 1838 (1992).

5. C. Kalyanaraman and N. Sathyamurthy, *Chem. Phys.* **187**, 219 (1994).

6. S. Lee, *J. Chem. Phys.* **103**, 3501 (1995).

7. G. Parlant and D. R. Yarkony, *J. Chem. Phys.* **110**, 363 (1999).

8. M. P. J. van der Loo and G. C. Groenenboom, *J. Chem. Phys.* **123**, 074310 (2005).

9. B. S. D. R. Vamhindi and M. Nsangou, *Mol. Phys.* **114**, 2204 (2016).

10. G. H. Dieke and H. M. Crosswhite, *J. Quant. Spectrosc. Radiat. Transfer* **2**, 97 (1962).

11. C. Carlone and F. W. Dalby, *Can. J. Phys.* **47**, 1945 (1969).

12. E. A. Moore and W. G. Richards, *Phys. Scr.* **3**, 223 (1971).

13. K. R. German, *J. Chem. Phys.* **63**, 5252 (1975).

14. T. Bergeman, P. Erman, and M. Larsson, *Chem. Phys.* **54**, 55 (1980).

15. J. A. Coxon, *Can. J. Phys.* **58**, 933 (1980).

16. J. B. Nee and L. C. Lee, *J. Chem. Phys.* **81**, 31 (1984).

17. R. A. Copeland, J. B. Jeffries, and D. R. Crosley, *J. Mol. Spectrosc.* **143**, 183 (1990).

18. R. J. Cody, C. Moralejo, and J. E. Allen, *J. Chem. Phys.* **95**, 2491 (1991).

19. M. Collard, P. Kerwin, and A. Hodgson, *Chem. Phys. Lett.* **179**, 422 (1991).

20. J. A. Coxon, A. D. Sappey, and R. A. Copeland, *J. Mol. Spectrosc.* **145**, 41 (1991).

21. E. de Beer, M. P. Koopmans, C. A. de Lange, Y. Wang, and W. A. Chupka, *J. Chem. Phys.* **94**, 7634 (1991).

22. J. A. Gray and R. L. Farrow, *J. Chem. Phys.* **95**, 7054 (1991).

23. D. E. Heard, D. R. Crosley, J. B. Jeffries, G. P. Smith, and A. Hirano, *J. Chem. Phys.* **96**, 4366 (1992).

24. J. J. L. Spaanjaars, J. J. ter Meulen, and G. Meijer, *J. Chem. Phys.* **107**, 2242 (1997).

25. E. S. Hwang, J. B. Lipson, R. W. Field, and J. A. Dodd, *J. Phys. Chem. A* **105**, 6030 (2001).

26. C. McRaven, J. Alnis, B. Furneaux, and N. Shafer-Ray, *J. Phys. Chem. A* **107**, 7138 (2003).

27. E. L. Derro, I. B. Pollack, L. P. Dempsey, M. E. Greenslade, Y. Lei, D. Č. Radenović, and M. I. Lester, *J. Chem. Phys.* **122**, 244313 (2005).

28. M. E. Greenslade, M. I. Lester, D. Č. Radenović, A. J. A. van Roij, and D. H. Parker, *J. Chem. Phys.* **123**, 074309 (2005).

29. Q. Xiong, A. Y. Nikiforov, L. Li, P. Vanraes, N. Britun, R. Snyders, X. P. Lu, and C. Leys, *Eur. Phys, J. D.* **66**, 281 (2012).

30. A. Fast, J. E. Furneaux, and S. A. Meek, *Phys. Rev. A* **98**, 052511 (2018).

31. J. Brzozowski, P. Erman, and M. Lyyra, *Phys. Scr.* **17**, 507 (1978).

32. D. Č. Radenović, A. J. A. van Roij, S.-M. Wu, J. J. ter Meulen, D. H. Parker, M. P. J. van der Loo, and G. C. Groenenboom, *Phys. Chem. Chem. Phys.* **11**, 4754 (2009).

33. W. Zhou, Y. Yuan, and J. Zhang, *J. Chem. Phys.* **119**, 9989 (2003).

34. D. Č. Radenović, A. J. A. van Roij, S.-M. Wu, J. J. Ter Meulen, D. H. Parker, M. P. J. van der Loo, L. M. C. Janssen, and G. C. Groenenboom, *Mol. Phys.* **106**, 557 (2008).

35. G. Sun, W. Zhou, Y. Qin, Y. Yuan, and J. Zhang, (2019).

36. G. Amaral, K. Xu, and J. Zhang, *J. Phys. Chem. A* **105**, 1115 (2001).

37. X. Zheng, J. Wu, Y. Song, and J. Zhang, *Phys. Chem. Chem. Phys.* **11**, 4761 (2009).

38. G. Sun, M. Lucas, Y. Song, J. Zhang, C. Brazier, P. L. Houston, and J. M. Bowman, *J. Phys. Chem. A* **123**, 9957 (2019).

39. G. Sun, X. Zheng, Y. Song, and J. Zhang, *J. Phys. Chem. A* **123**, 5849 (2019).

40. R. J. Buenker and S. D. Peyerimhoff, *Theor. Chim. Acta* **35**, 33 (1974).

41. R. J. Buenker, S. D. Peyerimhoff, and W. Butscher, *Mol. Phys.* **35**, 771 (1978).

42. R. J. Buenker and R. A. Phillips, *Journal of Molecular Structure: THEOCHEM* **123**, 291 (1985).

43. T. H. Dunning, *J. Chem. Phys.* **90**, 1007 (1989).

44. A. B. Alekseyev, H. P. Liebermann, G. J. Vázquez, and H. Lefebvre-Brion, *J. Chem. Phys.* **148**, 084302 (2018).

45. R. N. Zare, *Mol. Photochem.* **4**, 1 (1972).

46. A. Kramida, Y. Ralchenko, J. Reader,(2019), NIST Atmoic Spectra Database (ver 5.7.2). https://doi.org/10.18434/T4W30F.

47. B. Ruscic, *J. Phys. Chem. A* **119**, 7810 (2015).

Chapter 4

Photodissociation Dynamics of the Ethyl Radical via the $\tilde{A}^2A'$ (3s) State: H-atom Product Channels and Ethylene Product Vibrational State Distribution

Abstract

The photodissociation dynamics of jet-cooled ethyl radical (C_2H_5) via the $\tilde{A}^2A'$(3s) state and the H-atom product channels were studied in the wavelength region of 230-260 nm using the high-*n* Rydberg atom time-of-flight (HRTOF) technique. A non-statistical, repulsive H + C_2H_4($\tilde{X}\ ^1A_g$) product channel was observed with the C_2H_4 product vibrational state distribution partially resolved, giving geometry information of this direct dissociation pathway. A statistical H + C_2H_4($\tilde{X}\ ^1A_g$) product channel via unimolecular dissociation from the hot ground-state ethyl after internal conversion from the Rydberg state was also studied, with its dissociation time evaluated by energy-dependent angular distribution and pump-probe delay measurements. The branching ratio between the non-statistical repulsive product channel and the statistical product channel varied significantly with the photolysis excitation energy. A high-energy, adiabatic H + triplet $C_2H_4(\tilde{a}^3B_{1u})$ product channel was identified by energy-dependent angular distribution.

4.1 Introduction

In hydrocarbon combustion processes, ethyl radical (C_2H_5) is an important intermediate.[1] The dissociation of ground electronic state ethyl radical to H atom and ethylene and its reverse reaction have been studied extensively by experiments and theories.[2-11] The dissociation of ethyl radical via the excited electronic states has also drawn considerable attentions.[12-21]

The UV absorption spectrum of the ethyl radical is comprised of broad and structureless bands due to Rydberg transitions.[22-26] The first absorption band is around 230-265 nm and peaks at 245 nm, corresponding to the $2p_z \rightarrow 3s$ transition [$\tilde{X}\,^2A'$- $\tilde{A}^2A'(3s)$] on the α radical-center carbon atom. The second band in 190-230 nm peaks around 206 nm and has been assigned to the $2p_z \rightarrow 3p$ excitation. The H-atom loss dissociation channels of the ethyl radical are most important and are listed as[27-29]

$$C_2H_5(\tilde{X}\,^2A') \rightarrow H + C_2H_4(\tilde{X}\,^1A_g) \quad \Delta H_0 = 34.90 \text{ kcal/mol} \quad (4.1)$$

$$\rightarrow H + C_2H_4(\tilde{a}^3B_{1u}) \quad \Delta H_0 = 96.83 \text{ kcal/mol} \quad (4.2)$$

$$\rightarrow H + CH_3CH(\text{triplet}, {}^3A'') \quad \Delta H_0 = 106.69 \text{ kcal/mol} \quad (4.3)$$

$$\rightarrow H + CH_3CH(\text{singlet}, {}^1A') \quad \Delta H_0 = 109.67 \text{ kcal/mol} \quad (4.4)$$

Figure 4.1 shows the energy level and correlation diagram of C_2H_5 photodissociation to the H atom and C_2H_4 products in C_s and C_{2v} symmetry. In the C_s symmetry, the ground-state ethyl $C_2H_5(\tilde{X}\,^2A')$ correlates adiabatically with the H + ground-state $C_2H_4(\tilde{X}\,^1A_g)$ products, and the excited-state $C_2H_5[\tilde{A}^2A'(3s)]$ correlates

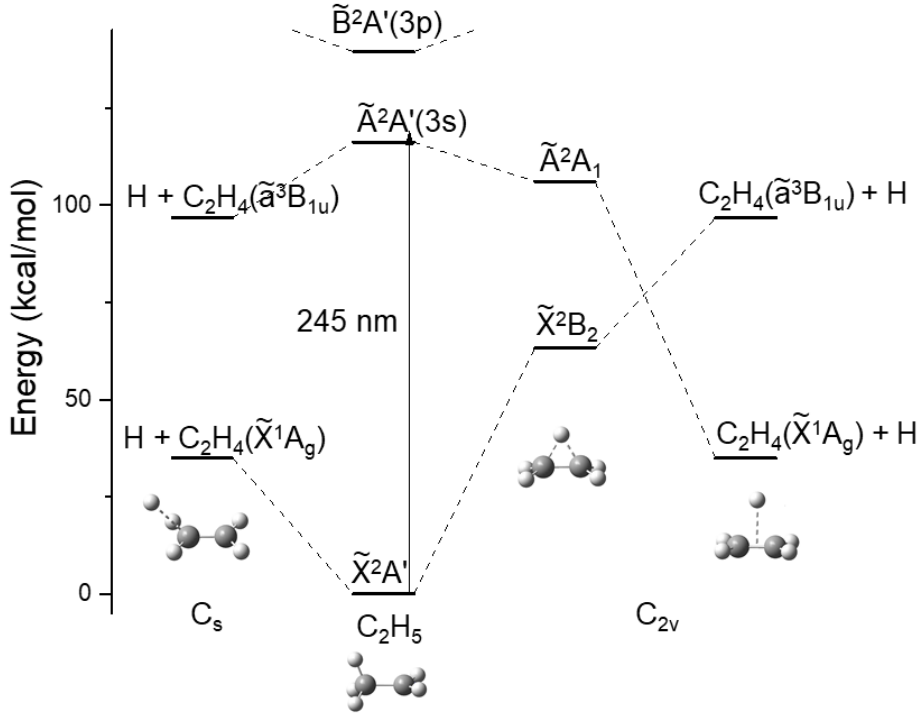

Figure 4.1. Potential energy diagram of the ethyl radical photodissociation system in C_s and C_{2v} symmetry. The energies of C_2H_5 [$\tilde{A}^2A'(3s)$] in C_s, C_2H_5 [$B^2A'(3p)$] in C_s, C_2H_5 ($\tilde{X}\ ^2B_2$) in C_{2v}, and C_2H_5 ($\tilde{A}^2A_1$) in C_{2v} are based on the adiabatic transition of UV absorption spectrum and Mebel's theoretical calculation (Ref 14).

adiabatically with H + excited-state $C_2H_4(\tilde{a}^3B_{1u})$. Theoretical studies have shown that upon excitation to the $\tilde{A}^2A'(3s)$ Rydberg state from the ground-state $\tilde{X}^2A'$ in the classical equilibrium geometry, one β H atom shifts to the C-C bond center into a non-classical H-bridged C_{2v} geometry (isomerization from $\tilde{A}^2A'(3s)$ in C_s to the lower energy $\tilde{A}^2A_1$ state in C_{2v}).[12-14] In the C_{2v} symmetry, the ethyl $\tilde{A}^2A_1$ excited state correlates adiabatically with the $H + C_2H_4(\tilde{X}^1A_g)$ products instead, and the H-bridged ground-state $C_2H_5(\tilde{X}^2B_2)$ correlates with $H + C_2H_4(\tilde{a}^3B_{1u})$ on the $^2B_2$ surface. The $^2A_1$ and $^2B_2$ surfaces cross with a conical intersection. Consequently, the excited ethyl radical in the $\tilde{A}^2A'(3s)$ state could migrate to the non-classical bridged structure, pass through the conical intersection, and decompose into H and ground-state ethylene, via either a direct, fast dissociation (with a large translational energy release) or an indirect dissociation after spending some time in potential well of the ground-state ethyl radical (with small translational energy release).[13,14]

Previous experimental studies[18,21] on the photodissociation of ethyl radical via $\tilde{A}^2A'(3s)$ revealed bimodal product translational energy and angular distributions and thus two H-atom product channels: fast H atoms with an anisotropic angular distribution and slow H atoms with an isotropic angular distribution, consistent with the dissociation pathways via the conical intersection.[12-14] A recent direct *ab initio* molecular dynamics simulation of the ethyl $\tilde{A}^2A'(3s)$ photodissociation by Chen and co-worker confirmed that nonadiabatic dissociation via the conical intersection produces the ground-state ethylene and fast H atom products with an anisotropic angular distribution (Channel 1a), as well as hot ground-state ethyl that undergoes unimolecular dissociation to C_2H_4 + H with small kinetic energy release (Channel 1b).[20] In addition, this work predicted an adiabatic

dissociation pathway of the 3s Rydberg state ethyl radical to the electronic excited triplet ethylene $C_2H_4(\tilde{a}^3B_{1u})$ and H atom with an anisotropic angular distribution (Channel 2).[20] Selective β H-atom elimination was observed in the photodissociation of ethyl 3s Rydberg state by using partially-deuterated samples.[15-18,21]

The dissociation rate of the H-atom product channels has been examined with both experimental and theoretical work.[17,20,21,30-33] The dissociation rates of ethyl via the $\tilde{A}^2A'(3s)$ state upon photoexcitation in the range of 264 to 245 nm were measured by Chen and co-workers to be ~ 10^7 s^{-1},[17] which were four to five orders of magnitude slower than the expected rate from the Rice-Ramsperger-Kassel-Marcus (RRKM) theory.[6,17] Recently, Fischer and co-worker measured the H-atom product kinetic energy distribution in the 250 nm photodissociation of ethyl as a function of pump and probe delay time, and showed a sub-nanosecond dissociation time constant for the H-atoms with large kinetic energy (Channel 1a) and confirmed a ~ 100 ns dissociation time for the slow H-atoms (Channel 1b).[21] The classical trajectory calculations by Chen and co-workers showed that in the unimolecular dissociation of ethyl at a total energy of 120 kcal/mol, close to the UV photoexcitation wavelength of 238 nm, 78% trajectories dissociate to H + C_2H_4 in ~ 1 ps on the RRKM time scale, while the remaining hot ground-state ethyl radical is non-RRKM and persists with a lifetime > 7 ps, presumably trapped in long-lived quasiperiodic trajectories.[30,31] The more recent surface hopping trajectory calculations by Chen and co-workers followed the dissociation dynamics from the excited $\tilde{A}^2A'(3s)$ state and found that the direct dissociation of ethyl to H + ground-state C_2H_4 (Channel 1a) has a lifetime of ~ 40 fs, the indirect dissociation to H + ground-state C_2H_4 via the hot ground-state ethyl

(Channel 1b) has a lifetime of ~ 1.5 ps, and the adiabatic dissociation from $\tilde{A}^2A'(3s)$ to H + $C_2H_4(\tilde{a}^3B_{1u})$ has a lifetime of ~ 60 fs.[20] It was then suggested that the previously observed unusually slow dissociation rate of ethyl[17] should arise from slow dissociation on the ground-state surface of ethyl.[20] A recent classical trajectory study of ethyl dissociation on the ground electronic state at the similar energy of 100-150 kcal/mol by Wagner and co-workers showed that ethyl dissociates in < 100 ps, consistent with the RRKM model, and there was no evidence of nanosecond lifetimes.[32] A roaming dissociation mechanism of ethyl was also proposed to explain the unusually slow production of H atoms, in which the ethyl radical dissociates initially to vinyl radical + H_2 in a roaming pathway and the hot vinyl radical undergoes secondary decomposition to produce H + C_2H_2 at a slow dissociation rate.[33] This slow H-atom production, however, would be a minor channel compared to H + C_2H_4 and is also limited to low kinetic energy H atoms (< 35 kcal/mol for 245 nm photoexcitation).

In this chapter, we report a further study on the photodissociation dynamics of jet-cooled ethyl radical via the $\tilde{A}^2A'(3s)$ state in the region of 230-260 nm by using the high-n Rydberg H-atom time-of-flight (HRTOF) technique. H-atom product TOF spectra were measured with linearly polarized photolysis laser radiation. The H-atom photofragment yield (PFY) spectrum (i.e. action spectrum) was obtained by integrating the H-atom signals in the TOF spectra at different photolysis wavelengths. From the H-atom TOF spectra at different photolysis laser polarizations, center-of-mass (CM) translational energy and angular distributions of the H and C_2H_4 products were derived. Three H-atom loss dissociation channels were observed, a fast and anisotropic one with large, repulsive

translational energy release, a slow and isotropic one with small translational energy release, and a fast and anisotropic one with very small translational energy release, consistent with Channel 1a, 1b and 2 by Chen and co-workers.[20] With improved resolution, vibrational state distribution of the ethylene product in the fast repulsive dissociation channel (Channel 1a) was partially resolved. The dissociation time scales of the H-atom products at different translational energies were examined by H-atom angular distribution and by measuring the H-atom TOF spectra as a function of pump-probe time delay. The branching ratios between the non-statistical repulsive product channel (Channel 1a) and the slow unimolecular dissociation channel (Channel 1b) were obtained as a function of photolysis wavelength. Initial evidence of the high-energy $C_2H_4(\tilde{a}^3B_{1u})$ + H product channel (Channel 2, anisotropic with small kinetic energy) is also presented.

4.2 Experimental

The experimental technique and apparatus of high-n Rydberg H-atom time-of-flight (HRTOF) have been described in previous publications.[18,34-37] Nitroethane ($C_2H_5NO_2$, Aldrich 99.5%) and 3-pentanone ($C_2H_5COC_2H_5$, Aldrich >99%) were employed as precursors to generate the ethyl radicals. The mixture of low-concentration precursors in Ar [0.2-2% (typically 0.2-0.5%)] at a total pressure of 1.2-1.5 atm was expanded from a pulsed nozzle. The pulsed ethyl radical beam was produced by photolyzing the precursors in front of the pulsed nozzle with a 193 nm radiation from an ArF excimer laser. The radicals formed from the photolysis were subsequently cooled by

supersonic expansion and entrained in the seeded molecular beam. In the photolysis region downstream, the ethyl radicals were photodissociated by a tunable UV laser beam (at 230-260 nm, 0.2-1.8 mJ/pulse). The H atoms formed from the photodissociation of the ethyl radicals were excited by two-color resonant excitation (121.6 nm + 366.3 nm), i.e., from 1^2S to 2^2P via the H-atom Lyman-α transition and then to a high-n Rydberg state. A small fraction of these metastable Rydberg H atoms drifted with their nascent velocities to a microchannel plate (MCP) detector that was positioned perpendicular to the molecular beam and were field-ionized in front of MCP and detected. The nominal flight distance was 37.14 cm, which was calibrated by 236 nm photodissociation of HBr utilizing the well-studied HBr dissociation energy and the spin-orbit energy splitting of the $Br(^2P_{3/2})$ and $Br(^2P_{1/2})$ products. A fast pre-amplifier amplified the ion signals, and the signals were averaged by a multichannel scaler. The H-atom TOF spectra were typically accumulated with 60 to 180 k laser firings. The polarization of the photolysis radiation can be changed by a Fresnel-Rhomb achromatic λ/2 plate for the H-atom product angular distribution measurements.

4.3 Results

The ethyl radical beams using the nitroethane and 3-pentanone precursors were characterized by vacuum ultraviolet (VUV) single-photon ionization TOF mass spectrometry using the Lyman-α radiation at 121.6 nm. The production of the ethyl radicals (ionization energy 8.1 eV) from 193-nm photolysis of the precursors was identified at m/z

29 in the mass spectra. The H-atom product TOF spectra of the photodissociation of ethyl were measured in the photolysis wavelength region of 230-260 nm. Background in the TOF spectra, such as that from the precursors, was properly removed, as described in previous studies.[18,34-37] Figure 4.2 shows the net H-atom product TOF spectra of photodissociation of C_2H_5 (using nitroethane precursor) at 245 nm, with the UV photolysis radiation polarization parallel ($\parallel$, $\theta = 0°$) and perpendicular ($\perp$, $\theta = 90°$) with respect to the TOF axis. The H-atom TOF spectra using the 3-pentanone precursor were also taken and were similar, showing that the ethyl radical was the common origin of the photodissociation signals. The photolysis laser power was kept mainly in the range of 0.5-1.5 mJ/pulse. A photolysis laser power dependence was examined at both parallel and perpendicular polarizations, showing that the H-atom product signals in the entire TOF spectra had a linear power dependence in the photolysis laser power range of 0.5-1.8 mJ/pulse.

The H-atom photofragment yield (PFY) spectrum of the ethyl radical was obtained in the photolysis wavelength region of 230-260 nm (Figure 4.3). The spectrum was acquired by integrating the net H-atom product TOF spectrum of the ethyl radical photodissociation as a function of UV photolysis radiation wavelength. To correct for the variation and drift of the experimental conditions, the H-atom signals at 245 nm were taken as references and monitored after every 3 measurements at other wavelengths. The H-atom signal intensities at other photolysis wavelengths were normalized for the photolysis laser power and number of shots and scaled to those at 245 nm. The H-atom PFY spectrum agrees well with the

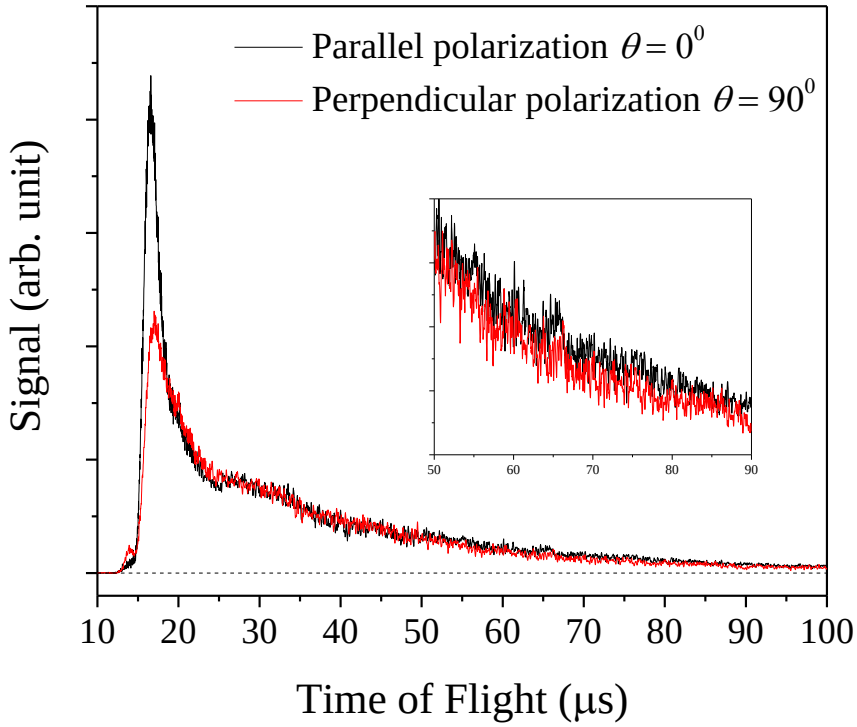

Figure 4.2. Net H-atom TOF spectra of 245 nm photodissociation of jet-cooled C_2H_5 (from nitroethane precursor 0.2% in 1000 Torr Ar), with the electric vector of the linear polarized photolysis radiation parallel and perpendicular to the TOF path. The signals have been normalized to the same laser power and laser shots.

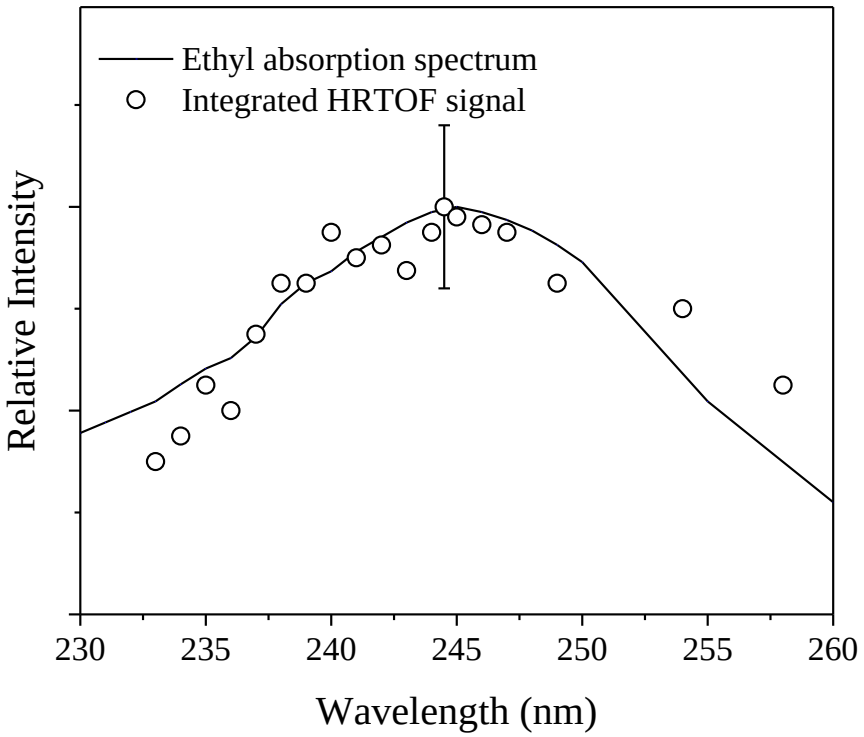

Figure 4.3. H-atom photofragment yield (PFY) spectrum as a function of photolysis radiation wavelength in the region of 230-260 nm. The PFY (in the open circles) was obtained by integrating the HRTOF signals at different photolysis excitation wavelength and was normalized with the laser power and shots. Both the PFY and absorption spectrum were scaled to 1 at their maximum intensities. The solid line represents the ethyl absorption spectrum taken from Fagerstrom's work (Ref 24).

ethyl UV absorption spectrum by Fagerström *et al*,[24] providing further confirmation that the net H-atom signals were from photodissociation of the ethyl radical.

The net H-atom TOF spectra of the ethyl radical photodissociation are transformed to total center-of-mass (CM) translational energy distributions, $P(E_T)$'s. The CM translational energy of the products, E_T, is converted from the H-atom flight time t_H using the following equation:[38]

$$E_T = \left(1 + \frac{m_H}{m_{C_2H_4}}\right) E_H + \frac{m_H}{m_{C_2H_4}} E_{C_2H_5} = \frac{1}{2} m_H \left(1 + \frac{m_H}{m_{C_2H_4}}\right) \left(\frac{L}{t_H}\right)^2 + \frac{m_H}{m_{C_2H_4}} E_{C_2H_5} \quad (4.5)$$

where E_T is the total CM translational energy of the H atom and ethylene products, E_H is the laboratory translational energy of the H-atom photofragment, and L is the flight length. The second term $\frac{m_H}{m_{C_2H_4}} E_{C_2H_5}$ is due to the parent C_2H_5 radical motion in the molecular beam which is orthogonal to the TOF path; it is very small compared with the first term (products' CM translation). By using equation (5), the product CM translational energy distributions of the H + C_2H_4 product channel at the 245 nm photodissociation wavelength with the linearly polarized photolysis radiation parallel and perpendicular, $P(E_T, \theta)$ at θ = 0° and 90° ($P_\parallel(E_T)$ and $P_\perp(E_T)$), are derived from the corresponding H-atom spectra in Figure 4.2 and are shown in Figure 4.4 (a) and (c), respectively. The product CM translational energy and photofragment angular distributions in the photodissociation can be related to the molecular properties in the following equation:[39]

$$P(E_T, \theta) = \left(\frac{1}{4\pi}\right)[1 + \beta P_2(cos\theta)] P(E_T) \quad (4.6)$$

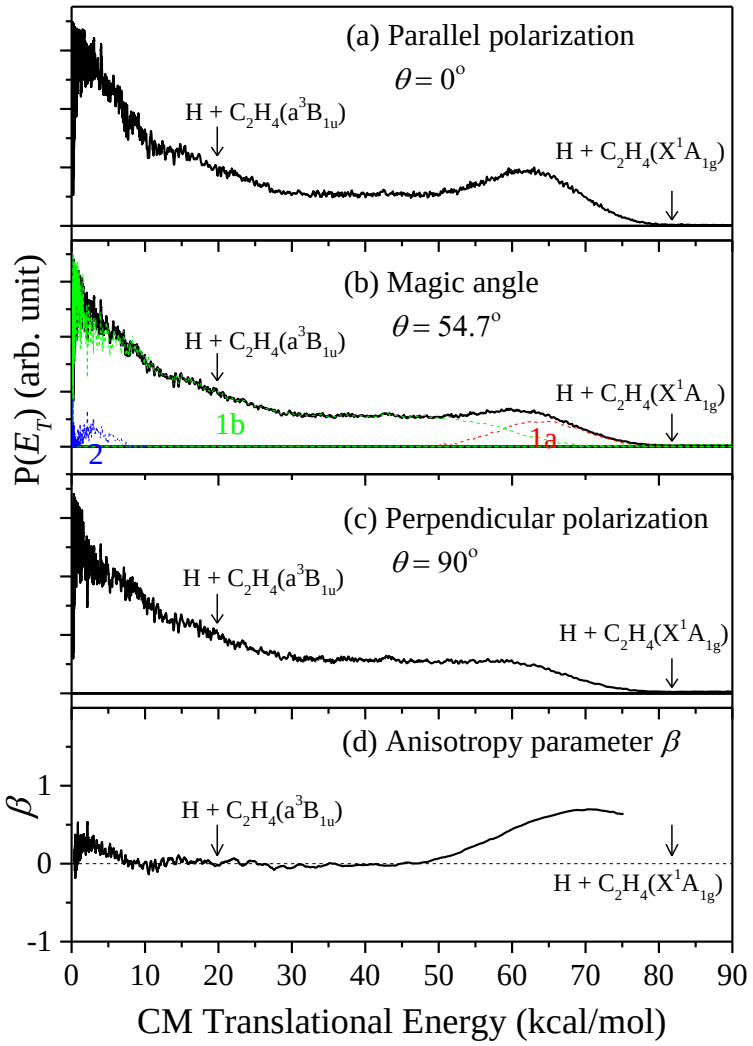

Figure 4.4. H + C_2H_4 products center-of-mass translational energy distribution $P(E_T, \theta)$ derived from the TOF spectra in Figure 4.2, with 245 nm photolysis radiation and the polarization of the photolysis (a) parallel to the TOF path, (c) perpendicular to the TOF path. (b) at the magic angle is calculated form (a) and (c). (d) the translational energy dependent anisotropy parameter $\beta(E_T)$. The magic angle distributions $P_m(E_T)$ are deconvoluted into the component 1a, 1b, and 2. See text for more details.

where β is the anisotropy parameter (-1$\leq \beta \leq$2), θ is the angle between the electric vector of the linearly polarized photolysis radiation and the recoiling velocity vector of the H-atom product (the direction of detection or the TOF axis), $P_2(cos\theta)$ is the second Legendre polynomial, and $P(E_T)$ is the angle-integrated translational energy distribution. The energy-dependent anisotropy parameter $\beta(E_T)$ is derived from Equation (6) and can be calculated by:[18]

$$\beta(E_T) = 2\frac{P_{\parallel}(E_T)-P_{\perp}(E_T)}{P_{\parallel}(E_T)+2P_{\perp}(E_T)} \quad (4.7)$$

and $\beta(\mathrm{E_T})$ is shown in Figure 4.4 (d). The $P(E_T, \theta)$ at magic angle $\theta = 54.7°$, $P_m(E_T) = \frac{1}{4\pi}P(E_T)$, is calculated from $P_{\parallel}(E_T)$ and $P_{\perp}(E_T)$ and presented in Figure 4.4(b).[39] $P_m(E_T)$ is independent of β and proportional to the angle-integrated $P(E_T)$; for convenience, $P_m(E_T)$ is used here to represent $P(E_T)$ for obtaining the product average translational energy release and the branching ratios.

The $P(E_\mathrm{T})$ distributions show a bimodal distribution, while the anisotropy parameter $\beta(E_\mathrm{T})$ have three different regions that could indicate three different regions of $P(E_\mathrm{T})$. From E_T at the maximum available energy in the 245 nm photodissociation (81.77 kcal/mol) to about 65 kcal/mol, $\beta(E_\mathrm{T})$ stays near a constant value of 0.67 $\pm$ 0.10. It gradually decreases to a constant value of ~ 0 with the CM translational energy E_T smaller than ~ 50 kcal/mol. When E_T is smaller than ~ 10 kcal/mol, $\beta(E_\mathrm{T})$ starts to increase and reaches a local maximum of 0.25 $\pm$ 0.10 at ~ 2 kcal/mol in this low E_T region. This behavior of the β parameter in the low E_T region is different from that of a typical statistical unimolecular dissociation, in which the β value is zero at low translational energy (for its

dissociation time scale is longer than the parent rotational period). The accurate measurement of the anisotropy parameter β requires reliable measurements of H-atom TOF spectra at both parallel and perpendicular polarizations with proper background removal. The background in this system was broad and significant in the small E_T region, which could potentially cause larger uncertainty in the β value in the small E_T region. Nevertheless, with the improved instrument sensitivity and the signal averaging accumulated with large numbers of laser shots in multiple measurements (with total 360 k laser shots), the positive β in the lowest energy region (E_T < 10 kcal/mol) was repeatedly observed, and the measured β value was considered to be reliable in this work.

The changing β parameter indicates at least three product channels. The observed $P(E_T)$ can be considered to be the sum of the contributions from different dissociation channels, and the changing β value with E_T is due to the different β parameters for these different product channels and their energy-dependence branching ratios.[18,40] The overall product translational energy distribution, $P(E_T)$, and product translational energy-dependent anisotropy parameter, $\beta(E_T)$, can be expressed as $P(E_T) = P_{1a}(E_T) + P_{1b}(E_T) + P_2(E_T)$ and $\beta(E_T) = x_{1a}(E_T)\beta_{1a} + x_{1b}(E_T)\beta_{1b} + x_2(E_T)\beta_2$, where β_i is the anisotropy parameter of the *i*th channel (assumed to be constant), $P_i(E_T)$ and $x_i(E_T)$ are the translational energy distribution and translational energy-dependent branching ratio of the *i*th product channel, $x_i(E_T) = \frac{P_i(E_T)}{P(E_T)}$, and $x_{1a}(E_T)+x_{1b}(E_T)+x_2(E_T) = 1$.[18,40] The third channel with anisotropic angular distribution ($\beta \sim 0.25$) but very small kinetic energy at E_T < 10 kcal/mol is consistent with the higher energy product channel H + $C_2H_4(\tilde{a}^3B_{1u})$ (Channel 2 predicted by Chen and co-workers,[20] discussed more in the following). The

maximum available energy of Channel 2 is 19.84 kcal/mol at the 245 nm photolysis wavelength,[27,29] and there is no contribution from Channel 2 at E_T larger than this threshold (i.e., $x_2(\mathrm{E_T}) = 0$, at E_T > 19.84 kcal/mol). At E_T > 19.84 kcal/mol, $P(E_T)$ and $\beta(E_T)$ can be expressed as $P_{1a}(E_T) + P_{1b}(E_T)$ and $x_{1a}(\mathrm{E_T})\beta_{1a} + x_{1b}(\mathrm{E_T})\beta_{1b}$. As shown in the previous studies,[18] the β_{1b} parameter for the slow, isotropic unimolecular dissociation channel (Channel 1b) is 0, then $\beta(\mathrm{E_T}) = x_{1a}(\mathrm{E_T})\beta_{1a}$ at E_T > 19.84 kcal/mol. $P_{1a}(E_T)$ for Channel 1a (the fast, anisotropic dissociation channel) is derived to be $\frac{2}{3\beta_{1a}}[P_{\parallel}(E_T) - P_{\perp}(E_T)]$. Assuming that near the maximum E_T, the contribution of Channel 1b is 0, then $x_{1a}(\mathrm{E_T}) = 1$, $\beta_{1a} = 0.67 \pm 0.1$, and $P_{1a}(E_T)$ is readily derived. Similarly, at E_T < ~ 50 kcal/mol, the contribution from Channel 1a is 0 and β_{1b} is 0, $\beta(\mathrm{E_T}) = x_2(\mathrm{E_T})\beta_2$, and $P_2(E_T)$ for Channel 2 (the lowest E_T, anisotropic dissociation channel) can be expressed as $\frac{2}{3\beta_2}[P_{\parallel}(E_T) - P_{\perp}(E_T)]$. Depending on the maximum $x_2(\mathrm{E_T})$ value in the lowest energy region, β_2 is in the range of 0.25 ± 0.10 to 2. The β value of the anisotropic $C_2H_4(\tilde{a}^3B_{1u})$ + H channel (Channel 2) was predicted to be ~1.3 by Chen and co-workers;[20] assuming this value for β_2, $P_2(E_T)$ can then be derived. The $P(E_T)$ is deconvoluted into $P_{1a}(E_T)$, $P_{1b}(E_T)$, and $P_2(E_T)$, for the three dissociation channels, Channel 1a, Channel 1b, and Channel 2, respectively, as shown in Figure 4.4 (b). In the 245 nm photodissociation of ethyl, the average translational energy release of the three dissociation channels, $\langle E_T \rangle$, are estimated to be 63.9, 22.2, and 3.6 kcal/mole, respective; the fraction of $\langle E_T \rangle$ of the three dissociation channels in the total available energy to the H + $C_2H_4(\tilde{X}\,^1A_g)$ products, $\langle f_T \rangle$, are 0.78, 0.27, and 0.04 (or 0.18 to the H + $C_2H_4(\tilde{a}^3B_{1u})$ products), respectively. The

branching ratios of the three dissociation channels are calculated to be 0.11:0.87:0.02. Note that depending on the assumed β_2 value, the contribution of Channel 2 could be from 0.01 (for β_2 = 2) to 0.10 (for β_2 = 0.25); nevertheless, Channel 2 is a minor channel, with the smallest branching fraction.

To study the photoexcitation energy dependence of the branching ratios, the net H-atom TOF spectra of the ethyl photodissociation obtained at different photolysis wavelengths are analyzed (Figure 4.5a and 4.5b). As shown in Figure 4.5a, the H-atom TOF spectra are normalized to the same laser shots and scaled to the intensity in the low translational energy component, and the intensity of the high translational component is observed to change significantly relative to that of the slow component at different photolysis wavelengths, with the highest intensity ratio at 244.5 nm. The H-atom TOF spectra were integrated in different time regions for Channel 1a and 1b (note that it is difficult to remove the contribution of Channel 2 from the integrated intensity of Channel 1b, but the contribution of Channel 2 is very small); the ratio of Channel 1a to 1b as a function of the photolysis wavelength is shown in Figure 4.5b. The ratio varies significantly with the photolysis wavelength; the branching ratio has a peak at 244.5 nm and decreases at both longer and shorter photolysis wavelengths.

In this study, the energy resolution in the $P(E_T)$ distribution was improved by using very diluted precursors (~ 0.5%) and better cooled radicals in the seeded molecular beam, and the detection sensitivity was also improved to achieve a good signal to noise ratio. As shown in Figure 4.4 (a), some fine structures are apparent in the anisotropic, high translational energy region (E_T > ~ 60 kcal/mol), showing partially resolved vibrational

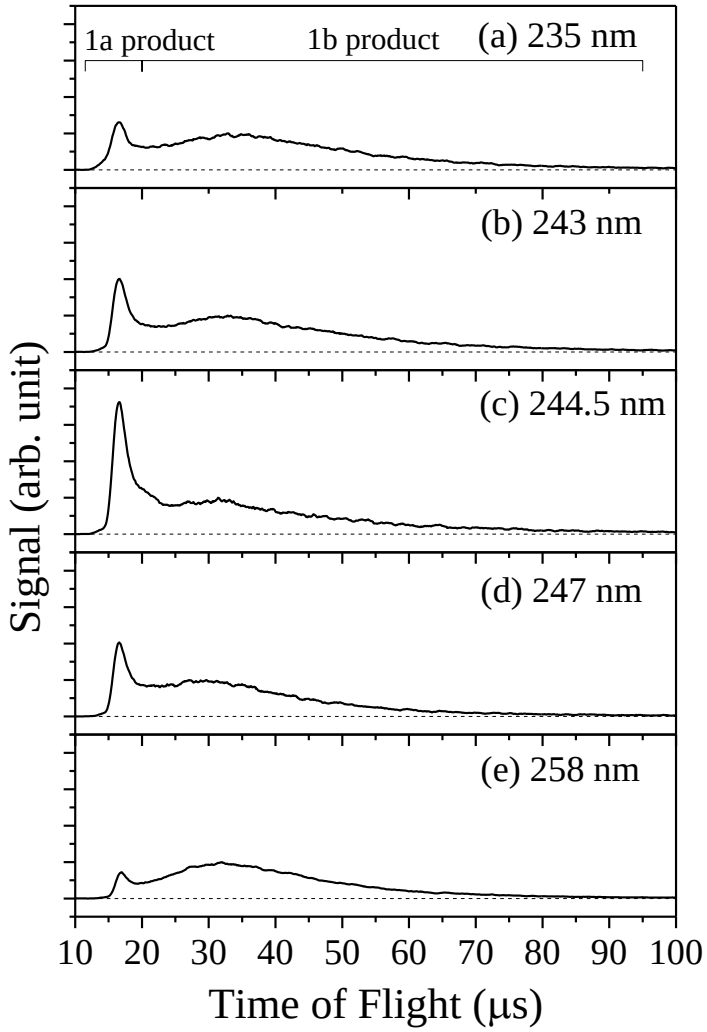

Figure 4.5a. Net H-atom TOF spectra of photodissociation of jet-cooled C_2H_5 at different photolysis wavelength (from nitroethane precursor 0.2% in 1000 Torr Ar). The signals are normalized to the same intensity for the low kinetic H-atom product. The photolysis laser polarization is parallel to the TOF path.

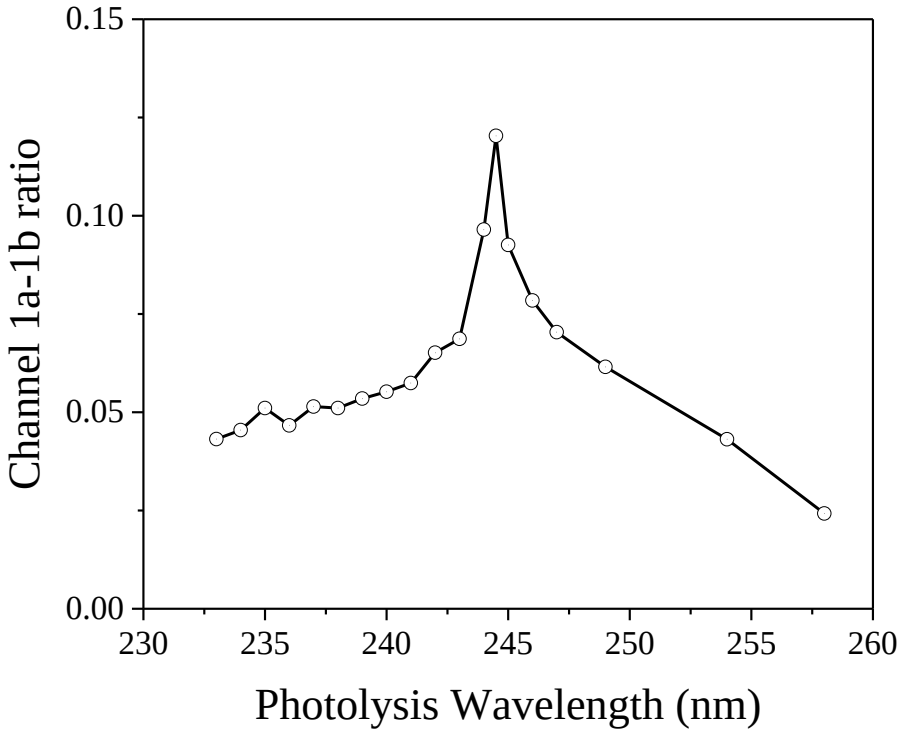

Figure 4.5b. Ratio between the integrated H-atom signals of product channel 1a and 1b from the photodissociation of ethyl radical (nitroethane precursor) as a function of the photolysis wavelength. The ratio varies significantly at different photolysis wavelength and reaches the maximum with 244.5 nm photodissociation radiation.

state distribution of the ethylene product in Channel 1a. As described above, the product CM translational energy distribution for Channel 1a, $P_{1a}(E_T)$, is obtained as $\frac{2}{3\beta_{1a}}[P_{\parallel}(E_T) - P_{\perp}(E_T)]$ and shown in Figure 4.4 (b). The available energy of the products is distributed to the translational, vibrational and rotational energy in the products. The maximum translational energy released is determined by the photolysis energy and the C-H bond dissociation energy, and corresponds to the internal ground state of the $C_2H_4(\tilde{X}\ ^1A_g)$ product. The internal energy distribution $P_{1a}(E_{int})$ of the $C_2H_4(\tilde{X}\ ^1A_g)$ product in the repulsive Channel 1a is calculated from the $P_{1a}(E_T)$ distribution and shown in Figure 4.6.

During the formation of the C=C double bond, the distance between these two carbons will decrease from 1.52 Å for the ethyl radical[14] to 1.339 Å for the ethylene product[41], then the C-C stretching vibrational mode is expected to be excited in the ethylene product. $P_{1a}(E_{int})$ peaks around 17 kcal/mole (6000 cm^{-1}), showing significant internal excitation of $C_2H_4(\tilde{X}\ ^1A_g)$. The vibrational energy levels and vibrational constants of ethylene have been well studied.[42-46] The 12 normal modes of C_2H_4 can be put into 4 categories: C-C stretching (ν_2), C-H stretching (ν_1, ν_5, ν_9 and ν_{11}), C-H bending in plane (ν_3, ν_6, ν_{10} and ν_{12}) and C-H bending out of plane (ν_4, ν_7 and ν_8). For ν_7 and ν_8, their frequencies are very close to each other and they are in the same category, then ν_7 and ν_8 are treated in one mode. To qualitatively model the vibrational state distributions of the $C_2H_4(\tilde{X}\ ^1A_g)$ product, $P_{1a}(E_{int})$ is fitted with multiple Gaussian peaks with adjustable height, position and width as shown in Figure 4.6. The ethylene product C-C stretching (ν_2) is expected to be excited due to the decreasing of the C-C bond length from the $\tilde{A}^2A_1$ state

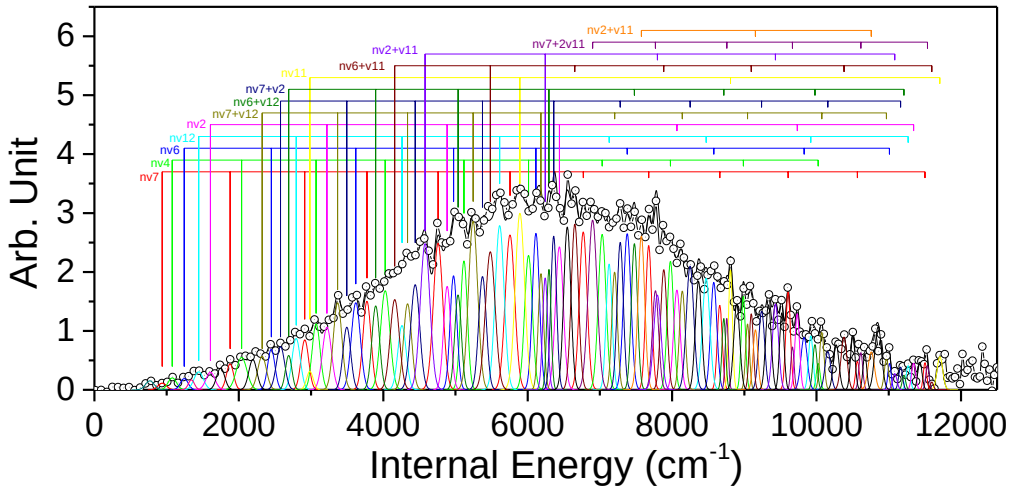

Figure 4.6. The internal energy distributions $P_{1a}(E_{int})$ of the $C_2H_4(\tilde{X}\ ^1A_g)$ product in the repulsive Channel 1a. The peaks in the distributions are fitted with Gaussian peaks of different vibrational levels of $C_2H_4(\tilde{X}\ ^1A_g)$. The vibrational progressions are shown. See text for more details.

of the C_2H_5 reactant to the ground state C_2H_4 product,[14,41] while the length of the C-H bonds should change little except for the cleaved C-H bond. In the fitting process, the ν_2 pattem was put in first, and found that was not enough to fill all the structures in the $P(E_{int})$, indicating other vibrational modes are excited in the ethylene product. In small internal energy region ($<$ 1600 cm^{-1}), several fundamental vibrational modes (ν_{10} around 770 cm^{-1}, ν_7 around 940 cm^{-1}, ν_4 around 1080 cm^{-1}, ν_6 around 1250 cm^{-1}, ν_3 around 1340 cm^{-1}, ν_{12} around 1440 cm^{-1} and ν_2 around 1600 cm^{-1}) were assigned with little ambiguity, and they match well with the observed structures. Next peak around 1750 cm^{-1} is assigned to ν_7 + ν_{10} combination vibrational motion. Based on Herman's work on vibrational frequencies and anharmonicities,[46] the positions of the vibrational peaks can be calculated. The first half of the $P(E_{int})$ ($<$ 6500 cm^{-1}) was filled with around 50 peaks and then signed to different vibrational modes. Adjustments on position, width and intensity were made if necessary to fit both the experimental data and prediction of the position during this process. The width of the peaks is determined by the instrumentation resolution and the rotational excitation in the ethylene product. Based on the conservation of angular momentum, the leaving of the H atom will excite the ethylene product to lower rotational state, which will have around 10 cm^{-1} on the vibrational peak width. These peaks are assigned to six pure vibrational modes progressions: ν_2, ν_4, ν_6, ν_7 (or ν_8), ν_{10}, ν_{11} and ν_{12}. Also, combination modes such as $\nu_7+\nu_{12}$, $\nu_6+\nu_{12}$, $\nu_7+\nu_2$ *et al.* are needed to fill in $P(E_{int})$. For the C-H stretching vibrational model ν_{11}, this progression has larger uncertainty than others due to the small difference in wavenumbers between the C-H stretching models and smaller intensities for ν_{11} pattern comparing to other peaks around them. Apparently, C-C

stretching, C-H bending in plane and out of plane are primarily excited in the $C_2H_4(\tilde{X}\ ^1A_g)$ product from C_2H_5 photodissociation. For large internal energy region (> 6500 cm^{-1}), the $P(E_{int})$ is getting noisy then we put the peaks based on the calculated wavenumbers and made adjustments on the width and intensity if necessary. The peaks assignments of the ethylene product in this region are more ambiguous and the fitted vibration distribution is qualitative and may not be unique. We can conclude that most of the vibrational modes in $C_2H_4(\tilde{X}\ ^1A_g)$ product from the ethyl photodissociation are excited, especially C-C stretching (ν_2). Possible peak assignments are shown in Figure 4.6 and information of major progression are summarized in Table 4.1. The H-atom product yield time profile in the UV photodissociation of ethyl radical was studied by measuring the HRTOF spectra as a function of the time delay between the photolysis laser and probe laser beams. Two precursors, nitroethane and 3-pentanone, were used in this study. The HRTOF spectra of ethyl radical (from nitroethane precursor) at the 244 nm photolysis wavelength with different pump-probe delay times are shown in Figure 4.7a. The H-atom product signals were integrated from the HRTOF spectra as a function of the photolysis-probe delay time and were scaled to the maximum for each time profile. Different time windows in the HRTOF spectra (different velocities of H atoms) are integrated to check any possible bias on the H-atom time profile due to the flight out of the H atoms and the H atoms formed from different dissociation channels. Figure 4.7b and 4.7c show the time profiles at the 244 nm photolysis laser wavelength, with both precursors. The pump-probe delay time profiles provide a measure of the microcanonical rate of the unimolecular dissociation of the ethyl radical. The rise of the signals in the 0 to 10 ns early delay time region indicates the

Table 4.1. Vibrational peak assignments of C_2H_4 internal energy distribution in Figure 4.6. Intensities and the positions of the fitted peaks for the vibrational excited $C_2H_4(\tilde{X}\ ^1A_g)$ product from Channel 1a. Vibrational frequencies and anharmonic parameters from Herman's work (Ref. 26) are used to predict the peak positions.

peak assignment	relative intensity	peak position in cm^{-1}	peak assignment	relative intensity	peak position in cm^{-1}
ν_7	0.11	939	$7\nu_6$	1.82	8576
$2\nu_7$	0.44	1878	$8\nu_6$	0.89	9827
$3\nu_7$	0.85	2914	$9\nu_6$	0.45	11010
$4\nu_7$	1.50	3774			
$5\nu_7$	2.49	4759	ν_{12}	0.30	1444
$6\nu_7$	2.63	5755	$2\nu_{12}$	0.87	2794
$7\nu_7$	2.68	6769	$3\nu_{12}$	1.09	4260
$8\nu_7$	2.45	7676	$4\nu_{12}$	2.79	5612
$9\nu_7$	1.43	8660	$5\nu_{12}$	2.13	7127
$10\nu_7$	1.66	9606	$6\nu_{12}$	1.89	8471
$11\nu_7$	0.48	10566	$7\nu_{12}$	0.91	9921
$12\nu_7$	0.46	11502	$8\nu_{12}$	0.41	11269
ν_4	0.20	1078	ν_2	0.30	1607
$2\nu_4$	0.55	2038	$2\nu_2$	1.06	3220
$3\nu_4$	1.12	3070	$3\nu_2$	1.76	4885
$4\nu_4$	1.68	4027	$4\nu_2$	2.43	6439
$5\nu_4$	2.19	5117	$5\nu_2$	1.69	8066
$6\nu_4$	2.28	6011	$6\nu_2$	1.29	9732
$7\nu_4$	2.64	7031	$7\nu_2$	0.45	11344
$8\nu_4$	2.18	7977			
$9\nu_4$	1.58	8986	$\nu_7+\nu_{12}$	0.57	2322
$10\nu_4$	0.45	10023	$2\nu_7+\nu_{12}$	1.48	3367
			$3\nu_7+\nu_{12}$	1.46	4336
ν_6	0.19	1243	$4\nu_7+\nu_{12}$	2.86	5244
$2\nu_6$	0.69	2449	$5\nu_7+\nu_{12}$	1.97	6184
$3\nu_6$	1.48	3620	$6\nu_7+\nu_{12}$	2.00	7204
$4\nu_6$	1.93	4973	$7\nu_7+\nu_{12}$	1.68	8141
$5\nu_6$	2.65	6114	$8\nu_7+\nu_{12}$	1.15	9044
$6\nu_6$	2.65	7378	$9\nu_7+\nu_{12}$	0.97	10073

Table 4.1 Continue

peak assignment	relative intensity	peak position in cm^{-1}	peak assignment	relative intensity	peak position in cm^{-1}
$10\nu_7+\nu_{12}$	0.52	10968	$\nu_7+\nu_2$	0.73	2577
			$2\nu_7+\nu_2$	1.06	3495
$\nu_6+\nu_{12}$	0.58	2690	$3\nu_7+\nu_2$	1.78	4442
$2\nu_6+\nu_{12}$	1.42	3895	$4\nu_7+\nu_2$	1.92	5374
$3\nu_6+\nu_{12}$	1.61	5036	$5\nu_7+\nu_2$	2.61	6360
$4\nu_6+\nu_{12}$	2.04	6294	$6\nu_7+\nu_2$	2.50	7281
$5\nu_6+\nu_{12}$	2.48	7478	$7\nu_7+\nu_2$	2.10	8248
$7\nu_6+\nu_{12}$	0.77	9978	$8\nu_7+\nu_2$	1.33	9239
$8\nu_6+\nu_{12}$	0.25	11210	$9\nu_7+\nu_2$	0.65	10156
			$10\nu_7+\nu_2$	0.38	11164

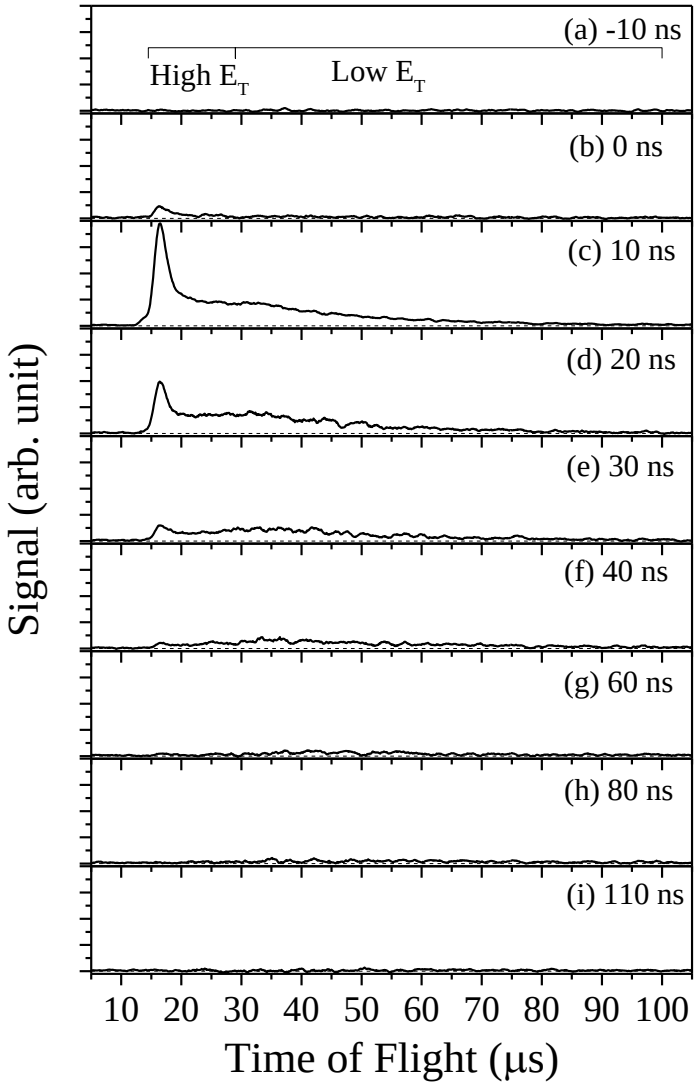

Figure 4.7a. H-atom TOF spectra of 244 nm photodissociation of ethyl radical (nitroethane precursor) at different pump-probe delay time. All the spectra are normalized to the same laser power and laser shots. The photolysis laser polarization is parallel to the TOF path.

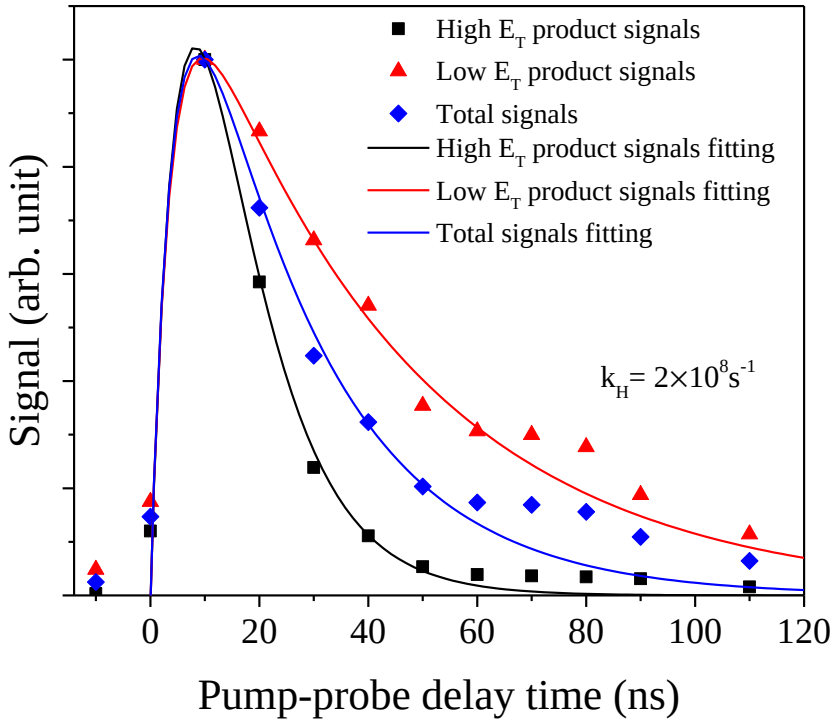

Figure 4.7b. Integrated H-atom product signal from the photodissociation of ethyl radical (nitroethane precursor) as a function of photolysis and probe laser delay time. The signals were obtained by integrating the HRTOF spectra in different TOF regions with different pump-probe delay times. The solid lines are the fittings using the expression based on the previous work from Chen's group (Ref. 17).

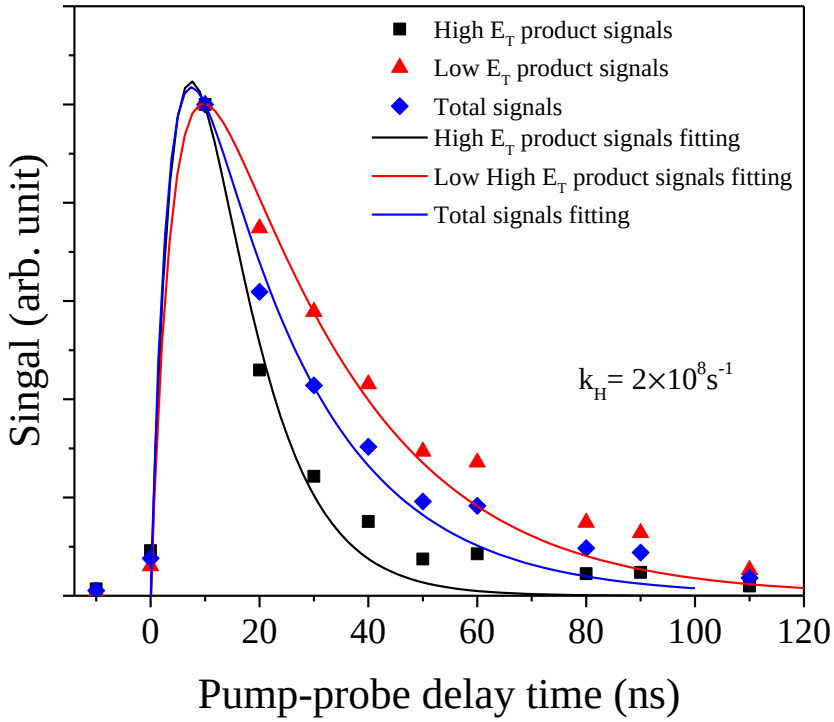

Figure 4.7c. Integrated H-atom product signal from the photodissociation of ethyl radical (3-pentatone precursor) as a function of photolysis and probe laser delay time. The signals were obtained by integrating the HRTOF spectra in different TOF regions with different pump-probe delay times. The solid lines are the fittings using the expression based on the previous work from Chen's group (Ref. 17).

formation of H-atom product from the ethyl radical, while the decay of the signals after the peak is due to H-atom flight out of the interaction region between the photolysis and probe radiations. The following expression based on the previous work from Chen's group[17] is used to describe the time dependence of the H-atom product from the unimolecular dissociation of the ethyl radical:

$$S_H(t) = N[1 - \exp(-k_H t)] \cdot [\frac{1}{\exp[(t-a)/b]+1}] \quad (4.8)$$

where $S_H(t)$ is the time profile of the H-atom signals, k_H is the unimolecular dissociation rate of the ethyl radical, and a and b are the constants to describe the width of the plateau region and the decay of the signals. The fittings in Figure 4.7b and 4.7c give the dissociation rate constant $k_H \sim 2 \times 10^8$ s^{-1} for different TOF regions from both precursors at 244 nm photolysis wavelength. The 10 ns time resolution of the pump and probe laser radiations limits the H-atom product appearance time resolution, then the k_H value gives the lower limit of the actual dissociation rate constant. The H-atom product from unimolecular dissociation channel (Channel 1b) have a modest kinetic energy release and they are in the slow time window. The selective β H-atom elimination[15-18,21] reveals that unimolecular dissociation happens after the internal conversion form the excited electronic state in a short time, otherwise the H-H shifting between the bridged H atom and normal positioned H atom would happen and the α-H atom elimination might be observed. The time profiles from different windows have essentially the same rise time but different decays due to different rate of H-atoms flight away from the interaction region. The rise times in all the time profiles are around 10 ns, approaching the limit of the laser resolution.

All the fittings give a close dissociation constant with $k_H \sim 2 \times 10^8$ s^{-1} for the unimolecular dissociation of the ethyl radical at 244 nm photolysis wavelength.

4.4 Discussions

Our previous study on the photodissociation of ethyl radical via $\tilde{A}\,^2A'$ (3s) state indicates that the H + C_2H_4($\tilde{X}\,^1A_g$) product with the large translational energy release ($\langle f_T \rangle \sim 0.78$) and anisotropic angular distribution ($\beta = 0.5 \pm 0.1$) is consistent with the direct C-H bond cleavage via a nonclassical H-bridged transition state from the 3s excited state;[18] and the theoretical prediction by Chen and co-workers shows the $\langle f_T \rangle$ is about 0.83 and anisotropic parameter is 0.82 for Channel 1a.[20] The previous also observed a slow ($\langle f_T \rangle \sim 0.35$) and isotropic product channel, which corresponds to the unimolecular dissociation of the internally hot radical on the ground electronic state after the internal conversion form the excited state.[18]

The behaviors of the $P(E_T)$ and $\beta(E_T)$ in the larger translational energy release region in this study is consistent with the previous experiment work by Zhang and co-workers[18] and the Channel 1a and Channel 1b in the theoretical study by Chen and colleagues[20]. The anisotropic product with the very small translational energy release is consistent the prediction of the triplet ethylene product channel from the photodissociation of the ethyl radical predicted by Chen and co-workers (Channel 2)[20], and it would be the first experimentally observation of this product channel.

4.4.1 Channel 1a

The Channel 1a component peaks at ~ 65 kcal/mol with $\langle f_T \rangle$ ~ 0.78 and an anisotropic angular distribution with β ~ 0.67 consistent with our previous photodissociation study of the ethyl radical[18]. The pump-probe delay study implies the dissociation time scale is shorter than ~ 5 ns, and the none-zero β parameter indicates that the dissociation time is shorter than one rotational scale of the ethyl radical (~ 10 ps). The dissociation mechanism of the Channel 1a would be the prompt, direct dissociation of the ethyl radical on the electronic excited state and then produce fast H-atom and $C_2H_4(\tilde{X}\ ^1A_g)$ with an anisotropic angular distribution.

The $C_2H_4(\tilde{X}\ ^1A_g)$ product was vibrational excited as expected. During the formation of the C=C double bond, the distance between these two carbons will decrease from 1.52 Å for the ethyl radical[14] to 1.339 Å for the ethylene product[41], then the C-C stretching vibrational mode is expected to be excited in the ethylene product. To simulate the C-C bond distance before the breaking of the C-H bond, a simple one-dimensional Franck-Condon calculation bas been performed based on the fitted vibrational population of the ν_2 progression (C-C stretch). In the calculation, Morse oscillator was used to simulate the C-C stretching in ethylene and a harmonic oscillator (on ground vibrational state the anharmonicity is very small, so harmonic oscillator is good enough to simulate the motion) was applied for the C-C stretching of the excited ethyl radical. To simplify the vibrational model, the CH_2 or CH_3 group in ethylene and ethyl radical are treated as a whole group without relative C-H motion. The Franck-Condon relative population distribution of the C-C stretching on the ethylene product can be calculated by projecting the C-C stretching

wavefunction of the excited ethyl radical onto the basis set of the ethylene C-C stretching. During the calculation, the excited ethyl radical C-C stretching frequency and C-C bond distance (used as the equilibrium distance in the harmonic oscillator) were adjusted until a best fitting of the experimental ethylene C-C stretching intensities was achieved. The parameters for ethylene are based on the Harmony's and Herman's works,[41,46] with R_{eq} (C-C) = 1.339 Å, ν_2 (C-C stretching frequency) = 1634.00 cm^{-1} and $\chi_{2,2}$ (C-C stretching anharmonicity parameter) = -2.46 cm^{-1}. When ν (C-C) ≈ 2060 cm^{-1} and R_{eq} (C-C) = 1.51 Å for the excited ethyl radical, the simulation reached the best fitting of the ethylene C-C stretching vibrational progression (shown in Figure 4.8).

Our Franck-Condon calculation result of the C-C bond distance of the $\tilde{A}^2A_1$ state ethyl when the C-H bond breaking matches well to Zyubin's theoretical work on the R_{eq} (C-C) of ethyl radical, which gives 1.52 Å at CASSCF level.[14] The highly excited C-H bending out of plane [ν4, ν7 (ν8)] of the ethylene product indicates that these six atoms are not on the same plane or even far away from a planar structure when the β H-atom elimination happening. The atoms except the H atom on the mirror plane in the non-classic C_{2v} structure ethyl have a nearly planar structure with around 89° dihedral angle between the mirror plane.[14] This slight bent plane could lead to a minor excited C-H bending out of plane motions of the ethylene product. The C-H bonding breaking happens when the $\tilde{A}^2A'(3s)$ state ethyl radical has a similar geometry to the ground state of ethyl.

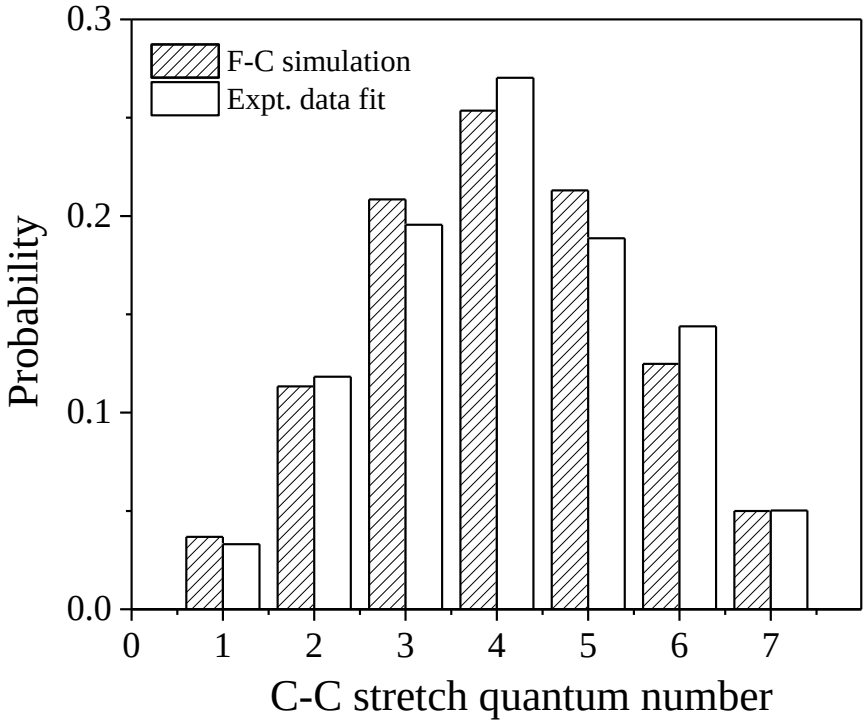

Figure 4.8. Franck-Condon calculated population distribution vs. the peak intensities from peak fitting of C-C stretching ν2 vibrational model. The total population of the calculated and the fitting vibrational distribution are both normalized to 1.

4.4.2 Channel 1b

The product formed in Channel 1b has a modest translational energy released ($\langle f_T \rangle$ ~ 0.27). The angular distribution of the H-atom produced from Channel 1b in Figure 4.4 shows an isotropic distribution. The isotropic distribution indicates the dissociation for Channel 1a should be equal or longer than one rotational period of the ethyl radical (~ 10 ps). The pump-probe experiment in this study provided a lower limited of the dissociation rate with 2×10^8 s^{-1} at 244 nm photolysis wavelength, due to the 10 ns laser resolution.

The early experimental study on the unimolecular dissociation rate by Chen's group, measured an ethyl dissociation rate constant of 1.8×10^7 s^{-1} at 250 nm (114 kcal/mol) excitation.[17] While Sloane's previous RRKM study indicates that at 100 kcal/mol energy, the dissociation rate is 1.7×10^{11} s^{-1},[6] 4 orders of magnitude faster. The lower limit of the dissociation rate constant measured in this study is more consistent with the RRKM theoretical study on the unimolecular dissociation of ethyl radical. Furthermore, the pump-probe delay in the photodissociation of OH was performed by the same experimental setup, and the time profiles with the fittings are shown in Figure 4.9. The early experimental and theoretical works on the OH unimolecular dissociation provide the dissociation time 130 $\pm$ 10 ns,[47,48] which matches well to our experimental study on the photodissociation of OH at $A^2\Sigma^+$, v=2 with the dissociation rate 1×10^7 s^{-1} (130 $\pm$ 30 ns). This also confirms that our method can actually measure slow H-atom product if present.

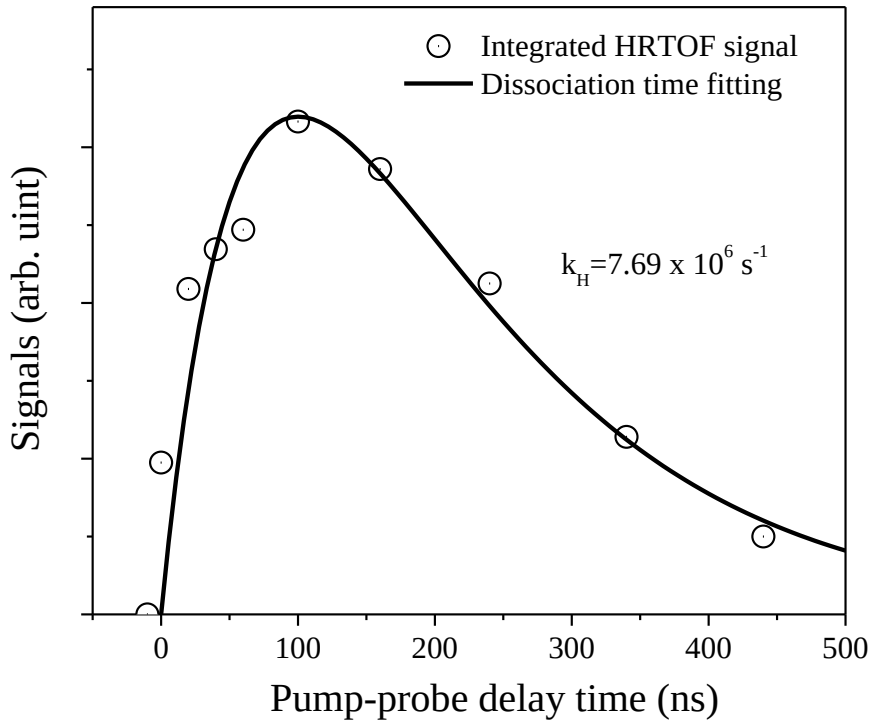

Figure 4.9. Integrated H-atom product signal from the photodissociation of OH radical from the $A^2\Sigma^+$, v'=2, N'=2 state as a function of photolysis and probe laser delay time. The signals were obtained by integrating the HRTOF spectra with different pump-probe delay times. The solid line represents the H-atom signal with the expression from Chen's previous work (Ref. 17).

4.4.3 Channel 2

The mechanism of the photodissociation of ethyl radical via $\tilde{A}^2A'$ state has been well studied theoretically and experimentally with a non-statistical, repulsive dissociation that towards $H + C_2H_4(\tilde{X}\,^1A_g)$ product and a unimolecular dissociation on the ground state after internal conversion from the excited state.[13,14,18,20] Chen and co-workers' theoretical investigation predicted an adiabatic dissociation channel of the ethyl radical on the $\tilde{A}^2A'$ state that towards the $H + C_2H_4(\tilde{a}^3B_{1u})$ product with an anisotropy angular distribution and a very small translational energy release.[20]

In Figure 4.4 (c), the anisotropy parameter β increases from 0 and reaches the maximum about 0.25 with a decreasing CM translational energy from 3500 to 0 cm^{-1}. The changing β indicates that there are at least two dissociation channels that makes the products have the translational energy in this region. Unimolecular dissociation of the ethyl radical after the internal conversion from the electronic state which can form the products with an isotropic angular distribution and the translational energy in this region is well studied.[13,14,18,20] The positive β here suggests another prompt and direct dissociation from the excited state into the $H + C_2H_4$ and the dissociation time scale is shorter than one rotational period of the ethyl radical and the CM translational energy for this product channel is consistent with the H atom and triplet ethylene ($\tilde{a}^3B_{1u}$) product channel. Similar to the treatment for Channel 1a, the product CM translation energy distribution for Channel 2, $P_2(E_T)$, is proportional to $P_{\parallel}(E_T) - P_{\perp}(E_T)$ ($P_2(E_T) = \frac{1}{\beta_2} \times \frac{2}{3} \times (P_{\parallel}(E_T) - P_{\perp}(E_T))$, β_2 is the anisotropy parameter for Channel 2). Then the observed average translational energy released, $\langle E_T \rangle$, for Channel 2 is calculated with ~ 4.6 kcal/mol (1600 cm^{-1}) and the

small translational energy release ($\langle f_T \rangle$ ~ 0.23) indicates an internally excited ethylene product. To figure out the anisotropy parameter for Channel 2, the $P_{1b}(E_T)$ is calculated to be $\frac{1}{3} \times (P_{\parallel}(E_T) + 2 \times P_{\perp}(E_T)) - \frac{1}{\beta_{II}} \times \frac{2}{3} \times (P_{\parallel}(E_T) - P_{\perp}(E_T))$. With the constrain condition $P_{1b}(E_T)$ and $P_2(E_T)$ are larger than 0, the β_2 is determined in the range of 1.0 to 2.0.

The dissociation mechanism of Channel 2 would be the direct β-CH bond cleavage in the C_S plane. The transition dipole momentum $\boldsymbol{\mu}$ of the initial $\tilde{A} \leftarrow \tilde{X}$ lays in the C_S mirror plane of the ethyl radical and perpendicular to the C-C bond. If the leaving H atom along the cleavage bond is 23° to the transition dipole momentum and makes the anisotropy parameter about 1.5 which is consistent with the prediction by Chen and colleague[20].

The structure of the $C_2H_4(\tilde{a}^3B_{1u})$ has been study theoretically.[29,49] At equilibrium, the two CH_2 planes are perpendicular (φ = 90°) to each other to form the D_{2d} symmetry group. The cleavage of the CH bond in the C_S plane of the ethyl radical would create the $C_2H_4(\tilde{a}^3B_{1u})$ in a nearly planar structure and the triplet C_2H_4 is not on the ground state geometry with some of the vibrational modes excited. Our observation on the anisotropy parameter also indicates the translational energy release of the H + $C_2H_4(\tilde{a}^3B_{1u})$ product channel is much smaller than the maximum available energy and other available energy should be distributed in the internal mode of the ethene product.

In conclusion, the H atom and triplet ethylene product channel is observed from the photodissociation of ethyl via the $\tilde{A}^2A'$ state for the first time. The mechanism would be an adiabatic dissociation alone the PES on the C_s symmetry and the cleavage of the CH bond

in the C_s plane creates the H atom and triplet ethylene product with a positive anisotropy parameter and the ethylene product is vibrationally excited.

4.4.4 Channel 1a/Channel 1b Branching Ratio

The branching ratio of the two different H + $C_2H_4(\tilde{X}\,^1A_g)$ channels, non-statistical dissociation channel (Channel 1a) and unimolecular dissociation channel (Channel 1b) was obtained with different photolysis wavelength (Figure 4.5b). The unimolecular dissociation after internal conversion (Channel 1b) is the major pathway and the channel 1a ratio increases with smaller photolysis wavelength (larger excitation energy) in general. Around 245 nm (116.7 kcal/mol), there is a sharp peak in the Channel 1a/Channel 1b branching ratio.

A similar phenomenon was observed in the photodissociation of thioanisole ($C_6H_5SCH_3$) by Jeong Sik Lim and San Kyu Kim.[50] The branching ratio of CH_3 + $C_6H_5S(\tilde{X})$ and CH_3 + $C_6H_5S(\tilde{A})$ was obtained at different S_1 vibronic bands. The $\tilde{X}/\tilde{A}$ ratio increased slowly as a function of the internal energy, but a dramatic growth was observed at an internal energy of 722 cm^{-1} at S_1 state results in a sharp peak there. They proposed that at 722 cm^{-1} vibronic band, the excited molecule merged to S_2 excited state via CI-1 (crossing of the S_1 and S_2 states) directly with less internal excitation and the larger translational energy would result in cleavage the C-S bond on the repulsive surface rather than have internal conversion to the S_0 state with larger probability.[50] Their observation was well consistent with the prediction of the Landau-Zener formula.[51]

In our photodissociation study on the ethyl radical, the ethyl radical on the electronic ground state was excited to the $\tilde{A}^2A'$ repulsive electronic excited state and the excited ethyl radical would go along the adiabatic potential energy surface with a β H-atom shifting to form a non-classical H-bridge structure then the radical would pass the conical intersection to form the H + $C_2H_4(\tilde{X}\,^1A_g)$ directly or have an internal conversion to the ground electronic state.[12,14] The larger excitation energy would result in the higher relative translational energy and our observation of the higher channel 1a branching ratio at shorter photolysis wavelength (larger excitation energy) might be due to the same effect predicted Clarence Zener.[51] The peak around 245 nm cannot be explained by this effect, other mechanism might be involved in this process. Based on Franck-Condon principle, the electronic excited ethyl radical geometry and the vibrational state should vary a little with different excitation energy because of different maximum vertical transition probabilities at different places for the diversity excitation energies. The initial locations would not be the same on the electronic excited state and the gradient of the surface will lead to different trajectories on the surface finally result in the difference on the probability of internal conversion to the ground electronic excited followed by unimolecular dissociation or have directly dissociation on the conical intersection to these dissociation channels.

4.5 Conclusions

The reinvestigation of photodissociation dynamics of ethyl radical by HRTOF gives more information about this β H-atom elimination. For the fast singlet ethylene

product channel, the ethylene product is highly internal excited and when the C-H bonding breaks the geometry of the excited ethyl radical is similar to the ground state of the ethyl radical. The unimolecular dissociation rate of the ethyl radical is larger than 2×10^8 s^{-1}, which is consistent to previous RRKM calculation.[6] The positive anisotropy parameter β in the small product kinetic energy region reveal the triplet ethylene ($\tilde{a}^3B_{1u}$) product channel. The channel 1a/1b branching ratio depends on the excitation energy and we give preliminary explanation which might be due to prediction of the Landau-Zener formula[51] and the different trajectories on the electronic excited state potential energy surface. Further theoretical investigations are needed to explain this phenomenon.

Reference

1. J. Warnatz, *Combustion Chemistry* (Springer New York, 1984).

2. W. Tsang and R. F. Hampson, *J. Phys. Chem. Ref. Data* **15**, 1087 (1986).

3. Y. Feng, J. T. Niiranen, A. Bencsura, V. D. Knyazev, D. Gutman, and W. Tsang, *J. Phys. Chem.* **97**, 871 (1993).

4. P. D. Lightfoot and M. J. Pilling, *J. Phys. Chem.* **91**, 3373 (1987).

5. W. L. Hase, G. Mrowka, R. J. Brudzynski, and C. S. Sloane, *J. Chem. Phys.* **69**, 3548 (1978).

6. W. L. Hase, R. J. Wolf, and C. S. Sloane, *J. Chem. Phys.* **71**, 2911 (1979).

7. W. L. Hase and D. G. Buckowski, *J. Comput. Chem.* **3**, 335 (1982).

8. W. L. Hase, D. Buckowskl, and K. N. Swamy, *J. Phys. Chem.* **87**, 2754 (1983).

9. K. N. Swamy and W. L. Hase, *J. Phys. Chem.* **87**, 4715 (1983).

10. W. L. Hase, H. B. Schlegel, V. Balbyshev, and M. Page, *J. Phys. Chem.* **100**, 5354 (1996).

11. J. Villà, A. González-Lafont, J. M. Lluch, and D. G. Truhlar, *J. Am. Chem. Soc.* **120**, 5559 (1998).

12. A. Sevin, H. T. Yu, and E. M. Evleth, *Journal of Molecular Structure: THEOCHEM* **104**, 163 (1983).

13. E. M. Evleth, H. Z. Cao, E. Kassab, and A. Sevin, *Chem. Phys. Lett.* **109**, 45 (1984).

14. A. S. Zyubin, A. M. Mebel, and S. H. Lin, *Chem. Phys. Lett.* **323**, 441 (2000).

15. J. L. Brum, S. Deshmukh, and B. Koplitz, *J. Chem. Phys.* **95**, 2200 (1991).

16. J. L. Brum, S. Deshmukh, Z. Wang, and B. Koplitz, *J. Chem. Phys.* **98**, 1178 (1993).

17. T. Gilbert, T. L. Grebner, I. Fischer, and P. Chen, *J. Chem. Phys.* **110**, 5485 (1999).

18. G. Amaral, K. Xu, and J. Zhang, *J. Chem. Phys.* **114**, 5164 (2001).

19. M. Zierhut, B. Noller, T. Schultz, and I. Fischer, *J. Chem. Phys.* **122**, 094302 (2005).

20. J. M. Hostettler, A. Bach, and P. Chen, *J. Chem. Phys.* **130**, 034303 (2009).

21. M. Steinbauer, J. Giegerich, K. H. Fischer, and I. Fischer, *J. Chem. Phys.* **137**, 014303 (2012).

22. J. Munk, P. Pagsberg, E. Ratajczak, and A. Sillesen, *J. Phys. Chem.* **90**, 2752 (1986).

23. H. R. Wendt and H. E. Hunziker, *J. Chem. Phys.* **81**, 717 (1984).

24. K. Fagerström, A. Lund, G. Mahmoud, J. T. Jodkowski, and E. Ratajczak, *Chem. Phys. Lett.* **204**, 226 (1993).

25. B. H. Lengsfield, P. E. M. Siegbahn, and B. Liu, *J. Chem. Phys.* **81**, 710 (1984).

26. M. R. A. Blomberg and B. Liu, *J. Chem. Phys.* **83**, 3995 (1985).

27. B. Ruscic, *J. Phys. Chem. A* **119**, 7810 (2015).

28. M. T. Nguyen, M. H. Matus, W. A. Lester, and D. A. Dixon, *J. Phys. Chem. A* **112**, 2082 (2008).

29. B. Gemein and S. D. Peyerimhoff, *J. Phys. Chem.* **100**, 19257 (1996).

30. A. Bach, J. M. Hostettler, and P. Chen, *J. Chem. Phys.* **123**, 21101 (2005).

31. A. Bach, J. M. Hostettler, and P. Chen, *J. Chem. Phys.* **125**, 24304 (2006).

32. A. F. Wagner, L. A. Rivera-Rivera, D. Bachellerie, J. W. Perry, and D. L. Thompson, *J. Phys. Chem. A* **117**, 11624 (2013).

33. A. Matsugi, *J. Phys. Chem. Lett.* **4**, 4237 (2013).

34. K. Xu, G. Amaral, and J. Zhang, *J. Chem. Phys.* **111**, 6271 (1999).

35. Y. Song, M. Lucas, M. Alcaraz, J. Zhang, and C. Brazier, *J. Chem. Phys.* **136**, 044308 (2012).

36. M. Lucas, J. Minor, J. Zhang, and C. Brazier, *J. Phys. Chem. A* **117**, 12138 (2013).

37. Y. Song, X. Zheng, W. Zhou, M. Lucas, and J. Zhang, *J. Chem. Phys.* **142**, 224306 (2015).

38. J. Zhang, M. Dulligan, and C. Wittig, *J. Phys. Chem.* **99**, 7446 (1995).

39. R. N. Zare, *Mol. Photochem.* **4**, 1 (1972).

40. J.-H. Wang, Y.-T. Hsu, and K. Liu, *J. Phys. Chem. A* **101**, 6593 (1997).

41. M. D. Harmony, V. W. Laurie, R. L. Kuczkowski, R. H. Schwendeman, D. A. Ramsay, F. J. Lovas, W. J. Lafferty, and A. G. Maki, *J. Phys. Chem. Ref. Data* **8**, 619 (1979).

42. W. L. Smith and I. M. Mills, *J. Chem. Phys.* **40**, 2095 (1964).

43. W. Knippers, K. Van Helvoort, S. Stolte, and J. Reuss, *Chem. Phys.* **98**, 1 (1985).

44. J. L. Duncan and A. M. Ferguson, *J. Chem. Phys.* **89**, 4216 (1988).

45. J. L. Duncan and G. E. Robertson, *J. Mol. Spectrosc.* **145**, 251 (1991).

46. R. Georges, M. Bach, and M. Herman, *Mol. Phys.* **97**, 279 (1999).

47. J. Brzozowski, P. Erman, and M. Lyyra, *Phys. Scr.* **17**, 507 (1978).

48. D. R. Yarkony, *J. Chem. Phys.* **97**, 1838 (1992).

49. X. Wang, W. E. Turner, 2nd, J. Agarwal, and H. F. Schaefer, 3rd, *J. Phys. Chem. A* **118**, 7560 (2014).

50. J. S. Lim and S. K. Kim, *Nature Chem.* **2**, 627 (2010).

51. C. Zener, *Proc. R. Soc. Lond. A* **137**, 696 (1932).

Chapter 5

Ultraviolet Photodissociation Dynamics of the *n*-Butyl, *s*-Butyl, and *t*-Butyl Radicals

Abstract

Photodissociation dynamics of jet-cooled *n*-butyl ($CH_2CH_2CH_2CH_3$) radical via the 3s Rydberg state and *s*-butyl ($CH_3CHCH_2CH_3$) radical via the 3p Rydberg states in the ultraviolet (UV) photolysis region of 233–258 nm, as well as *t*-butyl ($C(CH_3)_3$) radical via the 3d Rydberg states at the photolysis wavelengths of 226–244 nm, are studied using the high-*n* Rydberg atom time-of-flight (HRTOF) technique. The H-atom photofragment yield (PFY) spectra of the *n*-butyl, *s*-butyl, and *t*-butyl radicals show a broad feature centered around 247, 244, and 234 nm, respectively, with those of the *s*-butyl and *t*-butyl radicals in agreement with their UV absorption spectra. The translational energy distributions of the H + C_4H_8 products, $P(E_T)$'s, of the *n*-butyl, *s*-butyl, and *t*-butyl radicals are bimodal, with a slow (low E_T) component peaking at ~ 6 kcal/mol for all three radicals and a fast (high E_T) component peaking at ~ 52-57 kcal/mol for *n*-butyl, ~ 43 kcal/mol for *s*-butyl, and ~ 37 kcal/mol for *t*-butyl, respectively. The fraction of the average product translational energy in the total available energy, $\langle f_T \rangle$, is 0.31 for *n*-butyl, 0.30 for *s*-butyl, and 0.27 for *t*-butyl, respectively. The H-atom product angular distributions of the slow component are isotropic for all three radicals, while those of the fast component are anisotropic for *n*-butyl and *s*-butyl with an anisotropy parameter β ~ 0.7 and ~ 0.3, respectively, and that of the

fast component of the *t*-butyl radical is nearly isotropic. The average branching ratio of the fast and slow components are 0.43:1 for *n*-butyl, 0.65:1 for *s*-butyl, and 0.70:1 for *t*-butyl. The bimodal product translational energy and angular distributions indicate two dissociation pathways to the H + C_4H_8 products in these three radicals, a direct, prompt dissociation on the repulsive potential energy surface coupling with the Rydberg excited states and the ground electronic state, and a unimolecular dissociation of hot radical on the ground electronic state after internal conversion from the Rydberg states.

5.1 Introduction

Alkyl radicals are simple open-shell organic species. They are important intermediates in hydrocarbon combustion and cracking processes,[1,2] as the dissociation of these radicals influence the rate and efficiency of the combustion. The dissociation dynamics of the small alkyl radicals on the ground electronic state are well studied, while those from their electronic excited states are less understood. In this work, the photodissociation dynamics of the *n*-butyl, *s*-butyl, and *t*-butyl radicals via their Rydberg electronic excited states in the UV wavelength region of 230-260 nm are investigated.

The C_4H_9 radical species has four isomers, *n*-butyl ($CH_2CH_2CH_2CH_3$) (primary alkyl radical), *i*-butyl ($CH_2CH(CH_3)_2$) (primary), *s*-butyl ($CH_3CHCH_2CH_3$) (secondary), and *t*-butyl ($C(CH_3)_3$) (tertiary). The decomposition mechanisms and rate constants of these butyl radicals in the ground electronic state have been extensively studied.[3-21] The main dissociation channel of *n*-butyl is C-C bond fission to C_2H_5 and C_2H_4, while *s*-butyl mainly yields CH_3 and C_3H_6 and the H-atom elimination channel is minor.[11,13,17-19] The experimental study observed an insignificant isomerization between *n*-butyl and *s*-butyl,[19] consistent with the higher threshold energy for isomerization than for C-H bond cleavage.[15] In the decomposition of the *t*-butyl radical, the H + *i*-C_4H_8 product channel was studied,[14,16,21] and the temperature and pressure dependent reaction rate functions were determined.

The UV absorption spectrum of the *s*-butyl radical shows a shoulder peak at ~ 275 nm and two distinct broad peaks at 241 and 211 nm, assigned to the 3s, 3p, and 3d Rydberg

states, respectively.[22] The UV absorption spectrum of *t*-butyl has three broad peaks at 333, 253, and 233 nm, due to the 3s, 3p, and 3d Rydberg states.[22-26] There has been no reported UV absorption spectrum of the *n*-butyl radical, while the UV absorption spectrum of ethyl shows two broad peaks at 246 and 205 nm (assigned to the 3s and 3p Rydberg states)[22,24] and that of *n*-propyl has a broad peak at 245 nm due to the 3s Rydberg state.[27] As the Rydberg orbitals are localized on the radical center, it is expected that *n*-butyl has a UV absorption spectrum similar to those of other primary alkyl radicals. The Rydberg absorption peaks of the alkyl radicals are red shifted from primary, secondary, to tertiary radicals or with an increasing number of α methyl substitutions on the radical center, due to stabilization of the carbonium ion core of the Rydberg states by the methyl groups.[22,24]

The excited-state dynamics of the *t*-butyl radical on the 3s and 3p Rydberg states were investigated by Fischer and coworkers using femtosecond time-resolved photoionization and photoelectron spectroscopy, along with *ab initio* calculations.[26] The calculations showed that the *t*-butyl radical undergoes a geometry change from a slightly pyramidal C_{3v} ground electronic state to a planar structure upon the Rydberg excitations. The lifetimes of the 3s and 3p excited states were determined to be 69–180 fs and ~ 2 ps, respectively. 1,2 H-atom shift isomerization from *t*-butyl to *i*-butyl was not significant in the decay of the excited *t*-butyl radical. The calculations indicated that the 3s and 3p states, as well as the ground electronic state, cross with the lowest valence state at an extended C-C coordinate that leads to the dimethylcarbene (CH_3CCH_3) + methyl products; interactions between the 3s and the lowest valence state along the C-H coordinate were also identified. Fischer and coworkers also studied photodissociation of *t*-butyl from the 3s (excited

between 355 and 320 nm) and 3p (at 266 nm) Rydberg states.[28] The H + *i*-butene product channel was examined by detecting the H-atom product using time-resolved multiphoton ionization. The photodissociation was considered to proceed via internal conversion to the ground electronic state and then unimolecular dissociation. The unimolecular dissociation rate around 355 nm (via 3s) was determined to be on the order of 10^8 s^{-1} and consistent with simple RRKM calculations, while the rate constant decreased significantly by about an order of magnitude when the photolysis wavelength was shorter than 329 nm. The fraction of the total excess energy released in the H + *i*-butene products' translation, $\langle f_T \rangle$, was observed to be 0.38 from the H-atom Doppler-profile at the 266 nm excitation and was larger than expected from the statistical theory. Neumark and coworkers studied the photodissociation dynamics of *t*-butyl at 248 nm using photofragment translational spectroscopy.[29] The H + *i*-butene product channel has a large translational energy release, with $\langle f_T \rangle = 0.44$, and it was proposed that the dissociation occurred on the excited state surface or via non-statistical decay on the ground state. A methyl loss channel was observed with the dimethylcarbene coproduct in the excited state, with a large product translational energy release ($\langle f_T \rangle = 0.63$). The *t*-butyl radical could also have a 1,2 H shift isomerization to *i*-butyl radical followed by dissociation to the CH_3 + C_3H_6 products, but the higher energy barrier of the isomerization renders this dissociation pathway unimportant. The branching ratio of the H-/CH_3-loss channels was 1.1 ± 0.3. In 2015, Fischer and coworkers further investigated the H-atom elimination channel of *t*-butyl via the 3s, 3p, and 3d Rydberg states,[30] revealing bimodal product translational energy distributions. The anisotropy parameter, β, is around 0 for the slow H-atom component from the 3s, 3p, and

3d states, while that for the fast component is 0.10 for the 3s state, -0.31 for the 3p states, and -0.31 for the 3d states, respectively. The bimodal product translational energy and angular distributions indicated two dissociation channels. The fast H-atom loss channel is similar to that observed by Neumark and co-workers,[29] and the slow channel is consistent with unimolecular dissociation after internal conversion to the ground electronic state.[30]

UV photodissociation of *n*-butyl and *s*-butyl via the Rydberg states have not been investigated so far, while there have been a few studies on other primary and secondary alkyl radicals, such as ethyl,[31-33] *n*- and *i*-propyl,[30,34,35] and *n*-pentyl.[36] β-H atom elimination was confirmed by using partially deuterated ethyl and propyl radicals.[31,35] Bimodal translational energy and angular distributions were observed in the photodissociation of ethyl via the 3s Rydberg state, indicating two dissociation pathways.[31,32] The ethyl radical on 3s state undergoes a direct dissociation on the repulsive potential energy surface via a conical intersection near C_{2v} symmetry to form the H + C_2H_4 products with a large translational energy release and anisotropic angular distribution, as well as internal conversion to the ground electronic state via the conical intersection, followed by unimolecular dissociation with a small translational energy release and isotropic angular distribution.[31-33,37] The photodissociation of the *n*-propyl radical (via 3s) and *i*-propyl radical (via 3p) also show two dissociation channels. The H + propene product transitional energy distributions are bimodal, with an isotropic slow component for both propyls and an anisotropic ($\beta \approx 0.8$) fast component for *n*-propyl versus a nearly isotropic fast component for *i*-propyl. The photodissociation of *n*-propyl and *i*-propyl proceed via direct, prompt dissociation from the electronic excited state and/or the repulsive part of the ground

state potential energy surface, and unimolecular dissociation of internally excited radical on the ground electronic state after internal conversion.[35] The H-atom product channel from photodissociation of *n*-pentyl via 3s also has two product channels and is similar to that of the *n*-propyl radical.[36] The product angular distributions of the fast component from the primary alkyl radicals (ethyl, *n*-propyl, and *n*-pentyl) are anisotropic, while that from the secondary alkyl radical (*i*-propyl) is isotropic.

The photodissociation of the *n*-butyl, *s*-butyl, and *t*-butyl radicals could allow further investigation of the dynamics influenced by the different structural isomers (primary, secondary, and tertiary) and the different Rydberg states. In this work, the UV photodissociation dynamics of the jet-cooled *n*-butyl, *s*-butyl, and *t*-butyl radicals via the 3s, 3p, and 3d Rydberg states, respectively, were examined. The H-atom photofragment yield (PFY) spectra were obtained, confirming the UV absorption peaks of the *s*-butyl and *t*-butyl radicals and revealing the UV absorption feature of the *n*-butyl radical for the first time. The translational energy and angular distributions of the H-atom product channel were obtained from the H-atom time-of-flight (TOF) spectra. The dissociation mechanisms of the three butyl radicals were examined. Possible H-atom loss channels of the butyl radicals and their energetics are listed below.[38]

n-$C_4H_9 \rightarrow$ 1-C_4H_8 + H, $\Delta H_{rxn,0}$ = 32.1 kcal/mol.

s-$C_4H_9 \rightarrow$ 1-C_4H_8 + H, $\Delta H_{rxn,0}$ = 34.9 kcal/mol.

s-$C_4H_9 \rightarrow$ *cis*-2-C_4H_8 + H, $\Delta H_{rxn,0}$ = 33.3 kcal/mol.

s-$C_4H_9 \rightarrow$ *trans*-2-C_4H_8 + H, $\Delta H_{rxn,0}$ = 32.2 kcal/mol.

t-$C_4H_9 \rightarrow$ i-C_4H_8 + H, $\Delta H_{rxn,0}$ = 34.5 kcal/mol.

5.2 Experimental method

The high-*n* Rydberg-atom time-of-flight (HRTOF) technique was employed in this study, and the details of the experimental setup have been described in previous publications.[31,35,36,39] The radicals were generated by photolyzing suitable precursors seeded in He (~1% at a total pressure of ~ 120 kPa) using the 193 nm radiation from an ArF excimer laser. 1-Nitrobutane (Aldrich 98%) was employed as a precursor for the *n*-butyl radical, 2-nitrobutane (Acros 99%) for the *s*-butyl radical, and *tert*-nitrobutane (Acros 99%) for the *t*-butyl radical. The butyl radicals produced from the photolysis were cooled down by supersonic expansion and entrained in the molecular beam. In the high-vacuum interaction chamber, the butyl radicals were photodissociated with a tunable UV laser beam (233–257 nm for *n*-butyl, 234–258 nm for *s*-butyl, and 226-244 nm for *t*-butyl, 0.5-3 mJ/pulse). The linear polarization of the photolysis radiation can be rotated by a Fresnel-Rhomb achromatic λ/2 plate for product angular distribution measurements. The H-atom photoproducts were pumped by two-color resonant excitation (121.6 nm + 366.3 nm), i.e., from 1^2S to 2^2P via the H-atom Lyman-α transition and then to a metastable high-*n* Rydberg state. Part of the metastable Rydberg H atoms drifted perpendicular to the molecular beam with their nascent velocities to a microchannel plate (MCP) detector and were field-ionized in front the detector and detected. The flight path was 37.11 cm, which was calibrated by photodissociation of HBr at 236 nm with the well-known HBr dissociation energy and spin-orbit energy difference of the Br($^2P_{3/2}$) and Br($^2P_{1/2}$) products. The ion signals were

amplified by a fast pre-amplifier and averaged with a multichannel scaler. Typically, each H-atom TOF spectrum was accumulated with 50-100 k laser firings.

5.3 Results

The H-atom TOF spectra of the photodissociation of the *n*-butyl radical were obtained at the photolysis wavelengths of 233–257 nm with the polarization of the photolysis radiation parallel and perpendicular to the TOF path. Two types of H-atom TOF spectra were taken: (1) full spectrum, with the 193 nm radiation on and the UV photolysis laser beam on, plus the Rydberg atom tagging probe laser beams; and (2) precursor background spectrum, with the 193 nm radiation off but the UV photolysis radiation on, plus the Rydberg atom probe laser radiations. The net H-atom product TOF spectra were obtained by removing the precursor background spectra from the full spectra. Figure 5.1 shows the net H-atom product TOF spectra at the photolysis wavelength of 243 nm, with the photolysis radiation parallel and perpendicular to the TOF path. Both spectra have a peak around 17 μs, with a higher intensity at the parallel polarization, and an identical broad feature at the longer flight time. The photolysis laser power was kept around 2.0 mJ/pulse; the H-atom signals were shown to have a linear photolysis power dependence.

The H-atom PFY spectrum of the *n*-butyl radical was acquired by integrating the net H-atom TOF spectra of the *n*-butyl photodissociation as a function of the photolysis wavelength. The signals were normalized by the photolysis laser power and number of laser shots and scaled to those at 247 nm, which were repeated and used as a reference. The

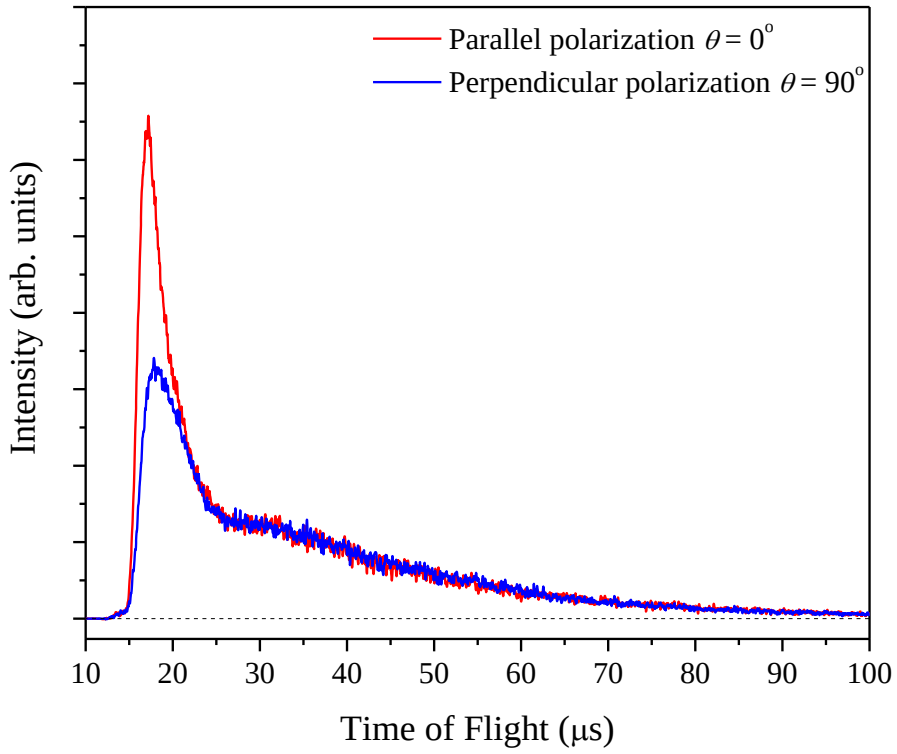

Figure 5.1. H-atom product TOF spectra of the jet-cooled *n*-butyl radical at the photolysis wavelength of 243 nm. The precursor photolysis backgrounds have been removed from these spectra. The polarizations of the electronic vector of the photolysis radiation are parallel (∥, $\theta = 0°$) and perpendicular (⊥, $\theta = 90°$) to the TOF path. These two TOF spectra were normalized to the same laser power and number of laser shots. The *n*-butyl radical was formed by photodissociation of 1-nitrobutane precursor with the 193 nm radiation.

H-atom PFY spectrum shows a broad peak in the region of 233-257 nm (Figure 5.2). There is no reported UV absorption spectrum of the *n*-butyl radical. As the Rydberg excitation is localized on the radical center, the *β*-alkyl substitutions on the ethyl radical to form *n*-propyl and *n*-butyl would not change the electronic state significantly.[22,24] Indeed, the UV absorption spectra of both ethyl[22] and *n*-propyl[27] have a broad peak around 245 nm, corresponding to the 3s Rydberg transition.[22,35] It is therefore expected that the peak around 247 nm in the PFY spectrum of *n*-butyl is also due to the 3s Rydberg transition.

The angular-dependent center-of-mass (c.m.) translational energy distributions, $P(E_T, \theta)$'s, of the H + C_4H_8 product channel can be derived from the net H-atom product TOF spectra at different photolysis polarizations. The following equation is used to convert the time-space TOF spectra to the energy-space $P(E_T, \theta)$:

$$E_T = \left(1 + \frac{m_H}{m_{C_4H_8}}\right) E_H = \frac{1}{2} m_H \left(1 + \frac{m_H}{m_{C_4H_8}}\right) \left(\frac{L}{t_H}\right)^2$$

where E_T is the c.m. translational energy of the H + C_4H_8 products, E_H is the laboratory translational energy of the H-atom product, L is the length of the flight path, and t_H is the H-atom flight time. Figure 5.3(a) shows the normalized c.m. translational energy distributions of the H + C_4H_8 products from the photodissociation of *n*-butyl at 243 nm, with the photolysis polarization parallel ($\parallel$, θ = 0°) and perpendicular ($\perp$, θ = 90°) to the TOF path. The c.m. translational energy distribution at the magic angle (θ = 54.7°), $P_m(E_T)$, is derived by combining the $P_\parallel(E_T)$ and $P_\perp(E_T)$ distributions and shown in Figure 5.3(b). The photofragment c.m. translational energy and angular distributions can be described with the following equation:[40]

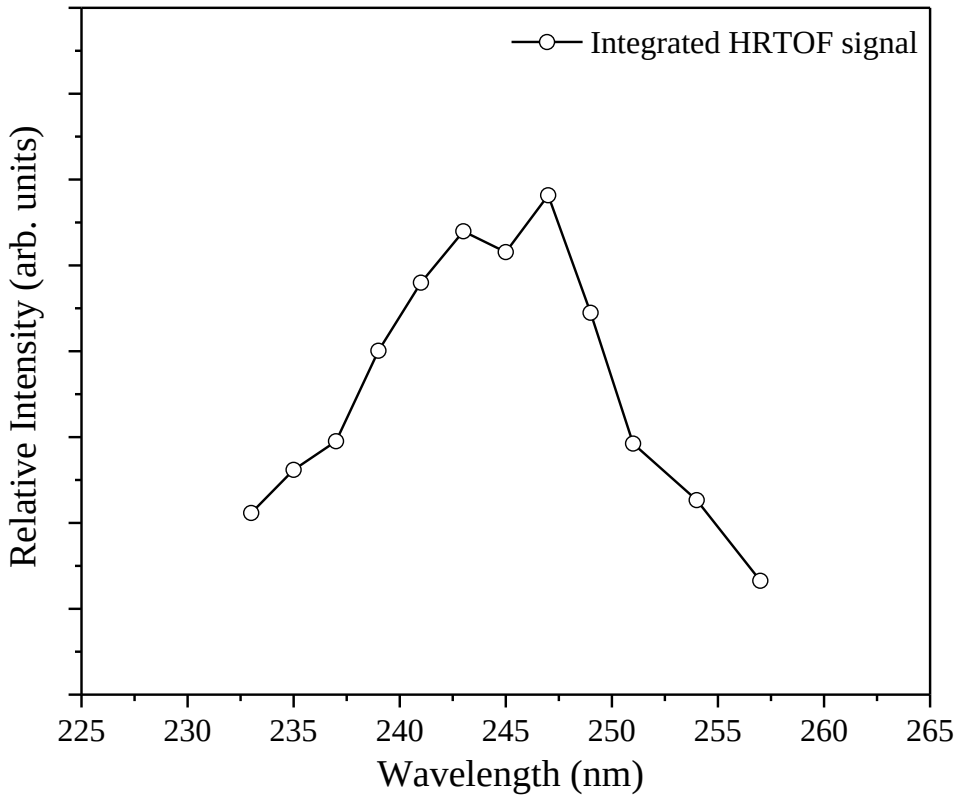

Figure 5.2. H-atom photofragment yield (PFY) spectrum of the *n*-butyl radical as a function of photolysis wavelength in the region of 233 to 257 nm. The H-atom signals (open circles (○)) were obtained by integrating the HRTOF signals of the *n*-butyl radical from the 1-nitrobutane precursor. The H-atom signals were normalized to the same laser power and number of shots and scaled at 247 nm.

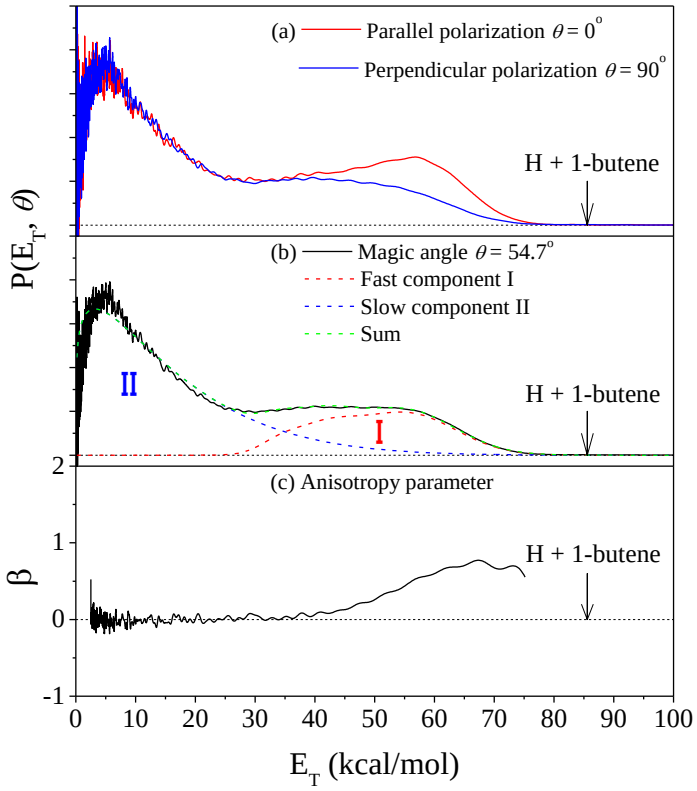

Figure 5.3. Center-of-mass (c.m.) translational energy distributions $P(E_T, \theta)$ and anisotropy parameter β of the H + C_4H_8 product channel from photodissociation of the *n*-butyl radical at 243 nm. The maximum available energy E_{avail} is 85.6 kcal/mol for the H + 1-butene (CH_2=$CHCH_2CH_3$) product channel (indicated by the vertical arrow). (a) $P(E_T, \theta)$ with the polarization of the photolysis radiation parallel ($\parallel$, θ = 0°) and perpendicular ($\perp$, θ = 90°) to the TOF path. (b) $P(E_T, \theta)$ at the magic angle, $P_m(E_T)$, derived by combining the $P_{\parallel}(E_T)$ and $P_{\perp}(E_T)$ distributions from (a). The de-convoluted fast (high E_T) component $P_I(E_T)$, slow (low E_T) component $P_{II}(E_T)$, and the summed fitting at the magic angle are plotted in Figure (b). (c) Translational energy-dependent anisotropy parameter $\beta(E_T)$. See the text for more details.

$$P(E_T, \theta) = \left(\frac{1}{4\pi}\right) P(E_T)[1 + \beta P_2(cos\theta)]$$

$P(E_T)$ is the angle-integrated product translational energy distribution, β is the anisotropy parameter ($-1 < \beta < 2$), θ is the angle between the electric vector of the linearly polarized photolysis radiation and the recoiling velocity vector of the H-atom product, and $P_2(cos\theta)$ is the second Legendre polynomial. The energy-dependent anisotropic parameter, $\beta(E_T)$, of the photofragment from photodissociation of the *n*-butyl radical is calculated from the translational energy distributions at the parallel and perpendicular polarizations, with $\beta(E_T) = 2\times[P_{\parallel}(E_T) - P_{\perp}(E_T)]/ [P_{\parallel}(E_T) + 2P_{\perp}(E_T)]$, and plotted in Figure 5.3(c).

The c.m. product translational energy distributions at 243 nm (Figure 5.3) show a broad bimodal feature, with a slow (low E_T) peak around 6 kcal/mol and a fast (high E_T) peak around 52-57 kcal/mol, and extending to the maximum available energy of the H + 1-butene product channel (E_{avail} = 85.6 kcal/mol at the photolysis wavelength of 243 nm). At $E_T < 40$ kcal/mol, β is at a constant value of ~ 0, and β increases with increasing E_T and reaches a maximum value of 0.7 ± 0.1 at $E_T > 65$ kcal/mol. The bimodal $P(E_T, \theta)$ distributions have a large E_T release peaking around 52-57 kcal/mol with $\beta > 0$ and a small E_T release peaking at ~ 6 kcal/mol with $\beta \approx 0$. The two E_T release regions with different β values indicate at least two dissociation channels. The observed $P(E_T, \theta)$ distributions are the sum of the different dissociation channels, and the varying $\beta(E_T)$ is due to the different β parameters and energy-dependent branching ratios of the two dissociation channels. In Figure 5.3(b), two Rice-Rampsperger-Kassel (RRK)-type functions, $P(E_T) = A(E_T)^p(E_0 - E_T)^q$, are used to deconvolute $P_m(E_T)$ into the fast and slow components.[35,36,41] In the equation above, A, p and q are adjustable parameters, and E_0 is the maximum available

energy (85.6 kcal/mol for the fast component and adjustable for the slow component). From the fitting, the average translational energy release $\langle E_T \rangle$ of these two product channels are calculated to be 50.3 kcal/mol ($\langle f_T \rangle$ = 0.59) for the fast channel (I) and 15.3 kcal/mol ($\langle f_T \rangle$ = 0.18) for the slow channel (II). The overall $\langle f_T \rangle$ for all the product channels is ~ 0.30. The branching ratio of the fast to slow component is estimated to be 0.41:1 based on the two-component fitting. The P(E_T) distributions at other photolysis wavelengths, 236, 247, and 249 nm, were also obtained (Figure 5.4). They all show a bimodal distribution, similar to those at 243 nm. The product translational energy releases and branching ratios are summarized in Table 5.1. The overall $\langle f_T \rangle$ increases with the decreasing photo-excitation energy. Interestingly, there is some variation in the branching ratio of the fast/slow channels with the photolysis wavelength, with a maximum value at 247 nm (which is also the peak absorption) (Figure 5.4 and Table 5.1).

The net TOF spectra of photodissociation of the *s*-butyl radical at 244 nm with both the parallel and perpendicular polarizations are shown in Figure 5.5. The spectra from both polarizations are similar. A fast peak at ~ 19 μs with a slightly stronger signal at the parallel polarization and a board feature at the longer flight time were observed. The H-atom PFY spectrum of the s-butyl radical was obtained in the region of 234-258 nm and is presented in Figure 5.6. Figure 5.6 also shows the UV absorption spectrum of the s-butyl radical from Wendt and Hunziker's work.[22] Compared to the UV absorption spectrum, the H-atom PFY spectrum peaks around 244 nm and has a red shift of ~ 3 nm, but the shape of these two spectra have a reasonable agreement, consistent with that the H-atom signals were from photodissociation of the *s*-butyl radical.

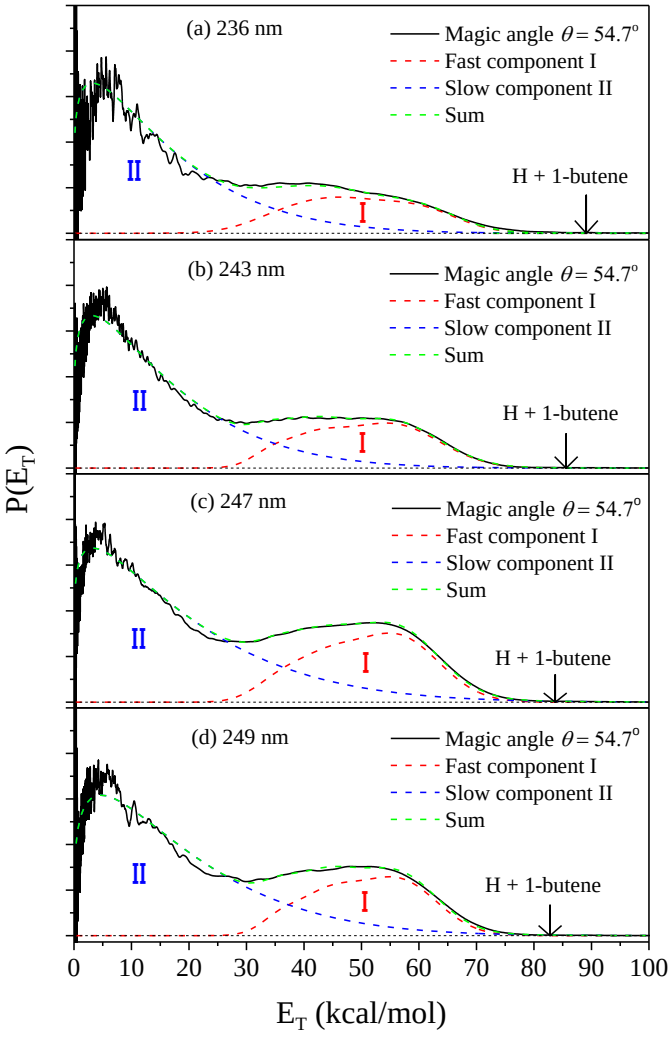

Figure 5.4. The magic-angle $P(E_T)$ distributions of the H + C_4H_8 product channel from photodissociation of the *n*-butyl radical at different photolysis wavelengths. The de-convoluted fast component $P_I(E_T)$, slow component $P_{II}(E_T)$, and the summed fitting are plotted. The arrows indicate the maximum available energies for the H + 1-butene (CH_2=$CHCH_2CH_3$) product channel.

Table 5.1. $\langle f_T \rangle$ values and fast-slow branching ratios of the H + C_4H_8 product channels from the photodissociation of the *n*-butyl, *s*-butyl, and *t*-butyl radicals at different photolysis wavelengths.

		$\langle f_T \rangle$ value			fast to slow ratio
	photolysis wavelength	total	fast component	slow component	
n-butyl	236 nm	0.25	0.55	0.13	0.40:1
	243 nm	0.30	0.59	0.18	0.41:1
	247 nm	0.35	0.61	0.22	0.48:1
	249 nm	0.34	0.61	0.22	0.43:1
	average	0.31	0.59	0.19	0.43:1
s-butyl	240 nm	0.30	0.50	0.12	0.66:1
	244 nm	0.30	0.51	0.16	0.64:1
	average	0.30	0.50	0.14	0.65:1
t-butyl	232 nm	0.27	0.43	0.14	0.70:1
	236 nm	0.26	0.43	0.14	0.72:1
	240 nm	0.28	0.45	0.15	0.67:1
	average	0.27	0.44	0.14	0.70:1

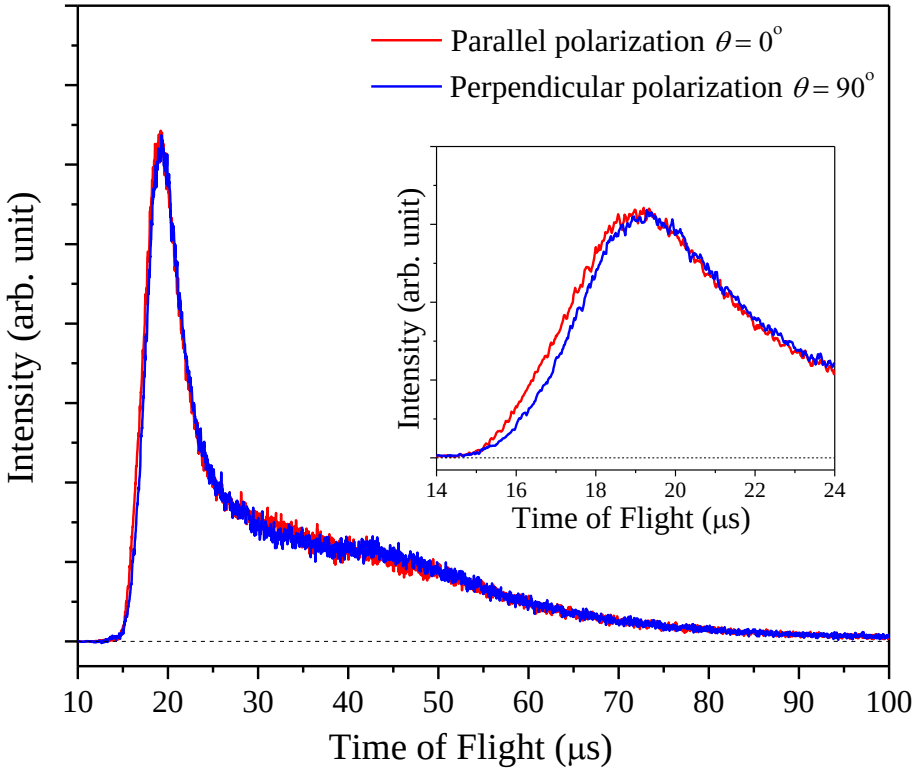

Figure 5.5 H-atom product TOF spectra of the jet-cooled *s*-butyl radical at the photolysis wavelength of 244 nm with the parallel (∥, θ = 0°) and perpendicular (⊥, θ = 90°) polarizations. The backgrounds were properly removed. These two spectra were normalized to the same laser power and number of shots. The *s*-butyl radical was formed by photodissociation of 2-nitrobutane at 193 nm.

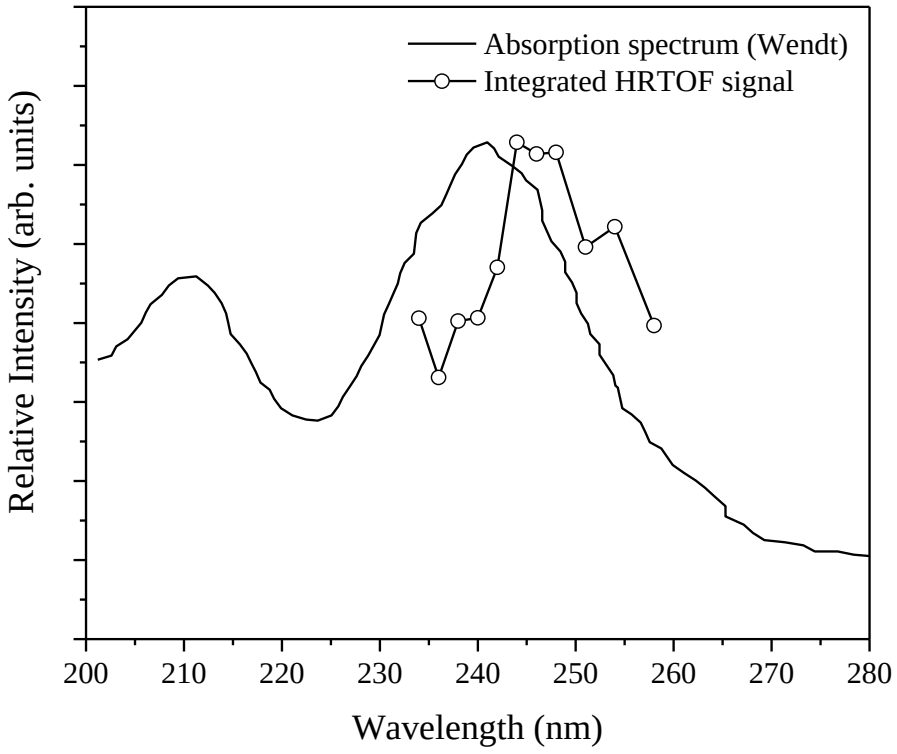

Figure 5.6. H-atom PFY spectrum of the *s*-butyl radical as a function of photolysis radiation wavelength in the region of 234 to 258 nm. Open circles (○) are the integrated HRTOF signals of the *s*-butyl radical using 2-nitrobutane precursor at different photolysis wavelength. The signals were normalized to the same laser power and shots. The solid line is the UV absorption spectrum of the *s*-butyl radical taken from Wendt and Hunziker (Ref. 22). Both the PFY and absorption spectrum were normalized to the same scale at their maximum intensities.

Figure 5.7(a) shows the $P(E_T)$ distributions of *s*-butyl at the parallel and perpendicular polarizations at 244 nm. Both the $P_{\parallel}(E_T)$ and $P_{\perp}(E_T)$ distributions have a bimodal feature, with a slow peak at ~ 6 kcal/mol and a fast peak at ~ 43 kcal/mol and extending to the maximum E_{avail} = 83.7 kcal/mol. As three possible H-loss product channels of *s*-butyl, H + 1-butene, H + *cis*-2-butene, and H + *trans*-2-butene, are close in energy, the $P(E_T)$ distributions could not differentiate them, and the E_{avail} value is based on the average bond dissociation energy of these three H + C_4H_8 channels. The β parameter is nearly a constant of 0 at E_T < 45 kcal/mol, and at larger E_T, the β parameter has a positive value and reaches a maximum of 0.3 ± 0.1 (Figure 5.7(c)). The $P_m(E_T)$ at the magic angle is derived from $P_{\parallel}(E_T)$ and $P_{\perp}(E_T)$ and deconvoluted into a fast component (I) and a slow component (II) by using the RRK-type function mentioned above. The $\langle E_T \rangle$ values for the fast component (I) and the slow component (II) are 42.8 kcal/mol ($\langle f_T \rangle$ = 0.51) and 13.3 kcal/mol ($\langle f_T \rangle$ = 0.16), respectively, and the total $\langle E_T \rangle$ is 25.2 kcal/mol with $\langle f_T \rangle$ ~ 0.30. The branching ratio of the fast and slow components is estimated to be ~ 0.64:1. The $P(E_T)$ distributions at 240 nm are essentially identical to those at 244 nm. Their results are listed in Table 5.1.

Figure 5.8 presents the net TOF spectra of photodissociation of the jet-cooled *t*-butyl radical at 232 nm at the parallel and perpendicular polarizations. These two TOF spectra are identical, showing a peak at ~ 20.5 μs and a broad feature at the longer time. The H-atom PFY spectrum was obtained in the region of 226-244 nm and is shown in Figure 5.9, along with the scaled absorption spectra of *t*-butyl from Wendt and Hunziker[22] and Parkes and Quinn.[42] The H-atom PFY spectrum peaks around 234 nm and basically

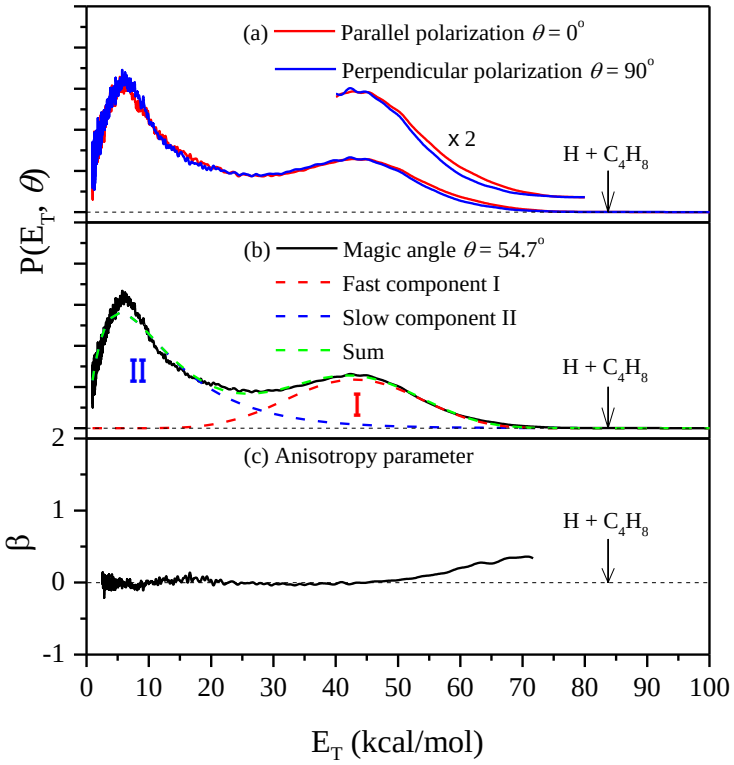

Figure 5.7. Center-of-mass translational energy distributions $P(E_T, \theta)$ and anisotropy parameter β of the H + C_4H_8 product channel from photodissociation of the *s*-butyl radical at 244 nm. The maximum available energy E_{avail} is 83.7 kcal/mol (indicated by the vertical arrow), which is based on the average bond dissociation energy of the H + 1-butene, H + *cis*-2-butene, and H + *trans*-2-butene product channels. (a) $P(E_T, \theta)$ at the parallel ($\parallel$, θ = 0°) and perpendicular ($\perp$, θ = 90°) photolysis polarizations. (b) $P(E_T, \theta)$ at the magic angle, $P_m(E_T)$, derived by combining $P_{\parallel}(E_T)$ and $P_{\perp}(E_T)$ from (a). The de-convoluted fast component $P_I(E_T)$, slow component $P_{II}(E_T)$, and the summed fitting at magic angle are also shown. (c) Translational energy-dependent anisotropy parameter $\beta(E_T)$. See the text for more details.

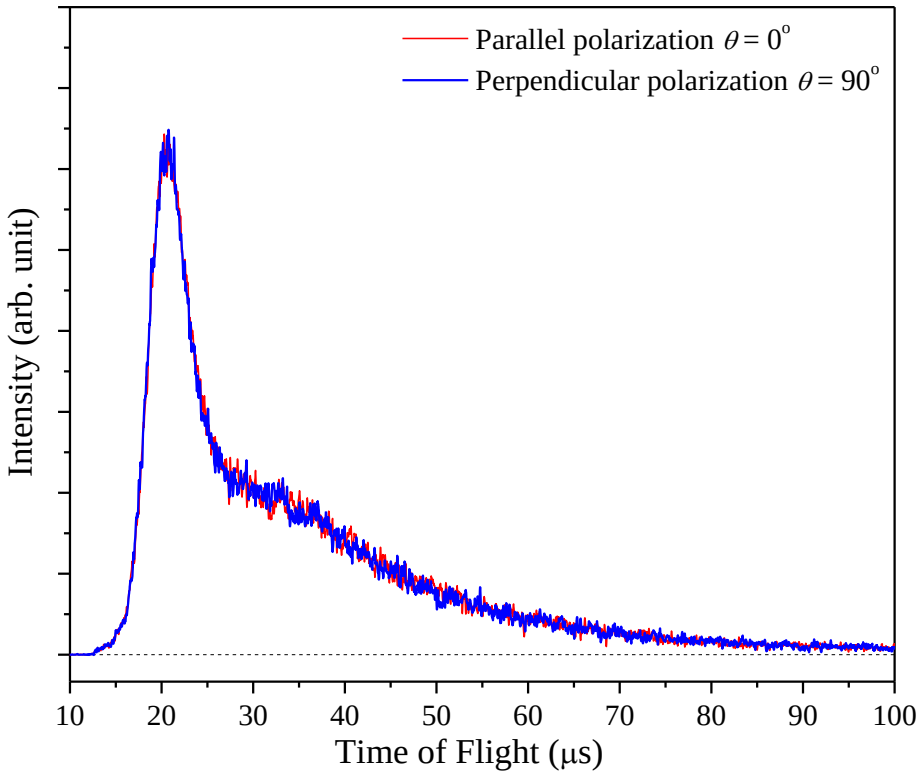

Figure 5.8. H-atom product TOF spectra of the jet-cooled *t*-butyl radical at the photolysis wavelength of 232 nm, with the parallel (∥, θ = 0°) and perpendicular (⊥, θ = 90°) polarizations. The backgrounds were removed from the spectra. These two spectra were normalized to the same laser power and shots. The *t*-butyl radical was formed by photodissociation of *t*-nitrobutane at 193 nm.

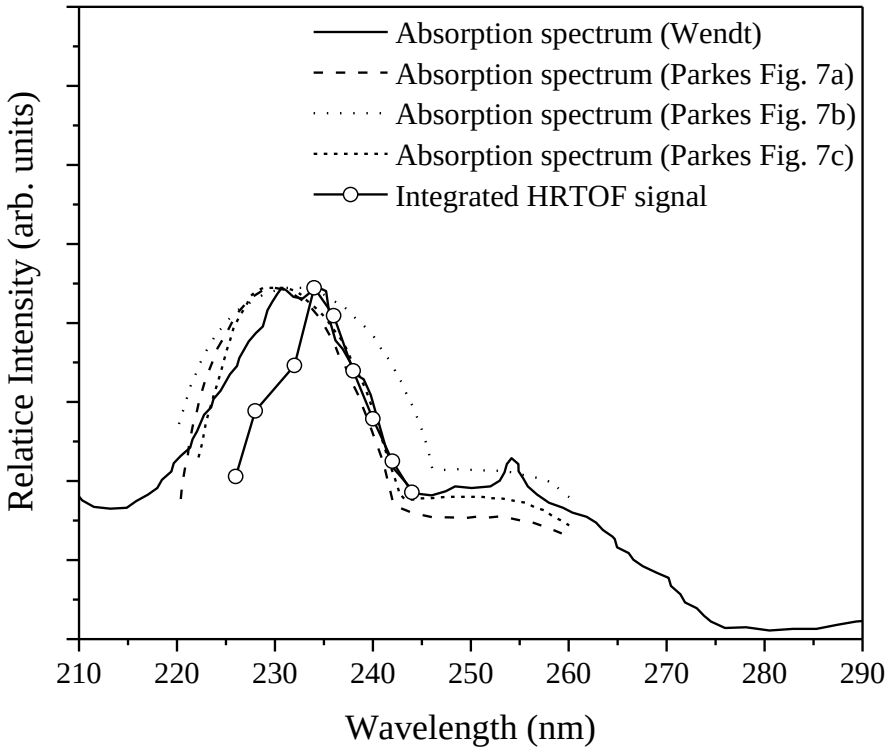

Figure 5.9. H-atom PFY spectrum of the *t*-butyl radical as a function of photolysis wavelength in the region of 226 to 244 nm. Open circles (○) are the integrated HRTOF signals of the *t*-butyl radical using *tert*-nitrobutane precursor at different photolysis wavelength. The signals were normalized to the same laser power and shots. The solid line is the UV absorption spectrum of the *t*-butyl radical taken from Wendt and Hunziker (Ref. 22). The dashed lines are the absorption spectra of *t*-butyl from Parkes and Quinn (Ref. 23). The PFY and absorption spectra were normalized to the same scale at their maximum intensities.

follows the absorption spectra, supporting that the H-atom signals were from the photodissociation of the *t*-butyl radical.

The $P(E_T)$ distributions of the H + C_4H_8 product channel in the 232 nm photodissociation of *t*-butyl are shown in Figure 5.10(a). The $P(E_T)$'s at the parallel and perpendicular polarizations are identical, and the β parameter is ~ 0 at all E_T. The $P(E_T)$ distributions are bimodal and consistent with the previous study by Fischer and coworkers.[30] The $P_m(E_T)$ at the magic angle is deconvoluted into two components by using the RRK-type function, and the result is presented in Figure 5.10(b). The fast component (I) peaks at 37 kcal/mol and extends to the maximum available energy of the H + *i*-butene product channel (88.7 kcal/mol at 232 nm), while the slow component (II) has a peak at ~ 6 kcal/mol. Both components have the isotropic product angular distribution with $\beta \approx 0$. The $\langle f_T \rangle$ values are 0.43 and 0.14 for the fast (I) and slow (II) component, respectively, and the overall $\langle f_T \rangle$ is ~ 0.27. The branching ratio between the fast and slow components is ~ 0.70:1. The $P(E_T)$ distributions at other two photolysis wavelengths, 236 and 240 nm, are essentially the same as those at 232 nm, with similar product energy releases and branching ratios. The results at these wavelengths are listed in Table 5.1.

5.4 Discussions

The UV photodissociation of the jet-cooled *n*-butyl radical was studied for the first time. The H-atom PFY spectrum of the *n*-butyl radical has a broad UV absorption in the region of 233–257 nm, peaking around 247 nm (Figure 5.1). This absorption feature is

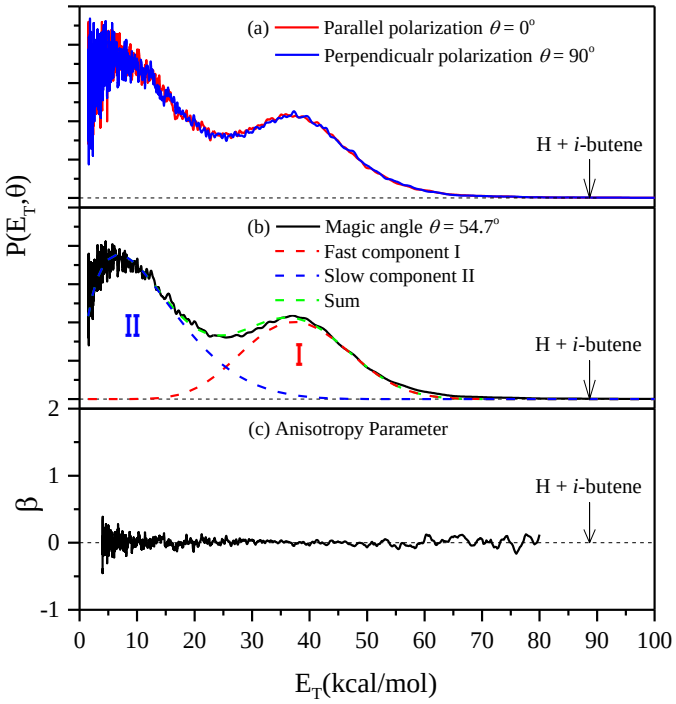

Figure 5.10. Center-of-mass translational energy distributions $P(E_T, \theta)$ and anisotropy parameter β of the H + C_4H_8 product channel from photodissociation of the *t*-butyl radical at 232 nm. The maximum available energy E_{avail} is 88.7 kcal/mol for the H + *i*-butene product channel (indicated by the vertical arrow). (a) $P(E_T, \theta)$ at the parallel ($\parallel$, θ = 0°) and perpendicular ($\perp$, θ = 90°) photolysis polarization. (b) $P(E_T, \theta)$ at the magic angle, $P_m(E_T)$, derived by combining the $P_{\parallel}(E_T)$ and the $P_{\perp}(E_T)$ from (a). The de-convoluted fast component $P_I(E_T)$, slow component $P_{II}(E_T)$, and the summed fitting at magic angle are also shown. (c) Translational energy-dependent anisotropy parameter $\beta(E_T)$. See the text for more details.

similar to the first absorption band (peaking at ~ 245 nm) of the ethyl and *n*-propyl radical and is also assigned to the $2p_z \rightarrow 3s$ transition.[22,25,35] As the Rydberg excitation is localized on the radical center,[22,24] the UV absorption spectra of the 3s Rydberg state of the primary alkyl radicals are nearly identical.[22,24,25,35,36] The board UV absorption feature of *n*-butyl indicates a short life time of the 3s Rydberg state due to either fast dissociation and/or internal conversion.

The $P(E_T)$ and angular distributions of the H + 1-butene products from the UV photodissociation of *n*-butyl in the region of 233–257 nm are bimodal (Figure 5.3 and 5.4). The anisotropic, fast component peaks around 52-57 kcal/mol with $\langle f_T \rangle \sim 0.6$ and $\beta \sim 0.7$, and the isotropic, slow component peaks at ~ 6 kcal/mol with $\langle f_T \rangle \sim 0.2$ and $\beta \sim 0$. These distributions of *n*-butyl are similar to those of ethyl, *n*-propyl, and *n*-pentyl, three similar primary alkyl radicals, via the 3*s* Rydberg state in the same UV photolysis region.[31,32,35,36] This similarity in the dynamic information further supports the assignment of the 3*s* Rydberg state of *n*-butyl. In the photodissociation of ethyl upon the $2p_z \rightarrow 3s$ excitation, the ethyl 3s Rydberg state decays to a H-bridged configuration and with two pathways via the conical intersection in C_{2v} symmetry, a direct dissociation from the excited state to the H + C_2H_4 ($\tilde{X}\,^1A_g$) products with a repulsive translational energy release and anisotropic product angular distribution, as well as internal conversion to the ground electronic state followed by unimolecular dissociation of the hot radical with a small translational energy release and isotropic angular distribution.[31-33,37] The 3s Rydberg state of *n*-propyl also dissociates via two pathways, a direct dissociation to the H + propene products with a large translational energy ($\langle f_T \rangle \approx 0.6$) and anisotropic angular distribution ($\beta \approx 0.8$) and internal

conversion to the ground electronic state followed by unimolecular dissociation with a small kinetic energy release ($\langle f_T \rangle \approx 0.2$) and isotropic product angular distribution.[35] The H-atom product channel from photodissociation of *n*-pentyl radical via the 3s Rydberg state also has two product channels and is similar.[36]

The study on the photodissociation of partially-deuterated ethyl and *n*-propyl radicals revealed site-selective β H atom eliminations.[31,35,43-45] The same is expected in the photodissociation of the *n*-butyl radical. Furthermore, isomerization between *n*-butyl and *s*-butyl has a higher energy barrier than the C-H bond fission,[19] also suggesting that β CH bond cleavage is a favorable channel in the photodissociation of *n*-butyl. The fast component (I) in the *n*-butyl photodissociation with β up to 0.7 should come from a prompt and direct dissociation from the electronic excited state to the H + 1-butene products, with a repulsive energy release and a dissociation time scale shorter than one rotational period of the *n*-butyl radical (< 10 ps). The lowest energy conformer of the *n*-butyl radical has the carbon backbone in a zig-zag configuration in a place and a β-CH bond eclipsed to the half-filled $2p_z$ orbital on the radical carbon (C_α), while the β-CC bond eclipsed conformer is at a slightly higher energy of ~ 0.2 kcal/mol.[46,47] In the ground electronic state, the α-CH_2 (methylene group) is slightly non-planar with respect to the α-CC bond,[46] while in the 3s excited state they are in a plane.[22] In the $2p_z \rightarrow 3s$ transition, the transition dipole moment $\boldsymbol{\mu}$ is along the $2p_z$ orbital and perpendicular to the methylene plane. The anisotropic parameter β value of 0.7 indicates a ~ 41° angle between this transition dipole moment $\boldsymbol{\mu}$ and the velocity vector of the recoiling H atom in the prompt dissociation (fast channel).[48] When the lowest energy, β-CH bond eclipsed conformer undergoes the prompt β-H

elimination, the C=C double bond and the 1-butene product are readily formed in this configuration.

In the photodissociation of ethyl 3s Rydberg state, the 3s Rydberg state isomerizes to a non-classical H-bridged configuration due to its lower energy, and the dissociation then proceeds via a conical intersection near the C_{2v} symmetry (the 3s Rydberg state is therefore directly dissociative to the H + ethylene products, leading to the bimodal distributions). In other alkyl radicals, the bridged structures in the Rydberg states are not favored.[22] However, the dissociation dynamics of the 3s Rydberg states of *n*-propyl, *n*-butyl and *n*-pentyl are very similar, indicating a common mechanism. While the 3s Rydberg state may no longer be connected directly and dissociatively to the H + olefin products, it is possible that a repulsive state (such as σ*(C-H)) crosses with the 3s Rydberg state and couples it repulsively to the H + ground-state olefin products, which gives rise to the high E_T and anisotropic component. The coupling could be far away from the equilibrium geometry (as the olefin shows a significant amount of internal energy excitation in the fast component with $\langle f_T \rangle \approx 0.6$) and possibly via a conical intersection.

The slow component (II) with $\beta \approx 0$ is consistent with unimolecular dissociation of the hot *n*-butyl radical on the ground electronic state after internal conversion from the excited state, with a dissociation time scale longer than or equal to one rotational period of *n*-butyl radical (> 10 ps). The internal conversion from the 3s Rydberg state probably involves with the crossing of the 3s Rydberg state with a repulsive state and the conical intersection, as in the case of *n*-propyl and *n*-pentyl. The $P(E_T)$ peaking at ~ 6 kcal/mol is

consistent with the ~ 3 kcal/mol exit channel energy barrier to the H + 1-butene products (i.e., the energy barrier of the reverse H + 1-butene addition reaction).[13]

The UV photodissociation of jet-cooled *s*-butyl radical was studied in the photolysis wavelength region of 234–258 nm for the first time. The H-atom PFY spectrum reasonably matches the UV absorption spectrum of the *s*-butyl radical, which is due to the 3p Rydberg states via the $2p_z \rightarrow 3p$ transition. The small difference between them might be due to other dissociation channels of *s*-butyl, such as the C-C bond cleavage,[6,13,19] or temperature difference of the *s*-butyl radical (room temperature in the absorption spectrum vs. jet-cooled low temperature in the PFY spectrum). The *s*-butyl radical is a secondary alkyl radical and can be viewed as the *i*-propyl radical with one of the methyl groups replaced by an ethyl group. The photodissociation of the *s*-butyl and *i*-propyl radical on the 3p Rydberg states should have a similar behavior. Two H-atom dissociation channels were observed for the photodissociation of *i*-propyl from the 3p states, with a site-selective β-CH bond cleavage.[35] The fast channel of *i*-propyl is the direct dissociation from the excited state with a repulsive energy release ($\langle f_T \rangle \sim 0.5$) and a nearly isotropic angular distribution, which is due to the combination of the positive β parameter of the dissociation from the $3p_z$ Rydberg state and the negative β parameters from the dissociation from the $3p_{x,y}$ Rydberg states. The slow channel is assigned to unimolecular dissociation of the electronic ground state after internal conversion via the conical intersection from the 3p Rydberg states with a small translational energy released ($\langle f_T \rangle \sim 0.1$) and isotropic product angular distribution. The similarity allows two dissociation pathways with a bimodal translational energy distribution for the *s*-butyl radical as well. A dominant β H atom elimination in the

s-butyl radical is also expected as in the case of *i*-propyl radical, while isomerization between *n*-butyl and *s*-butyl is not expected due to the higher energy barrier.[19]

The $P(E_T)$ distributions of the H-atom product channel from the photodissociation of *s*-butyl in the region of 234-258 nm have a similar feature (Figure 5.7). Both H+ 1-butene and H + *cis*- or *trans*-2-butene can be the H-elimination products of *s*-butyl. The fast component peaks at ~ 43 kcal/mol ($\langle f_T \rangle \sim 0.51$) and is consistent with a repulsive energy release but smaller than that for *n*-butyl. The anisotropy parameter β has a maximum value of ~ 0.3 at high kinetic energy. Similar to *i*-propyl, the absorption band of *s*-butyl would involve with all the $3p_{x,y,z}$ Rydberg states, as their energy levels are close to each other.[22] Previous theoretical study revealed that in the lowest energy configuration the half-filled $2p_z$ orbital of *s*-butyl is approximately perpendicular to the plane of the radical-center carbon and the two β-carbons (CCC plane) and eclipses to two β-CH bonds (one each on each of the β-carbon).[49,50] Elimination of the β H atom on the methyl group readily leads to the 1-butene product, while that from the ethyl group leads to the 2-butene products. The transition dipole moment of $2p_z \rightarrow 3p_z$ is approximately perpendicular to the CCC plane, and the prompt β H atom dissociation would eject the H atom along the transition dipole moment and have a positive anisotropy parameter, while the $2p_z \rightarrow 3p_{x,z}$ transition dipole moments are approximately in the CCC plane, and the prompt β H atom elimination would have a negative anisotropy parameter. The mixture of the β H atom dissociations from these three transitions could result in the observed slightly anisotropic product angular distribution in the fast dissociation channel. The 3p states of *n*-butyl dissociate presumably via crossing to a repulsive surface along the C-H coordinate or conical intersection. The

smaller $\langle f_T \rangle$ in the fast dissociation channel in *s*-butyl compared to *n*-butyl suggests a hotter internal excitation in the *s*-butyl radical before dissociation in the butene products. The mechanism of the photodissociation would be direct dissociation on the $3p_{x,y,z}$ Rydberg states, possible via a conical intersection, to produce the observed slightly anisotropic angular distribution with a repulsive kinetic energy release. The slow channel in the photodissociation of *s*-butyl is similar to those in the photodissociation of other alkyl radicals. The $P(E_T)$ distribution peaking at ~ 6 kcal/mol with $\langle f_T \rangle \sim 0.16$ is consistent with unimolecular dissociation of internally hot radical after internal conversion from the Rydberg excited states to the ground state. The anisotropy parameter $\beta \sim 0$ indicates that the dissociation time scale is comparable or longer than one rotation period of the *s*-butyl radical and is consistent with the unimolecular dissociation mechanism.

The *t*-butyl radical, as a prototypical tertiary alkyl radical, can be viewed as an ethyl radical with both α H atoms substituted with methyl groups. The H-atom PFY spectrum in the region of 226–244 nm matches with the UV absorption spectra from previous studies,[22,42] showing that the absorption band of the *t*-butyl radical in this region is due to the 3d Rydberg states via the $2p_z \rightarrow 3d$ transitions. The ground electronic state of *t*-butyl has a slightly pyramidal geometry with the C_{3v} symmetry. The $2p_z$ orbital of the radical center is perpendicular to the plane of the three methyl carbons and one of the β-CH bonds in each of the three methyl groups eclipsed to the $2p_z$ orbital.[51-53]

In the $P(E_T)$ distribution, the fast component peaks at ~ 37 kcal/mol with $\langle f_T \rangle \sim 0.43$, revealing a repulsive energy release; but its $\langle f_T \rangle$ is the smallest among the three butyl radical isomers in this study. The $\langle f_T \rangle$ value of the fast component was determined to be 0.35 by

Fischer and co-workers[30] and 0.44 by Neumark and co-workers.[29] The product angular distribution of the fast channel (I) in *t*-butyl is isotropic ($\beta \sim 0$), while Fischer and coworkers observed a negative anisotropy parameter ($\beta = -0.31$) for this fast component.[30] The broad absorption peak of the *t*-butyl radical at ~ 236 nm suggests that all the $2p_z \rightarrow 3d$ transitions are involved. The $2p_z \rightarrow 3d_z$ would have the transition dipole moment along the $2p_z$ orbital and parallel to the eclipsed β-CH bonds but perpendicular to the plane of the three methyl carbons. In this case, the prompt β H-atom cleavage following the $2p_z \rightarrow 3d_z$ excitation would readily produce the close-shell *i*-butene and the departing H atom with its nascent velocity approximately along the transition dipole moment, giving rise a positive anisotropy parameter. For other $2p_z \rightarrow 3d$ transitions, the transition dipole moments could be approximately parallel or at other angles to the plane of the three methyl carbons and perpendicular or at other angles to the $2p_z$ orbital and the eclipsed β-CH bonds. The β H-atom eliminations following these excitations would produce H atoms approximately perpendicular to the transition dipole moments with the negative anisotropic parameter. The observed isotropic product angular distribution result from a mixture of the H atoms produced following these $2p_z \rightarrow 3d$ transitions. The equilibrium geometry of the *t*-butyl radical changes from the pyramidal to the planar structure with all 4 carbons on the same plane during the excitation from the ground state to the Rydberg states.[26,52] The smaller $\langle f_T \rangle$ of 0.43 in the fast dissociation channel in *t*-butyl also suggests a hotter internal excitation in the *t*-butyl radical before dissociation and in the *i*-butene product.

The slow dissociation channel of the *t*-butyl radical is similar to those in ethyl, *n*- and *i*-propyl, *n*- and *s*-butyl radicals. The small translational energy release of $\langle f_T \rangle \sim 0.14$

shows a typical statistical energy distribution in the unimolecular dissociation. This $\langle f_T \rangle$ is in agreement with a value of 0.15 by Fischer and co-workers.[30] The anisotropic parameter β for this channel is ~ 0 (the same by Fischer and co-workers[30]), indicating that the dissociation time scale is comparable or longer than one rotational period (~ 10 ps) of the *t*-butyl radical and consistent with the unimolecular dissociation mechanism. The 1,2-H shift to form the *i*-butyl radical has a higher energy barrier (48 kcal/mol)[26] than the direct C-H bond cleavage (37.5 kcal/mol),[29] thus isomerization of *t*-butyl to *i*-butyl followed by unimolecular dissociation would be a minor H product channel. The mechanism of the slow product channel would be the unimolecular dissociation to the H + *i*-butene after internal conversion to the ground-electronic state probably via a conical intersection from the 3d Rydberg states.

It is worthwhile to compare the photodissociation of the primary alkyls (ethyl, *n*-propyl, *n*-butyl, and *n*-pentyl) via the 3s state, secondary alkyls (*i*-propyl and *s*-butyl) via the 3p states, and the tertiary alkyl (*t*-butyl) via the 3d states. They all have the bimodal $P(E_T)$ distributions, presumably due to some repulsive states that cross with the Rydberg states, leading to the repulsive dissociation (the fast components) and plausibly the competing internal conversion that is followed by unimolecular dissociation on the ground state. However, the $\langle f_T \rangle$ values of the fast components decrease in the trend of primary (3s), secondary (3p), and tertiary (3d), possibly due to the different locations of the crossings between the repulsive states along the C-H coordinate and the 3s, 3p, and 3d Rydberg states. The $\langle f_T \rangle$ values of the slow components from the primary (3s), secondary (3p), and tertiary (3d) radicals, on the other hand, are all small and similar, again supporting that the

slow components are due to the statistical unimolecular dissociation on the ground state after internal conversion. The anisotropy of the product angular distributions of the fast component decreases in the trend of primary (3s), secondary (3p), and tertiary (3d), while that of the slow component is isotropic for all theses alkyl radicals.

5.5 Conclusion

The H + C_4H_8 channel in the UV photodissociation of the jet-cooled *n*-butyl radical via the 3s Rydberg state, *s*-butyl radical via the 3p Rydberg states and *t*-butyl radical via the 3d Rydberg states were studied in the photolysis wavelength region of 233–257 nm, 234–258 nm and 226–244 nm respectively. The photodissociation of the *s*-butyl and *t*-butyl radicals were confirmed by the agreement of the H-atom PFY spectra and their UV absorption spectra, respectively, while the H-atom PFY spectrum of the *n*-butyl radical contains a broad structure and reveals its UV absorption feature for the first time. The H-atom product channel translational energy distributions of all these three radicals are bimodal, with the slow component peaking at ~ 6 kcal/mol and the fast component peaking at ~ 52-57 kcal/mol, ~ 43 kcal/mol, and ~ 37 kcal/mol for the *n*-butyl, *s*-butyl, and *t*-butyl radical, respectively. The fast-slow components branching ratio is ~ 0.43 (*n*-butyl), ~ 0.65 (*s*-butyl), and ~ 0.70 (*t*-butyl). The fraction of the average products translational energy in the total available energy, $\langle f_T \rangle$, is in the range of 0.25-0.35 for *n*-butyl, ~ 0.30 for *s*-butyl and ~ 0.27 for *t*-butyl, respectively. The anisotropic parameter β for the slow channel is 0 for all the radicals, while that of the fast channel is ~ 0.7 for *n*-butyl, ~ 0.3 for *s*-butyl, and

0 for *t*-butyl. The bimodal translational energy indicates two H + C_4H_8 product channels for all these three radicals. The excited radicals on the 3s, 3p and 3d Rydberg states have a direct, prompt H-atom dissociation via the repulsive potential energy surface and an internal conversion to the ground electronic state followed by the unimolecular dissociation. From the primary (3s), secondary (3p) then to tertiary butyl radical (3d), the $\langle f_T \rangle$ and β parameter for the fast component decrease, which was also observed in the photodissociation of the *n*-propyl (at 3s Rydberg state with $\langle f_T \rangle \sim 0.6$ and $\beta \sim 0.8$) and *i*-propyl (at 3p Rydberg states with $\langle f_T \rangle \sim 0.5$ and $\beta \sim 0$).[35] The different orientations of the transition dipole moments in the excitations from $2p_z$ to 3s, 3p, or 3d states could reduce the anisotropy parameter of the fast dissociation channels.

Reference

1. J. Warnatz, *Combustion Chemistry* (Springer New York, 1984).

2. C. K. Westbrook and F. L. Dryer, *Progr. Energy Combust. Sci.* **10**, 1 (1984).

3. J. T. Gruver and J. G. Calvert, *J. Am. Chem. Soc.* **78**, 5208 (1956).

4. J. R. McNesby, C. M. Drew, and A. S. Gordon, *J. Chem. Phys.* **24**, 1260 (1956).

5. J. G. Calvert, *Chem. Rev. (Washington, DC, U. S.)* **59**, 569 (1959).

6. B. S. Rabinovitch and R. W. Diesen, *J. Chem. Phys.* **30**, 735 (1959).

7. R. N. Birrell and A. F. Trotman-Dickenson, *J. Chem. Soc.*, 4218 (1960).

8. R. E. Harrington, B. S. Rabinovitch, and H. M. Frey, *J. Chem. Phys.* **33**, 1271 (1960).

9. J. A. Kerr and A. F. Trotman-Dickenson, *J. Chem. Soc.*, 1602 (1960).

10. E. L. Metcalfe and A. F. Trotman-Dickenson, *J. Chem. Soc.*, 5072 (1960).

11. W. E. Morganroth and J. G. Calvert, *J. Am. Chem. Soc.* **88**, 5387 (1966).

12. D. H. Slater, S. S. Collier, and J. G. Calvert, *J. Am. Chem. Soc.* **90**, 268 (1968).

13. O. Horie and H. Nguyen Hieu, *J. Phys. Chem.* **80**, 1657 (1976).

14. C. E. Canosa and R. M. Marshall, *Int. J. Chem. Kinet.* **13**, 303 (1981).

15. T. Gierczak, J. Gawlowski, and J. Niedzielski, *J. React Kinet Catal Lett* **36**, 435 (1988).

16. V. D. Knyazev, I. A. Dubinsky, I. R. Slagle, and D. Gutman, *J. Phys. Chem.* **98**, 5279 (1994).

17. V. D. Knyazev, I. A. Dubinsky, I. R. Slagle, and D. Gutman, *J. Phys. Chem.* **98**, 11099 (1994).

18. V. D. Knyazev and I. R. Slagle, *J. Phys. Chem.* **100**, 5318 (1996).

19. N. Yamauchi, A. Miyoshi, K. Kosaka, M. Koshi, and H. Matsui, *J. Phys. Chem. A* **103**, 2723 (1999).

20. V. D. Knyazev and W. Tsang, *J. Phys. Chem. A* **104**, 10747 (2000).

21. X. Zheng and P. Blowers, *AIChE J.* **52**, 3216 (2006).

22. H. R. Wendt and H. E. Hunziker, *J. Chem. Phys.* **81**, 717 (1984).

23. D. A. Parkes and C. P. Quinn, *J. Chem. Soc., Faraday Trans. 1* **72**, 1952 (1976).

24. B. H. Lengsfield, P. E. M. Siegbahn, and B. Liu, *J. Chem. Phys.* **81**, 710 (1984).

25. C. Chatgilialoglu and M. Guerra, *J. Am. Chem. Soc.* **112**, 2854 (1990).

26. B. Noller, R. Maksimenka, I. Fischer, M. Armone, B. Engels, C. Alcaraz, L. Poisson, and J.-M. Mestdagh, *J. Phys. Chem. A* **111**, 1771 (2007).

27. H. Adachi and N. Basco, *Int. J. Chem. Kinet.* **13**, 367 (1981).

28. M. Zierhut, W. Roth, and I. Fischer, *J. Phys. Chem. A* **108**, 8125 (2004).

29. B. Negru, G. M. Just, D. Park, and D. M. Neumark, *Phys. Chem. Chem. Phys.* **13**, 8180 (2011).

30. J. Giegerich and I. Fischer, *J. Chem. Phys.* **142**, 044304 (2015).

31. G. Amaral, K. Xu, and J. Zhang, *J. Chem. Phys.* **114**, 5164 (2001).

32. J. M. Hostettler, A. Bach, and P. Chen, *J. Chem. Phys.* **130**, 034303 (2009).

33. M. Steinbauer, J. Giegerich, K. H. Fischer, and I. Fischer, *J. Chem. Phys.* **137**, 014303 (2012).

34. B. Noller and I. Fischer, *J. Chem. Phys.* **126**, 144302 (2007).

35. Y. Song, X. Zheng, W. Zhou, M. Lucas, and J. Zhang, *J. Chem. Phys.* **142**, 224306 (2015).

36. G. Sun, Y. Song, and J. Zhang, *Chin. J. Chem. Phys.* **31**, 439 (2018).

37. A. S. Zyubin, A. M. Mebel, and S. H. Lin, *Chem. Phys. Lett.* **323**, 441 (2000).

38. B. Ruscic, *J. Phys. Chem. A* **119**, 7810 (2015).

39. Y. Song, X. Zheng, M. Lucas, and J. Zhang, *Phys. Chem. Chem. Phys.* **13**, 8296 (2011).

40. R. N. Zare, *Mol. Photochem*. **4**, 1 (1972).

41. G. Amaral, K. Xu, and J. Zhang, *J. Phys. Chem*. *A* **105**, 1115 (2001).

42. D. A. Parkes and C. P. Quinn, *Chem*. *Phys. Lett.* **33**, 483 (1975).

43. J. L. Brum, S. Deshmukh, and B. Koplitz, *J. Chem*. *Phys.* **95**, 2200 (1991).

44. J. L. Brum, S. Deshmukh, Z. Wang, and B. Koplitz, *J. Chem*. *Phys.* **98**, 1178 (1993).

45. T. Gilbert, T. L. Grebner, I. Fischer, and P. Chen, *J. Chem*. *Phys.* **110**, 5485 (1999).

46. J. Pacansky, R. J. Waltman, and L. A. Barnes, *J. Phys. Chem*. **97**, 10694 (1993).

47. V. V. Turovtsev and Y. D. Orlov, *Russ. J. Gen. Chem*. **80**, 749 (2010).

48. R. N. Zare, *Mol. Photochem*. **4**, 1 (1972).

49. Y. Chen, A. Rauk, and E. Tschuikow-Roux, *J. Phys. Chem*. **94**, 6250 (1990).

50. M. J. Pilling, J. Gang, S. H. Robertson, and G. Zeng, *Ber. Bunsenges. Phys. Chem.* **101**, 524 (1997).

51. D. E. Wood, L. F. Williams, R. F. Sprecher, and W. A. Lathan, *J. Am*. *Chem*. *Soc.* **94**, 6241 (1972).

52. M. N. Paddon-Row and K. N. Houk, *J. Am*. *Chem*. *Soc.* **103**, 5046 (1981).

53. J. Pacansky, W. Koch, and M. D. Miller, *J. Am*. *Chem*. *Soc.* **113**, 317 (1991).

Chapter 6

Ultraviolet Photodissociation Dynamics of the 1-Pentyl Radical

Abstract

The ultraviolet (UV) photodissociation of jet-cooled 1-pentyl radical is investigated in the wavelength region of 236-254 nm using the high-*n* Rydberg-atom time-of-flight (HRTOF) technique. The H-atom photofragment yield spectrum of the 1-pentyl radical shows a broad UV absorption feature peaking near 245 nm, similar to the $2p_z \rightarrow 3s$ absorption bands of ethyl and *n*-propyl. The center-of-mass translational energy distribution, $P(E_T)$, of the H + C_5H_{10} product channel is bimodal, with a slow peak at ~5 kcal/mol and a fast peak at ~50 kcal/mol. The fraction of the average translational energy release in the total available energy, $\langle f_T \rangle$, is 0.30, with those of the slow and fast components being 0.13 and 0.58, respectively. The slow component has an isotropic product angular distribution, while the fast component is anisotropic with an anisotropy parameter ~0.4. The bimodal translational energy and angular distributions of the H + C_5H_{10} products indicate two H-atom elimination channels in the photodissociation of 1-pentyl: (i) a direct, prompt dissociation from the electronic excited state and/or the repulsive part of the ground electronic state potential energy surface; and (ii) a unimolecular dissociation of internally hot radical in the ground electronic state after internal conversion from the electronic excited state.

6.1 Introduction

Alkyl radicals are important intermediates in the oxidation processes of alkanes such as combustion. They can undergo extensive unimolecular reactions such as dissociation and isomerization and bimolecular reactions such as with oxygen;[1,2] the dissociation of the alkyl radicals can influence the rate as well as the efficiency of combustion. Many studies have reported the dissociation mechanism of the alkyl radicals on the ground electronic state, while the studies on their excited states are relatively limited because of the short lifetime and the high reactivity. In this chapter, the study on the photodissociation of the 1-pentyl radical in the UV region of 236 to 254 nm is reported.

The dissociation and isomerization reactions of the 1-pentyl radical on the electronic ground state have been studied for decades experimentally[3-12] and theoretically[11,13-18]. The allylic C-C bond cleavage to yield ethene (C_2H_4) and *n*-propyl radical (*n*-C_3H_7) product would be the main dissociation channel in the thermal decomposition of the 1-pentyl because of the low bond energy and dissociation energy barrier, and the *n*-propyl radical could further decompose to the ethene and methyl radical products.[9,10] Miyoshi *et. al.* observed isomerization of the 1-pentyl radical to the 2-pentyl radical via a 1,4 H-atom shift with a five-member ring transition state firstly, and in their Rice-Ramsperger-Kassel-Marcus (RRKM)/master-equation analyses estimated an energy barrier of this five-member ring isomerization lower than that of the C-C or C-H bond fission of 1-pentyl.[10] Unlike the three- or four-member ring isomerization that has an energy barrier close or higher than the C-C or C-H bond cleavage process,[19,20] the lower

energy barrier of the 1,4 H-atom shift isomerization in 1-pentyl would be an important competing channel with the decomposition reactions. Jitariu *et. al.*'s theoretical calculation of the 1,4 H-atom shift isomerization in the 1-pentyl radical[21] confirmed the result from Miyoshi *et. al.*[10]. Figure 6.1 shows

the energy diagram and reaction pathways of the 1-pentyl radical based on the theoretical work by Jitariu *et. al.* [21]. Manion *et. al.* studied the thermal decomposition of 1-pentyl radical between 80 to 680 kPa and 833 to 1130 K by using the shock tube technique.[11] The product branching ratios of ethene and propene were determined to be in the range of 3 to 5 under the experimental conditions and the ethene product was dominant especially at higher temperature and pressure. The propene product was due to cleavage of the allylic C-C bond in the 2-pentyl radical, indicating that the competing isomerization channel is important in the decomposition of 1-pentyl radical. The ethene and propene products formed can be related to the concentration of the 1-pentyl and 2-pentyl radicals. The dissociation channels are shown below based on Jitariu *et. al.*'s theoretical work:[21]

$$1\text{-}C_5H_{11} \rightarrow H + 1\text{-}C_5H_{10} \qquad \Delta H_{r,0} = 35.0 \text{ kcal/mol}$$

$$\rightarrow H + 2\text{-}C_5H_{10} \qquad \Delta H_{r,0} = 33.0 \text{ kcal/mol}$$

$$\rightarrow C_2H_4 + n\text{-}C_3H_7 \qquad \Delta H_{r,0} = 28.8 \text{ kcal/mol}$$

$$\rightarrow CH_3 + 1\text{-}C_4H_8 \qquad \Delta H_{r,0} = 26.2 \text{ kcal/mol}$$

$$\rightarrow C_2H_5 + C_3H_6 \qquad \Delta H_{r,0} = 25.8 \text{ kcal/mol}$$

Based on the potential energy diagram, 1-pentyl radical could undergo cleavage of the β C-H bond to produce the 1-pentene + H products or allylic C-C bond fission leading to the *n*-propyl + ethene products. A second dissociation pathway to the 1-pentene + H

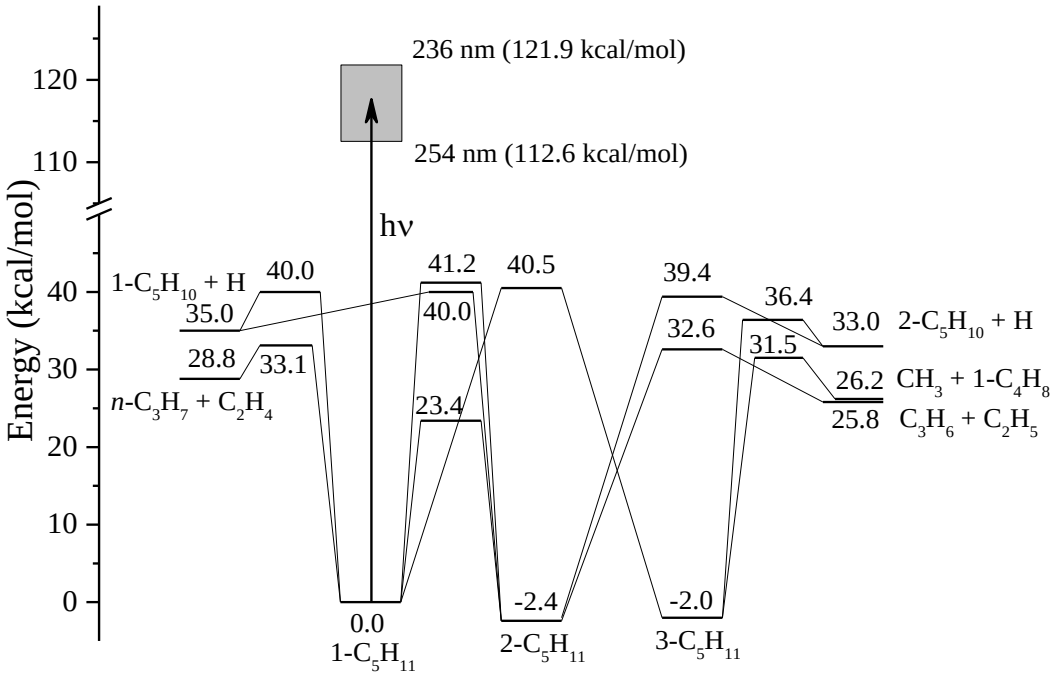

Figure 6.1. Potential energy diagram of the 1-pentyl dissociation channels. The energies and reaction pathways are based on the theoretical calculations by Jitariu *et. al.* (Ref. 21).

products is via isomerization of the 1-pentyl to 2-pentyl first, then followed by dissociation of the 2-pentyl radical. The isomerization of 1-pentyl to 2-pentyl radical has two pathways, 1,2 H-shift via a three-member ring transition state (energy barrier of 41.2 kcal/mol) and 1,4 H-shift with a five-member ring transition state (energy barrier of 23.4 kcal/mol), while the isomerization from 1-pentyl to 3-pentyl radical has one pathway via a four-member ring translation state (energy barrier of 40.5 kcal/mol), as shown in Figure 6.1.[21] Two dissociation pathways lead to the 2-pentene + H products: (i) isomerization of 1-pentyl to 2-pentyl then dissociation to 2-pentene + H, and (ii) isomerization of 1-pentyl to 3-pentyl followed by dissociation to 2-pentene + H. $C_2H_5 + C_3H_6$ products could be formed from the dissociation of 2-pentyl radical after isomerization from 1-pentyl. The 1-pentyl could also isomerize to 3-pentyl then followed by unimolecular dissociation to produce CH_3 + 1-C_4H_8. The C-C bond scission of 2-pentyl and 3-pentyl product channels were confirmed by thermal decomposition studies with single-pulse shock tube technique.[22]

The UV photodissociation dynamics investigation of 1-pentyl radical is limited, while there have been a few studies on other small *n*-alkyl radical such as ethyl[23-25], *n*-propyl[26,27] and *n*-butyl[28,29] radicals. The β-H atom elimination of ethyl and propyl radicals were confirmed by using partially deuterated precursors.[24,27] The studies on the photodissociation of ethyl radical via 3s Rydberg state revealed bimodal product translational energy distribution and energy-dependence angular distribution of the H + ethene products and two dissociation pathways.[24,25] At the 3s Rydberg excited state, the ethyl radical decays via a non-classical H-bridged structure producing a fast and anisotropic channel with the direct, prompt H-atom elimination and a slow and isotropic

product channel from the unimolecular dissociation of the internally hot radical after the internal conversion to the ground electronic state.[24,25,30] The H-atom loss channels in the photodissociation of the *n*-propyl[27] and *n*-butyl[28] radicals via the 3s Rydberg state also have bimodal product translational energy distribution and angular distribution. The dissociation mechanism of the H-atom loss in the photodissociation of *n*-propyl and *n*-butyl radicals is proposed to be a direct, prompt dissociation coupling the Rydberg state and the repulsive part of the radical ground state surface with a large product translational energy release and anisotropic product angular distribution and a unimolecular dissociation of the internally excited radical on the ground electronic state after internal conversion with a small translational energy release and isotropic angular distribution.

This current work reports the study on the H-atom loss photodissociation dynamics of the jet-cooled 1-pentyl radical in the UV region of 236–254 nm. The H-atom photofragment yield (PFY) spectrum was obtained, revealing the UV absorption feature of the 1-pentyl radical for the first time. The product translational energy and angular distribution of the H + C_5H_{10} channel were obtained from the H-atom time-of-flight (TOF) spectra, and the photodissociation mechanism of the H-loss channel of the 1-pentyl radical was investigated.

6.2 Experimental

The high-*n* Rydberg time-of-flight (HRTOF) technique was employed in this study, and the details of this technique and experimental setups have been described in previous

publications.[24,27,31] The 1-pentyl radical molecular beam was formed by photolysis of 1-nitropentane precursor (Aldrich 97%) in He carrier gas in front of a pulsed nozzle with a 193 nm radiation from an ArF excimer laser. The 1-pentyl radicals produced from the photolysis were cooled down by supersonic expansion in the molecular beam. In the reaction chamber, the 1-pentyl radicals were photodissociated by a tunable linearly polarized UV radiation (236-254 nm, 1.2-2.4 mJ/pulse). A Fresnel-Rhomb achromatic λ/2 plate was used to rotate the polarization of the photolysis radiation for the product angular distribution measurements. The H atoms produced from the photodissociation were pumped by two-color resonant excitation (121.6 nm + 366.3 nm), *i.e*, from 1^2S to 2^2P via the H-atom Lyman-α transition and then to a metastable high-*n* Rydberg state. A fraction of the high-*n* Rydberg state H atoms drifted with their nascent velocities to a microchannel plate (MCP) detector installed perpendicular to the molecular beam and the metastable H atoms were field-ionized in front of the detector and detected. The distance of the flight path was calibrated to be 37.06 cm by photodissociation of HBr at 236 nm with the spin-orbit splitting energy of $Br(^2P_{3/2})$ and $Br(^2P_{1/2})$ and the HBr bond dissociation energy. The ion signals were amplified by a fast preamplifier and averaged by a multichannel scaler to collect the H-atom product TOF spectra.

6.3 Results

The H-atom TOF spectra of the photodissociation of the 1-pentyl radical (from 1-nitropentane precursor) were taken in the UV photolysis wavelength region of 236 to 254

nm with the polarization of the photolysis radiation parallel and perpendicular to the TOF axis. For background removal, the H-atom TOF spectra of the photodissociation of the 1-nitropentane precursor were also taken (with the 193-nm radical production photolysis laser off) in the UV photolysis wavelength region of 236 to 254 nm. The net H-atom TOF spectra were obtained after proper background subtractions (with the radical production photolysis laser on minus off). In Figure 6.2, the open circles (○) in (a) and (b) show the net H-atom TOF spectra of the photodissociation of the 1-pentyl radical at 240 nm after proper background subtraction with the polarization of the photolysis parallel (∥, θ = 0°) and perpendicular (⊥, θ = 90°) to the TOF path. The power of the photolysis radiation was kept in the region of 1.2 – 2.4 mJ/pulse, and the H-atom signal had a linear dependence on the photolysis laser power. Both TOF spectra show a peak at ~17 μs and the parallel spectrum has a stronger signal at the peak. In the longer flight time region, both the spectra have an identical broad feature but with large noise.

The H-atom photofragment yield (PFY) spectrum (action spectrum) of the 1-pentyl radical was obtained by integrating the net H-atom TOF spectra from photodissociation of 1-pentyl as a function of photolysis wavelength. All the integrated signals were normalized to that at 240 nm with the same photolysis power and laser shots. Figure 6.3 shows the H-atom PFY spectrum of 1-pentyl in the region of 236–254 nm, with a broad feature peaking around 245 nm. There is no 1-pentyl UV absorption spectrum reported yet. Other primary alkyl radicals such as ethyl[32,33] and *n*-propyl[27,34] radicals show a strong absorption at ~ 245 nm which are assigned to the 3s Rydberg state via the $2p_z \rightarrow 3s$ transition. As the β substitution by an alkyl group on the ethyl would not change the electronic state

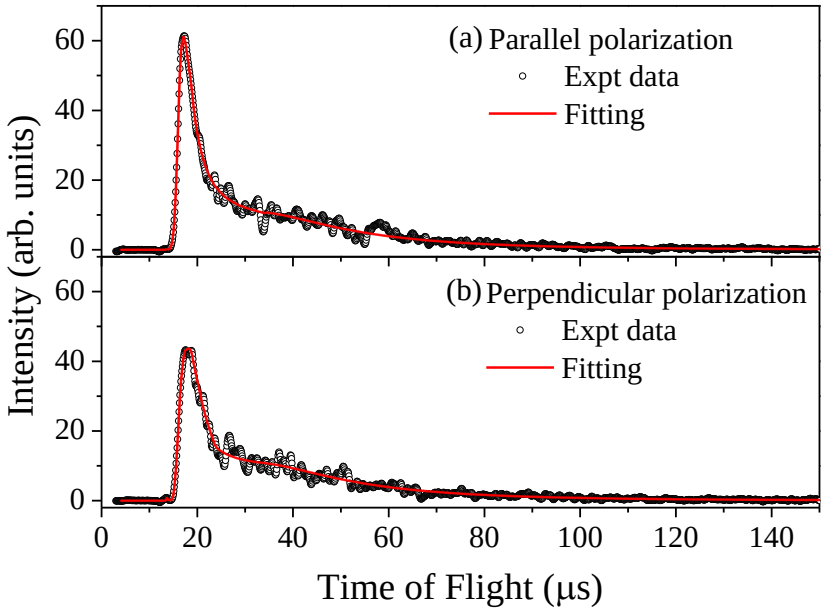

Figure 6.2. H-atom TOF spectra of photodissociation of jet-cooled 1-pentyl radical with 240 nm photolysis radiation. The 1-pentyl radical was formed by photolysis of the 1-nitropentane precursor at 193 nm. (a) TOF spectra with the polarization of the linearly polarized photolysis radiation parallel (∥, $\theta = 0°$) to the flight path. (b) TOF spectra with the polarization of the photolysis radiation perpendicular (⊥, $\theta = 90°$) to the flight path. The laser power and laser shots are normalized to the same scale. For both figures, the open circles (○) represent experimental data and the solid lines are forward convolution fittings for the experimental TOF spectra.

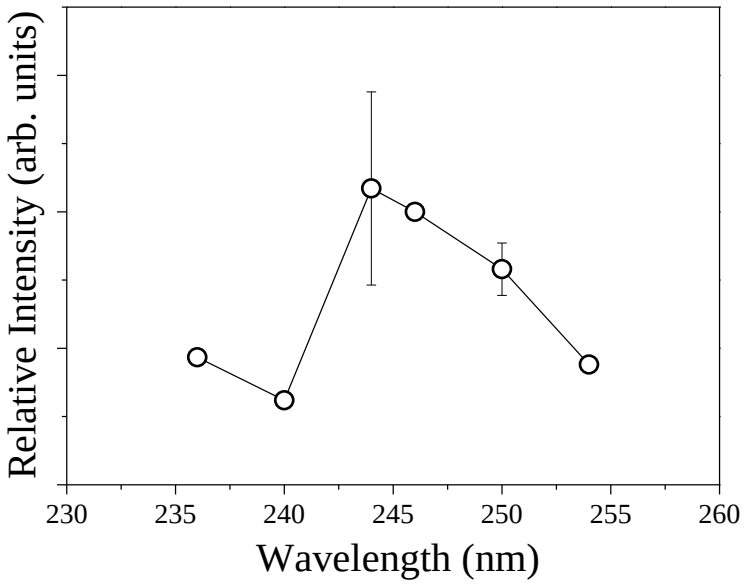

Figure 6.3. H atom photofragment yield (PFY) spectrum of 1-pentyl radical as a function of the photolysis wavelength in the region of 236 – 254 nm. Open circles (○) are the integrated HRTOF signals of the 1-pentyl by using the 1-nitropentane precursor. All the signals are normalized to the same laser shots and power. The error bars indicate the 95% confidence limit from multiple measurements.

significantly because of the localized Rydberg excitation on the radical center,[32,33] the peak at 245 nm in the H-atom PFY spectrum of 1-pentyl could also be due to the $2p_z \rightarrow 3s$ Rydberg state transition as well. The H-atom PFY spectrum reveals the UV absorption features of the 1-pentyl radical for the first time.

The center-of-mass (CM) product translational energy distributions, $P(E_T)$'s, of the H + C_5H_{10} product channel can be derived from the H-atom TOF spectra of the 1-pentyl radical. The CM translational energy of the products, E_T, is derived from the flight time of the H atom t_H base on the following equation:[27,35-37]

$$E_T = \left(1 + \frac{m_H}{m_{C_5H_{10}}}\right) E_H + \frac{m_H}{m_{C_5H_{10}}} E_{C_5H_{11}} = \frac{1}{2} m_H \left(1 + \frac{m_H}{m_{C_5H_{10}}}\right) \left(\frac{L}{t_H}\right)^2 + \frac{m_H}{m_{C_5H_{10}}} E_{C_5H_{11}}$$

where E_H and $E_{C_5H_{11}}$ are the laboratory translational energy of the H-atom product and the parent 1-pentyl radical, L is the length of flight. The second term is due to the parent 1-pentyl radical motion in the molecular beam which is perpendicular to the TOF axis, and it is much smaller compared to the first term and can be neglected. Using direct conversion from time to energy,[27,35-37] the product CM translational energy distributions of the H + C_5H_{10} product channel at 240 nm photodissociation wavelength with parallel ($\parallel$, θ = 0°) and perpendicular ($\perp$, θ = 90°) photolysis radiations are derived and shown in Figure 6.4 (a) and (b) in the solid black lines. The $P(E_T)$ distributions can also be derived from modeling the H-atom TOF spectra in a forward-convolution procedure.[38,39] In this modeling process, the H-atom product TOF spectrum is calculated by using a trial $P(E_T)$ distribution convoluted with the instrument and molecular beam functions. The calculated TOF spectrum is iteratively optimized by comparison with the experimental TOF spectrum and readjustment of the trial $P(E_T)$ distribution until an optimized $P(E_T)$ is reached. This

forward-convolution method is helpful when the experimental TOF spectrum is noisy. The forward-convolution fittings for the H-atom product TOF spectra at 240 nm are shown in the red curves in Figure 6.2. The optimized $P(E_T)$ distributions used in the forward-convolution fitting are showed in red lines in Figure 6.4 (a) and (b), and they have a good agreement with the $P(E_T)$ distributions from the direct conversion. The product CM translational energy and the photofragment angular distribution can be described in the equation shown below:[40]

$$P(E_T, \theta) = \left(\frac{1}{4\pi}\right) P(E_T)[1 + \beta P_2(cos\theta)]$$

where $P(E_T)$ is the angle-integrated product translational energy distribution, β is the anisotropy parameter ($-1 \leq \beta \leq 2$), θ is the angle between the electric vector of the linear polarized photolysis radiation and the recoiling velocity of the H-atom product, and $P_2(cos\theta)$ is the second Legendre polynomial. At the parallel polarization,

$$P_{\parallel}(E_T) = \left(\frac{1}{4\pi}\right) P(E_T)(1 + \beta)$$

and at the perpendicular polarization,

$$P_{\perp}(E_T) = \left(\frac{1}{4\pi}\right) P(E_T)(1 - \frac{1}{2}\beta)$$

By combing the $P_{\parallel}(E_T)$ and $P_{\perp}(E_T)$ distributions from the direct conversion and from the forward-convolution process, the CM translational energy distributions at the magic angle (θ = 54.7°), $P_m(E_T) = \left(\frac{1}{4\pi}\right) P(E_T)$, are calculated and shown in Figure 6.5 in solid black line and solid red line, respectively. The $P_m(E_T)$ distribution is proportional to the angle-integrated product translational energy distribution $P(E_T)$. Figure 6.4 (c) shows the translational energy-dependent anisotropy parameter $\beta(E_T)$, which is calculated from the

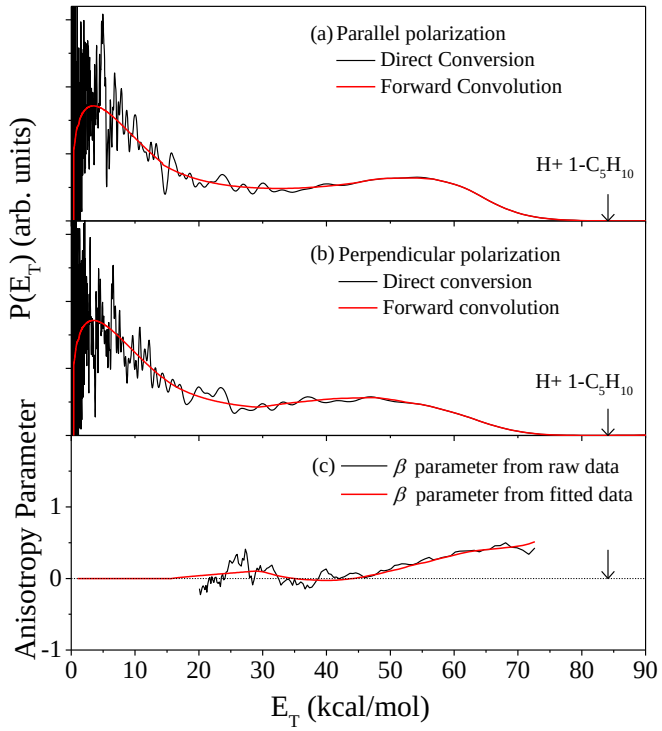

Figure 6.4. Center-of-mass product translational energy distributions, $P(E_T)$'s, of the H-atom product channel from the photodissociation of 1-pentyl radical at 240 nm with the linearly polarized photolysis radiation (a) parallel and (b) perpendicular to the TOF path and (c) the translational energy dependence anisotropy parameter $\beta(E_T)$. In (a) and (b), the $P(E_T)$ distributions are converted from the H-atom TOF spectra and are scaled with the same laser shots and power. The black lines are the $P(E_T)$'s and $\beta(E_T)$ from the direct conversion of the H-atom TOF spectra and the red curves are based on the forward-convolution fitting. The arrows indicate the maximum available energy for the H + 1-pentene product channel at 240 nm.

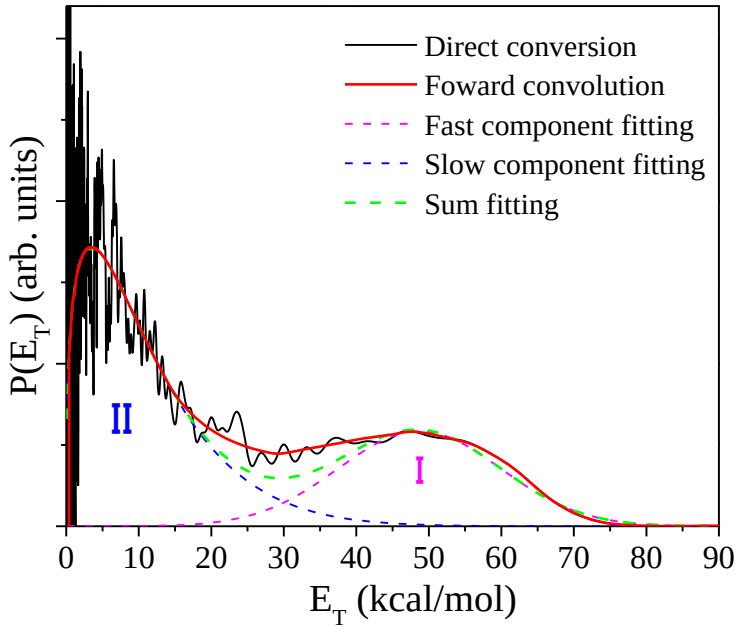

Figure 6.5. Center-of-mass product translational energy distributions of the H-atom product channel from the photodissociation of 1-pentyl radical at 240 nm with the linearly polarized photolysis radiation at the magic angle (θ = 54.7°), $P_m(E_T)$'s. The $P_m(E_T)$ distributions are obtained by combining the $P_{\parallel}(E_T)$ and $P_{\perp}(E_T)$ distributions from Figure 6.4; the solid black line is for $P_m(E_T)$ from the direct conversion and the red solid line is from the forward convolution. The magic-angle $P_m(E_T)$ distributions are de-convoluted and fitted with a fast component, $P_I(E_T)$ (pink dashed line), and slow component, $P_{II}(E_T)$ (blue dashed line); the summed fitting from $P_I(E_T)$ and $P_{II}(E_T)$ is shown in the green dashed line.

translational energy distributions with parallel and perpendicular polarization with $\beta(E_T) = 2\times[P_{\parallel}(E_T) - P_{\perp}(E_T)]/ [P_{\parallel}(E_T) + 2P_{\perp}(E_T)]$; the black line is from the raw data and the red line is based on the forward-convolution distributions.

The CM product translational energy distributions with parallel and perpendicular polarization show two peaks, with the slow one at ~ 5 kcal/mol and the fast one at ~ 50 kcal/mol and extending to the maximum available energy of the H + 1-pentene ($CH_2CHCH_2CH_2CH_3$) products channel (84.1 kcal/mol at 240 nm photolysis wavelength). The anisotropy parameter β is about 0 (with large noise) when E_T < 40 kcal/mol and increases to a maximum value of 0.4 ± 0.1 at a large E_T value of ~ 70 kcal/mol. The different β values indicate at least two dissociation channels. In Figure 6.5, two Rice-Ramsperger-Kassel (RRK)-type functions, $P(E_T) = A(E_T)^p(E_0 - E_T)^q$, are used to deconvolute the $P_m(E_T)$ into a fast and slow components part.[27] A, p, and q are variable parameters, and E_0 is 84.1 kcal/mol for the fast component and adjustable for the slow component.[27] The two fitted components (I for the fast one and II for the slow one) are shown in Figure 6.5. Based on the fitting, the average translational energy release, $\langle E_T \rangle$, and the fraction of the average translational energy in the total available energy, $\langle f_T \rangle$, can be calculated for each component. For the fast channel (I), $\langle E_T \rangle$ = 48.7 kcal/mol and $\langle f_T \rangle$ = 0.58; and for the slow channel (II), $\langle E_T \rangle$ = 11.1 kcal/mol and $\langle f_T \rangle$ = 0.13, respectively. The overall $\langle f_T \rangle$ value the H-loss product channel is 0.30. The integrated signals of component I and II give the branch ratio of the fast to slow component of ~ 0.6.

6.4 Discussions

The UV photodissociation dynamics of the jet-cooled 1-pentyl radial was investigated in the wavelength region of 236–254 nm for the first time. The H-atom product channels were observed from the H-atom TOF spectra. While there has been no UV absorption spectrum of the 1-pentyl radical reported before, the H-atom PFY spectrum showed a broad UV absorption feature peaking near 245 nm in the region of 236 to 254 nm for the first time. The UV absorption spectra of the ethyl and *n*-propyl radicals were observed with a peak at ~ 245 nm and the theoretical study assigned this peak to be the 3s Rydberg state via the $2p_z \rightarrow 3s$ transition.[27,32-34] The 1-pentyl PFY spectrum peaking at ~ 245 nm would be assigned to the 3s Rydberg state via the $2p_z \rightarrow 3s$ transition as well. Furthermore, similar to the photodissociation of other primary alkyl radicals via the 3s Rydberg state, the $P(E_T)$ distribution and $\beta(E_T)$ of the photodissociation of the 1-pentyl radical show a bimodal distribution (more discussion in the following). The fast component with a positive β parameter and the slow component with an isotropic angular distribution indicate two distinct dissociation pathways in the photodissociation of the 1-pentyl radical. This photodissociation dynamic information is also consistent with the $2p_z \rightarrow 3s$ Rydberg state excitation observed in the H-atom PFY spectrum of 1-pentyl in the region of 236 to 254 nm.

The CM translational energy distribution has a broad feature (the fast component) at ~ 50 kcal/mol and extending to the maximum available for the H + 1-pentene product channel. The $\langle f_T \rangle$ value for this fast component is 0.58, supporting a non-statistical

dissociation mechanism, and the β value of 0.4 indicates that the dissociation time scale is shorter than one rotational period of the 1-pentyl radical (~ 10 ps). The dissociation mechanism for the fast component would be a direct, prompt dissociation of the electronic excited 1-pentyl radical on a repulsive potential energy surface to the ground state product probably via a conical intersection, coupling the 3s Rydberg state and the repulsive part of the ground state. The positive anisotropy parameter indicates that the velocity vector of the H-atom product is close to a parallel direction with respect to the $2p_z \rightarrow 3s$ transition dipole moment. In going from ethyl to 1-pentyl, the β-substitution by an alkyl group would not change the Rydberg electronic transition of the primary alkyl radicals significantly, as the localized $2p_z \rightarrow 3s$ Rydberg excitation is mainly on the radical center.[32,33] As in other *n*-alkyl radicals, the $2p_z$ orbital is perpendicular to the α-CHH plane, and a β-CC bond or a β-CH bond is eclipsed to the $2p_z$ orbital to form two lowest energy conformers of the 1-pentyl radical, with the β-CH eclipsed conformer having a lower energy of about 0.1 kcal/mol.[41] The elimination of the eclipsed β-H atom would create another $2p_z$ orbital on the β-carbon which is parallel to the $2p_z$ orbital of the radical center and then form the π bond in the ground state of the 1-pentene product; the ejection of the β-H atom along the eclipsed CH bond will result in a positive anisotropy parameter, which is consistent with the experimental observation. The mechanism for the fast component would be the direct, prompt cleavage of the β-CH bond that is eclipsed to the $2p_z$ orbital of the 1-pentyl radical on a repulsive excited state surface and/or on a repulsive part of the ground state surface of 1-pentyl to produce the H atom and the ground state 1-pentene.

The anisotropy parameter β is around 0 for the slow component (II) with a small CM translational energy release (E_T < 40 kcal/mol), indicating another dissociation channel of the 1-pentyl radical to the H + C_5H_{10} products, and the dissociation time scale is longer than one rotation period of the 1-pentyl radical (~ 10 ps). The $P(E_T)$ distribution of the slow component peaks at ~ 5 kcal/mol with the average translational energy release $\langle f_T \rangle$ of ~ 0.13, showing a typical statistical energy distribution in the unimolecular dissociation. The slow component is consistent with unimolecular dissociation of the internally hot 1-pentyl radical on the ground electronic state after internal conversion from the electronic excited state. Based on the ground state potential energy diagram shown in Figure 6.1, the pentyl system has multiple minima: 1-pentyl can isomerize to 2-pentyl via a 1,4 H-shift over the energy barrier of 23.4 kcal/mol or to 3-pentyl via a 1,3 H-shift over the energy barrier of 40.5 kcal/mol. The C-C bond fissions such as *n*-C_3H_7 + C_2H_4 have the lowest dissociation energy barriers, but our experimental technique could only detect the H-atom product channels. As the isomerization barrier of 1-pentyl to 2-pentyl is lower than the barriers of the β H atom eliminations to the H + 1-pentene products from 1-pentyl and 2-pentyl, the H + 1-pentene product channel could occur from both the 1-pentyl and 2-pentyl radicals. Among the H-atom loss product channels, the H + 1-pentene product channel from the 1-pentyl radical has overall a low energy barrier and requires no additional isomerization step, and thus this pathway could be more likely. The peak of ~ 5 kcal/mol in the $P(E_T)$ distribution is consistent with the 5 kcal/mol exit channel barrier of the unimolecular dissociation of 1-pentyl to the H + 1-pentene products. The H-elimination of the 2-pentyl radical after the isomerization from the 1-pentyl radical could create H + 1-pentene and H

+ 2-pentene, and the unimolecular dissociation of the 3-pentyl radical to H + 2-pentene should have a smaller probability due to the higher isomerization energy barrier from 1-pentyl radical.

6.5 Conclusion

The UV photodissociation of the 1-pentyl radical via the 3s Rydberg state was studied in the UV region of 236–254 nm. The H-loss channel was confirmed directly from the H-atom TOF spectra, and the H-atom photofragment yield spectrum revealed the UV absorption feature of the 1-pentyl radical for the first time. The H-atom product translational energy release and angular distribution have a bimodal distribution. The slow component peaks at ~ 5 kcal/mol and has an isotropic distribution, while the fast component peaks at ~ 50 kcal/mol and has an anisotropic angular distribution. The fraction of the average CM product translational energy release in the total available energy is about 0.30, and the branching ratio of the fast to the slow component is 0.6. The bimodal product translational energy distribution and angular distribution suggest two dissociation channels in the photodissociation of the 1-pentyl radical; (i) a direct, prompt H-atom elimination on the repulsive potential energy surface of the electronic excited state and/or the repulsive part of the ground electronic state; and (ii) a unimolecular dissociation of the hot 1-pentyl radical on the ground electronic state after the internal conversion from the excited state.

Reference

1. J. Warnatz, *Combustion Chemistry* (Springer New York, 1984).

2. C. K. Westbrook and F. L. Dryer, *Progr. Energy Combust. Sci.* **10**, 1 (1984).

3. A. S. Gordon and J. R. McNesby, *J. Chem. Phys.* **31**, 853 (1959).

4. C. P. Quinn, *Trans. Faraday Soc.* **59**, 2543 (1963).

5. L. Endrenyi and D. J. L. Roy, *J. Phys. Chem.* **70**, 4081 (1966).

6. K. Watkins and D. Lawson, *J. Phys. Chem.* **75**, 1632 (1971).

7. D. V. Dearden and J. L. Beauchamp, *J. Phys. Chem.* **89**, 5359 (1985).

8. R. M. Marshall, *Int. J. Chem. Kinet.* **22**, 935 (1990).

9. N. Yamauchi, A. Miyoshi, K. Kosaka, M. Koshi, and H. Matsui, *J. Phys. Chem. A* **103**, 2723 (1999).

10. A. Miyoshi, J. Widjaja, N. Yamauchi, M. Koshi, and H. Matsui, *Proc. Combust. Inst.* **29**, 1285 (2002).

11. I. A. Awan, D. R. Burgess, and J. A. Manion, *J. Phys. Chem. A* **116**, 2895 (2012).

12. A. Comandini, I. A. Awan, and J. A. Manion, *Chem. Phys. Lett.* **552**, 20 (2012).

13. W. Tsang, V. Bedanov, and M. R. Zachariah, *Ber. Bunsen-Ges. Phys. Chem.* **101**, 491 (1997).

14. B. Bankiewicz, L. K. Huynh, A. Ratkiewicz, and T. N. Truong, *J. Phys. Chem. A* **113**, 1564 (2009).

15. C. J. Hayes and D. R. Burgess, *J. Phys. Chem. A* **113**, 2473 (2009).

16. J. Zheng and D. G. Truhlar, *J. Phys. Chem. A* **113**, 11919 (2009).

17. A. C. Davis and J. S. Francisco, *J. Phys. Chem. A* **115**, 2966 (2011).

18. T. Yu, J. Zheng, and D. G. Truhlar, *Chem. Sci.* **2**, 2199 (2011).

19. A. S. Gordon, D. C. Tardy, and R. Ireton, *J. Phys. Chem.* **80**, 1400 (1976).

20. T. Gierczak, J. Gawłowski, and J. Niedzielski, *React. Kinet. Catal. Lett.* **36**, 435 (1988).

21. L. C. Jitariu, L. D. Jones, S. H. Robertson, M. J. Pilling, and I. H. Hillier, *J. Phys. Chem. A* **107**, 8607 (2003).

22. J. A. Manion and I. A. Awan, *Proc. Combust. Inst.* **34**, 537 (2013).

23. T. Gilbert, T. L. Grebner, I. Fischer, and P. Chen, *J. Chem. Phys.* **110**, 5485 (1999).

24. G. Amaral, K. Xu, and J. Zhang, *J. Chem. Phys.* **114**, 5164 (2001).

25. M. Steinbauer, J. Giegerich, K. H. Fischer, and I. Fischer, *J. Chem. Phys.* **137**, 014303 (2012).

26. Z. Min, R. Quandt, and R. Bersohn, *Chem. Phys. Lett.* **296**, 372 (1998).

27. Y. Song, X. Zheng, W. Zhou, M. Lucas, and J. Zhang, *J. Chem. Phys.* **142**, 224306 (2015).

28. B. Negru, G. M. P. Just, D. Park, and D. M. Neumark, *Phys. Chem. Chem. Phys.* **63**, 919 (1975).

29. F. J. Adrian, V. A. Bowers, and E. L. Cochran, *J. Chem. Phys.* **63**, 919 (1975).

30. J. M. Hostettler, A. Bach, and P. Chen, *J. Chem. Phys.* **130**, 034303 (2009).

31. W. Zhou, Y. Yuan, and J. Zhang, *J. Chem. Phys.* **119**, 9989 (2003).

32. B. H. Lengsfield, P. E. M. Siegbahn, and B. Liu, *J. Chem. Phys.* **81**, 710 (1984).

33. H. R. Wendt and H. E. Hunziker, *J. Chem. Phys.* **81**, 717 (1984).

34. H. Adachi and N. Basco, *Int. J. Chem. Kinet.* **13**, 367 (1981).

35. K. Xu, G. Amaral, and J. Zhang, *J. Chem. Phys.* **111**, 6271 (1999).

36. Y. Song, M. Lucas, M. Alcaraz, J. Zhang, and C. Brazier, *J. Phys. Chem. A* **119**, 12318 (2015).

37. M. Lucas, Y. Song, J. Zhang, C. Brazier, P. L. Houston, and J. M. Bowman, *J. Phys. Chem. A* **120**, 5248 (2016).

38. X. X. Zhao, *Ph.D Dissertation*, Berkeley: University of California, (1988).

39. J. Zhang, M. Dulligan, and C. Wittig, *J. Phys. Chem*. **99**, 7446 (1995).

40. R. N. Zare, *Mol. Photochem*. **4**, 1 (1972).

41. J. Pacansky, R. J. Waltman, and L. A. Barnes, *J. Phys. Chem*. **97**, 10694 (1993).

Chapter 7

H-atom Product Channels in the Ultraviolet Photodissociation of the 2-Propenyl Radical

Abstract

The H-atom product channels in the ultraviolet photodissociation of 2-propenyl (CH_2CCH_3) radical were investigated in the wavelength region of 224-248 nm using photofragment translational spectroscopy. The CH_2CCH_3 radicals were generated by 193-nm photodissociation of 2-chloropropene and 2-bromopropene precursors. The H-atom photofragment yield spectra from both precursors revealed a broad feature peaking near 232 nm. The translational energy distributions of the H + C_3H_4 products peaked around 7-8 kcal/mol and extended close to the maximum excess energy. The fraction of the total available energy released as products' translation was nearly a constant (~ 0.16 using the 2-chloropropene precursor and ~ 0.18 using the 2-bromopropene precursor) in the wavelength range of 224-248 nm. The angular distribution of the H-atom product was isotropic. Quasi-classical trajectory (QCT) calculations were performed on the ground-state potential energy surface of CH_2CCH_3 for its decomposition at a 124 kcal/mol excitation energy (equivalent to 230 nm photolysis photon energy). The calculations yielded branching ratios for different dissociation product channels, 32% H + allene, 35% H + propyne, 0.5% H + cyclopropene, and 32% methyl + acetylene. The experimental and

QCT translational energy distributions of the H-atom loss channels qualitatively agreed, consistent with the main H-atom product channels being the H + allene and H + propyne dissociations. The time scale of the 2-propenyl dissociation on the ground electronic state was calculated to be ~ 2 ps, smaller compared to that of the overall UV photodissociation (≥ 10 ps, implied on the basis of the isotropic H-atom product angular distribution). The mechanism of the UV photodissociation of 2-propenyl is consistent with unimolecular dissociation proceeding on the ground electronic state after internal conversion of the electronic excited states.

7.1 Introduction

The chemical species C_3H_5 has four isomers, cyclopropyl (c-C_3H_5), allyl (CH_2CHCH_2), 1-propenyl ($CHCHCH_3$), and 2-propenyl (CH_2CCH_3). Cyclopropyl is the smallest cyclic alkyl radical, while the other three are alkenyl radicals with π electrons. The allyl radical is a π conjugated system with three sp^2 hybridized carbon atoms and three unpaired π electrons that are resonance-delocalized. The 1-propenyl and 2-propenyl radicals are vinyl radicals with a β H atom or α H atom replaced by a CH_3 group, respectively. The alkenyl C_3H_5 radicals are important reactive intermediates in combustion processes, such as the formations of aromatic hydrocarbons and polycyclic aromatic hydrocarbons.[1-10] The four isomers of C_3H_5 provide a good system to investigate *isomer-specific* photochemistry. Photodissociation can be initiated from different isomers (local minima of the global ground-state potential energy surface (PES)) and access different parts of the excited-state surfaces and dissociation dynamics. We have previously reported the photodissociation dynamics of the allyl and 1-propenyl radicals in the UV region of 220-250 nm.[11,12] This current study aims to explore the UV photodissociation dynamics of the 2-propenyl radical, the third isomer in the alkenyl C_3H_5 series.

Among the three alkenyl isomers, the allyl radical has been extensively examined.[13-21] The first absorption band of the allyl radical is via the $\tilde{A}^2B_1 \leftarrow \tilde{X}^2A_2$ transition in the region of 370-410 nm.[13,19] In the ultraviolet (UV) region of 210-250 nm, allyl has a strong absorption feature with diffuse structure that is attributed to four Rydberg electronic states, $\tilde{B}^2A_1$ (3s) (250 nm), $\tilde{C}^2B_2$ ($3p_y$) (241 nm), $\tilde{D}^2A_1$ ($3p_z$) (237 nm), and

$\tilde{E}^2B_1$ ($3p_x$) (231 nm).[14-18,20,21] The electronic excited states and spectroscopy of the 1-propenyl and 2-propenyl radicals were less studied. Theoretical calculations using equation-of-motion coupled cluster methods indicated that the two propenyl radicals have similar electronic structures due to their vinyl moiety, and predicted that 1-propenyl has electronically excited states $\tilde{A}^2A''$ (n ← π, 408 nm (vertical excitation)), $\tilde{B}^2A''$ (π^* ← n, 242 nm), $\tilde{C}^2A'$ (π^* ← π, 221 nm), and $\tilde{D}^2A'$ (3s ← n, 202 nm), and 2-propenyl has $\tilde{A}^2A''$ (n ← π, 377 nm), $\tilde{B}^2A''$ (π^* ← n, 255 nm), $\tilde{C}^2A'$ (π^* ← π, 221 nm), and $\tilde{D}^2A'$ (3s ← n, 218 nm).[22] The H-atom photofragment yield (PFY) spectra of 1-propenyl revealed a broad UV absorption structure peaking at 230 nm in the photodissociation study of 1-propenyl,[12] possibly due to the excited $\tilde{B}^2A''$ or $\tilde{C}^2A'$ state.

The potential energy diagram and dissociation pathways of the C_3H_5 system are shown in Figure 7.1.[9,23] The allyl radical is the most stable isomer (at the global minimum, GM), while 1-propenyl (local minimum, LM2) and 2-propenyl (LM1) are at higher energies. There are three possible H-atom-elimination channels, H + CH_2CCH_2 (allene), H + CH_3CCH (propyne), and H + c-C_3H_4 (cyclopropene), and two CH_3-elimination channels, CH_3 + C_2H_2 (acetylene) and CH_3 + CCH_2 (vinylidene). The predominant H-atom product channel in the thermal decomposition of allyl is H + allene.[2,24,25] Near-UV photodissociation of allyl via its $\tilde{A}^2B_1$ state mainly produces H + allene from dissociation on the ground electronic state after internal conversion,[24,25] with an isotropic product angular distribution and small kinetic energy release. The UV photodissociation of allyl via the $\tilde{B}^2A_1$, $\tilde{C}^2B_2$, and $\tilde{E}^2B_1$ excited states in the wavelength range of 216-249 nm has been studied by experiments[11,24,26,27] and theories.[23,24,27,28] The H-atom and

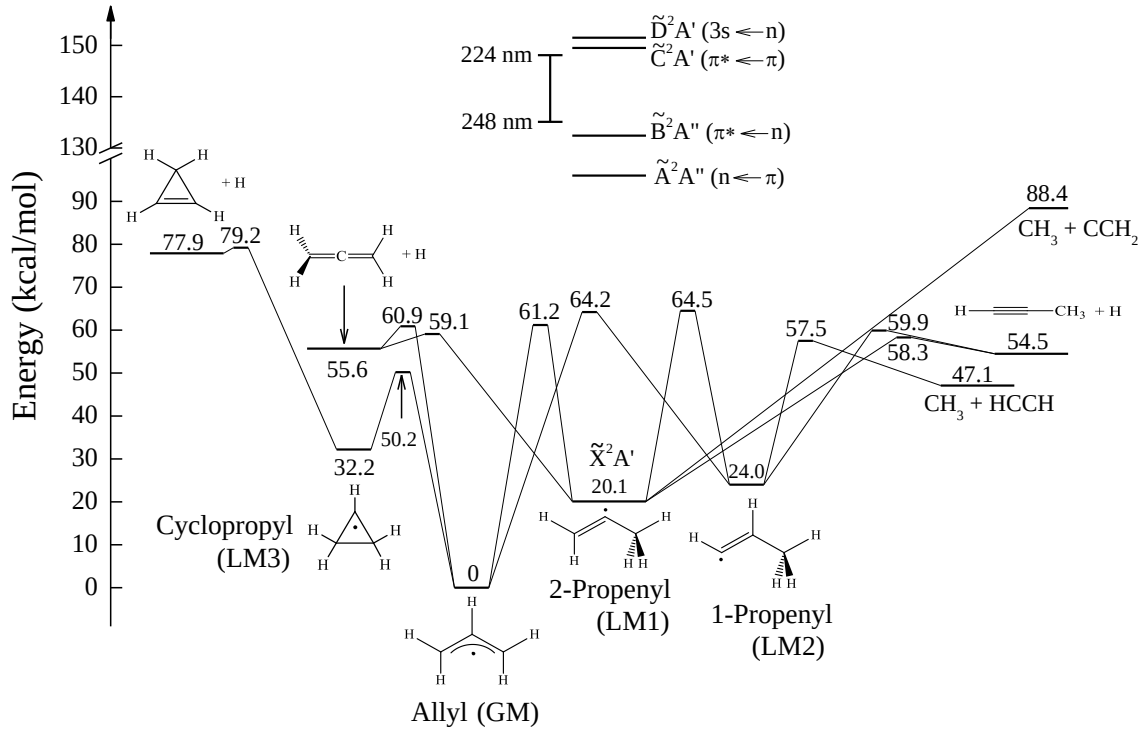

Figure 7.1. Potential energy diagram of the C_3H_5 system. The energies are referenced to that of the most stable isomer, allyl radical (set to be 0). Three H-loss channels and two CH_3-loss channels are shown. The energies (with zeropoint energy corrections) and pathways are from previous theoretical studies (refs 9 and 23). The electronic excited state energies of the 2-propenyl radical are based on theoretical calculation (ref 22). The excitation photon energy of the photolysis wavelength 224 to 248 nm (from the vibrational ground state of LM1) is shown next to the electronic excited states.

CH_3-elimination channels were characterized by experiments and quasi-classical trajectory (QCT) calculations, showing that the H-loss channel is dominant.[23,24,26,27] The allyl radical undergoes internal conversion from the electronically excited states and then unimolecular decomposition on the ground electronic state.[11,23,24,26] The H-loss channel has a modest translational energy release. Its product translational energy distribution $P(E_T)$ peaks around 8.5 kcal/mol. The fraction of the average product kinetic energy release in the total available energy, $\langle f_T \rangle$, is ~ 0.18-0.20 in the UV photolysis wavelength range of 216-249 nm.[11] The H-atom product angular distribution is isotropic. The QCT calculations showed that direct dissociation of allyl to H + allene is the main H-loss channel, and the H + propyne channel is less probable as isomerization of allyl to 1-propenyl or 2-propenyl over higher energy barriers is required before dissociation. The QCT calculated branching ratio of the H + allene to H + propyne channel is ~ 6:1 at the 248 nm (115 kcal/mol) excitation energy.[23]

Compared to allyl, the dissociation dynamics of 1-propenyl and 2-propenyl were not well studied. Niedzielski and co-workers investigated thermal dissociation of internally excited 1-propenyl and 2-propenyl radicals by addition of hot H atoms to allene or propyne (at 22.9 kcal/mol collision energy).[29,30] The hot 1-propenyl radical was observed to mainly dissociate to $CH_3 + C_2H_2$ via C-C bond fission. The Rice–Ramsperger–Kassel–Marcus (RRKM) theory calculation also indicated a minor amount of dissociation to H + propyne and isomerization to allyl and that the alkenyl C_3H_5 radicals are interconnected via isomerizations.[29,30] Butler and co-workers studied the thermal dissociation of 1-propenyl via secondary photodissociation of *cis*-1-bromopropene at 193 nm.[31,32] The $CH_3 + C_2H_2$

dissociation was the main channel, and both H + propyne and H + allene product channels were observed. Lucas *et al.* investigated photolysis of jet-cooled 1-propenyl radical in the UV wavelength region of 224-248 nm, along with QCT calculations at a 124 kcal/mol excitation energy (equivalent to 230 nm).[12] The $P(E_T)$ distribution of the H-elimination products peaks around 8 kcal/mol. The $\langle f_T \rangle$ value is around a constant of ~ 0.12 in the 224-248 nm photolysis wavelength region. QCT calculations showed that dissociation products are 75% CH_3 + C_2H_2, 20% H + propyne, 5% H + allene, and ~ 1% H + c-C_3H_4. The experimental and QCT $P(E_T)$ distributions of the H-loss channel are in a reasonable agreement, consistent with that the main H-loss product channel is H + propyne. The H + allene dissociation channel is less important, as isomerization of 1-propenyl to allyl or 2-propenyl need take place before the C-H bond fission. The H-elimination product channel has an isotropic angular distribution, implying a photodissociation time scale of ≥ 10 ps. Similar to allyl, the mechanism of the UV photodissociation of 1-propenyl is internal conversion followed by dissociation of internally hot radical on the ground electronic state.[33]

The 2-propenyl radical is another local minimum (LM1) in the C_3H_5 system, higher in energy than allyl (GM) but more stable than 1-propenyl (LM2) and connected to allyl and 1-propenyl with energy barriers of 41.1 and 44.4 kcal/mol, respectively. The dissociation channels of 2-propenyl and their energetics are listed in the following (Figure 7.1).[9,23]

$$CH_2CCH_3 \rightarrow H + CH_3CCH, \qquad \Delta H_{rxn,0} = 34.4 \text{ kcal/mol}$$

$$\rightarrow H + CH_2CCH_2, \qquad \Delta H_{rxn,0} = 35.5 \text{ kcal/mol}$$

$\rightarrow H + c\text{-}C_3H_4$, $\Delta H_{rxn,0} = 57.8$ kcal/mol

$\rightarrow CH_3 + C_2H_2$, $\Delta H_{rxn,0} = 27.0$ kcal/mol

$\rightarrow CH_3 + CCH_2$, $\Delta H_{rxn,0} = 68.3$ kcal/mol

The thermal dissociation experiment of internally excited 2-propenyl (at a 22.9 kcal/mol excess energy) by Niedzielski and co-workers indicated that the hot 2-propenyl radical mainly dissociates to H + propyne and to a minor extent to H + allene.[29,30]. The RRKM calculation also showed that isomerization of 2-propenyl to allyl could be significant.[29,30] Butler with co-workers[34,35] and Pratt with co-workers[36,37] studied the secondary decomposition of 2-propenyl in the photodissociation of 2-chloropropene and 2-bromopropene at 193 nm, together with the RRKM calculations. Both groups observed that the H + propyne dissociation was the main H-elimination channel, consistent with its slightly lower energy barrier.[34-36] The Butler group also found that at higher internal energy, the yield of H + allene was ~ 2 times larger than that at lower internal energy.[34,35] The overall decomposition rate of the 2-propenyl radical is $\sim 5 \times 10^6$ s^{-1} at the excess energy of 3 kcal/mol above the dissociation threshold and increases to $\sim 1 \times 10^8$ s^{-1} at 6.2 kcal/mol above the threshold.[36]

In this chapter, the UV photodissociation of jet-cooled 2-propenyl radical was investigated at wavelengths of 224-248 nm for the first time by using the high-*n* Rydberg-atom time-of-flight (HRTOF) technique (photofragment translational spectroscopy). H-atom product TOF spectra from two different precursors (2-chloropropene and 2-bromopropene) were recorded with the linearly polarized UV photolysis laser radiation. The H-atom PFY spectra were measured, showing the UV absorption feature of 2-propenyl

for the first time. The center-of-mass (CM) kinetic energy distributions and the angular distributions of the H + C_3H_4 products were obtained from the H-atom TOF spectra. QCT calculations were performed to compare with the experimental dynamic information on the 2-propenyl dissociation.

7.2 Experimental and Computational Methods

Experiments were carried out using the high-*n* Rydberg-atom time-of-flight (HRTOF) technique, which has been described in previous publications.[11,12,33,38] 2-chloropropene (Aldrich 98%) and 2-bromopropene (Acros Organics > 99%) were employed as precursors of the 2-propenyl radical. The 2-propenyl radical beam was generated by photodissociating a ~ 10% mixture of the precursors in Ar (at a total pressure of ~115 kPa) with an ArF excimer laser (193 nm). The 2-propenyl radicals formed from the photolysis were supersonically cooled and entrained in the molecular beam. Downstream in a high-vacuum chamber, the 2-propenyl radicals were photolyzed by a tunable UV laser beam (224-248 nm, 0.3-1.25 mJ/pulse). The polarization of the linearly polarized UV photolysis laser radiation can be rotated by a Fresnel-Rhomb achromatic λ/2 plate for measurements of product angular distributions. The H-atom products from the photodissociation of the 2-propenyl radicals were pumped by two-color resonant excitation (121.6 nm + 366.3 nm) from 1^2S to 2^2P and then to a metastable high-*n* Rydberg state. The Rydberg H atoms flew away from the interaction region with their nascent velocities. A small portion of them reached a microchannel plate detector and were field-ionized and

detected. The flight distance, *L*, for the H atoms was 37.02 cm (calibrated by photolysis of HBr at 236 nm). The ion signals were amplified by a fast preamplifier and recorded by a multichannel scaler.

To simulate the dissociation of 2-propenyl, QCT calculations were performed by using the *ab initio* ground-state PES. The method was reported in the previous publication,[23] with the assumption that 2-propenyl undergoes unimolecular dissociation on the ground electronic state after internal conversion. The starting geometry of the trajectories was the 2-propenyl (CH_2CCH_3) radical structure (LM1).[23] To compare with the UV photodissociation, a total energy was selected to be 58190 cm^{-1} above LM1 (which has a zero-point energy of 14711 cm^{-1}), corresponding to a 230 nm photoexcitation energy (124 kcal/mol) from the lowest vibrational energy state of the 2-propenyl radical. To examine the dependence on the excitation energy, another simulation was carried out at a lower energy of 48112 cm^{-1} above LM1, corresponding to a 300 nm excitation energy (95 kcal/mol). A total 2300 trajectories for 124 kcal/mol and 2750 for 95 kcal/mol were carried out with steps of 0.120 *fs* for the simulations. From the final frame of each trajectory, the relative product kinetic energy was determined, and the product kinetic energy distributions were accumulated from these trajectories. In each simulation, the trajectories kept tracks of the identities of the different carbons and hydrogens, and the multiple channels for each product were examined and the product branching ratios were obtained. The overall reaction rate was calculated in the following approach: a histogram, $P(i)$, of the number of reacting trajectories (to any product) vs. the reaction time was constructed in the time bin i (width ~ 0.65 ps). The number of unreacted trajectories at any time were

calculated as $N(i) = N_{tot} - \Sigma_i P(i)$. The value ln[N($i$)] and time were then fitted with a linear relationship, whose slope gave the reaction rate constant.

7.3 Results

Vacuum-ultraviolet (λ = 121.6 nm) single-photon ionization time-of-flight mass spectrometry (VUV-SPI-TOFMS) was utilized to characterize the 2-propenyl radicals in the molecular beam. The production of the 2-propenyl radicals from the 193 nm photodissociation of 2-chloropropene and 2-bromopropene was confirmed at m/z 41 in the mass spectra. The allyl radical byproduct was searched using resonance-enhanced multiphoton ionization (REMPI),[33] but no signal was identified, indicating that the photolytically produced 2-propenyl radical did not isomerize to the allyl radical in the molecular beam.[12,21,33] Because the isomerization barrier from 2-propenyl to 1-propenyl is higher than that to allyl,[9,23] the formation of 1-propenyl from isomerization of 2-propenyl in the molecular beam was also unlikely. The H-atom product TOF spectra from the photolysis of jet-cooled 2-propenyl radical were obtained at the wavelengths of 224-248 nm, with the photolysis radiation polarization perpendicular and parallel to the TOF axis. Backgrounds in the H-atom TOF spectra were properly removed, as discussed in the previous publications.[11,12,33,38] The net H-atom product TOF spectra (with the background removed) of 2-propenyl at UV photolysis wavelengths of 230, 232, 238, and 240 nm (with parallel polarization) are shown in Figure 7.2. The photolysis laser power was maintained

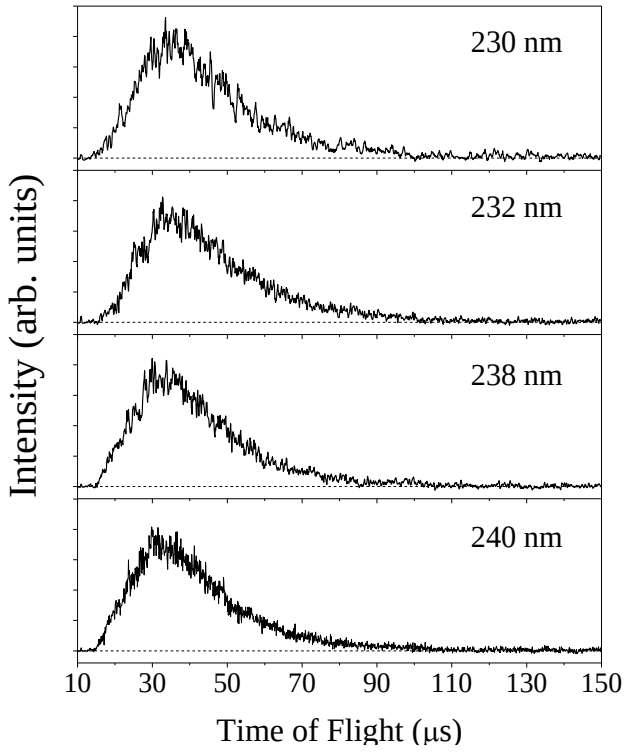

Figure 7.2. H-atom product TOF spectra of jet-cooled 2-propenyl radical at photolysis wavelength of 230, 232, 238, and 240 nm. The 2-propenyl radical was produced from photolysis of 2-chloropropene at 193 nm. These are the net H-atom TOF spectra with the background removed. The polarization of the photolysis radiation was parallel to the TOF axis. Each TOF spectrum was scaled to its maximum intensity.

at low values (0.3 to 1.25 mJ/pulse), and the H-atom signals were shown to depend linearly on the photolysis laser power.

The H-atom PFY spectra of the 2-propenyl radical were acquired by the integration of H-atom signals in the net HRTOF spectra from both precursors as a function of the photodissociation wavelengths. The integrated H-atom signal intensities were normalized by the photolysis laser shots and power and were scaled to those at 232 nm to account for possible drift of the experimental conditions. Figure 7.3 shows the H-atom PFY spectra of the 2-propenyl radical in the region of 224-248 nm from both precursors. The two spectra demonstrate a similar trend (but somewhat different relative intensities) and peak near 232 nm, consistent with that the 2-propenyl radical was the source of the H-atom signals.

The CM translational energy distributions, $P(E_T)$, of the H + C_3H_4 products in the photodissociation of 2-propenyl are derived from the net H-atom product TOF spectra. The H + C_3H_4 product CM translational energy, E_T, is transformed from the H-atom flight time, t_H, in the following equation:

$$E_T = \left(1 + \frac{m_H}{m_{C_3H_4}}\right) E_H = \frac{1}{2} m_H \left(1 + \frac{m_H}{m_{C_3H_4}}\right) \left(\frac{L}{t_H}\right)^2$$

where E_H is the laboratory kinetic energy of the H-atom photoproduct. Figure 7.4 shows the $P(E_T)$ distributions at 230, 232, 238, and 240 nm. These $P(E_T)$s have a broad feature peaking around 7-8 kcal/mol and extending to ~ 70 kcal/mol (close to the maximum excess energy). These distributions show a modest product kinetic energy release. The $\langle f_T \rangle$ values (assuming the lowest energy product channel, H + propyne) in the wavelength range of 224-248 nm from both the 2-chloropropene and 2-bromopropene precursors are in

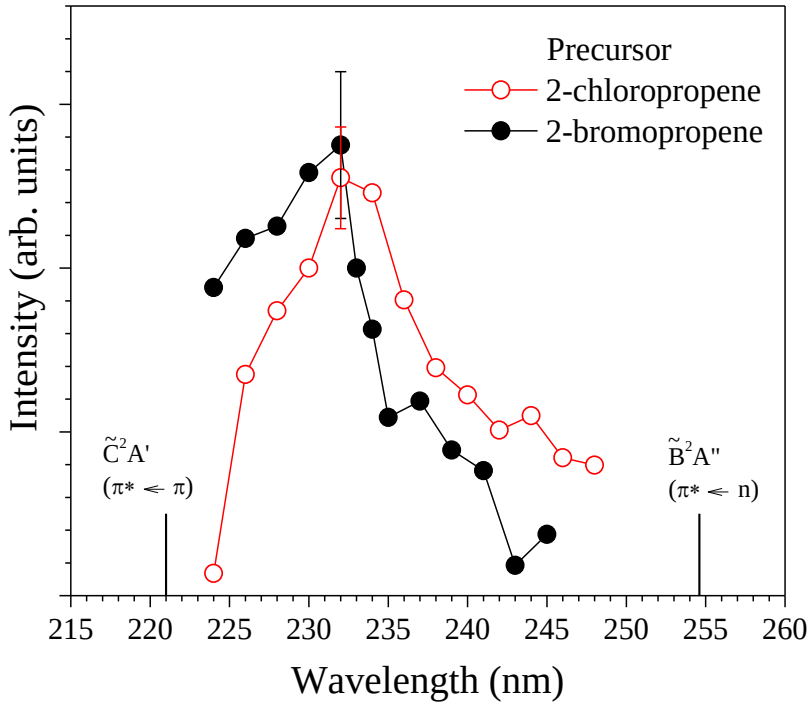

Figure 7.3. H-atom photofragment yield (PFY) spectra of 2-propenyl radical as a function of photolysis wavelength in the region of 224 to 248 nm. Open circles (○) represent the integrated HRTOF signals of 2-propenyl using the 2-chloropropene precursor and the filled circles (•) indicate those from the 2-bromopropene precursor. All the signals were normalized to the same photolysis laser power and number of shots and scaled to the intensity at 232 nm. The error bars indicate the 95% confidence limits from multiple measurements. The vertical excitation energies of the $\tilde{B}^2A''$ and $\tilde{C}^2A'$ states (from ref 22) are marked as vertical lines in the figure.

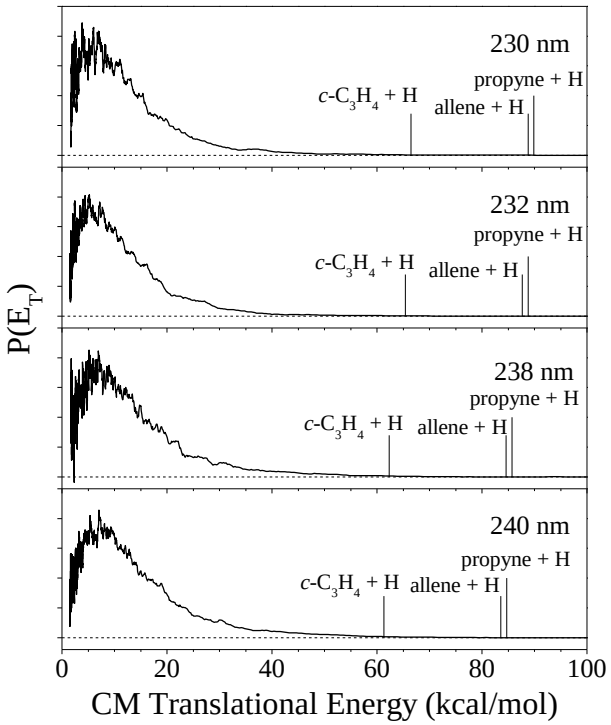

Figure 7.4. Center-of-mass (CM) $P(E_T)$ distribution of the 2-propenyl radical at 230, 232, 238, and 240 nm with the photolysis laser polarization parallel to the TOF path. The 2-propenyl radical was produced from the 2-chloropropene precursor. Each distribution was normalized to its maximum. The maximum translational energies of the three H-loss dissociation channels are marked in the figure as the vertical lines. The energies are based on previous theoretical works (refs 9 and 23).

agreement (Figure 7.5). The $\langle f_T \rangle$'s stay at an average value of ~ 0.16 ± 0.01 using the 2-chloropropene precursor and ~ 0.18 ± 0.01 using the 2-bromopropene precursor. The small $\langle f_T \rangle$ values indicate that the C_3H_4 product is highly internally excited and are consistent with a hot radical unimolecular dissociation mechanism.

The H-atom product TOF spectra from the 232 nm photolysis at both perpendicular and parallel polarizations are presented in Figure 7.6. These two TOF spectra were identical and showed an isotropic angular distribution. The photoproduct angular distribution is related in the following equation:[39]

$$I(\theta) = \left(\frac{1}{4\pi}\right)[1 + \beta P_2(cos\theta)]$$

where θ is the angle between the recoiling velocity of the H-atom product (the TOF axis) and the polarization direction of the linearly polarized laser radiation, $P_2(\cos\theta)$ is the second Legendre polynomial, and β is the anisotropy parameter ($-1 \leq \beta \leq 2$). The β value of ~ 0 is obtained using the above equation and the H-atom TOF spectra.

The time profile of the H-atom production in the UV photolysis was measured in a pump-probe experiment using integrated H-atom signals in the TOF spectra as a function of the photolysis-probe delay time.[11,12] The time profile can be used to obtain the microcanonical rate of the unimolecular dissociation of 2-propenyl. The initial rise was determined by the rate of H atom formation from the dissociation of 2-propenyl, while the decay of signal was because of the H atom flight out of the interaction region between the two laser beams. Figure 7.7 shows the H-atom product yield time profiles of 2-propenyl photodissociation at 232 nm using the 2-chloropropene precursor and at 234 nm using the 2-bromopropene precursor. The time profiles of the H atom signals, $S_H(t)$, were fitted using

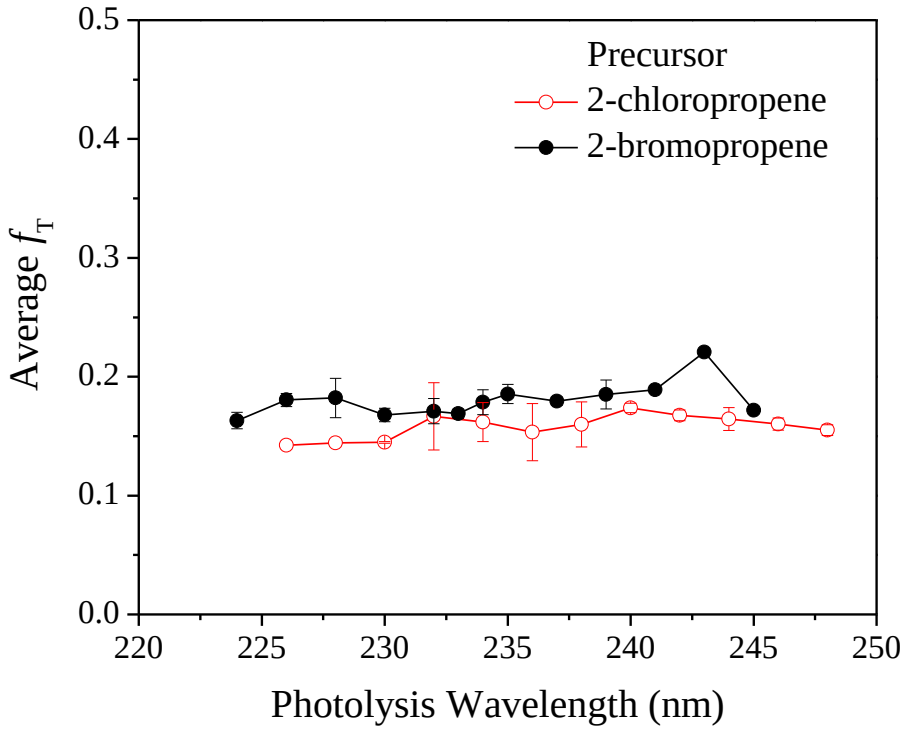

Figure 7.5. Fraction of average product translational energy in the total available energy, $\langle f_T \rangle$, as a function of the photolysis wavelength. The $\langle f_T \rangle$ values were calculated from the $P(E_T)$ distributions at various photolysis wavelengths, assuming the dissociation energy of the lowest energy H + propyne product channel. The $\langle f_T \rangle$'s from the 2-chloropropene precursor are represented by the open circles (○), and those from the 2-bromopropene precursor by the filled circles (●). The error bars indicate the 95% confidence limits from multiple measurements.

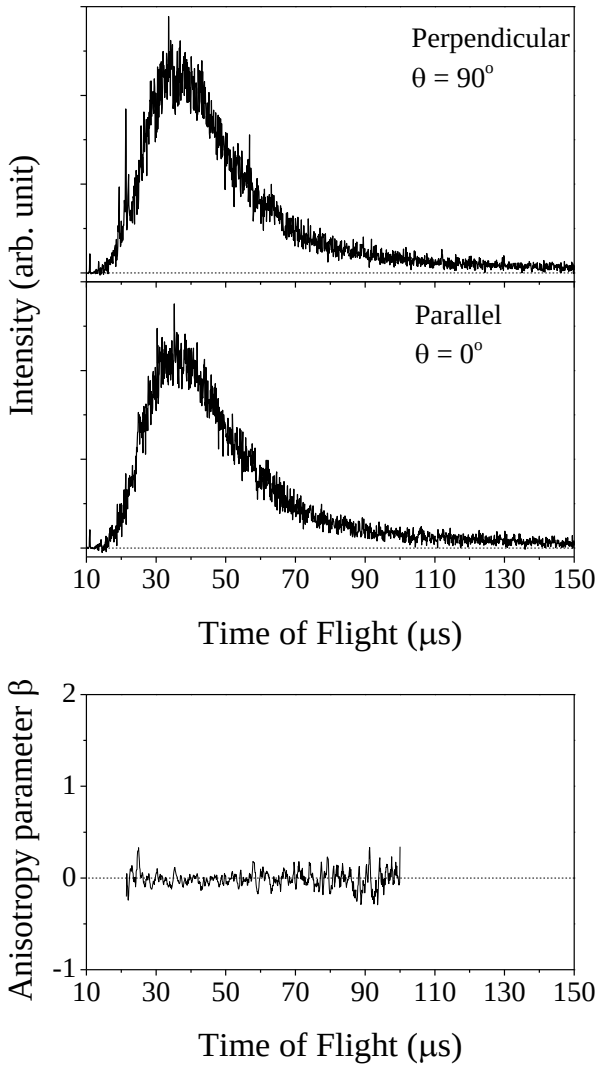

Figure 7.6. H-atom TOF spectra of 2-propenyl (from the 2-chloropropene precursor) at 232 nm photolysis wavelength with the photolysis radiation polarization perpendicular (θ = 90°) and parallel (θ = 0°) to the TOF axis. The two sharp peaks around 20 μs at the perpendicular polarization were due to photolysis of the HCl byproduct from the 193 nm photolysis of the 2-chloropropene precursor. The anisotropy parameter β is plotted as a function of the H-atom flight time and stays close to 0.

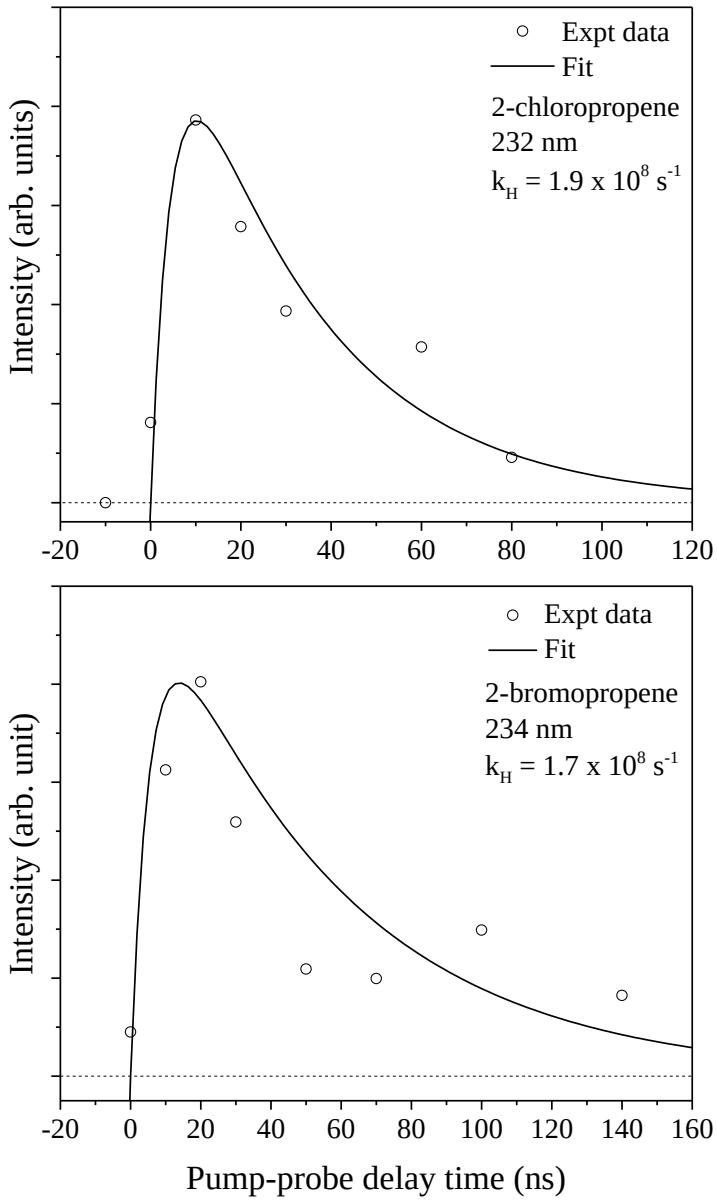

Figure 7.7. H-atom product signals of the 2-propenyl radical as a function of photolysis and probe laser delay time using the 2-chloropropene and 2-bromopropene precursors, respectively. The signals were obtained by integrating the HRTOF spectra at various photolysis-probe delay times. The photolysis wavelength of the 2-propenyl radical from the 2-chloropropene precursor was 232 nm, and 234 nm for the 2-bropropene precursor. The solid lines are the fits.

an expression based on the previous work from Chen's group to estimate the unimolecular dissociation rates of the 2-propenyl radical:[40]

$$S_H(t) = N[1 - \exp(-k_H t)] \cdot \left[\frac{1}{\exp[(t-a)/b]+1}\right]$$

where k_H is the unimolecular dissociation rate constant for the H atom formation from 2-propenyl, and a and b are constants that describe the width of the plateau region and the decay of the signal. The rate of H atom formation in the 230 nm photodissociation of 2-propenyl was determined from the time profile to be $\geq \sim 2 \times 10^8$ s^{-1} (Figure 7.7). This dissociation rate constant provides only a lower limit, as the resolution of the time profile measurement was restricted by the 10-*ns* laser pulse duration.

The results from the QCT simulation of the unimolecular dissociation of 2-propenyl with the 124 kcal/mol internal energy (equivalent to 230 nm photon energy) are listed in Table 7.1. The calculated branching ratios were 32% to H + allene, 35% to H + propyne, 0.5% to H + cyclopropene, and 32% to methyl + acetylene, with both the H + propyne and H + allene channels being significant. Figure 7.8 shows the calculated P(E_T)'s of the three different H + C_3H_4 product channels and the total H-atom loss channel, in comparison with the experimental $P(E_T)$ at 230 nm. Among the three individual H-loss channels, the H + allene channel had a slightly larger translational energy release. The different H atoms in the trajectories were identified and the H eliminations from the various sites in the H + allene and H + propyne dissociations are shown in Figure 7.9. The overall unimolecular dissociation rate constant of 2-propenyl was estimated to be 5×10^{11} s^{-1} at the 124 kcal/mol internal energy. For comparison, the QCT results at the 95 kcal/mol (300 nm) excitation energy are also listed in Table 7.1. The H + propyne channel had a larger branching ratio

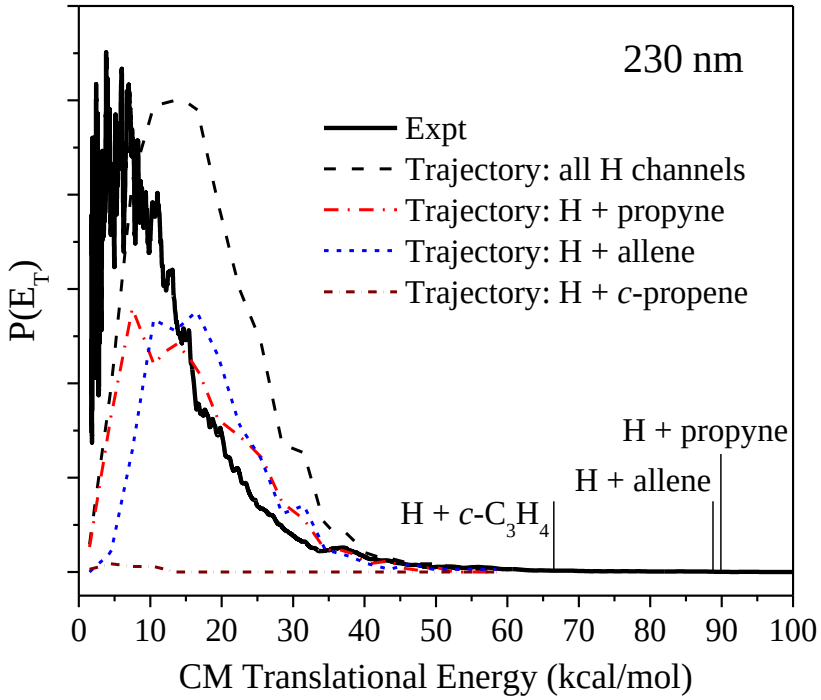

Figure 7.8. Experimental $P(E_T)$ distribution and QCT calculated $P(E_T)$ distributions of the H-atom product channels in the 2-propenyl photodissociation at 230 nm. The QCT $P(E_T)$ distributions of the three individual H-atom product channels are shown along with the total distribution.

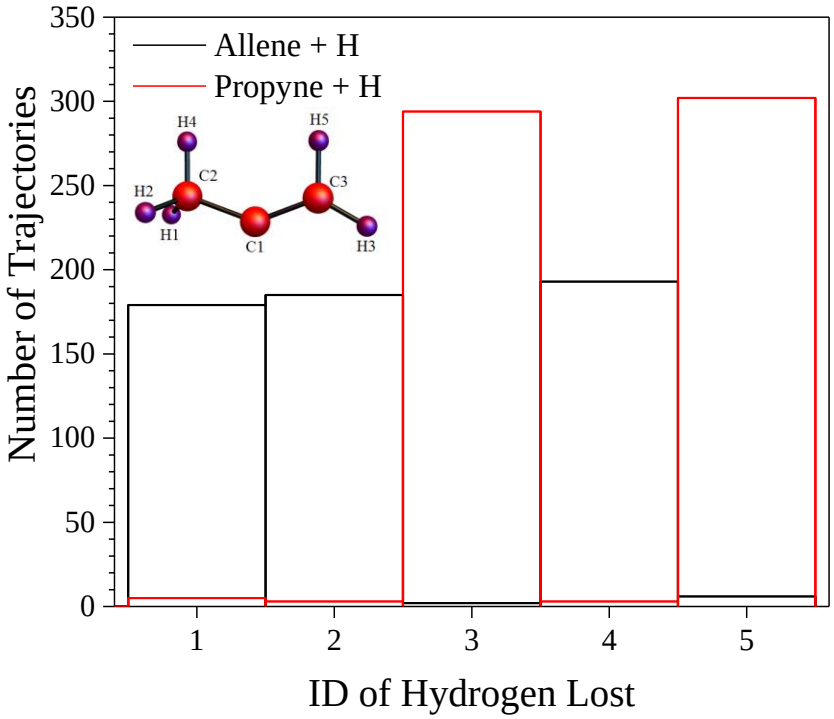

Figure 7.9. Calculated number of trajectories for the different H-atom loss pathways in the H + allene and H + propyne product channels. The five H atoms in the 2-propenyl radical are labeled as shown in the figure. The geometry of the 2-propenyl radical (LM1) is from the theoretical calculation (ref 23). H1, H2, and H4 eliminations predominantly lead to the H + allene product channel, and H3 and H5 eliminations predominantly to the H + propyne product channel.

Table 7.1. QCT simulations of unimolecular dissociation of 2-propenyl radical with 124 and 95 kcal/mol internal energy (equivalent to 230 and 300 nm photon energy).

Internal energy 124 kcal/mol (equivalent to 230 nm photon energy)				
product channel	branching ratio (%)	$P(E_T)$ distribution		
		peak (kcal/mol)	$\langle E_T \rangle$ (kcal/mol)	$\langle f_T \rangle$[a]
total H-loss (sum)	68	~ 13	17	0.19
H + allene	32	~ 15	18	0.20
H + propyne	35	~ 10	16	0.18
H + c-propene	0.5	~ 4	6	0.10
CH_3 + acetylene	32			
Internal energy 95 kcal/mol (equivalent to 300 nm photon energy)				
product channel	branching ratio (%)	$P(E_T)$ distribution		
		peak (kcal/mol)	$\langle E_T \rangle$ (kcal/mol)	$\langle f_T \rangle$[a]
Total H-loss (sum)	84	~ 12	14	0.23
H + allene	34	~ 13	15	0.26
H + propyne	50	~ 10	13	0.22
CH_3 + acetylene	16			

[a] For the total H loss, $\langle f_T \rangle$ is calculated on the basis of the maximum available energy of the lowest energy channel, H + propyne. The $\langle f_T \rangle$ value of the individual H-atom product channel is based on the maximum available energy of each individual channel.

than the H + allene channel. The overall dissociation rate constant of 2-propenyl was ~ 3 $\times 10^{11}$ s^{-1} at the 95 kcal/mol internal energy.

7.4 Discussions

The H-atom PFY spectra of 2-propenyl in the region of 224-248 nm from both precursors have a similar trend and reveal the UV absorption of 2-propenyl peaking near 232 nm. The previous theoretical study on the electronic structures of 2-propenyl identified two electronically excited states, $\tilde{B}^2A''$ ($\pi^* \leftarrow$ n, 255 nm vertical excitation) and $\tilde{C}^2A'$ ($\pi^* \leftarrow \pi$, 221 nm vertical excitation),[22] in the UV photolysis wavelength range of this study. The $\tilde{B}^2A''$ state was predicted to have an oscillator strength ~ 3 times larger than that of the $\tilde{C}^2A'$ state. The UV absorption feature in the PFY spectra could be due to the $\tilde{B}^2A''$ state, although contribution from the $\tilde{C}^2A'$ state is still possible. The H-atom PFY spectra of 2-propenyl are similar to those of 1-propenyl, consistent with the electronic excitation ($\tilde{B}^2A''$ and/or $\tilde{C}^2A'$) localized on their common vinyl structure. The H-atom PFY spectra may represent just part of the UV absorption feature of 2-propenyl, as the methyl-elimination channel could also contribute. As discussed in the following, the electronically excited state of 2-propenyl presumably decays to the ground electronic state via internal conversion, and the hot 2-propenyl radical then undergoes unimolecular decomposition on the ground-state surface.

The H-atom products from the 2-propenyl photodissociation at 232 nm have an isotropic angular distribution with $\beta \sim 0$. Several dissociation mechanisms could give rise

to the isotropic product angular distribution. The most common one is that the dissociation time scale is longer than one rotational period of the parent molecule so that the initially polarized excitation is lost prior to the dissociation due to the parent rotation. A prompt axial dissociation with the H-atom recoil velocity coincidentally at ~ 55° (the "magic angle") to the transition dipole moment can have $\beta \sim 0$. And a prompt dissociation with overlapping electronic transitions but differently aligned transition dipole moments could potentially yield an isotropic product angular distribution if the different components offset each other. However, the latter two (prompt dissociations) are typically associated with a large product translational energy release, which was not observed in the current study. The observed isotropic H-atom product angular distribution is more consistent with the most common mechanism, where the time scale of the UV photodissociation of 2-propenyl is greater than or equal to its rotational period. The previous studies from this lab showed that the rotational temperatures of jet-cooled polyatomic radicals in the molecular beam were in the range of 15-30 K (e.g., the rotational temperature of the allyl radical was measured to be ~ 15 K[11]). It is plausible that the 2-propenyl radical had a similar rotational temperature in the molecular beam, with an estimated rotational period of ~ 10 ps. These then imply that the UV photodissociation of 2-propenyl has a time scale ≥ ~ 10 ps. The QCT calculations indicated a lifetime of ~ 2 ps for the 2-propenyl radical with an internal energy of 124 kcal/mol (equivalent to the 230 nm) on the electronic ground state. Our RRKM calculation using the transition states and energetics of the C_3H_5 system from the theory (Figure 7.1)[9,23] suggested that the overall dissociation rate constant of 2-propenyl at 124 kcal/mol was ~ 2×10^{13} s^{-1} (a lifetime of 0.05 ps), much faster than that from the QCT

calculations. The QCT lifetime is close to but smaller than the photodissociation time scale inferred from the H-atom product angular distribution. Note that the QCT and RRKM calculations were for unimolecular decomposition of 2-propenyl on the electronic ground state, and the decay time for internal conversion of the electronically excited state to the electronic ground state was not included in these calculations. Alternatively, this time difference could suggest that the internal conversion of 2-propenyl is on a time scale of ~ 10 ps.

The H + C_3H_4 product $P(E_T)$ distributions at the different UV photolysis wavelengths have a similar shape, with a broad peak around 7-8 kcal/mol and a modest kinetic energy release. The $\langle f_T \rangle$ values in the wavelength range of 224 to 248 nm stay around a constant (~ 0.16-0.18). The experimental $P(E_T)$ distributions, their similarity regardless of the excitation wavelengths, and the small $\langle f_T \rangle$ values are consistent with unimolecular dissociation of hot 2-propenyl radical proceeding on the electronic ground state after internal conversion. This is also consistent with the QCT calculations of the unimolecular decomposition of 2-propenyl from the ground electronic state and supports that the QCT calculations can provide more insights into the dissociation mechanism.

The QCT calculations have identified the H-atom loss sites in the 2-propenyl dissociation (Figure 7.9). The direct H-atom loss of H3 or H5 from the CH_2 group (over an energy barrier of 38.2 kcal/mol) is the main pathway for the H + propyne products. As H3 and H5 on the CH_2 group are essentially equivalent, their removals have about the same number of trajectories (Figure 7.9). The H + propyne products could also be produced via the 1,2 H-atom shift to 1-propenyl and subsequent H-atom loss from the central C1 atom,

but this pathway is unlikely due to the higher isomerization barrier (44.4 kcal/mol) (Figure 7.1). The number of trajectories for H1, H2, and H4 loss from the CH_3 group to form H + propyne is negligible, as this is a higher-energy, multiple-step pathway from 2-propenyl to allyl via the 1,2 H shift and then from allyl to 1-propenyl via the 1,3 H shift before dissociation (Figure 7.1). For the H + allene channel, the QCT calculations show that the main dissociation pathway is the direct C-H bond breaking (H1, H2, and H4) from the CH_3 group (over a 39.0 kcal/mol barrier), more probable than via isomerization of 2-propenyl to allyl (over a 41.1 kcal/mol barrier) and subsequent dissociation of allyl. The H + allene product pathway via H3 or H5 loss proceeds through higher-energy isomerization steps and is negligible (as shown by the small number of trajectories).

The QCT calculations show that at the 124 kcal/mol excitation energy both the H + allene and H + propyne dissociation channels are important, with branching ratios of 0.32:0.35 (for their similar direct dissociation energy barriers from 2-propenyl), and the H + cyclopropene product channel is negligible (for its higher overall barrier of 59.1 kcal/mol). The methyl + acetylene channel, which proceeds after isomerization of 2-propenyl to 1-propenyl, has a similar branching ratio (0.32) as the H + allene and H + propyne channels. Our RRKM calculation at this excitation energy indicates that branching ratios of the H + allene and H + propyne channels are 0.27:0.70, and a small fraction (0.025) undergoes isomerization to 1-propenyl (which presumably dissociates into the methyl + acetylene channel due to its lower energy barrier from 1-propenyl). At the lower excitation energy of 95 kcal/mol, the QCT calculations show that the H + allene channel is less important than H + propyne (branching ratios of 0.34:0.50), consistent with the slightly

lower energy barrier of the H + propyne channel, and that the methyl + acetylene channel is also reduced (branching ratio of 0.16).

The comparison between the experimental and QCT $P(E_T)$ distributions for the overall H-atom elimination of the 2-propenyl radical with the 124 kcal/mol (230 nm) excitation energy shows a qualitative agreement (Figure 7.8). But the calculated $P(E_T)$ distribution has a slightly larger kinetic energy release than the experimental $P(E_T)$ ($\langle f_T \rangle \approx$ 0.19 vs. 0.16-0.18) and peaks at higher energy (~ 13 kcal/mol vs. 7-8 kcal/mol). Similar results from this comparison were also observed in the previous studies of allyl and 1-propenyl.[11 12] This comparison suggests that the theoretical ground-state PES near the regions of the H + propyne and H + allene exit channels might be more repulsive than the actual one. The better agreement between the $\langle f_T \rangle$ values than between the $P(E_T)$ distributions implies that the $P(E_T)$ distribution is a more sensitive probe of the dissociation dynamics. The QCT calculations also show that the H + allene product channel has a higher kinetic energy release than the H + propyne channel (although the exit channel barriers of these two channels are comparable (Figure 7.1)).

Finally, it is worthwhile to compare the H-elimination product $P(E_T)$ distributions and angular distributions in the UV (~ 230 nm) photodissociation of the three alkenyl C_3H_5 isomers. All three systems show isotropic H-atom product angular distributions, consistent with unimolecular decomposition after internal conversion. The experimental $P(E_T)$ distribution of the allyl radical peaks at ~ 9 kcal/mol with $\langle f_T \rangle \sim 0.20$,[11] that of 2-propenyl peaks at ~ 7-8 kcal/mol with $\langle f_T \rangle \sim 0.16$ (this work), and 1-propenyl peaks at ~ 8 kcal/mol with $\langle f_T \rangle \sim 0.13$.[12] The experimental product translational energy release $\langle f_T \rangle$'s show a clear

difference among the three isomers. The trend of the $\langle f_T \rangle$ values is consistent with the variation in the QCT branching ratios of the two main H-loss product channels, H + allene and H + propyne: ~ 7:1 in allyl, ~ 1:1 in 2-propenyl, and ~ 1:5 in 1-propenyl, as well as their translational energy releases. As the H + allene channel has a larger translational energy release than the H + propyne channel (based on the QCT calculations), the overall translational energy release decreases from allyl, 2-propenyl, to 1-propenyl, as the H + allene contribution decreases and the H + propyne contribution increases in this trend. Note that the QCT calculations were performed by assuming that GM, LM1, and LM2 were the starting geometries for unimolecular dissociation of allyl, 2-propenyl, and 1-propenyl, respectively, as the details of internal conversion of the excited states were not known. If the explanation of the trend of the experimental $\langle f_T \rangle$ values of the three isomers based on the QCT calculation results is reasonable, it would suggest that each isomer largely preserves its isomeric configure following the internal conversion to the ground state PES and the assumptions used in the QCT calculations are acceptable. The comparison of the UV photodissociation dynamics of the three alkenyl C_3H_5 isomers reveals some evidence of the isomer-specific dissociation. Due to the *different starting geometries* of the three isomers on the ground electronic state PES following internal conversion, the three isomers at GM, LM1, and LM2 are influenced by the topology and the dissociation and isomerization energy barriers on the ground-state PES and lead to different branching ratios of the H + allene and H + propyne product channels. And due to the slightly different translational energy releases in the two main H-atom product channels, the overall $P(E_T)$

distributions and translational energy releases of the H-elimination channel reveal this variation among the three isomers and more details of the dissociation mechanisms.

7.5 Conclusion

The H-atom product photodissociation channels of the 2-propenyl radical were examined at the UV wavelengths of 224-248 nm. The H-elimination PFY spectra show that 2-propenyl has a broad UV absorption feature peaking near 232 nm. The comparison of this UV absorption with the theoretical calculation suggests that the UV photodissociation of 2-propenyl in the 224-248 nm region is initiated from the $\widetilde{B}^2A''$ and/or $\widetilde{C}^2A'$ excited states. The H-atom product $P(E_T)$ distributions show a modest kinetic energy release with the peak around 7-8 kcal/mol, and $\langle f_T \rangle$ is close to a constant of ~ 0.16-0.18 in the photolysis wavelength range of 224-248 nm. The QCT calculations were performed with the 124 kcal/mol excitation energy (equivalent to the 230 nm photolysis wavelength). The calculated branching ratios of the different product channels are 32% H + allene, 35% H + propyne, 0.5% H + cyclopropene, and 32% methyl + acetylene, confirming that the main H-elimination channels are H + allene and H + propyne. The most probable reaction pathways of these two H-elimination channels are the direct C-H bond cleavages of 2-propenyl. The H-atom photofragment angular distribution is isotropic, implying that the overall UV photodissociation time scale is $\geqslant$ 10 ps, while the trajectory calculations estimate that the ground-state unimolecular dissociation time is ~ 2 ps. The UV

photodissociation mechanism of the 2-propenyl radical is hot radical dissociation on the ground state after internal conversion from the electronically excited states.

References

1. W. Tsang and J. A. Walker, *J. Phys. Chem.* **96**, 8378 (1992).

2. R. X. Fernandes, B. R. Giri, H. Hippler, C. Kachiani, and F. Striebel, *J. Phys. Chem. A* **109**, 1063 (2005).

3. C. S. McEnally, L. D. Pfefferle, B. Atakan, and K. Kohse-Höinghaus, *Progr. Energy Combust. Sci.* **32**, 247 (2006).

4. N. Hansen, J. A. Miller, C. A. Taatjes, J. Wang, T. A. Cool, M. E. Law, and P. R. Westmoreland, *Proc. Combust. Inst.* **31**, 1157 (2007).

5. H. R. Zhang, E. G. Eddings, and A. F. Sarofim, *Energy Fuels* **22**, 945 (2008).

6. L. K. Huynh, H. R. Zhang, S. Zhang, E. Eddings, A. Sarofim, M. E. Law, P. R. Westmoreland, and T. N. Truong, *J. Phys. Chem. A* **113**, 3177 (2009).

7. N. Hansen, W. Li, M. E. Law, T. Kasper, P. R. Westmoreland, B. Yang, T. A. Cool, and A. Lucassen, *Phys. Chem. Chem. Phys.* **12**, 12112 (2010).

8. J. A. Miller, S. J. Klippenstein, Y. Georgievskii, L. B. Harding, W. D. Allen, and A. C. Simmonett, *J. Phys. Chem. A* **114**, 4881 (2010).

9. B. S. Narendrapurapu, A. C. Simmonett, H. F. Schaefer, J. A. Miller, and S. J. Klippenstein, *J. Phys. Chem. A* **115**, 14209 (2011).

10. V. V. Kislov, A. M. Mebel, J. Aguilera-Iparraguirre, and W. H. Green, *J. Phys. Chem. A* **116**, 4176 (2012).

11. Y. Song, M. Lucas, M. Alcaraz, J. Zhang, and C. Brazier, *J. Phys. Chem. A* **119**, 12318 (2015).

12. M. Lucas, Y. Song, J. Zhang, C. Brazier, P. L. Houston, and J. M. Bowman, *J. Phys. Chem. A* **120**, 5248 (2016).

13. C. L. Currie and D. A. Ramsay, *J. Chem. Phys.* **45**, 488 (1966).

14. A. B. Callear and H. K. Lee, *Trans. Faraday Soc.* **64**, 308 (1968).

15. H. E. van den Bergh and A. B. Callear, *Trans. Faraday Soc.* **66**, 2681 (1970).

16. J. A. Blush, D. W. Minsek, and P. Chen, *J. Phys. Chem.* **96**, 10150 (1992).

17. D. W. Minsek, J. A. Blush, and P. Chen, *J. Phys. Chem*. **96**, 2025 (1992).

18. M. E. Jenkin, T. P. Murrells, S. J. Shalliker, and G. D. Hayman, *J. Chem*. *Soc., Faraday Trans.* **89**, 433 (1993).

19. K. Tonokura and M. Koshi, *J. Phys. Chem*. *A* **104**, 8456 (2000).

20. M. Gasser, A. M. Schulenburg, P. M. Dietiker, A. Bach, F. Merkt, and P. Chen, *J. Chem*. *Phys.* **131**, 014304 (2009).

21. M. Gasser, J. A. Frey, J. M. Hostettler, A. Bach, and P. Chen, *J. Phys. Chem*. *A* **114**, 4704 (2010).

22. L. Koziol, S. V. Levchenko, and A. I. Krylov, *J. Phys. Chem*. *A* **110**, 2746 (2006).

23. C. Chen, B. Braams, D. Y. Lee, J. M. Bowman, P. L. Houston, and D. Stranges, *J. Phys. Chem*. *A* **115**, 6797 (2011).

24. D. Stranges, M. Stemmler, X. Yang, J. D. Chesko, A. G. Suits, and Y. T. Lee, *J. Chem*. *Phys.* **109**, 5372 (1998).

25. L. Castiglioni, A. Bach, and P. Chen, *Phys. Chem*. *Chem*. *Phys.* **8**, 2591 (2006).

26. H. J. Deyerl, I. Fischer, and P. Chen, *J. Chem*. *Phys.* **110**, 1450 (1999).

27. D. Stranges, P. O'Keeffe, G. Scotti, R. Di Santo, and P. L. Houston, *J. Chem*. *Phys.* **128**, 151101 (2008).

28. C. Chen, B. Braams, D. Y. Lee, J. M. Bowman, P. L. Houston, and D. Stranges, *J. Phys. Chem*. *Lett.* **1**, 1875 (2010).

29. J. Niedzielski, J. Gawłowski, and T. Gierczak, *J. Photochem*. **21**, 195 (1983).

30. T. Gierczak, J. Gawlowski, and J. Niedzielski, *J. Photochem*. *Photobiol., A* **43**, 1 (1988).

31. J. L. Miller, M. L. Morton, L. J. Butler, F. Qi, M. J. Krisch, and J. Shu, *J. Phys. Chem*. *A* **106**, 10965 (2002).

32. M. L. Morton, J. L. Miller, L. J. Butler, and F. Qi, *J. Phys. Chem*. *A* **106**, 10831 (2002).

33. Y. Song, X. Zheng, W. Zhou, M. Lucas, and J. Zhang, *J. Chem*. *Phys.* **142**, 224306 (2015).

34. J. A. Mueller, J. L. Miller, L. J. Butler, F. Qi, O. Sorkhabi, and A. G. Suits, *J. Phys. Chem. A* **104**, 11261 (2000).

35. J. A. Mueller, B. F. Parsons, L. J. Butler, F. Qi, O. Sorkhabi, and A. G. Suits, *J. Chem. Phys.* **114**, 4505 (2001).

36. H. Fan, S. T. Pratt, and J. A. Miller, *J. Chem. Phys.* **127**, 144301 (2007).

37. H. Fan, L. B. Harding, and S. T. Pratt, *Mol. Phys.* **105**, 1517 (2007).

38. G. Amaral, K. Xu, and J. Zhang, *J. Chem. Phys.* **114**, 5164 (2001).

39. R. N. Zare, *Mol. Photochem.* **4**, 1 (1972).

40. H. J. Deyerl, I. Fischer, and P. Chen, *J. Chem. Phys.* **111**, 3441 (1999).

Chapter 8

Photodissociation Dynamics of Vinoxy Radical via the $\widetilde{B}^2A''$ State: H-atom Product Dissociation Channel

Abstract

The photodissociation dynamics of jet-cooled vinoxy radical (CH_2CHO) via the $\widetilde{B}^2A''$ state was studied in the near ultraviolet (near UV) region of 308 – 328 nm using the high-*n* Rydberg H-atom time-of-flight (HRTOF) and resonance-enhanced multiphoton ionization (REMPI) techniques. The H + CH_2CO product channel was observed directly from the H-atom TOF spectrum. The H-atom REMPI spectrum showed several vibronic bands of the $\widetilde{B}^2A''$ state. The product center-of-mass (CM) translational energy distributions at different photolysis wavelength were obtained. All of them were essentially the same in the near-UV region of 308-328 nm, with a broad feature peaking at ~ 3500 cm^{-1} (10 kcal/mol) and the average translational energy release in the maximum available energy, $\langle f_T \rangle$, being 0.24-0.26. The product angular distribution was slightly anisotropic, with the β parameter in the range of 0.10 to 0.24. of the near-UV photodissociation mechanism of the H-atom product channel of the vinoxy radical would be the unimolecular dissociation on the electronic ground state ($\widetilde{X}^2A''$) and first excited state ($\widetilde{A}^2A'$) after internal conversion from the $\widetilde{B}^2A''$ state.

8.1 Introduction

The vinoxy radical (CH_2CHO) is a prototype of the unsaturated alkoxy radical, and it plays an important role in both combustion and atmospheric chemistry processes. Vinoxy can be produced from the reactions of small organic compounds with oxygen atom or hydroxyl radical such as $O(^3P) + C_2H_4$,[1-3] $O(^3P) + C_2H_3$,[4] $OH + C_2H_2$,[5] $OH + C_2H_4O$,[6] and $OH + C_2HO$.[7] The vinoxy radical can have further reactions with O_2,[8-11] NO_2,[12] and NO[8] to generate CH_2O, CO, OH, $(CHO)_2$, and CH_2CO, etc. The vinoxy radical is also involved as an intermediate in atmospheric ozone and alkene reactions.

Numerous theoretical studies have reported the energetics, geometries, vibrational, and rotational structures of the vinoxy radical.[13-30] The calculations indicated that the three lowest-lying electronic states of vinoxy radical, $\tilde{X}^2A''$, $\tilde{A}^2A'$, and $\tilde{B}^2A''$ have a planar geometry with C_S symmetry, while the $\tilde{C}^2A'$ state has a nonplanar equilibrium geometry.[16,19,23-26] Theoretical studies determined that the ground-state vinoxy radical has two possible valence bond structures: CH_2=CH-O (vinoxy radical) and CH_2-CH=O (formyl methyl radical).[13-15] Microwave spectroscopy study found that the methylene carbon atom has the largest unpaired spin density, indicating that the latter structure is more favorable for the vinoxy radical.[31] The reaction rate of vinoxy with O_2 is about two orders of magnitude faster than that of methoxyl (CH_3O) with O_2, giving additional evidence that the formyl methyl is more favorable as the structure of the ground state vinoxy.[9] For the $\tilde{B}^2A''$ state, the CO bond has more double-bond character than the CC bond, indicating that the vinoxy radical on the $\tilde{B}^2A''$ state has a structure more towards the formyl methyl

radical.[24] Compared to the ground electronic state, the $\widetilde{A}^2A'$ state vinoxy radical has a shorter CC bond and a longer CO bond, more towards to the structure with the CC double-bond.[19-21,24,26,30]

A series of theoretical studies have been carried out on the interactions between the electronic states. Yarkony and coworkers suggested that avoided crossings between the $\widetilde{B}^2A''$ and $\widetilde{A}^2A'$ states would induce non-radiation decay from the $\widetilde{B}^2A''$ state, and the $\widetilde{A}^2A'$ - $\widetilde{X}^2A''$ conical intersections could provide the pathways for the decay from the $\widetilde{A}^2A'$ state.[22] Later on, another study by Yarkony and coworkers investigated the conical intersection topography of the transition states which is en route to the H + CH_2CO products, and this conical intersection does not support any nonadiabatic recrossing to annihilate the H + CH_2CO product channel.[25] Several studies done by Piechowsk-Strumik *et. al.* examined a non-planar conical intersection between the $\widetilde{A}^2A'$ - $\widetilde{X}^2A''$ states with two active angular coordinates. This conical intersection could play an important role in the dissociation of the vinoxy radical with a large internal energy in the $\widetilde{A}^2A'$ state.[26,27]

The spectroscopy of vinoxy radical has received extensive attention for decades.[1,17-22,30,32-41] The first absorption spectrum of the vinoxy radical was reported with a band head around 28790 cm^{-1} by Ramsay in 1965.[32] This observation was confirmed later by Hunziker *et. al.* with the prominent 0-0 band at 28760 cm^{-1}, along with the discovery of another absorption band origin at 8006 cm^{-1}.[1] These observations are in good agreement with the theoretical predicted energies of the $\widetilde{B}^2A'' \leftarrow \widetilde{X}^2A''$ and $\widetilde{A}2A' \leftarrow \widetilde{X}^2A''$ transitions, respectively.[15,18-20,24,28,30] In the absorption spectra of the vinoxy radical, several vibronic bands of the $\widetilde{B}^2A'' \leftarrow \widetilde{X}^2A''$ transitions were observed from the origin around 28760 cm^{-1}

up to 35700 cm^{-1}.[1,41] In contrast, the laser induced fluorescence (LIF) spectra of the $\tilde{B}^2A''$ state presented no fluorescence above 30200 cm^{-1} (1400 cm^{-1} above the origin of the $\tilde{B}^2A''$ state).[33,35,39,40] The photofragment yield (PFY) spectra of the CH_3 + CO product channel from the photodissociation of the vinoxy radical via the $\tilde{B}^2A''$ state were obtained by Neumark and coworkers and showed very weak signals when the photolysis energy was just above the $\tilde{B}^2A''$ state origin, with the signals increased rapidly with the increasing photolysis energies, even though the Franck-Condon (FC) factors for the absorption increases only slightly in this region.[20] These observations indicate a competition between fluorescence and non-radiative decay (dissociation), and the dissociation channel dominates when the photon energy is above 30200 cm^{-1}.

Possible dissociation channels of the vinoxy radical and their energetics are listed as follows:

$$CH_2CHO(\tilde{X}^2A'') \rightarrow CH_3(\tilde{X}^2A_2'') + CO(\tilde{X}^1\Sigma^+) \quad \Delta H_0 = 3.25 \pm 0.18 \text{ kcal/mol}^{42} \qquad (1)$$

$$\rightarrow H(^2S) + CH_2CO(\tilde{X}^1A_1) \quad \Delta H_0 = 35.43 \pm 0.18 \text{ kcal/mol}^{42} \qquad (2)$$

$$\rightarrow H(^2S) + CH_2CO(\tilde{a}^3A'') \quad \Delta H_0 = 89.94 \text{ kcal/mol}^{20} \qquad (3)$$

Figure 8.1 presents the potential energy diagram of vinoxy radical dissociation to the H + CH_2CO and CH_3 + CO product channels based on previous theoretical calculation.[20] The ground state vinoxy radical could undergo 1,2 H shifting to the acetyl radical via transition state 1 (TS1) with an energy barrier of 41.05 kcal/mol and the acetyl could have CC bond cleavage to form the CH_3 + CO products by going over an energy barrier of 17.30 kcal/mol (TS3) or have CH bond fission to generate H + $CH_2CO(\tilde{X}^1A_1)$ with a higher energy barrier (TS2, 47.27 kcal/mol). The ground state vinoxy radical could

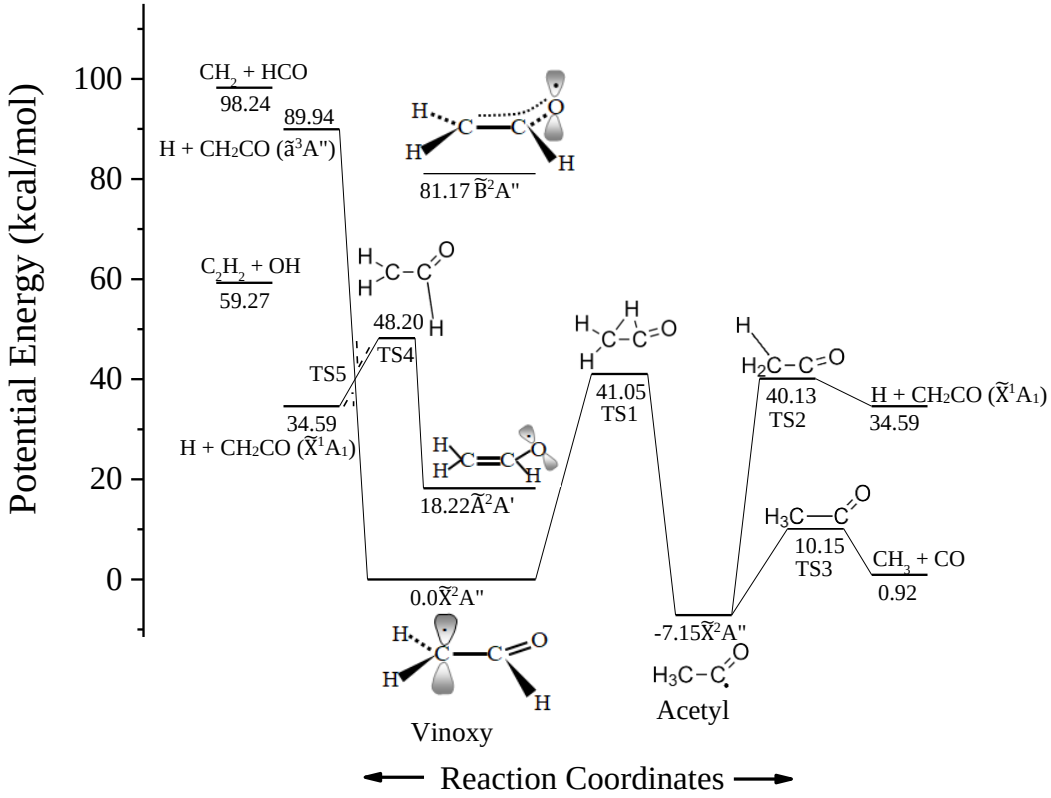

Figure 8.1. Potential energy diagram of the vinoxy radical system. The dissociation channels toward the $CH_3(\tilde{X}^2A_2'') + CO(\tilde{X}^1\Sigma^+)$ and $H(^2S) + CH_2CO(\tilde{X}^1A_1)$ product channels are shown. The energies are in kcal/mol with zero-point energy correction, and relative to $CH_2CHO(\tilde{X}^2A'')$. All the energies are based on previous theoretical calculations. (Ref. 20) See text for details.

also have the CH bond stretching in the C_s plane and asymptotically correlate with the H atom and $CH_2CO(\tilde{a}^3A'')$ products. The $\tilde{A}^2A'$state vinoxy radical can undergo a C-H bond cleavage to the H + $CH_2CO(\tilde{X}^1A_1)$ product channel via the TS4 with an energy barrier of 29.98 kcal/mol. The repulsive part of this channel is crossed with the dissociation pathway of the $\tilde{X}^2A''$vinoxy to the H + $CH_2CO(\tilde{a}^3A'')$ product, and an avoid crossing is formed. The TS5 is formed at the avoided crossing with the breaking of the C_s symmetry by the out-of-plane motion of the CH bond.

Butler and coworkers studied the unimolecular dissociation of the internally excited vinoxy radical on the ground electronic state, which was prepared from the photolysis of chloroacetaldehyde (CH_2ClCHO) at 193 nm.[43] They observed the CH_3 + CO product channel through acetyl radical and did not find the evidence of the C-H fission to form H + CH_2CO (with a branching ratio < 0.5%). The vinoxy radical created with the internal energy larger than 41.0 $\pm$ 2.0 kcal/mol could isomerize to acetyl, which is consistent with the calculated barrier to this channel in their study. Morton *et. al.* observed that in the photodissociation of the methyl vinyl ether at 193 nm, most of the vinoxy radical, created from the reaction were in the $\tilde{A}^2A'$ state.[44] The secondary dissociation of the vinoxy radical ($\tilde{A}^2A'$) predominantly leads to the H and CH_2CO products. A few years later, Butler and coworkers reinvestigated the unimolecular dissociation of the vinoxy radical prepared from photodissociation of chloroacetaldehyde at 157 nm.[45] The vinoxy radicals created in this study were mostly in the $\tilde{A}^2A'$ state, and the branching ratio between the H + CH_2CO and CH_3 + CO channels was determined to be ~ 2.1:1,[45] different from their previous work in 2004.[43] The internally excited vinoxy radical would undergo internal conversion to the

electronic state. With a large amount of internal energy which is greater than k0 kcal/mol, the vinoxy radical towards to have the C-H bond cleavage to produce H + CH_2CO products. The barrier height for the H + CH_2CO channel was determined to be 4.0 $\pm$ 0.5 kcal/mol higher than the isomerization barrier to the CH_3 + CO products. The photodissociation dynamics of vinoxy on the $\widetilde{B}^2A''$ state was investigated by Neumark and coworkers by using fast radical beam photofragment translational spectroscopy.[20] The excited vinoxy would undergo predissociation to the CH_3 + CO and H + CH_2CO products channels with a branching ratio of about 1:4. The center-of-mass (CM) product translational energy distributions are modest for both channels, and the product angular distribution is anisotropic ($\beta > 0$) for the CH_3 + CO product channel with the photolysis energy upto 1400 cm^{-1} above the $\widetilde{B}^2A'' \leftarrow \widetilde{X}^2A''$ transition origin. The P(E_T) distributions for the H + CH_2CO product channel has a peak near zero kinetic energy. Several vibrational progressions of the $\widetilde{B}^2A''$ state can be observed from the PFY spectra of the CH_3 + CO product channel. The dissociation rate increases dramatically above 1400 cm^{-1}, indicating a surface crossing of the $\widetilde{B}^2A''$ state followed by internal conversion, $\widetilde{B}^2A'' \rightarrow \widetilde{A}^2A' \rightarrow \widetilde{X}^2A''$, to the ground electronic state. The unimolecular dissociation of the ground state vinoxy over the TS5 transition state could generate the H + CH_2CO product, while the CH_3 + CO product channel would be the CC bond cleavage of the acetyl radical over a low barrier after the 1,2 hydrogen shift from the ground-state vinoxy radical.

In this chapter, we report our work on the photodissociation of the vinoxy radical via several vibrational levels on the $\widetilde{B}^2A''$ state in the near UV region of 308 to 328 nm. The H + C_2H_2O product channel was observed directly from the H-atom time-of-flight

(TOF) spectra. The H-atom photofragment yield (PFY) spectra (i.e. action spectrum) of vinoxy were obtained using the high-*n* Rydberg H-atom time-of-flight (HRTOF) and resonance-enhanced multiphoton ionization (REMPI) techniques. By comparing the H-atom PFY spectra in this current work with the absorption spectrum and the PFY spectra of the CH_3 + CO products from previous studies of the vinoxy radical, the H + C_2H_2O signals form the photodissociation of vinoxy was confirmed. The product CM translational energy distributions, P(E_T), and product angular distributions for the H-atom product channel were derived from the TOF spectra, and with this information, the photodissociation mechanism of the vinoxy radicals was investigated.

8.2 Experimental

The high-*n* Rydberg time-of-flight (HRTOF) technique was employed in this study and the experimental setup was reported previously.[46-48] Previous studies indicated that the vinoxy radical can be generated from the photolysis of alkyl vinyl ether.[10,31,44] Ethyl vinyl ether (EVE, Fluka ~99%) was used as the precursor to produce the vinoxy radical in this work. The vinoxy radical beam was generated by photolyzing the precursor in Ar or He (~10%) at a total pressure of ~ 1.3 atm with 193-nm radiation from an ArF excimer laser in front of the pulsed nozzle. The vinoxy radicals produced from the photolysis were cooled down by supersonic expansion in the molecular beam. In the reaction chamber, the vinoxy radicals were photodissociated by a tunable near UV laser beam (308 – 328 nm, 6 – 10 mJ/pulse). A Fresnel-Rhomb achromatic λ/2 was used to change the polarization of

the photolysis radiation for the H-atom product angular distribution study. The H atoms produced from the photodissociation of vinoxy radicals were pumped by two-color resonant excitation (121.6 nm + 366.3 nm), i.e., from 1^2S to 2^2P via the H atom Lyman-α transition and then to a metastable high-*n* Rydberg state. A small fraction of the high-*n* Rydberg state H atoms drifted with their nascent velocities to a microchannel plate (MCP) detector that was installed perpendicular to the molecular beam and then were field ionized in front of the MCP and detected. The length of the flight path is 37.28 cm which was calibrated by the photodissociation of HBr at 236 nm with the well-studied bond dissociation energy and the spin-orbit energy splitting of the Br($^2P_{3/2}$) and Br($^2P_{1/2}$) products. The ion signals were amplified by a fast pre-amplifier and averaged by a multichannel scale to obtain the H-atom TOF spectra. The TOF spectra were typically accumulated with 60 – 300 k laser shots each.

The H atoms produced from photodissociation of the vinoxy radicals were also monitored by using resonance enhanced multiphoton ionization (REMPI) technique. This experiment was carried out in a TOF mass spectrometry (TOFMS) mode on the same HRTOF instrument. The H atoms were detected by 1 + 1′ REMPI with one Lyman-*α* radiation exciting the H atoms from 1^2S to 2^2P and the UV radiation at ~364 nm ionizing the H atoms. The delay time between the photolysis and the REMPI probe lasers was set as ~10 ns. The H^+ ions were then extracted and accelerated in the TOF mass spectrometer and monitored by the MCP detector. These signals were amplified by a pre-amplifier and recorded by a Boxcar averager (SR250), and the information were transferred to the computer. The H-atom PFY spectra by REMPI were obtained by scanning the photolysis

wavelengths. At each wavelength, the REMPI signal was accumulated with ~100 laser shots. The PFY spectra were normalized by the laser power and number of laser shots

8.3 Results

The H-atom product TOF spectra from the photodissociation of jet-cooled vinoxy radical were measured in the near UV region of 308 to 327 nm with the polarization of the photolysis radiation parallel (∥, θ = 0°) and perpendicular (⊥, θ = 90°) to the TOF path. Two types of H-atom TOF spectra were taken in this experiment: (1) full spectrum, with the 193 nm radical producing radiation on and the UV photolysis radiation on, plus the Rydberg atom tagging probe laser radiations; and (2) precursor background spectrum, with the 193 nm radiation off but the UV photolysis radiation on, plus the Rydberg atom tagging probe laser radiations. The net H-atom TOF spectra from the photodissociation of the vinoxy radical were obtained by subtracting the precursor background spectra from the full spectra. Figure 8.2 presents the net H-atom product TOF spectra of the photodissociation of the vinoxy radical at 323.76 nm with the linearly polarized photolysis radiation parallel (∥, θ = 0°) and perpendicular (⊥, θ = 90°) to the TOF axis. Both TOF spectra have a broad feature with the peak at ~32 μs, and the parallel spectrum has a slightly stronger signal in the entire flight time the region.

By integrating the net H-atom TOF signals at different photolysis energies, the H-atom PFY spectrum can be obtained. The green full circles in Figure 8.3 (b) are the integrated HRTOF signals at different photolysis wavelengths from 308 to 327 nm, and

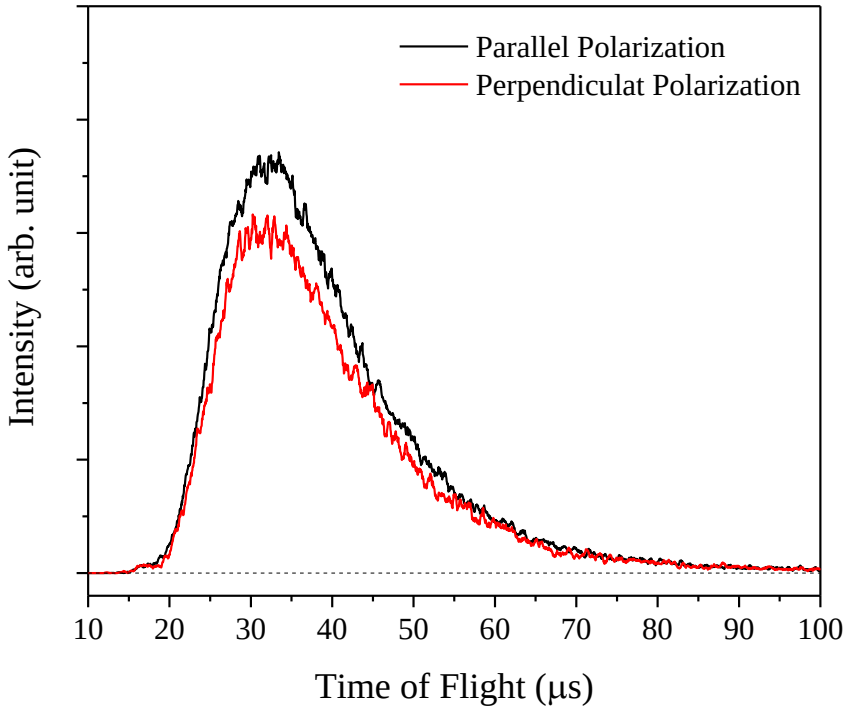

Figure 8.2. H-atom TOF spectra of the photodissociation of vinoxy radical at 323.76 nm, with the polarization of the photolysis radiation parallel to the TOF axis, ∥, θ = 0° (black curve), and perpendicular to the TOF axis, ⊥, θ = 90° (red curve). The signals were normalized to the same photolysis laser power and number of laser shoots. Both spectra peaks at ~ 32 μs and the parallel one has a slightly stronger signal. See text for details.

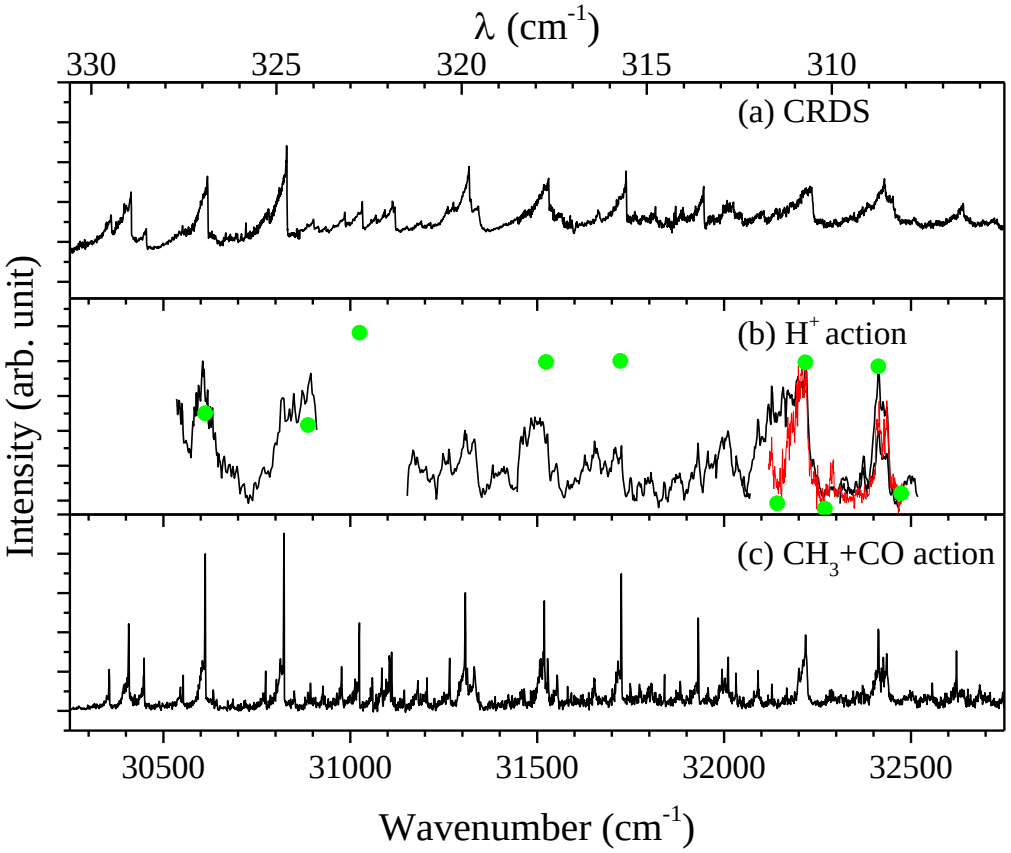

Figure 8.3. (a) CRDS absorption spectrum of the $\tilde{B}^2A'' \leftarrow \tilde{X}^2A''$ transition of the vinoxy radical in the region of 30250 to 32750 cm^{-1}. (Ref. 41) (b) H-atom PFY spectrum from photodissociation of the vinoxy radical using the H-atom REMPI technique. The full green circles (●) are the integrated H atom HRTOF signals from the photodissociation of vinoxy radical at different photolysis energies. (c) PYF spectrum of the CH_3 + CO product channel of the vinoxy photodissociation via the $\tilde{B}^2A''$ state. (Ref. 20)

these signals are normalized to the same photolysis laser power and number of laser shoots. The PFY signals on the vinoxy radical vibronic transition resonances are stronger compared to those off the transition resonances (32142.29, 32270.00, and 32474.12 cm^{-1}). The curve in Figure 8.3 (b) is the H-atom PFY spectrum by REMPI. The REMPI PFY spectrum can reasonably reproduce the vibronic features of the vinoxy radical via the $\widetilde{B}^2A'' \leftarrow \widetilde{X}^2A''$ transitions, and the REMPI spectrum agrees with the vinoxy absorption spectrum (Figure 8.3 (a))[41] and the PFY spectrum of the CH_3 + CO product channel from the photodissociation of the vinoxy via the $\widetilde{B}^2A''$ state (Figure 8.3 (c)).[20] These pieces of evidences confirm that the H-atom signals were from the photodissociation of the vinoxy radical.

The CM product translational energy distributions, $P(E_T)$, of the H + CH_2CO product channel can be converted from the net H-atom TOF spectra. The CM translational energy, E_T, can be derived from the H-atom product flight time t_H via the following equation:

$$E_T = \left(1 + \frac{m_H}{m_{CH_2CO}}\right) E_H + \frac{m_H}{m_{CH_2CO}} E_{CH_2CHO}$$

$$= \frac{1}{2} m_H \left(1 + \frac{m_H}{m_{CH_2CO}}\right) \left(\frac{L}{t_H}\right)^2 + \frac{m_H}{m_{CH_2CO}} E_{CH_2CHO}$$

in which, E_H and E_{CH_2CHO} are the laboratory translational energy of the H-atom product and the parent vinoxy radical, and L is the length of the TOF path. The second term is due to the motion of the parent vinoxy radical in the molecular beam which is perpendicular to the TOF axis, and this term is very small (~ 15 cm^{-1}, based on the estimation of the beam velocity of 560 m/s for the EVE/Ar gas mixture) compared to the first term and can be

neglected. The CM product translational energy dependent photofragment angular distributions in the dissociation can be described as the equation mentioned below:[49]

$$P(E_T,\theta) = \left(\frac{1}{4\pi}\right) P(E_T)[1 + \beta P_2(cos\theta)]$$

where $P(E_T)$ is the angle-integrated product translational energy distribution, β is the anisotropy parameter ($-1 \leq \beta \leq 2$), θ is the angle between the nascent velocity of the H-atom produced from photodissociation and the electric vector of the photolysis, and $P_2(cos\theta)$ is the second Legendre polynomial. By combining the product translational energy distributions at parallel ($P_{\parallel}(E_T)$) and perpendicular ($P_{\perp}(E_T)$) polarization, the product translational energy dependent anisotropy parameter, $\beta(E_T)$, can be calculated with $\beta(E_T) = 2 \times [P_{\parallel}(E_T) - P_{\perp}(E_T)] / [P_{\parallel}(E_T) + 2 \times P_{\perp}(E_T)]$.

Figure 8.4 shows the CM product translational energy distributions, $P(E_T)$, with the photolysis polariation parallel and perpendicular to the TOF path and the product translational energy dependent anisotropy parameter, $\beta(E_T)$, at several photolysis photon energies. The $P(E_T)$ distributions are converted directly from the H-atom TOF spectra and the distributions with parallel photolysis have slightly stronger signals than the perpendicular distributions. The $P(E_T)$ distributions have a broad feature peaks at ~3500 cm^{-1} (~10 kcal/mol) and extends to the maximum available energy for the H + $CH_2CO(\tilde{X}\,^1A_1)$ product channel in all the $P(E_T)$ distributions at different photolysis wavelengths. The $\beta(E_T)$ is positive in the range of 0.10 to 0.24 in the near UV region studied. The observed anisotropic product angular distribution indicates the dissociation time scale is shorter than one rotational period of the vinoxy radical. The translational energy release of the H-atom loss channel is modest and the average CM product

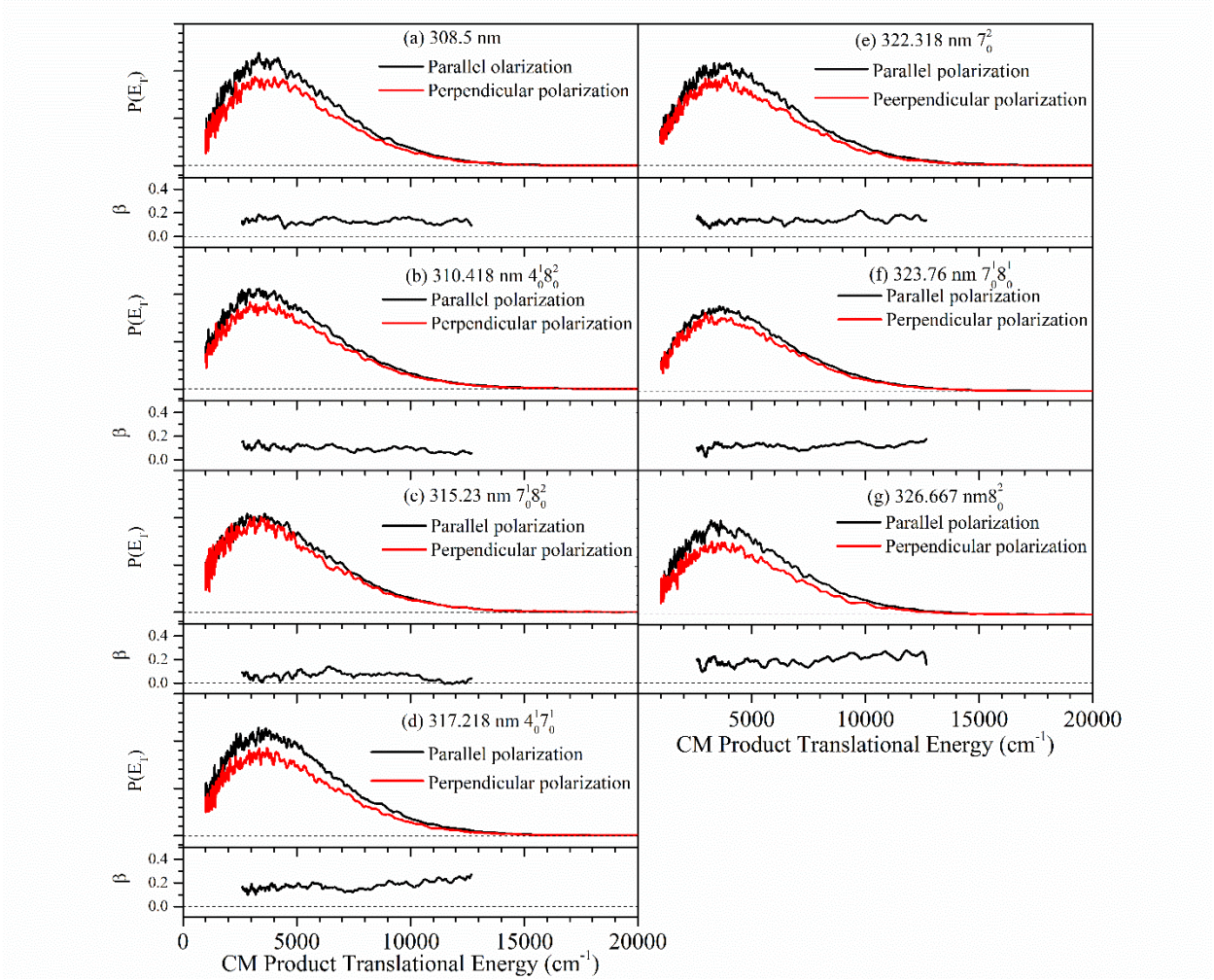

Figure 8.4. Photofragment translational energy distributions $P(E_T)$ and translational energy dependent anisotropy parameter, $\beta(E_T)$, for the H + $CH_2CO(\tilde{X}^1A_1)$ product channel. The black curves in $P(E_T)$ present the distribution with the polarization of the photolysis radiation parallel to the TOF axis, ∥, $\theta = 0°$, while the red curves indicate the perpendicular (⊥, $\theta = 90°$) polarization. The distributions at parallel polarization have slightly stronger signals, indicating an anisotropic product angular distribution. Vibronic assignments are given in addition to the photon energies.

translational energy, $\langle E_T \rangle$, can be calculated from the $P(E_T)$ distributions to be a value about 4850 cm^{-1}, and the fraction of $\langle E_T \rangle$ in the maximum available of the H + $CH_2CO(\tilde{X}^1A_1)$ product channel, $\langle f_T \rangle$, is obtained for each photolysis wavelength. Figure 8.5 presents the $\langle f_T \rangle$ values in the photolysis region of 308 to 328 nm, and the $\langle f_T \rangle$ values are in the range of 0.24 to 0.26 for the H-atom product channel. This small $\langle f_T \rangle$ is likely due to the statistical like dissociation of the vinoxy radical on the ground electronic state over a small exit barrier.

8.4 Discussions

The near UV photodissociation dynamics of the vinoxy radical was studied via the $\tilde{B}^2A''$ state in the region of 308 to 327 nm. The H-atom product channels are observed directly from the H-atom TOF spectra. The H-atom REMPI spectrum shows vibronic structures of the $\tilde{B}^2A''$state of the vinoxy radical, and the structures in the REMPI spectrum have a reasonable agreement with previous the absorption features of the vinoxy radical[1,41] and the PFY spectrum of the CH_3 + CO product channel from the photodissociation of vinoxy radical.[20] This indicates that the H-atom signals detected in this study are from the photodissociation of the vinoxy radical.

The CM product translational energy distributions of the H-atom product channel show a modest translational energy release with the peak at ~ 3500 cm^{-1} (10 kcal/mol) for all the distributions at different photolysis wavelengths. The $\langle f_T \rangle$value is about a constant around 0.25 in the photolysis wavelength region of 308 – 328 nm. These indicate that the

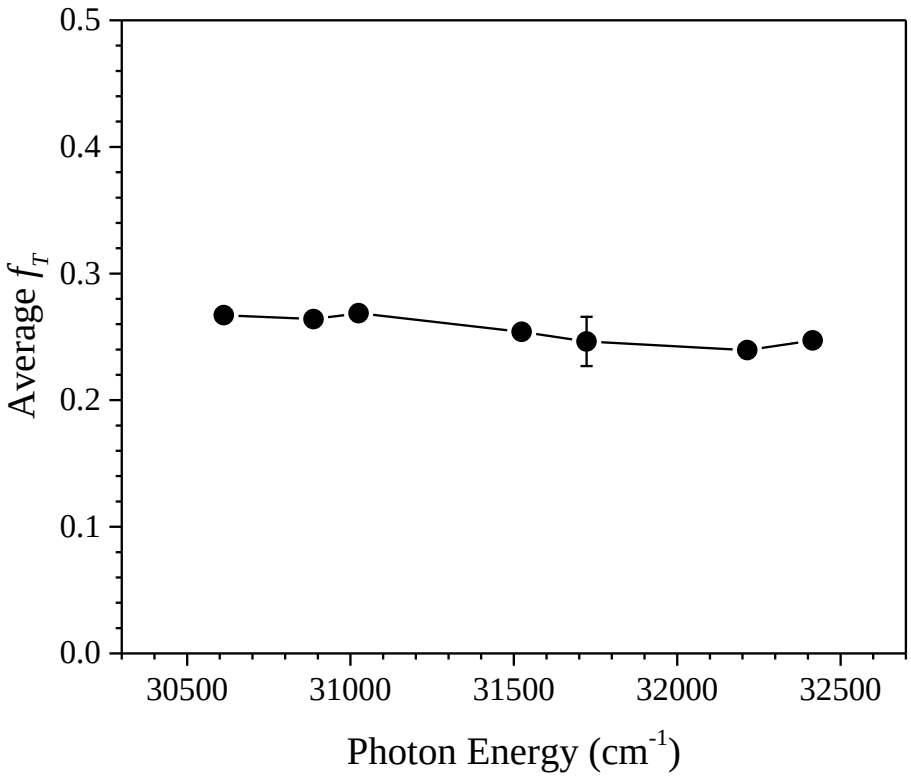

Figure 8.5. Fraction of the average translational energy released in the total available energy, $\langle f_T \rangle$, in the photodissociation of the vinoxy radical as a function of the photon energy. The average translational energies are calculated from the experimental $P(E_T)$ distributions, and the total available energies are derived from the corresponding photon energy and the bond dissociation energy of the vinoxy radical to H + ketene products. The error bar represents the 95% confident limit from repeated measurements.

dissociation dynamics would be the internal conversion from the electronic excited state first, then followed by the C-H bond cleavage to the products. Our observation is consistent with the study by Neumark and coworkers, and they also found that for the CH_3 + CO product channel the P(E_T) distribution is modest for the photodissociation of the vinoxy radical via the $\widetilde{B}^2A''$ state.[20] The product angular distribution for the H-atom loss channel is anisotropic (β = 0.10 to 0.24) at all the photolysis wavelengths in this study. The non-zero β parameter indicates that the dissociation time scale is shorter than or equal to the rotational period of the vinoxy radical, but the modest translational energy release in the H + C_2H_2O channel suggests a slow dissociation process.

As shown in Figure 8.1, there are three possible dissociation channels that lead to the H + $CH_2CO(\widetilde{X}^1A_1)$ products. The $\widetilde{B}^2A''$ state vinoxy radical could undergo internal conversion to the $\widetilde{A}^2A'$ state then have the C-H bond cleavage over an energy barrier (TS4) with the exit barrier of 11.30 kcal/mol (3950 cm^{-1}), or have internal conversion to the ground electronic state followed by the C-H bond breaking through an avoided crossing (TS5) with the exit barrier of 3.00 kcal/mol (1050 cm^{-1}) given by Benson.[50] The third channel is the dissociation of the acetyl radical (CH_3CO) after the isomerization. This channel is not likely the main dissociation channel for the H + $CH_2CO(\widetilde{X}^1A_1)$ products because of the competing channel leading to the CH_3 + CO products with a much lower energy barrier (17.30 kcal/mol eV for CH_3 + CO channel and 47.27 kcal/mol eV for H + $CH_2CO(\widetilde{X}^1A_1)$). The dissociation pathways for the H product channels would be the internal conversion first to $\widetilde{A}^2A'$ state or $\widetilde{X}^2A''$ state from the $\widetilde{B}^2A''$ followed by the C-H bond cleavage. The convoluted CM distributions from these two channels would give the

overall $P(E_T)$ distribution with a broad feature and the peak around 3500 cm^{-1}, which is consistent with the exit barriers of these two channels.

The product angular distribution of the H + $CH_2CO(\tilde{X}^1A_1)$ channel is anisotropic. Typically, the unimolecular dissociation of the hot free radical would have an isotropic product angular distribution, for example, allyl, 1-propenyl, and 2-propenyl radicals.[51-53] Our previous studies on the photodissociation of ethyl, *n*-propyl, *i*-propyl, and 1-penyl radicals on the same experimental apparatus show bimodal CM product translational energy distributions.[47,48,54] The fast channel with the large translational energy release has an anisotropic product angular distribution ($\beta > 0$) for all these three radicals, which indicate a direct dissociation of the radical to the products and the dissociation time shorter than one rotational period of the radical. The slow channel has a modest translational energy released with an isotropic product angular distribution ($\beta = 0$) with the dissociation time scale longer than one rotational period of the parent radical.

The initial UV excitation in the photodissociation of the vinoxy radical involves the $\tilde{B}^2A'' \leftarrow \tilde{X}^2A''$ transition, whose transition dipole moment is in the C_s plane of the ground state vinoxy radical. Neumark and coworkers observed a positive anisotropy parameter (β up to ~ 0.5) for the CH_3 + CO product channel.[20] This indicates that the velocity vector of the dissociating product is ~ 45° relative to the transition dipole moment of the $\tilde{B}^2A'' \leftarrow \tilde{X}^2A''$ transition. Our observation of the product angular distribution for the H-atom product channel has a positive β parameter as well, with the β in the range of 0.10 to 0.24 in the UV region studied. The maximum β parameter could give a constrain of the velocity vector of the leaving H-atom to be ~ 50° relative to the transition dipole moment of the $\tilde{B}^2A'' \leftarrow$

$\tilde{X}^2A''$ transition. As predicted by Neumark and coworkers, the TS5 geometry in Figure 8.1 breaks the C_s symmetry with the out-of-plane motion of the CH bond on the CHO group.[20] The leaving H-atom on the CHO group would give the slightly positive anisotropy parameter which is consistent with our observation, and the dissociation time scale is shorter than the rotational period of the vinoxy radical.

The H + CH_2CO product channel observed in this study and the CH_3 + CO product channel investigated by Neumark and coworkers[20] from the photodissociation of the vinoxy radical via the $\tilde{B}^2A''$ state have a modest translational energy released with anisotropic product angular distributions indicate a shorter time scale for the entire process (internal conversion and unimolecular dissocaition) than the rotational period of the vinoxy radical.

8.5 Conclusion

The photodissociation of the vinoxy radical via the $\tilde{B}^2A''$ state was study. The H-atom REMPI spectrum and H-atom PFY spectrum are in a reasonable agreement with the vinoxy radical absorption spectrum and the CH_3 product PYF spectrum, which confirming the H-atom product from the photodissociation of the vinoxy radical. The CM product translational energy distribution has a broad feature with the peak around 3500 cm^{-1} with the anisotropy parameter in the range of 0.10 to 0.24. The dissociation time scale is shorter than one rotational period of the vinoxy radical. The dissociation mechanism would be the

internal conversion of the vinoxy radical from the $\widetilde{B}^2A''$ state to $\widetilde{A}^2A'$ or $\widetilde{X}^2A''$ state followed by a rapid breaking of the C-H bond.

Reference

1. H. E. Hunziker, H. Kneppe, and H. R. Wendt, *J. Photochem.* **17**, 377 (1981).

2. A. M. Schmoltner, P. M. Chu, R. J. Brudzynski, and Y. T. Lee, *J. Chem. Phys.* **91**, 6926 (1989).

3. P. Casavecchia, G. Capozza, E. Segoloni, F. Leonori, N. Balucani, and G. G. Volpi, *J. Phys. Chem. A* **109**, 3527 (2005).

4. D. J. Donaldson, I. V. Okuda, and J. J. Sloan, *Chem. Phys.* **193**, 37 (1995).

5. V. Schmidt, G. Y. Zhu, K. H. Becker, and E. H. Fink, *Ber. Bunsenges, Phys. Chem.* **89**, 321 (1985).

6. K. Lorenz and R. Zellner, *Ber. Bunsenges, Phys. Chem.* **88**, 1228 (1984).

7. T. J. Wallington, R. Liu, P. Dagaut, and M. J. Kurylo, *Int. J. Chem. Kinet.* **20**, 41 (1988).

8. D. Gutman and H. H. Nelson, *J. Phys. Chem.* **87**, 3902 (1983).

9. K. Lorenz, D. Rhasa, R. Zellner, and B. Fritz, *Ber. Bunsenges, Phys. Chem.* **89**, 341 (1985).

10. L. Zhu and G. Johnston, *J. Phys. Chem.* **99**, 15114 (1995).

11. J. D. Weidman, R. T. Allen, K. B. Moore, and H. F. Schaefer, *J. Chem. Phys.* **148**, 184308 (2018).

12. K. I. Barnhard, A. Santiago, M. He, F. Asmar, and B. R. Weiner, *Chem. Phys. Lett.* **178**, 150 (1991).

13. N. C. Baird, R. R. Gupta, and K. F. Taylor, *J. Am. Chem. Soc.* **101**, 4531 (1979).

14. N. C. Baird and K. F. Taylor, *Can. J. Chem.* **58**, 733 (1980).

15. M. Dupuis, J. J. Wendoloski, and W. A. Lester, *J. Chem. Phys.* **76**, 488 (1982).

16. E. S. Huyser, D. Feller, W. T. Borden, and E. R. Davidson, *J. Am. Chem. Soc.* **104**, 2956 (1982).

17. Y. Endo, S. Saito, and E. Hirota, *J. Chem. Phys.* **83**, 2026 (1985).

18. M. Yamaguchi, T. Momose, and T. Shida, *J. Chem. Phys.* **93**, 4211 (1990).

19. M. Yamaguchi, *Chem. Phys. Lett.* **221**, 531 (1994).

20. D. L. Osborn, H. Choi, D. H. Mordaunt, R. T. Bise, D. M. Neumark, and C. M. Rohlfing, *J. Chem. Phys.* **106**, 3049 (1997).

21. L. S. Alconcel, H.-J. Deyerl, V. Zengin, and R. E. Continetti, *J. Phys. Chem. A* **103**, 9190 (1999).

22. S. Matsika and D. R. Yarkony, *J. Chem. Phys.* **117**, 7198 (2002).

23. M. C. Bacchus-Montabonel, K. Piechowska, Y. S. Tergiman, and J. E. Sienkiewicz, *J. Mol. Struct. (THEOCHEM)* **729**, 115 (2005).

24. P. Botschwina, *Mol. Phys.* **103**, 1441 (2005).

25. R. A. Young and D. R. Yarkony, *J. Chem. Phys.* **123**, 084315 (2005).

26. K. Piechowska-Strumik, M.-C. Bacchus-Montabonel, Y. S. Tergiman, and J. E. Sienkiewicz, *Chem. Phys. Lett.* **425**, 225 (2006).

27. K. Piechowska-Strumik, D. Lauvergnat, M. C. Bacchus-Montabonel, and M. Desouter-Lecomte, *Chem. Phys. Lett.* **425**, 16 (2006).

28. M. Yamaguchi, S. Inomata, and N. Washida, *J. Phys. Chem. A* **110**, 12419 (2006).

29. D. I. G. Bennett, L. J. Butler, and H.-J. Werner, *J. Chem. Phys.* **127**, 094309 (2007).

30. P. S. Thomas, R. Chhantyal-Pun, N. D. Kline, and T. A. Miller, *J. Chem. Phys.* **132**, 114302 (2010).

31. H. Su and R. Bersohn, *J. Chem. Phys.* **115**, 217 (2001).

32. D. A. Ramsay, *J. Chem. Phys.* **43**, S18 (1965).

33. G. Inoue and H. Akimoto, *J. Chem. Phys.* **74**, 425 (1981).

34. M. Heaven, L. Dimauro, and T. A. Miller, *Chem. Phys. Lett.* **95**, 347 (1983).

35. L. F. DiMauro, M. Heaven, and T. A. Miller, *J. Chem. Phys.* **81**, 2339 (1984).

36. R. D. Mead, K. R. Lykke, W. C. Lineberger, J. Marks, and J. I. Brauman, *J. Chem. Phys.* **81**, 4883 (1984).

37. T. Gejo, M. Takayanagi, T. Kono, and I. Hanazaki, *Chem. Lett.* **22**, 2065 (1993).

38. K. I. Barnhard, M. He, and B. R. Weiner, *J. Phys. Chem.* **100**, 2784 (1996).

39. R. Wan, X. Chen, F. Wu, and B. R. Weiner, *Chem. Phys. Lett.* **260**, 539 (1996).

40. L. R. Brock and E. A. Rohlfing, *J. Chem. Phys.* **106**, 10048 (1997).

41. L. Wang and J. Zhang, *Chin. J. Chem. Phys.* **17**, 357 (2004).

42. B. Ruscic, *J. Phys. Chem. A* **119**, 7810 (2015).

43. J. L. Miller, L. R. McCunn, M. J. Krisch, L. J. Butler, and J. Shu, *J. Chem. Phys.* **121**, 1830 (2004).

44. M. L. Morton, D. E. Szpunar, and L. J. Butler, *J. Chem. Phys.* **115**, 204 (2001).

45. C.-S. Lam, J. D. Adams, and L. J. Butler, *J. Phys. Chem. A* **120**, 2521 (2016).

46. G. Amaral, K. Xu, and J. Zhang, *J. Chem. Phys.* **114**, 5164 (2001).

47. Y. Song, X. Zheng, W. Zhou, M. Lucas, and J. Zhang, *J. Chem. Phys.* **142**, 224306 (2015).

48. G. Sun, Y. Song, and J. Zhang, *Chin. J. Chem. Phys.* **31**, 439 (2018).

49. R. N. Zare, *Mol. Photochem.* **4**, 1 (1972).

50. S. W. Benson, *Thermochemical Kinetics* (Wiley, New York, 1968).

51. Y. Song, M. Lucas, M. Alcaraz, J. Zhang, and C. Brazier, *J. Phys. Chem. A* **119**, 12318 (2015).

52. M. Lucas, Y. Song, J. Zhang, C. Brazier, P. L. Houston, and J. M. Bowman, *J. Phys. Chem. A* **120**, 5248 (2016).

53. G. Sun, M. Lucas, Y. Song, J. Zhang, C. Brazier, P. L. Houston, and J. M. Bowman, *J. Phys. Chem. A* **123**, 9957 (2019).

54. G. Amaral, K. Xu, and J. Zhang, *J. Chem. Phys.* **114**, 5164 (2001).

Chapter 9

H-atom Product Channel in the Ultraviolet Photodissociation of the Thiomethoxy Radical (CH_3S) via the $\tilde{B}^2A_2$ State

Abstract

The photodissociation dynamics of jet-cooled thiomethoxy radical (CH_3S) via the $\tilde{B}^2A_2 \leftarrow \tilde{X}^2E$ transition was studied in the ultraviolet (UV) region of 216–225 nm using the high-*n* Rydberg H-atom time-of-flight (HRTOF) technique. The H-atom product channel was directly observed from the H-atom TOF spectra (using both dimethyl disulfide and dimethyl sulfide precursors). The H-atom photofragment yield (PFY) spectrum showed a broad feature in the region of 216–225 nm and three $\tilde{B}^2A_2$ vibronic peaks at 217.7, 220.3, and 221.5 nm. Several H-atom dissociation pathways were identified. The excited state CH_3S had a repulsive, prompt dissociation pathway to the ground-state $H_2CS(\tilde{X}^1A_1) + H$ products, with the product translational energy peaking near the maximum available energy, a predominant C-S stretch vibrational excitation in $H_2CS(\tilde{X}^1A_1)$, and an anisotropic angular distribution. The main pathway was the $H_2CS(\tilde{X}^1A_1) + H$ product channel via unimolecular dissociation of internally hot CH_3S radical in the ground electronic state after internal conversion from the electronic excited state, with a modest translational energy release (peaking at a low translational energy of ~ 11 kcal/mol and extending near the maximum available energy) and a nearly isotropic angular distribution. The H +

$H_2CS(\tilde{A}^1A_2)$ and H + $H_2CS(\tilde{a}^3A_2)$ product channels were also observed but were minor channels. The C-H bond dissociation energy of CH_3S to the H + $H_2CS(\tilde{X}^1A_1)$ products was determined to be 48.8 $\pm$ 0.7 kcal/mol.

9.1 Introduction

The thiomethoxy (CH_3S) radical is an important intermediate in the atmospheric oxidation processes of sulfur compounds such as methanethiol (CH_3SH), dimethyl sulfide (DMS, CH_3SCH_3), and dimethyl disulfide (DMDS, CH_3SSCH_3),[1-6] and further oxidation of the CH_3S radical leads to SO_2 and SO_3 and contributes to acid precipitation in the atmosphere.

The spectroscopy of thiomethoxy radical has been studied for decades since its ultraviolet (UV) absorption band was first observed at 218.5 nm.[7,8] The geometric and spectral information of the CH_3S radical in the ground electronic state $\tilde{X}^2E$ and the first electronic excited state $\tilde{A}^2A_1$ was provided by the studies on near-UV absorption spectra,[9] electronic emission spectra,[10] microwave spectroscopy,[11] photoelectron and photodetachment spectroscopy,[12-14] laser-induced fluorescence (LIF),[15-19] fluorescence depletion spectroscopy (FDS),[19] four-wave mixing spectroscopy,[20,21] and photofragment yield (PFY) spectra.[22-24] The $\tilde{A}^2A_1 \leftarrow \tilde{X}^2E$ transition is characterized with predominant vibrational progressions in the C-S stretch (ν_3) mode, 3^n, and its combination band with the CH_3 umbrella (ν_2) mode, $2^1 3^n$.[15-23] The UV absorption band observed around 218.5 nm was diffuse and structureless,[7-9,25] and was assigned to the $\tilde{B}^2A_2 \leftarrow \tilde{X}^2E$ transition.[26] The CH_3 + $S(^3P_J)$ PFY spectrum from photodissociation of CH_3S in the region of 215 to 222 nm confirmed this UV absorption band and resolved the transitions from the $\tilde{X}^2E_{3/2}$ and $\tilde{X}^2E_{1/2}$ states.[22]

The possible dissociation product channels of the CH_3S radical are listed as follows (the energetics of the $H + H_2CS(\tilde{X}^1A_1)$ channel is based on the current study):[19,22,23,26-28]

$CH_3S(\tilde{X}^2E) \rightarrow H + H_2CS(\tilde{X}^1A_1)$ $\Delta H_0 = 48.8 \pm 0.7$ kcal/mol

$\rightarrow H + H_2CS(\tilde{a}^3A_2)$ $\Delta H_0 = 90.3 \pm 0.7$ kcal/mol

$\rightarrow H + H_2CS(\tilde{A}^1A_2)$ $\Delta H_0 = 95.6 \pm 0.7$ kcal/mol

$\rightarrow CH_3(\tilde{X}^2A_2'') + S(^3P_J)$ $\Delta H_0 = 70.2 \pm 0.3$ kcal/mol

$\rightarrow CH_3(\tilde{X}^2A_2'') + S(^1D)$ $\Delta H_0 = 96.6 \pm 0.3$ kcal/mol

Figure 9.1 shows the potential energy diagram of CH_3S dissociation along the C-S and C-H reaction coordinate based on previous theoretical calculations[26,27] and experimental studies.[19,22,28] The ground state $CH_3S(\tilde{X}^2E)$ correlates asymptotically to the $CH_3(\tilde{X}^2A_2'') + S(^3P_J)$ products in C_{3v} symmetry and the $H + H_2CS(\tilde{X}^1A_1)$ and $H_2CS(\tilde{a}^3A_2)$ products in C_s symmetry. The first electronic excited state $CH_3S(\tilde{A}^2A_1)$ correlates asymptotically to the $CH_3(\tilde{X}^2A_2'') + S(^1D)$ products in C_{3v}, and this surface is crossed by three repulsive states, $^4A_2$, ^4E, and $\tilde{B}^2A_2$. These three repulsive states correlate to the $CH_3(\tilde{X}^2A_2'') + S(^3P_J)$ product channel and induce predissociation in the electronic excited state $CH_3S(\tilde{A}^2A_1)$. In the C_s symmetry, the first electronic excited state $\tilde{A}^2A_1$ correlates asymptotically to the higher energy $H + H_2CS(\tilde{b}^3A_1)$ products.

The photodissociation dynamics of the thiomethoxy radical has been studied experimentally[19-24,26,29] and theoretically.[26,27] The radiative and nonradiative decays of the

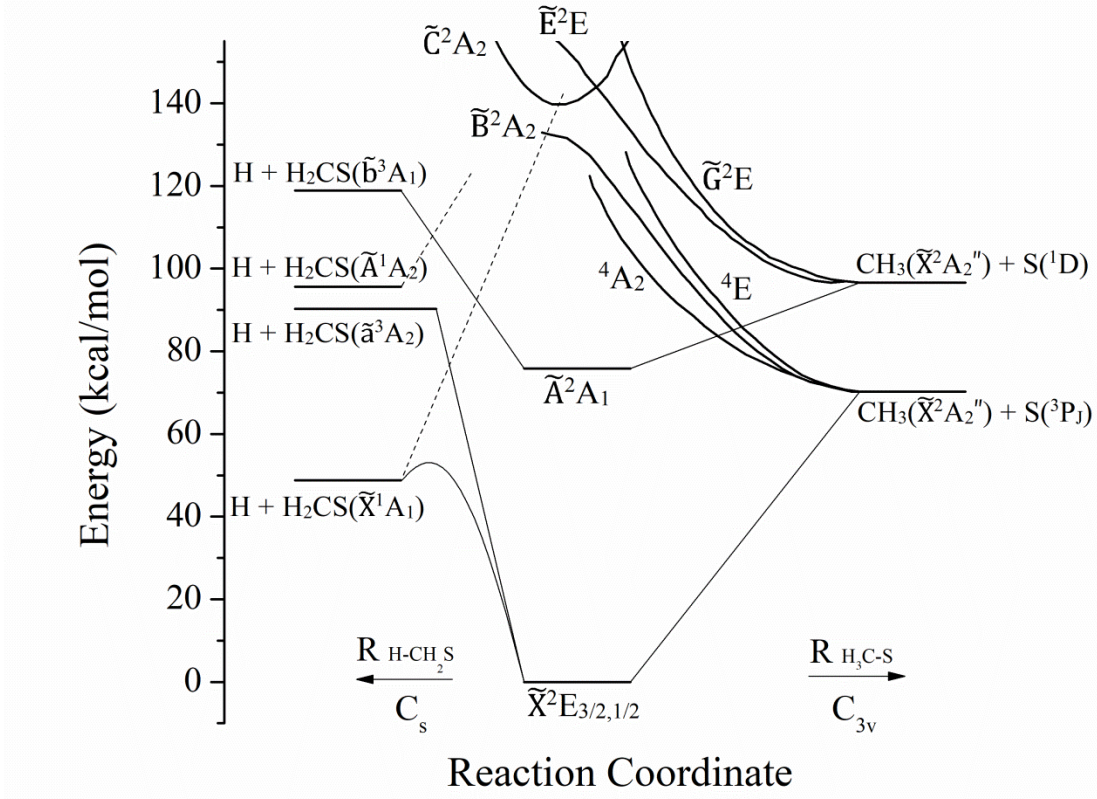

Figure 9.1. Potential energy diagram of the CH_3S system. The dissociation channels leading to H + H_2CS and CH_3 + S products are shown. The energies are based on previous theoretical calculations (refs 26, 27) and experimental studies (refs 19, 22, and 28). The dashed lines show possible correlations from the excited-states of CH_3S to the H + H_2CS products.

CH_3S radical in the $\widetilde{A}^2A_1$ state have been examined by Miller and co-workers using LIF and FDS,[19] and Lee and co-workers using four-wave mixing spectroscopy.[20,21] The lifetimes of the predominant 3^n and 2^13^n vibronic bands of the $\widetilde{A}^2A_1$ state decreased with increasing excitation energy, indicating mode specificity in the nonradiative processes and that the C-S stretch (ν_3) mode was the promoting mode for dissociation to the $CH_3(\widetilde{X}^2A_2'')$ + $S(^3P_J)$ products.[19-21] The comparison among the LIF, FDS and four-wave mixing spectroscopy indicated that ~ 80%, 94%, and 98% of the 3^2, 2^13^1, and 2^13^2 states of $CH_3S(\widetilde{A}^2A_1)$ would undergo nonradiative decay, respectively. Miller and co-workers also suggested another nonradiative channel such as unimolecular dissociation to the H + H_2CS product after internal conversion from the excited $\widetilde{A}^2A_1$ state.[19] Neumark and co-workers investigated the photodissociation of CH_3S via the $\widetilde{A}^2A_1$ state in the photolysis wavelength range of 310 to 370 nm with photofragment translational spectroscopy.[22] Only the $CH_3(\widetilde{X}^2A_2'')$ + $S(^3P_J)$ product channel was observed, with a large translational energy release peaking near the maximum available energy and the anisotropy parameter β varying from -0.2 to -1.0 as the photon energy increased. The $CH_3(\widetilde{X}^2A_2'')$ + $S(^3P_J)$ product channel is via a fast dissociation in the repulsive states, $^4A_2$, ^4E, and $\widetilde{B}^2A_2$, after surface crossing and predissociation of the electronic excited $\widetilde{A}^2A_1$ state. The PFY spectrum of the $CH_3(\widetilde{X}^2A_2'')$ + $S(^3P_J)$ products from the $\widetilde{A}\,^2A_1$ state revealed predominant 3^n and 2^13^n vibronic progressions.[22] Zhang and co-workers investigated the H-atom product channel from the photodissociation of CH_3S via the $\widetilde{A}^2A_1$ state at the photolysis wavelength of 344–362 nm using the high-*n* Rydberg H-atom time-of-flight (HRTOF) technique.[23,24] The H + $H_2CS(\widetilde{X}^1A_1)$ product translational energy release is modest with a peak at ~ 9 kcal/mol and

the product angular distribution is isotropic. The mechanism of the H + $H_2CS(\tilde{X}^1A_1)$ product channel via the $\tilde{A}^2A_1$ state is consistent with unimolecular dissociation in the ground electronic state after internal conversion. Mode specificity was observed in the dissociation, two vibronic levels of $\tilde{A}^2A_1$, 2^13^1 and 2^13^2, dissociate to H + $H_2CS(\tilde{X}^1A_1)$, whereas the others in the vicinity (2^13^3 and 3^n, n = 3-6) dissociate to CH_3 + $S(^3P_J)$.[24, 25]

Neumark and co-workers also investigated the photodissociation dynamics of CH_3S via the $\tilde{B}^2A_2$ state in the UV region of 215 to 222 nm.[22] The CH_3 + $S(^3P_J)$, CH_3 + $S(^1D)$, and CH_2 + $SH(^2\Pi)$ product channels were observed, with CH_3 + $S(^3P_J)$ as the dominant product channel. The H-atom product channel was not observed due to limited detection geometry and efficiency for the H + H_2CS products in this experiment. The CH_3 + $S(^3P_J)$ PFY spectrum shows two peaks at 45620 cm^{-1} (219.2 nm) and 45350 cm^{-1} (220.5 nm), assigned to transitions from the $\tilde{X}^2E_{3/2}$ and $\tilde{X}^2E_{1/2}$ states, respectively. The CH_3 + $S(^3P_J)$ photofragments have a highly anisotropic angular distribution with $\beta = -0.98 \pm 0.10$ and a large translational energy release, consistent with direct dissociation on the electronic excited $\tilde{B}^2A_2$ state. Ashfold and co-workers investigated secondary photolysis of the primary product $CH_3S(\tilde{X}^2E)$ in the UV photodissociation of methanethiol using the HRTOF technique.[29] The H-atom loss product channel of CH_3S was observed in the range of 213 to 220 nm, and the H_2CS co-fragment was produced mainly in the $\tilde{A}^1A_2$ electronic excited state.[29] The bond dissociation energy D_0(H-CH_2S) was determined to be 48.9 kcal/mol. Ng and co-workers investigated the S-atom product channel in the secondary photodissociation of CH_3S (from the CH_3SCH_3 photolysis) at 193 nm using 2 + 1 resonance-enhanced multiphoton ionization (REMPI) technique.[26] The product branching

ratio of $S(^3P_J)/S(^1D)$ was determined to be 0.15/0.85 and the spin-orbit fine-structure population of the $S(^3P_{2,1,0})$ product was nearly statistical. Their *ab initio* calculation indicated that the CH_3S radical was excited to the $\tilde{C}^2A_2$ Rydberg state at 193 nm, and the predissociation from the $\tilde{C}^2A_2$ state via crossing with the repulsive $\tilde{E}^2E$ state would yield the $S(^1D) + CH_3(\tilde{X}^2A_2'')$ products, whereas the predissociation via an avoided crossing with the repulsive $\tilde{B}^2A_2$ state could lead to the $S(^3P_J) + CH_3(\tilde{X}^2A_2'')$ products.

In this chapter, the photodissociation dynamics of jet-cooled thiomethoxy radical is investigated via the $\tilde{B}^2A_2$ state in the UV region of 216 to 225 nm using the HRTOF technique. The H-atom product channel was directly observed from the H-atom TOF spectra. H-atom PFY spectrum was obtained and showed a broad feature and several vibronic bands. The product translational energy and angular distributions of the H-atom product channel were converted from the H-atom TOF spectra. Several H-atom dissociation channels of CH_3S were identified. A fast and repulsive dissociation channel to the $H + H_2CS(\tilde{X}^1A_1)$ products was observed, with the translational energy peaking near the maximum available energy. The CH_3S radical could also undergo unimolecular dissociation in the ground electronic state after internal conversion from the electronic excited state, producing the $H + H_2CS(\tilde{X}^1A_1)$ products with a modest translational energy release. The $H + H_2CS(\tilde{A}^1A_2)$ and $H + H_2CS(\tilde{a}^3A_2)$ product channels were observed as minor dissociation channels.

9.2 Experimental

The HRTOF technique was employed and the details were reported previously.[23,30-32] Dimethyl disulfide (DMDS, CH_3SSCH_3, ACROS 99%) and dimethyl sulfide (DMS, CH_3SCH_3, ACROS 99+%) were used as the precursors to generate the thiomethoxy radicals.[33] The mixture of the precursor in Ar (~1% for DMDS or ~5% for DMS) at a total pressure of ~1.2 atm was expanded from a pulse valve. The thiomethoxy radicals were produced by photolyzing the precursor molecules with a 193 nm radiation from an ArF excimer laser and then cooled internally (~ 15 K)[31] by supersonic expansion in the molecular beam before entering the photodissociation region in the reaction chamber. The radical beam produced from the DMDS precursor was characterized using 121.6 nm vacuum ultraviolet (VUV) photoionization TOF mass spectrometry (TOFMS), and the production of the thiomethoxy radical was confirmed. Downstream in the reaction chamber, the thiomethoxy radicals were photodissociated by a tunable, linearly polarized UV laser beam (216-225 nm, $\leq$ 0.3 cm^{-1} linewidth, 1.0-3.0 mJ/pulse) that was properly delayed following the ArF laser for radical production. The polarization of the UV photolysis radiation can be changed by a Fresnel-Rhomb achromatic $\lambda/2$ plate for the H-atom product angular distribution study. Immediately following the UV photolysis laser beam (~10 ns), the H-atom products from the photodissociation of the thiomethoxy radical were pumped by two-color resonant excitation (121.6 nm + 366.3 nm),that is, from 1^2S to 2^2P via the H-atom Lyman-α transition and then to a metastable high-*n* Rydberg state. A small fraction of these high-*n* Rydberg state H atoms drifted with their nascent velocities

to a microchannel plate (MCP) detector which was positioned perpendicular to the molecular beam, and the metastable H atoms were field-ionized in front of the detector and detected. The length of the flight path was 37.28 cm, which was calibrated by photodissociation of HBr with the well-studied HBr bond dissociation energy and spin-orbit splitting of the Br($^2P_{3/2}$) and Br($^2P_{1/2}$) products. The ion signals were amplified by a fast preamplifier and averaged by a multichannel scaler to obtain the H-atom TOF spectra. The H-atom TOF spectra were acquired with 90–240 k laser shots each spectrum.

9.3 Results

The thiomethoxy radical molecular beam from the DMDS precursor was characterized by VUV photoionization mass spectrometry using the Lyman-α radiation (10.2 eV). The net TOF mass spectrum of the DMDS precursor with the 193 nm radical production photolysis radiation on minus off is shown in Figure 9.2. The CH_3S radical was characterized at m/z = 47 and other byproduct photofragments such as CH_3, H_2CS, SS and CH_3SS were observed at m/z = 15, 46, 64, and 79, respectively. The observed photoproducts were consistent with the previous studies of photodissociation of DMDS.[8,33]

The H-atom TOF spectra from the photodissociation of CH_3S (produced from 193 nm photolysis of the DMDS and DMS precursors) were measured in the UV photolysis region of 216–225 nm. The H-atom product angular distributions were obtained with the polarization of the photolysis laser radiation parallel (∥, θ = 0°) and perpendicular (⊥, θ = 90°) to the TOF path. Four types of TOF spectra were taken: (1) full spectrum with 193

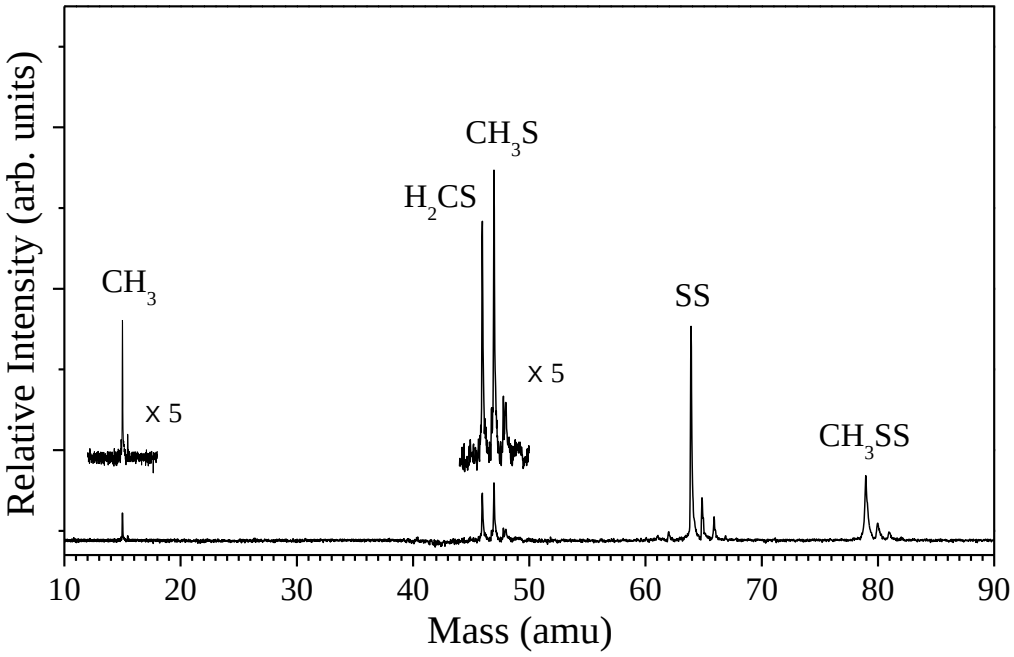

Figure 9.2. 121.6 nm VUV photoionization mass spectrum of the thiomethoxy radical beam by using the dimethyl disulfide (DMDS) precursor in the Ar gas. This net mass spectrum was obtained by subtracting the background spectrum with 193 nm photolysis laser off from the full spectrum with 193 nm on. The peak at m/z = 47 is assigned to the thiomethoxy radical.

nm radiation on for the thiomethoxy radical production, the UV photolysis radiation on, and the Rydberg H-atom tagging probe-laser radiations (121.6 nm + 366.3 nm) on; (2) precursor background spectrum, with the 193 nm radiation off but the UV photolysis radiation and the probe-laser radiations on; (3) radical background spectrum, with the UV photolysis radiation off and the 193 nm radical producing radiation and probe-laser radiations on; (4) probe-laser background, with both 193 nm radiation and UV photolysis radiation off but the probe-laser radiations on. The background spectra of (3) and (4) were observed with negligibly small signals, and the precursor background spectrum (2) had a broad feature that was less than 20% of that in the full spectrum (1). The net H-atom TOF spectrum from the photodissociation of the thiomethoxy radical was obtained by subtracting the precursor background spectrum (2) from the full spectrum (1). Figure 9.3 shows the net TOF spectra from the photodissociation of CH_3S at 220.5 nm from both the DMDS and DMS precursors, with the polarization of the photolysis laser radiation parallel and perpendicular to the TOF path. All TOF spectra were normalized to the same laser power and number of shots. The TOF spectra from these two precursors were very similar, confirming that the main H-atom signals were from the photodissociation of the CH_3S radical. The photolysis laser power dependence of the photodissociation of CH_3S (from the DMDS precursor) was studied at perpendicular polarization with the photolysis radiation power in the range of 1.0 to 2.5 mJ/pulse. The signals at flight time < 22 μs had a linear dependence on the photolysis laser power, whereas those in the longer flight time region showed a nonlinear power dependence at > 1 mJ/pulse, indicating that some of the H atoms produced in this region were due to multiphoton processes. The H-atom TOF spectra used

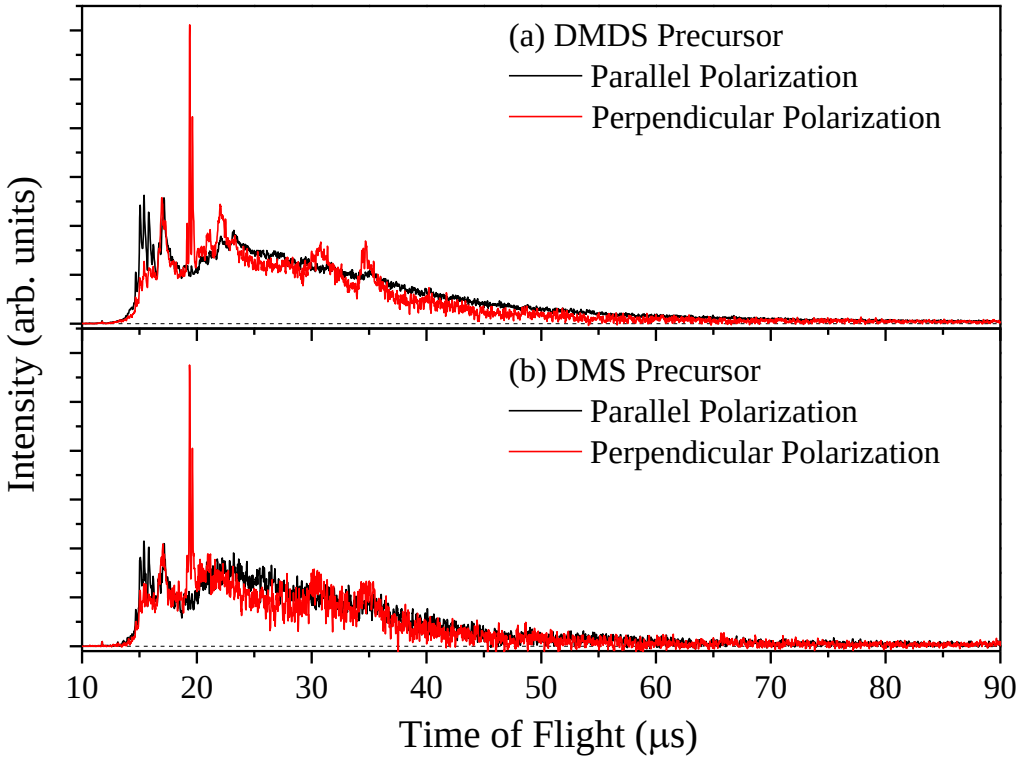

Figure 9.3. H-atom TOF spectra of the photodissociation of jet-cooled CH_3S radical (from the DMDS and DMS precursors) at 220.5 nm photolysis wavelength, with the electric vector of the photolysis radiation parallel and perpendicular to the TOF axis. The spectra are scaled to the same number of laser shots and power (kept at ≤ 1 mJ/pulse).

for data analysis in this work were taken with modest photolysis energy ≤ 1 mJ/pulse in order to minimize multiphoton signals in the longer flight time region.

The H-atom TOF spectra in Figure 9.3 show several anisotropic peaks (more intense at the parallel polarization) around 15 μs and an isotropic peak around 17 μs. The sharp, anisotropic peaks around 19 μs (predominantly at the perpendicular polarization) were due to repulsive $^2\Sigma^- \leftarrow X^2\Pi_{3/2,1/2}$ photodissociation of the SH radical (byproduct in the CH_3S beam) and more details can be found in previous publications.[32,34] The two peaks at ~ 31 and 35 μs were identified as due to photodissociation of the CH_3 radical (byproduct in the CH_3S beam) via the 3s Rydberg states,[35,36] consistent with the production of the H + $CH_2(\tilde{a}^1A_1)$ products from vibrationally excited (hot-band) CH_3 radical in the $\tilde{X}^2A_2''$ state. Although other byproducts such as CH_3SS and H_2CS were found in the beam with the DMDS precursor, they were unlikely to contribute to the H-atom product signals. CH_3SS is more likely to undergo cleavage of the weak C-S or S-S bond; furthermore, the nearly identical H-atom TOF spectra from the DMDS and DMS precursors indicate negligible contribution of CH_3SS (produced only from DMDS). H_2CS has a very weak absorption near 220 nm,[37] as compared with the strong absorption of CH_3S,[7,8] and is unlikely to contribute significantly to the H-atom photodissociation signals. Furthermore, the bond dissociation energy D_0(H-CHS) of H_2CS is ~90 kcal/mol,[38] and the H atoms from photodissociation of the H_2CS byproduct, if produced at all, would only be in the longer time region of > 22 μs at the 220.5 nm photolysis wavelength. The H-atom signals from 14 to 22 μs (except the SH signals at 19 μs) were completely due to the photodissociation of the CH_3S radical. Figure 9.4 presents the TOF spectra in the flight time region of 12 to

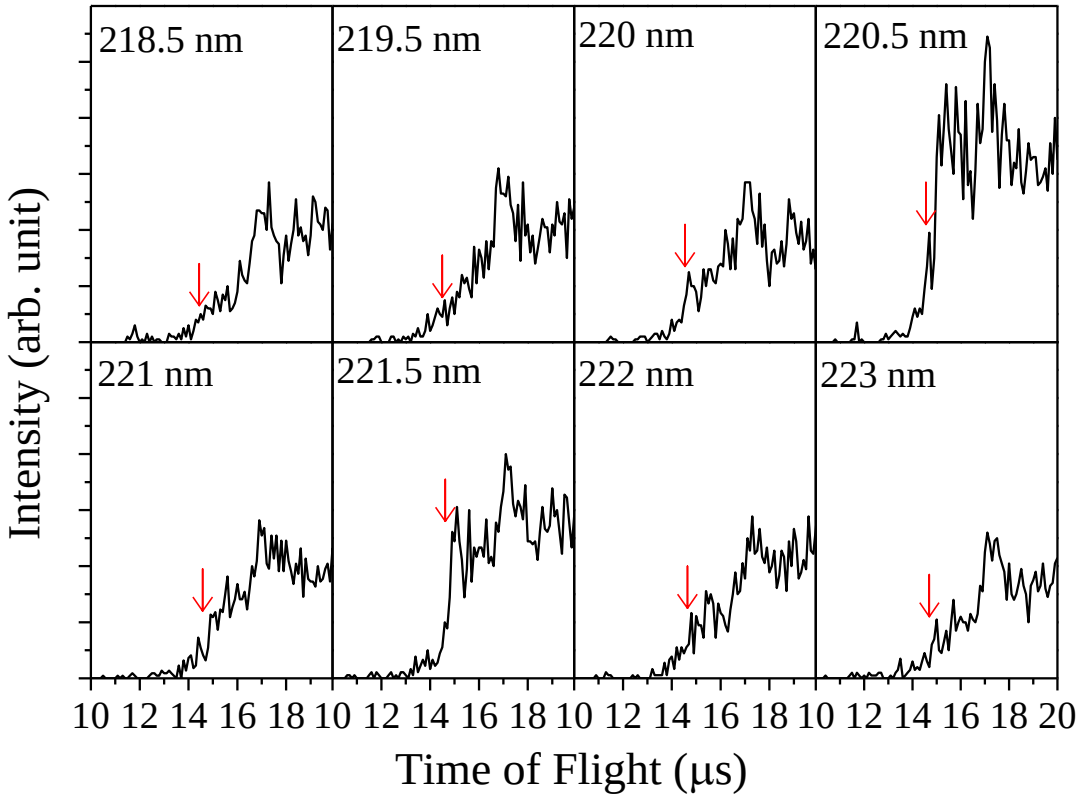

Figure 9.4. 12 to 20 μs flight time region of the H-atom TOF spectra from photodissociation of the CH_3S radical (DMDS precursor) at different wavelengths with parallel photolysis radiation. The arrows indicate the onsets of the H + $H_2CS(\tilde{X}^1A_1)$ product channel at the various photolysis wavelengths. The spectra are scaled to the same number of laser shots and power ($\leq$ 1 mJ/pulse). Note that the sharp, anisotropic peaks around 19 μs due to photodissociation of SH showed up only at the perpendicular polarization.

20 μs at different photolysis wavelengths (at the parallel polarization). The relative intensity of the peaks at ~15 μs varied with the photolysis wavelengths and reached a maximum at 220.3 nm and a second maximum at 221.5 nm. The peak intensity at ~17 μs also varied, but to a lesser extent, with the photolysis wavelengths. This observation suggests that the dissociation mechanism of the CH_3S radical depends on the initial photoexcitation energy (thus the vibronic levels of the electronic excited state of CH_3S) and has at least two H-atom loss dissociation channels in the TOF region of 14 to 20 μs.

The H-atom PFY spectrum (action spectrum) from the UV photodissociation of CH_3S was obtained by integrating the H-atom TOF signals at the parallel photolysis radiation polarization in the short flight time region (14-18 μs) (in order to avoid adding H-atom signals produced from the photodissociation of SH and CH_3, mainly at the perpendicular photolysis polarization) at various photolysis wavelengths. All the integrated signals were normalized with the same laser power and shots and scaled to that at the 220.5 nm photolysis wavelength. Figure 9.5 shows the H-atom PFY spectrum in the region of 216 to 225 nm. A broad feature was observed in this region, in addition to three peaks around 217.7, 220.3 and 221.5 nm. The H-atom PFY spectrum is, in general, consistent with the UV absorption spectra of the CH_3S radical, the diffuse, structureless absorption at 218.5 nm from photolysis of DMS and DMDS by Callear and co-workers,[7,8] the broad peak at ~219 nm from the radiolysis of a mixture of CH_3SH and SF_6 by Anastasi and co-workers,[25] and the broad absorption peaking near ~ 220 nm from the infrared (IR) multiphoton dissociation of DMDS by Kumar and co-workers.[9] Neumark and co-workers acquired the PFY spectrum of the $CH_3 + S(^3P_J)$ product channel in the UV photolysis of

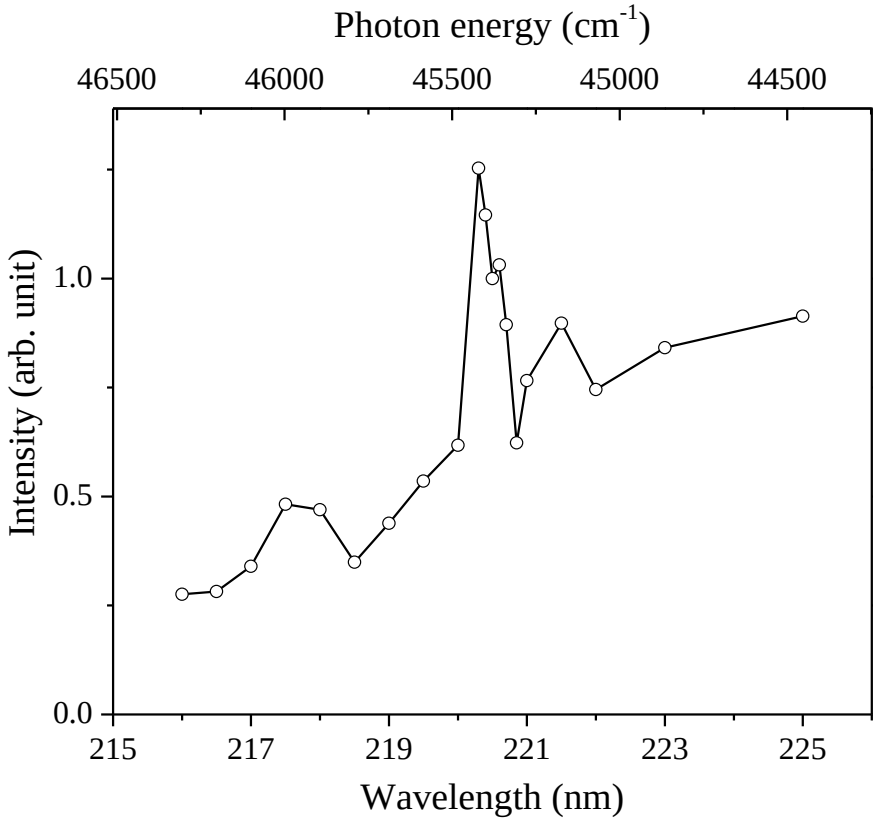

Figure 9.5. H-atom photofragment yield (PFY) spectrum (action spectrum) from the photodissociation of the CH_3S radical (DMDS precursor) as a function of the photolysis wavelength in the region of 216-225 nm. Open circles (○) are the integrated H-atom signals from the TOF spectra at the parallel photolysis polarization in the short flight time region (14-18 μs) (This avoids contributions from photodissociation of SH and CH_3, mainly at the perpendicular photolysis polarization.). All the integrated signals are normalized with the same laser power and number of shots and scaled to that at the 220.5 nm photolysis wavelength.

CH_3S from 215 to 222 nm, showing two peaks at 45620 cm^{-1} (219.2 nm) and 45350 cm^{-1} (220.5 nm) (assigned to transitions from the $\tilde{X}^2E_{3/2}$ and $\tilde{X}^2E_{1/2}$ states, respectively).[22] In our H-atom PFY spectrum, one peak (at 220.3 nm) matched with the 220.5 nm peak in the CH_3 + $S(^3P_J)$ PFY spectrum, whereas the other two were at different wavelengths, possibly due to the difference in the H-atom loss and the CH_3 + $S(^3P_J)$ product channels. The three peaks in the H-atom loss PFY spectrum of CH_3S seem to be due to vibronic structure of CH_3S ($\tilde{B}^2A_2$) (discussed later).

The H-atom product channel center-of-mass (CM) translational energy distribution, $P(E_T)$'s, can be derived from the net H-atom TOF spectra by using the following equation:[23,30,31]

$$E_T = \left(1 + \frac{m_H}{m_{H_2CS}}\right) E_H + \frac{m_H}{m_{H_2CS}} E_{CH_3S} = \frac{1}{2} m_H \left(1 + \frac{m_H}{m_{H_2CS}}\right) \left(\frac{L}{t_H}\right)^2 + \frac{m_H}{m_{H_2CS}} E_{CH_3S}$$

where E_H and E_{CH_3S} are the laboratory translational energy of the H-atom product and the parent thiomethoxy radical, L is the length of the flight path, and t_H is the flight time of the H-atom product. The second term is due to motion of the parent CH_3S radical in the molecular beam, which is perpendicular to the TOF axis, and is very small (~ 15 cm^{-1}, based on an estimated beam velocity of 560 m/s for the DMDS/Ar gas mixture). The resulting $P(E_T)$ distributions of the H + H_2CS product channel at the 220.5 nm photolysis wavelength with parallel and perpendicular polarization using the DMDS precursor are shown in Figure 9.6(a) and (b). The product CM translational energy and the photofragment angular distribution are described by the following equation:[39]

$$P(E_T, \theta) = \left(\frac{1}{4\pi}\right) P(E_T)[1 + \beta P_2(cos\theta)]$$

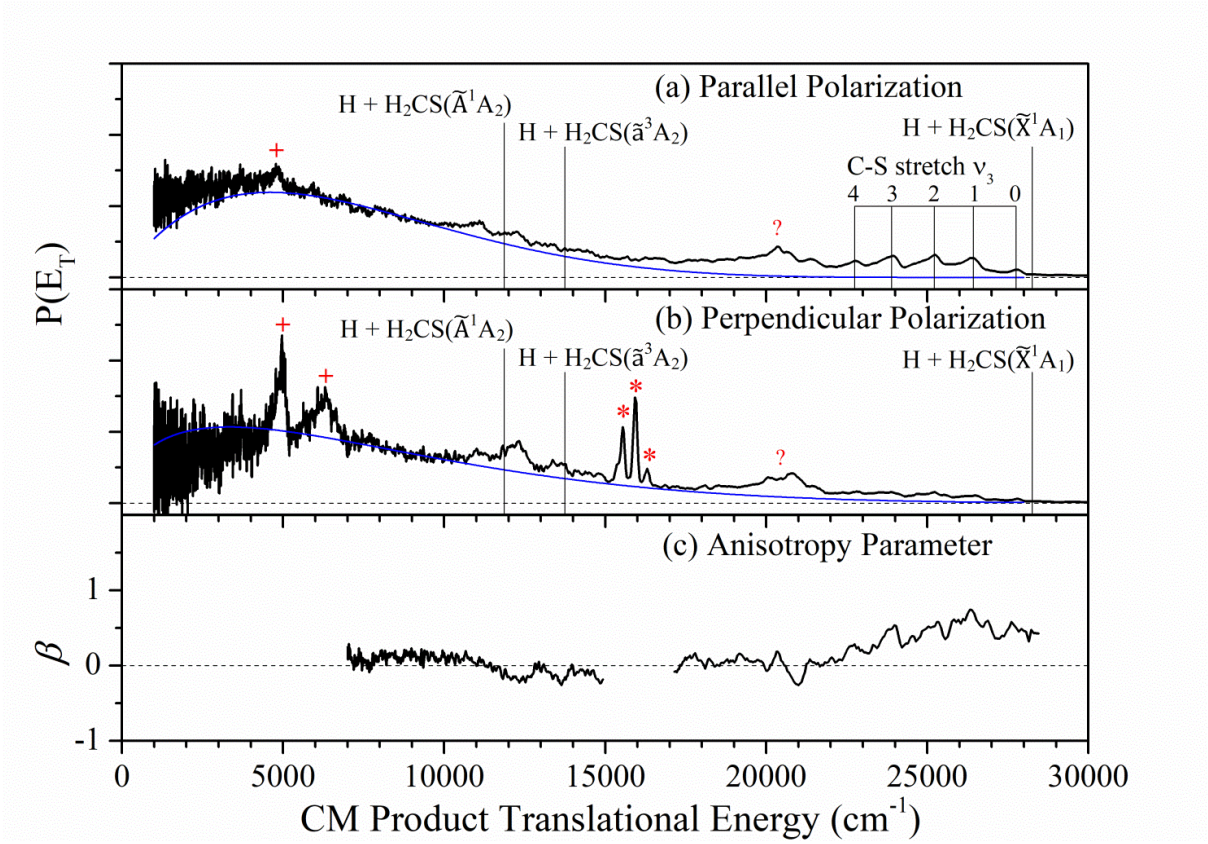

Figure 9.6. Center-of-mass H-atom product channel translational energy distribution from the photodissociation of the thiomethoxy radical at 220.5 nm with the linearly polarized photolysis radiation (a) parallel and (b) perpendicular to the TOF axis, and (c) translational energy-dependent anisotropy parameter $\beta(E_T)$. The $P(E_T)$ distributions in panels a and b are scaled to the same laser power and number of shots. The blue curves are fitted to the broad feature with a modest translational energy release. The maximum available energies of the H + $H_2CS(\tilde{X}^1A_1)$, H + $H_2CS(\tilde{a}^3A_2)$, and H + $H_2CS(\tilde{A}^1A_2)$ product channels are indicated in panels a and b. The contribution from the SH radical is indicated by *, and that from the CH_3 radical is marked by +. The β parameter is shown for the regions free of interferences from other species.

where β is the anisotropy parameter ($-1 \leq \beta \leq 2$) and θ is the angle between the electric vector of the linearly polarized photolysis radiation and the recoiling velocity of the H-atom product and $P_2(cos\theta)$ is the second Legendre polynomial. The translational energy-dependent anisotropy parameter, $\beta(E_T)$, is derived from the product translational energy distributions at the parallel ($P_{\parallel}(E_T)$) and perpendicular ($P_{\perp}(E_T)$) polarization, with $\beta(E_T) = 2\times[P_{\parallel}(E_T) - P_{\perp}(E_T)]/ [P_{\parallel}(E_T) + 2P_{\perp}(E_T)]$, and the result is shown in Figure 9.6(c).

As discussed for the H-atom TOF spectra, the $P(E_T)$ distributions at 220.5 nm have multiple peaks in different E_T regions. The sharp, anisotropic peaks around 16000 cm^{-1} at the perpendicular polarization were due to the repulsive $^2\Sigma^- \leftarrow X^2\Pi_{3/2,1/2}$ photodissociation of the SH radical.[32,34] The two peaks at ~5000 and 6300 cm^{-1} (mainly at the perpendicular polarization) were from the photodissociation of the CH_3 radical via the 3s Rydberg states.[35,36] The rest of the signals in the $P(E_T)$ distributions show multiple features due to the CH_3S radical. A broad, nearly isotropic ($\beta \approx 0$) feature peaks at ~4000 cm^{-1} and extends to the maximum available energy of the $H + H_2CS(\tilde{X}^1A_1)$ product channel (~28250 cm^{-1} at the 220.5 nm photolysis wavelength; more details in the following). Both $P(E_T)$ distributions at the parallel and perpendicular photolysis polarization have a nearly isotropic peak at ~21000 cm^{-1} (the TOF peak at ~17 μs), and three nearly isotropic peaks in the region of 11000 to 14000 cm^{-1}. The $P(E_T)$ distributions at both polarizations show a progression of peaks in the high translational energy region of 22000 to 28000 cm^{-1} (the TOF peaks around 15 μs), with significantly higher intensity at the parallel polarization. The anisotropy parameter β stays at 0.55 ± 0.15 from the maximum available energy to ~24000 cm^{-1}, and it decreases to a value close to 0 at E_T smaller than ~21000 cm^{-1}. The

behavior of the β parameter and the different features in the $P(E_T)$ distributions indicate several different H-atom dissociation channels of CH_3S. The observed $P(E_T)$ is the sum of the contributions from different dissociation channels, and the β parameter with a changing value is due to the different β parameters of these dissociation channels and their energy-dependence branching ratios.[40,41] The broad feature in the $P(E_T)$ distributions with β close to 0 is consistent with unimolecular dissociation of internally hot radical on the ground electronic state after internal conversion from the electronic excited state on a dissociation time scale longer than one rotational period of the CH_3S radical. The fast product with E_T > 22000 cm^{-1} and an anisotropic angular distribution with β of ~0.55 indicates a prompt, direct dissociation initiated from the excited $\widetilde{B}^2A_2$ state of CH_3S to the H + $H_2CS(\widetilde{X}^1A_1)$ products, with a dissociation time scale shorter than one rotational period of CH_3S. In the large E_T region of 22000 to 28000 cm^{-1}, the dominant contribution to the $P(E_T)$ distribution is this prompt dissociation channel (repulsive and with the fast dissociation time scale).

The overall product translational energy-dependent distribution, $P(E_T)$ and the product translational energy-dependent anisotropy parameter, $\beta(E_T)$, can be written as $P(E_T) = \sum_i P_i(E_T)$ and $\beta(E_T) = \sum_i x_i(E_T) \times \beta_i$ (assuming incoherent excitation), where $P_i(E_T)$ and $x_i(E_T)$ are the product translational energy distribution and the product translational energy-dependent branching ratio of the *i*th channel, $x_i(E_T) = \frac{P_i(E_T)}{P(E_T)}$, and $\sum_i x_i(E_T) = 1$.[40,41] In the high product translational energy region of E_T > 22000 cm^{-1} (where only the H + $H_2CS(\widetilde{X}^1A_1)$ product channel is energetically possible), the only contributions are the unimolecular dissociation channel (slow channel) and the prompt, repulsive dissociation channel (fast channel). Assuming that the β parameter is 0 for the

slow channel and 0.55 for the fast channel, the relative contribution from the fast channel can be derived as $P_{fast}(E_T) = \frac{2}{3} \times \frac{1}{\beta_{fast}} \times [P_{\parallel}(E_T) - P_{\perp}(E_T)]$ and is plotted in Figure 9.7. The fast channel has a large translational energy release, with the fraction of the average translational energy in the total available energy, $\langle f_T \rangle$, being 0.89. The slow, broad, and nearly isotropic feature peaking at ~4000 cm^{-1} is extracted by fitting with a Rice-Ramsperger-Kassel (RRK)-type function, $P(E_T) = A(E_T)^p(E_0 - E_T)^q$, where A, p, and q are adjustable parameters and E_0 is the maximum available energy,[42] as shown in Figure 9.6(a) and (b). This is a reasonable approach that removes the contributions from other channels in the $P(E_T)$ distributions. The $\langle f_T \rangle$ value of this slow component is estimated to be 0.27.

During the formation of the C=S double bond in the direct, repulsive dissociation channel, the equilibrium C-S bond distance decreases from 1.767 Å in the CH_3S parent to 1.615 Å in the $H_2CS(\tilde{X}^1A_1)$ product.[17,38] It is then expected that the C-S stretch vibration in the $H_2CS(\tilde{X}^1A_1)$ product would be excited. The vibrational progression of the $H_2CS(\tilde{X}^1A_1)$ product in the fast dissociation channel (Figure 9.7) indicates the C-S stretch vibrational excitation in $H_2CS(\tilde{X}^1A_1)$. This vibrational distribution of $H_2CS(\tilde{X}^1A_1)$ was fitted using double Gaussian peaks with adjustable height, position, and width. The black solid curve is the fitted vibrational structure of the C-S stretch mode with different quantum numbers, and the width and tail of these peaks (vibrational levels) imply that the $H_2CS(\tilde{X}^1A_1)$ product was moderately rotationally excited. The separation between these peaks is ~1100 cm^{-1}, which is consistent with the C-S stretch vibrational frequency of 1059 cm^{-1} of H_2CS $(\tilde{X}^1A_1)$.[38] Some residue between the experimental and the fitted distributions might be due

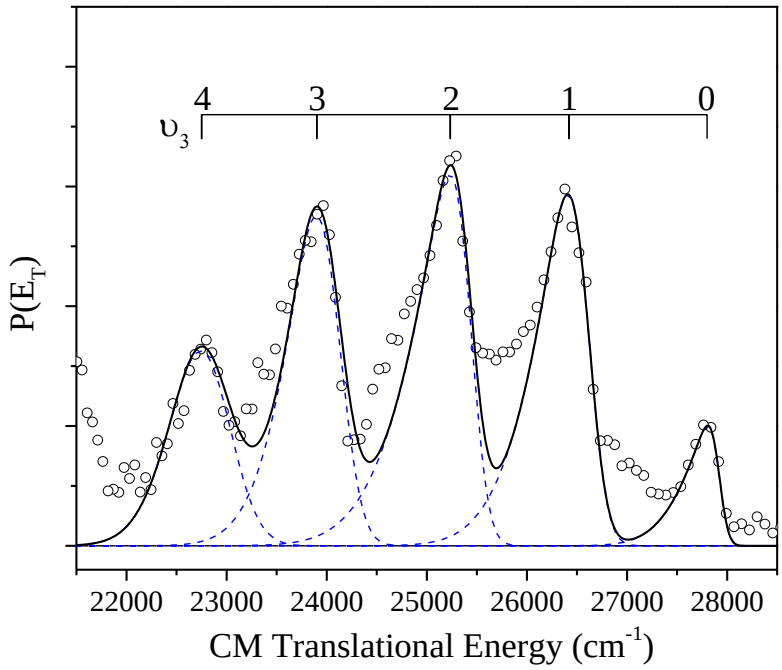

Figure 9.7. The center-of-mass product translational energy distribution of the fast, anisotropic channel at E_T > 22000 cm^{-1}, from the photodissociation of CH_3S (DMDS precursor) at 220.5 nm. The vibrational structure indicates C-S stretch vibration of the $H_2CS(\tilde{X}^1A_1)$ product. Open circles (○) are for the experimental $P(E_T)$ distribution, blue dash curves are the fitted C-S stretch vibrational peaks, and the black solid curve is the sum of the fitted distribution.

to excitation of other vibrational modes (although their contribution was small). The maximum available energy of the H + $H_2CS(\tilde{X}\,^1A_1)$ product channel from the photodissociation of CH_3S can be determined from the onset of the $v = 0$ vibrational peak of $H_2CS(\tilde{X}^1A_1)$ as $E_{max} = 28250 \pm 250$ cm^{-1} at the 220.5 nm photolysis wavelength. This gives a value of 48.8 ± 0.7 kcal/mol for the C-H bond dissociation energy of the CH_3S radical. This value is in agreement within the error limit with that of 48.9 kcal/mol by Ashfold and co-workers,[29] 48 ± 2 kcal/mol by Gutman and co-workers,[43] and 47.5 ± 1.8 kcal/mol by Neumark and co-workers.[22]

The $P(E_T)$ distributions at 220.5 nm discussed above are compared with those at other photolysis wavelengths (218.5 nm and 221.5 nm) (Figure 9.8). Besides the variation in the integrated H-atom signal intensities (shown in the PFY spectrum in Figure 9.5), the structures of the $P(E_T)$ distributions (and thus the various H-atom product channels) also change as a function of the photolysis wavelength, as also shown in the TOF spectra (Figure 9.4). In particular, the fast, anisotropic component at $E_T > 22000$ cm^{-1}, while near its maximum intensity around 220.5 nm, reduces in intensity at 221.5 nm and essentially vanishes at 218.5 nm. Note that these changes take place in a relatively narrow wavelength range of a few nanometers, suggesting a strong energy dependence of the dissociation mechanism.

9.4 Discussions

The electronic configuration of the ground electronic state of CH_3S (in C_{3v}) is

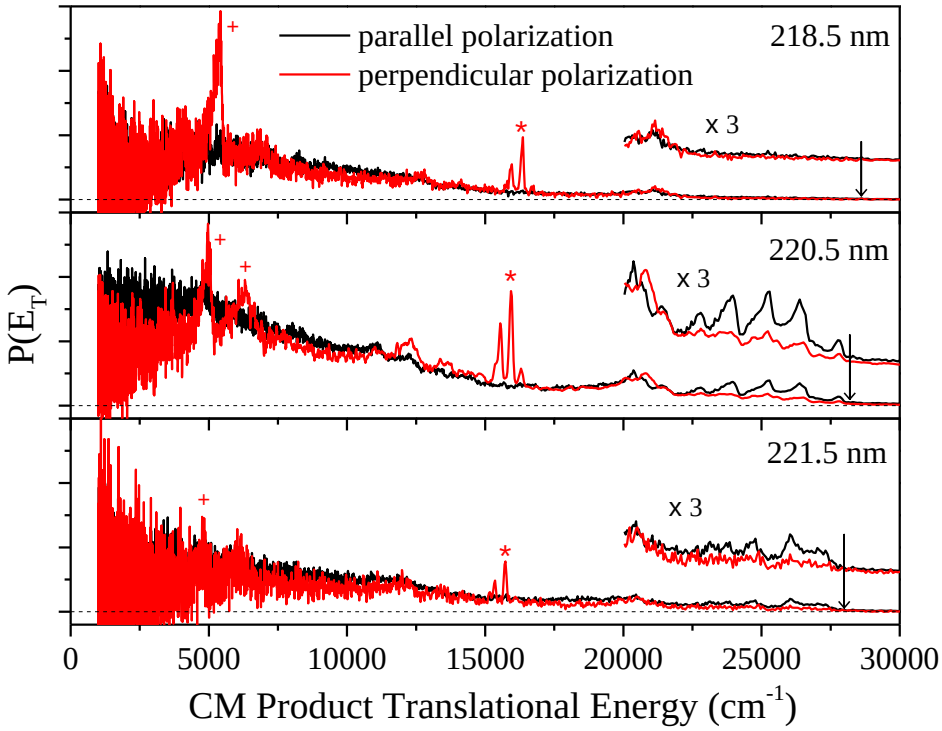

Figure 9.8. The center-of-mass H-atom product channel translational energy distribution from the photodissociation of the thiomethoxy radical at 218.5, 220.5, and 221.5 nm with the photolysis radiation polarization parallel and perpendicular to the TOF axis. The $P(E_T)$ distributions at each wavelength are scaled to the same laser power and number of shots. The maximum available energies of the H + $H_2CS(\tilde{X}^1A_1)$ product channel at each wavelength are indicated by the arrows. The contribution from the SH radical is indicated by *, and that from the CH_3 radical is marked by +.

$\cdots(7a_1)^2(3e)^3(8a_1)^0\cdots$, where the $7a_1$ orbital is the σ(C-S) bonding orbital, $3e$ orbitals are the ($3p_x$, $3p_y$) orbitals of sulfur, and $8a_1$ is the σ^*(C-S) antibonding orbital.[26] The ground electronic state of CH_3S is the doubly degenerate $\tilde{X}\ ^2E_{3/2,1/2}$, while the Jahn-Teller effect is small in comparison with the spin-orbit splitting.[44] The $\tilde{A}^2A_1$ state in the near UV region is due to the $\sigma \rightarrow n$ transition ($7a_1 \rightarrow 3e$). It predissociates via three repulsive states, $^4A_2$, ^4E, and $\tilde{B}^2A_2$, to the $CH_3(\tilde{X}^2A_2'') + S(^3P_J)$ products,[22] and some vibronic levels could undergo internal conversion to the ground state and dissociate to $H + H_2CS(\tilde{X}^1A_1)$.[23, 24] The $\tilde{B}^2A_2$ state in the UV region of ~220 nm is due to the $n \rightarrow \sigma^*$(C-S) transition ($3e \rightarrow 8a_1$). It can dissociate directly and repulsively to the $CH_3(\tilde{X}^2A_2'') + S(^3P_J)$ products.[22] A higher energy excited state $\tilde{C}^2A_2$ (at ~200 nm) is Rydberg in nature (likely due to the $n \rightarrow 4sa_1$ transition). Its predissociation could lead to the $CH_3(\tilde{X}^2A_2'') + S(^1D)$ products.[26]

The H-atom dissociation product channel of CH_3S in the UV region of 213-220 nm was first observed in the secondary photolysis of CH_3SH by Ashfold and co-worker,[29] presumably via the $\tilde{B}$ and/or $\tilde{C}$ state, and mainly producing the $H + H_2CS(\tilde{A}^1A_2)$ products. However, the internal energy of the CH_3S radical was not well-defined in this previous study, as the CH_3S radical was produced internally hot in the UV photolysis of CH_3SH and had a broad internal energy distribution in the secondary photolysis process. In the current work, the H-atom product channel from the photodissociation of the jet-cooled CH_3S radical in the region of 216 to 225 nm was studied, and the $H + H_2CS$ product channel was observed directly from the H-atom TOF spectra.

The H-atom PFY spectrum of CH_3S has a broad feature in the region of 216-225 nm and three peaks at 217.7, 220.3, and 221.5 nm, consistent with the UV absorption

spectra of CH_3S in this region.[7-9,25] The $CH_3 + S(^3P_J)$ PFY spectrum obtained by Neumark and co-workers showed two peaks at 219.2 nm and 220.5 nm (assigned to transitions from the $\tilde{X}^2E_{3/2}$ and $\tilde{X}^2E_{1/2}$ states, respectively).[22] The two peaks at 220.3 and 221.5 nm in our H-atom PFY spectrum are separated by ~ 250 cm^{-1}, also close to the spin-orbit splitting (259 cm^{-1}) of CH_3S ($\tilde{X}^2E_{3/2,1/2}$).[13,15,17,18] However, our early work on the $\tilde{X}^2E \rightarrow \tilde{A}^2A_1$ photodissociation of CH_3S under the same radical beam conditions did not show any signal from the $\tilde{X}^2E_{1/2}$ initial state,[23,24] suggesting that the $\tilde{X}^2E_{1/2}$ state may not have a significant population in the beam and contribution in the current UV photodissociation, and these two peaks could be due to vibronic bands. Furthermore, the peak at 217.7 nm is separated by ~560 cm^{-1} from the 220.3 nm peak, possibly by one quantum in the HCH deformation mode of CH_3S. These three peaks in the broad background in the H-atom PFY spectrum are likely due to the vibronic structure of the $\tilde{B}^2A_2$ state.

The line width of these three vibronic peaks is on the order of 200 cm^{-1}, similar to that in the $CH_3 + S(^3P_J)$ PFY spectrum in the same region obtained by Neumark and co-workers, and is not as broad as expected for the purely repulsive $\tilde{B}^2A_2$ state. As pointed out by Neumark and co-workers,[22] the theoretical study by Ng and co-workers suggested an avoided crossing between the $\tilde{B}$ and $\tilde{C}$ states in the Franck-Condon (FC) region,[26] which causes the $\tilde{B}$ state to be relatively flat in the FC region. Consequently, several vibronic levels of the $\tilde{B}$ state could exist in the FC region before they dissociate rapidly along the repulsive part of the $\tilde{B}$ state. The two peaks in the $CH_3 + S(^3P_J)$ PFY spectrum and the three in the H-atom PFY spectrum are in different positions, except for the one at 220.3 nm. This seems to suggest some mode specificity in the dissociation pathways, as observed in the

$\widetilde{X}^2E \rightarrow \widetilde{A}^2A_1$ photodissociation of CH_3S.[23,24] This could be caused by the different mechanisms of the $CH_3 + S(^3P_J)$ and the H-atom loss product channels. Whereas the $CH_3 + S(^3P_J)$ product channel proceeds beyond the FC region on the repulsive $\widetilde{B}$ state along the C-S coordinate, the H-atom loss product channel requires coupling of the $\widetilde{B}/\widetilde{C}$ states with a repulsive surface along the C-H coordinate (at least for the fast $H + H_2CS(\widetilde{X}^1A_1)$ channel, as discussed in the following).

The H-atom loss product translational energy and angular distributions reveal several dissociation channels. The fast product channel with $E_T > 22000$ cm^{-1}, a vibrationally resolved structure, and an anisotropic angular distribution with β up to 0.55 indicates a repulsive dissociation, with the dissociation time scale shorter than one rotational period of the CH_3S radical (on the order of ~ 10 ps, estimated for a 15 K rotational temperature based on the earlier work[31]). The initial UV excitation involves the $\widetilde{B}^2A_2 \leftarrow \widetilde{X}^2E$ transition, whose transition dipole moment is perpendicular to the C-S bond. For the prompt, repulsive $CH_3 + S(^3P_J)$ dissociation channel along the C-S coordinate, the negative β parameter of -0.98 is consistent with the perpendicular transition.[22] For the repulsive, fast $H + H_2CS(\widetilde{X}^1A_1)$ dissociation channel observed in this study, the positive β parameter of ~0.55 is also consistent with the initial $\widetilde{B}^2A_2 \leftarrow \widetilde{X}^2E$ transition, as the dissociating C-H bond is at a small angle with respect to the transition dipole moment that is perpendicular to the C-S bond (e.g., ~25° in the equilibrium geometry of CH_3S ($\widetilde{X}^2E$)). In the prompt, fast $H + H_2CS(\widetilde{X}^1A_1)$ dissociation channel, the measured β value of 0.55 would indicate that the velocity vector of the dissociating H atom is ~45° relative to the transition dipole moment of the $\widetilde{B}^2A_2 \leftarrow \widetilde{X}^2E$ transition. However, the $\widetilde{B}^2A_2$ state does not correlate repulsively with

the H + $H_2CS(\tilde{X}^1A_1)$ products along the C-H coordinate. Whereas the $\tilde{B}^2A_2$ state could interact with the higher energy $\tilde{C}^2A_2$ state, the $\tilde{C}^2A_2$ Rydberg state is presumably not directly dissociative along the C-H coordinate. Therefore, it is plausible that an antibonding σ^*(C-H) state crosses with the $\tilde{B}^2A_2$ or $\tilde{C}^2A_2$ state, leading to the repulsive dissociation along the C-H coordinate.

The fast H + $H_2CS(\tilde{X}^1A_1)$ product channel, initiated from the $\tilde{B}^2A_2$ state, competes with the repulsive dissociation on the $\tilde{B}^2A_2$ state to the CH_3 + $S(^3P_J)$ products. Because the photodissociation of the $\tilde{B}^2A_2$ state shows some mode specificity to the fast H + $H_2CS(\tilde{X}^1A_1)$ and the CH_3 + $S(^3P_J)$ product channels, certain vibronic modes of the $\tilde{B}^2A_2$ state (observed in the H-atom PFY spectrum in Figure 9.5 and the wavelength dependent $P(E_T)$ distributions in Figure 9.8) may be preferentially coupled with the antibonding σ^*(C-H) state, leading to the repulsive dissociation along the C-H coordinate. This crossing along the C-H coordinate may also provide a mechanism for internal conversion of the excited $\tilde{B}^2A_2$ state to lower electronic excited states and the ground electronic $\tilde{X}^2E$ state, and the subsequent unimolecular decomposition of CH_3S in the ground electronic state gives rise to the slow, nearly isotropic component in the H-atom loss product translational energy distribution (discussed in the following). This behavior is similar to the bimodal H-atom loss product translational energy and angular distributions in the UV photodissociation of alkyl radicals via the Rydberg states, with a repulsive and anisotropic component and a slow and isotropic component, which is due to the interaction of the excited Rydberg state with plausibly an antibonding σ^*(C-H) state, leading to both the repulsive direct dissociation and the unimolecular decomposition in the ground electronic state.[42,45] In

summary, the fast H + $H_2CS(\tilde{X}^1A_1)$ product channel is consistent with a direct dissociation that is initiated on the excited $\tilde{B}^2A_2$ state and leads to the repulsive part of the ground state potential energy surface of the H + $H_2CS(\tilde{X}^1A_1)$ products.

When CH_3S eliminates an H atom (with the C_{3v} symmetry reduced to C_s) in the prompt dissociation channel, it is plausible that the C-H bond with the departing H atom is eclipsed to the half-filled $3p_{x/y}$ orbital of the S atom. During the departure of the H atom and formation of the C=S double bond in this direct, repulsive dissociation, the equilibrium C-S bond distance decreases from 1.767 Å initially in the ground-state $CH_3S(\tilde{X}^2E)$ to 1.615 Å in the $H_2CS(\tilde{X}^1A_1)$ product,[17,38] resulting in C-S stretch vibrational excitation in the $H_2CS(\tilde{X}^1A_1)$ product. The vibrational state distribution of the $H_2CS(\tilde{X}^1A_1)$ product in the fast dissociation channel (Figure 9.7) shows the C-S stretch vibrational progression with a ~1100 cm^{-1} spacing.[38] On basis of the fitted C-S stretch vibrational state population (Figure 9.7), a one-dimensional FC calculation was performed to model the C-S bond distance in CH_3S before cleavage of the C-H bond. The C-S stretch in the CH_3S reactant was simulated by a harmonic oscillator in the ground vibrational state (anharmonicity is small in the ground vibrational state), and a Morse oscillator was used for the C-S stretch vibrational mode in the $H_2CS(\tilde{X}^1A_1)$ product. The vibrational parameters of $H_2CS(\tilde{X}^1A_1)$ have been well studied,[38,46] with R_{eq} (C-S) = 1.615 Å, ν_3 (C-S stretch frequency) = 1059 cm^{-1} and $\chi_{3,3}$ (C-S stretch anharmonicity) = -4.68 cm^{-1}. The FC modeling reached the best fitting to the experimental population when the CH_3S C-S bond distance was 1.75 Å and vibrational frequency was 830 cm^{-1}. Figure 9.9 shows the modeled C-S stretch vibrational state distribution of H_2CS compared with the fitted experimental population. Compared with the

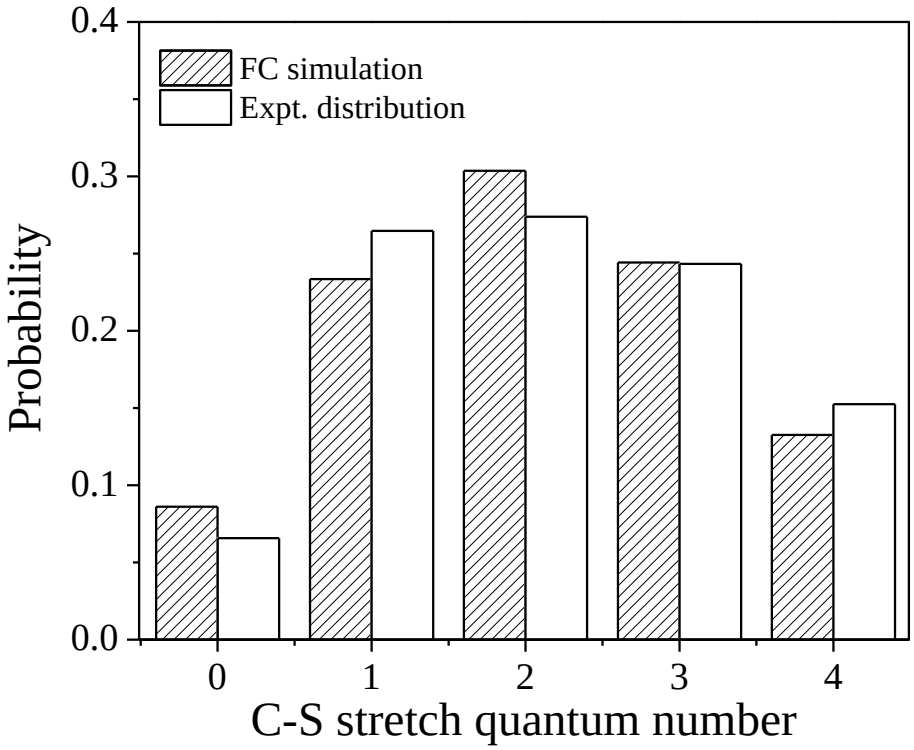

Figure 9.9. Experimental versus Franck-Condon model population distribution of the C-S stretch vibrational mode of the $H_2CS(\tilde{X}^1A_1)$ product from the photodissociation of CH_3S at 220.5 nm. The total probability of each distribution is normalized to 1.

C-S bond distance and stretch vibrational frequency of the ground-state $CH_3S(\tilde{X}^2E)$, the FC modeling suggests a slightly stronger C-S bond and shorter C-S distance in CH_3S before the departure of the H atom. This result indicates that in the prompt, repulsive H-loss dissociation, the C-S distance is shortened when the C-H bond cleaves before forming the C=S double bond.

The feature between 20000 to 22000 cm^{-1} in the $P(E_T)$ distributions (the TOF peak at ~17 μs) at 220.5 nm is also due to photodissociation of the CH_3S radical and has a large and repulsive translational energy release. Although it should correspond to the vibrationally excited $H_2CS(\tilde{X}^1A_1)$ + H products, it does not seem to be part of the fast, anisotropic dissociation channel at E_T > 22000 cm^{-1} (with the C-S stretch vibrational progression of $H_2CS(\tilde{X}^1A_1)$) because it has a nearly isotropic product angular distribution and a different dependence on the photolysis wavelength (Figure 9.4 and 8.8). The mechanism of this dissociation channel remains unassigned at this time.

The broad feature with the peak around 4000 cm^{-1} and a nearly isotropic angular distribution ($\beta \approx 0$) corresponds to a statistical, unimolecular dissociation of the internally hot CH_3S radical in its ground electronic state to the H + $H_2CS(\tilde{X}^1A_1)$ products, presumably following internal conversion from the electronic excited state to the ground electronic state. The possible crossing of an antibonding σ^*(C-H) state with the $\tilde{B}^2A_2$ or $\tilde{C}^2A_2$ state along the C-H coordinate may provide a mechanism for the internal conversion of the excited $\tilde{B}^2A_2$ state to the lower electronic excited states and the ground electronic state, as well as the bimodal (fast and slow) product translational energy distribution, although other internal conversion mechanisms could also take place. The isotropic angular distribution

indicates that the dissociation time scale is longer than one rotational period of CH_3S, consistent with the statistical unimolecular dissociation in the CH_3S ground electronic state. It is noted that in the unimolecular decomposition of the ground electronic state CH_3S, the H + $H_2CS(\tilde{X}^1A_1)$ product channel is more favorable than the CH_3 + $S(^3P_J)$ product channel due to its lower energy (Figure 9.1).

Several small features peaking around 13500, 12200, and 11200 cm^{-1} were also identified in the $P(E_T)$ distributions (Figure 9.6). They could be attributed to the production of electronic excited H_2CS products. The excited states of H_2CS, $\tilde{A}^1A_2$ and $\tilde{a}^3A_2$, are 16395 and 14507 cm^{-1} above the ground state $\tilde{X}^1A_1$, respectively.[28] The H + $H_2CS(\tilde{A}^1A_2)$ product channel would have a maximum available energy, E_{max} = 11800 $\pm$ 250 cm^{-1}, in the 220.5 nm photodissociation, and the peak around 11200 cm^{-1} could be due to this channel. This channel shows an isotropic angular distribution. E_{max} of the H + $H_2CS(\tilde{a}^3A_2)$ product channel is 13700 $\pm$ 250 cm^{-1}. The peak at ~13500 cm^{-1} could correspond to the vibrational ground-state $H_2CS(\tilde{a}^3A_2)$ + H products, the peak at ~12200 cm^{-1} could correspond to the vibrationally excited $H_2CS(\tilde{a}^3A_2)$ product with a quantum in CH_2 scissor mode (ν = 1319 cm^{-1}),[47] and, alternatively, the peak at ~11200 cm^{-1} could correspond to the vibrationally excited $H_2CS(\tilde{a}^3A_2)$ product with an additional quantum in C-S stretch mode (ν = 860 cm^{-1}).[47] The main part of the H + $H_2CS(\tilde{a}^3A_2)$ product channel has a slightly negative anisotropy parameter. The product translational energy releases of these two excited $H_2CS(\tilde{A}^1A_2)$ and $H_2CS(\tilde{a}^3A_2)$ product channels peak near their maximum available energies, showing repulsive dissociation mechanisms. These two excited $H_2CS(\tilde{A}^1A_2)$ and $H_2CS(\tilde{a}^3A_2)$ product channels are of minor contribution compared to the two H +

$H_2CS(\tilde{X}^1A_1)$ product channels. This observation is different from that by Ashfold and co-workers in the secondary photolysis of $CH_3S(\tilde{X}^2E)$ from CH_3SH, where the H_2CS co-fragment was thought to be produced mainly in the $\tilde{A}^1A_2$ electronic excited state.[29]

9.5 Conclusion

The UV photodissociation dynamics of jet-cooled CH_3S radical via the $\tilde{B}^2A_2$ state was studied in the region of 216 to 225 nm. The H-atom product channel was observed from the H-atom TOF spectra. The H-atom PYF spectrum showed a broad feature in the region of 216–225 nm and three $\tilde{B}^2A_2$ vibronic peaks at 217.7, 220.3, and 221.5 nm. Several H-atom dissociation channels were identified. The electronic excited CH_3S radical can undergo the repulsive dissociation with a large translational energy release ($\langle f_T \rangle \approx 0.89$) and an anisotropic product angular distribution (β up to 0.55) to form the C-S stretch vibrationally excited $H_2CS(\tilde{X}^1A_1)$ + H products. The Franck-Condon simulation indicated that the C-S bond distance was 1.75 Å (slightly shorter than the equilibrium C-S distance in $CH_3S(\tilde{X}^2E)$) when the C-H bond cleaved. The C-H bond dissociation energy was determined to be 48.8 $\pm$ 0.7 kcal/mol. CH_3S can also undergo unimolecular dissociation to the H + $H_2CS(\tilde{X}^1A_1)$ products with a modest translational energy release ($\langle f_T \rangle \approx 0.27$) and isotropic angular distribution, after internal conversion from the electronic excited state to the ground electronic state. The $H_2CS(\tilde{A}^1A_2)$ and $H_2CS(\tilde{a}^3A_2)$ product channels were also observed, but they were minor channels.

Reference

1. D. Grosjean and R. Lewis, *Geophys. Res. Lett.* **9**, 1203 (1982).

2. S. Hatakeyama and H. Akimoto, *J. Phys. Chem*. **87**, 2387 (1983).

3. H. Niki, P. D. Maker, C. M. Savage, and L. P. Breitenbach, *Int. J. Chem*. *Kinet.* **15**, 647 (1983).

4. R. J. Charlson, J. E. Lovelock, M. O. Andreae, and S. G. Warren, *Nature* **326**, 655 (1987).

5. G. S. Tyndall and A. R. Ravishankara, *Int. J. Chem*. *Kinet.* **23**, 483 (1991).

6. T. S. Bates, B. K. Lamb, A. Guenther, J. Dignon, and R. E. Stoiber, *J. Atmos. Chem.* **14**, 315 (1992).

7. A. B. Callear, J. Connor, and D. R. Dickson, *Nature* **221**, 1238 (1969).

8. A. B. Callear and D. R. Dickson, *Trans. Faraday Society* **66**, 1987 (1970).

9. A. Kumar, P. K. Chowdhury, K. V. S. Rama Rao, and J. P. Mittal, *Chem*. *Phys. Lett.* **198**, 406 (1992).

10. K. Ohbayashi, H. Akimoto, and I. Tanaka, *Chem*. *Phys. Lett.* **52**, 47 (1977).

11. Y. Endo, S. Saito, and E. Hirota, *J. Chem*. *Phys.* **85**, 1770 (1986).

12. P. C. Engelking, G. B. Ellison, and W. C. Lineberger, *J. Chem*. *Phys.* **69**, 1826 (1978).

13. B. K. Janousek and J. I. Brauman, *J. Chem*. *Phys.* **72**, 694 (1980).

14. S. Moran and G. B. Ellison, *J. Phys. Chem*. **92**, 1794 (1988).

15. M. Suzuki, G. Inoue, and H. Akimoto, *J. Chem*. *Phys.* **81**, 5405 (1984).

16. G. Black and L. E. Jusinski, *J. Chem*. *Soc. Faraday Trans. 2* **82**, 2143 (1986).

17. Y. C. Hsu, X. Liu, and T. A. Miller, *J. Chem*. *Phys.* **90**, 6852 (1989).

18. S. Y. Chiang and Y. P. Lee, *J. Chem*. *Phys.* **95**, 66 (1991).

19. M. B. Pushkarsky, B. E. Applegate, and T. A. Miller, *J. Chem. Phys.* **113**, 9649 (2000).

20. C.-P. Liu, Y. Matsuda, and Y.-P. Lee, *J. Chem. Phys.* **119**, 12335 (2003).

21. C. P. Liu, S. A. Reid, and Y. P. Lee, *J. Chem. Phys.* **122**, 124313 (2005).

22. R. T. Bise, H. Choi, H. B. Pedersen, D. H. Mordaunt, and D. M. Neumark, *J. Chem. Phys.* **110**, 805 (1999).

23. X. Zheng, Y. Song, J. Wu, and J. Zhang, *Chem. Phys. Lett.* **467**, 46 (2008).

24. X. Zheng, Y. Song, J. Wu, and J. Zhang, *Chin. J. Chem. Phys.* **20**, 377 (2007).

25. C. Anastasi, M. Broomfield, O. J. Nielsen, and P. Pagsberg, *Chem. Phys. Lett.* **182**, 643 (1991).

26. C. W. Hsu, C. L. Liao, Z. X. Ma, P. J. H. Tjossem, and C. Y. Ng, *J. Chem. Phys.* **97**, 6283 (1992).

27. Q. Cui and K. Morakuma, *Chem. Phys. Lett.* **263**, 54 (1996).

28. D. J. Clouthier, D. A. Ramsay, and F. W. Birss, *J. Chem. Phys.* **79**, 5851 (1983).

29. S. H. S. Wilson, M. N. R. Ashfold, and R. N. Dixon, *J. Chem. Phys.* **101**, 7538 (1994).

30. Y. Song, X. Zheng, M. Lucas, and J. Zhang, *Phys. Chem. Chem. Phys.* **13**, 8296 (2011).

31. Y. Song, M. Lucas, M. Alcaraz, J. Zhang, and C. Brazier, *J. Phys. Chem. A* **119**, 12318 (2015).

32. W. Zhou, Y. Yuan, S. Chen, and J. Zhang, *J. Chem. Phys.* **123**, 054330 (2005).

33. S. B. Barone, A. A. Turnipseed, T. Gierczak, and A. R. Ravishankara, *J. Phys. Chem.* **98**, 11969 (1994).

34. X. Zheng, J. Wu, Y. Song, and J. Zhang, *Phys. Chem. Chem. Phys.* **11**, 4761 (2009).

35. G. Wu, J. Zhang, S. A. Harich, and X. Yang, *Chin. J. Chem. Phys.* **19**, 109 (2006).

36. S. Marggi Poullain, D. V. Chicharro, A. Zanchet, M. G. González, L. Rubio-Lago, M. L. Senent, A. García-Vela, and L. Bañares, *Phys. Chem. Chem. Phys.* **18**, 17054 (2016).

37. C. R. Drury and D. C. Moule, *J. Mol. Spectrosc.* **92**, 469 (1982).

38. C.-H. Lai, M.-D. Su, and S.-Y. Chu, *J. Phys. Chem. A* **105**, 6932 (2001).

39. R. N. Zare, *Mol. Photochem.* **4**, 1 (1972).

40. J.-H. Wang, Y.-T. Hsu, and K. Liu, *J. Phys. Chem. A* **101**, 6593 (1997).

41. G. Amaral, K. Xu, and J. Zhang, *J. Chem. Phys.* **114**, 5164 (2001).

42. Y. Song, X. Zheng, W. Zhou, M. Lucas, and J. Zhang, *J. Chem. Phys.* **142**, 224306 (2015).

43. J. Berkowitz, G. B. Ellison, and D. Gutman, *J. Phys. Chem.* **98**, 2744 (1994).

44. A. V. Marenich and J. E. Boggs, *J. Phys. Chem. A* **108**, 10594 (2004).

45. J. Giegerich and I. Fischer, *J. Chem. Phys.* **142**, 044304 (2015).

46. A. Yachmenev, I. Polyak, and W. Thiel, *J. Chem. Phys.* **139**, 204308 (2013).

47. J. R. Dunlop, J. Karolczak, D. J. Clouthier, and S. C. Ross, *J. Phys. Chem.* **95**, 3063 (1991).

Chapter 10

Preliminary Results and General Conclusions

The previous nine chapters have introduced the studies of the photodissociation dynamics of several free radicals using the HRTOF technique. This chapter will briefly discuss the photodissociation of the HBr molecule in which a series of rovibrational levels of the parent HBr are initially prepared observed and the determination of the dissociation timescale based on it. The general conclusions of this dissertation is also provided.

10.1 UV photodissociation of HBr

Figure 10.1 shows the potential energy curves of the HBr system.[1] The ground state $X^1\Sigma_0^+$ correlates with the ground state products $Br(^2P_{3/2}) + H(^2S)$. Several excited states are present. The $a^3\Pi_1$ and $A^1\Pi_1$ states correlate with $Br(^2P_{3/2}) + H(^2S)$, while $a^3\Pi_0^+$ and $t^3\Sigma_0$ states asymptotically correlate with the excited product $Br(^2P_{1/2}) + H(^2S)$. The $A^1\Pi_1$ and $a^3\Pi_0^+$ across with each other at a H-Br distance of around 4 bohr.

The experimental setup of the HRTOF technique has been reported in the previous chapters. The rovibrationally excited HBr in the molecular beam was generated by photodissociation of the vinyl bromide precursor at 193 nm in Ar carrier gas. The HBr molecules were then photodissociated by a UV photolysis radiation at 241 nm with the polarization of the photolysis radiation perpendicular ($\theta = 90°$) and parallel ($\theta = 90°$) to the

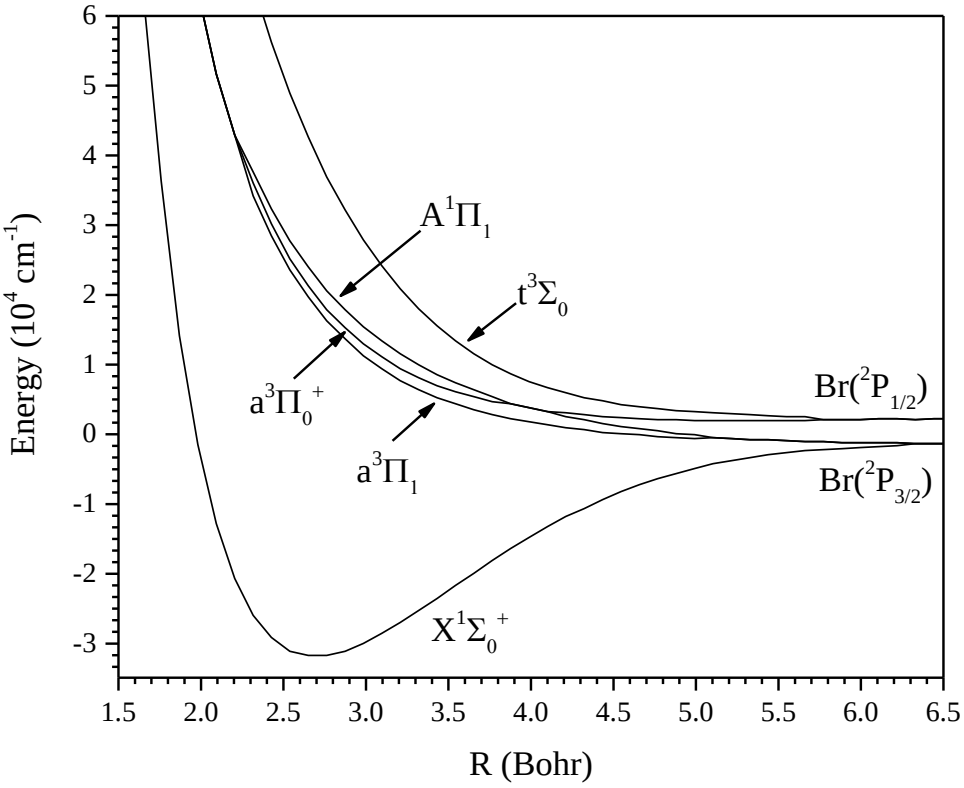

Figure 10.1 Potential energy diagram of the HBr system. The curves are based on the previous theoretical work (Ref. 1). More details can be found in text.

TOF path. The H atoms produced were tagged by two-color resonant excitation (121.6 + 366.3 nm) from 1^2S to 2^2P via the H-atom Lyman-α transition and then further to a high-n Rydberg state. A small fraction of the metastable H atoms drifted with their nascent velocities towards a microchannel plate (MCP) detector which was positioned perpendicular to the molecular beam. The metastable H atoms were field ionized in front of the detector and then detected. The flight distance was calibrated by the well-studied HBr bond dissociation energy and the spin-orbit energy splitting of the Br($^2P_{3/2}$) and Br($^2P_{1/2}$). The ion signals were amplified by a fast preamplifier and recorded and averaged with a multichannel scaler, and the H-atom TOF spectra were then obtained. The product center-of-mass (CM) translational energy distributions, $P(E_T)$'s, can be derived from the H-atom TOF spectra with the following equation:

$$E_T = \left(1 + \frac{m_H}{m_{Br}}\right) E_H + \frac{m_H}{m_{Br}} E_{HBr} = \frac{1}{2} m_H \left(1 + \frac{m_H}{m_{\mathrm{Br}}}\right) \left(\frac{L}{t_H}\right)^2 + \frac{m_H}{m_{Br}} E_{HBr}$$

in which E_{H} and E_{HBr} are the laboratory translational energies of the H-atom product and the parent HBr molecule, L is the length of the flight path, and t_{H} is the H-atom flight time. The second term is due to the motion of the HBr molecule in the molecular beam and this term can be neglected. Figure 10.2 presents the $P(E_T)$ distributions of the H + Br products at 241 nm with the photolysis radiation perpendicular ($P_{\perp}(E_{\mathrm{T}})$, θ = 90°) and parallel ($P_{\parallel}(E_{\mathrm{T}})$, θ = 0°) to the TOF path, which are converted from the TOF spectra. The $P(E_T)$ distributions are scaled to the same photolysis laser power and the number of laser shots. The product center-of-mass (CM) translational energy and photofragment angular distribution can be described with the following equation:[2]

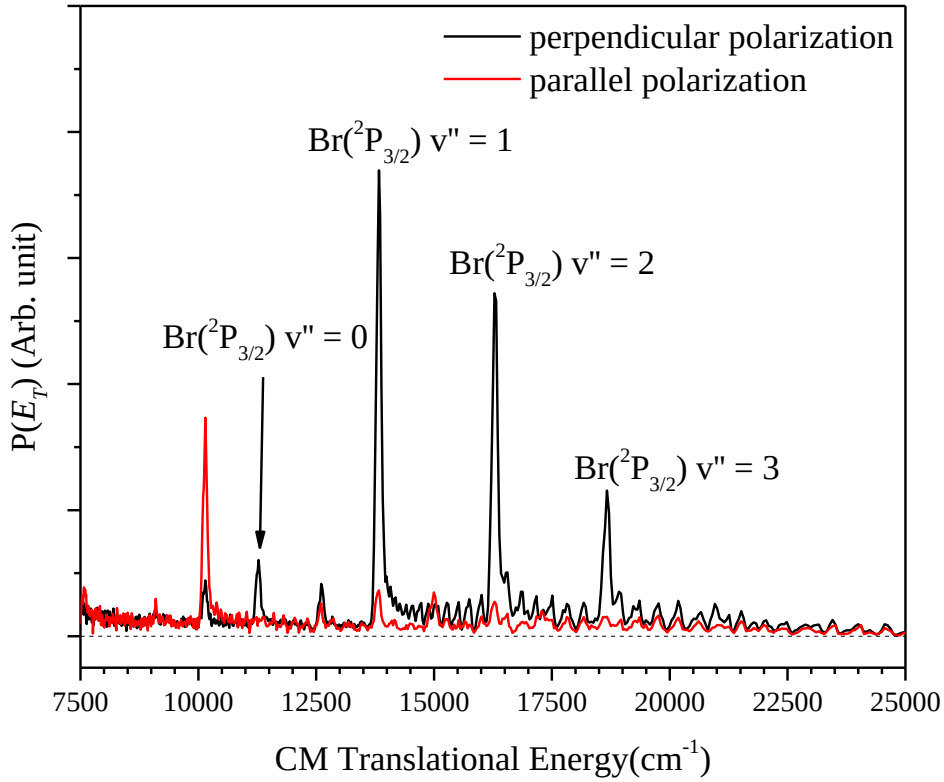

Figure 10.2 CM product translational energy distributions from the photodissociaiton of rovibrationally excited HBr at 241 nm with the photolysis perpendicular and parallel to the TOF path. The peaks are labeled with the different spin-orbit spillting of the Br product and the vibtational levels of the HBr parent.

$$P(E_T, \theta) = \left(\frac{1}{4\pi}\right)[1 + \beta P_2(cos\theta)]P(E_T)$$

in which β is the anisotropy parameter ((-1$\leq \beta \leq$2), θ is the angle between the electric vector of the linearly polarized photolysis radiation and the recoiling velocity vector of the H-atom product, and $P_2(cos\theta)$ is the second Legendre polynomial. The energy-dependent anisotropic parameter, $\beta(E_T)$, can be calculated from the translational energy distributions with $\beta(E_T) = 2\times[P_{\parallel}(E_T) - P_{\perp}(E_T)]/[P_{\parallel}(E_T) + 2P_{\perp}(E_T)]$. Several peaks can be found in both parallel and perpendicular translational energy distributions. The distances between these peaks are consistent with the vibrational and rotational levels of the HBr parent.[3] These peaks are fitted with the Gaussian functions for which the width is fixed, and the intensity is adjustable. The anisotropy parameter, β, of each rotational level can be calculated based on the intensity of the fitted Gaussian peaks.

During the photodissociation, if the dissociation process is not immediate after the excitation, but instead with a lifetime τ, the parent HBr will have time to rotate during the dissociation and the observed angular distribution will be different from the limiting anisotropy parameter β which can be calculated from the angle between the recoil velocity of the photofragment and the transition dipole moment for a prompt dissociation. A reduced effective anisotropy parameter, β_{eff}, is introduced to characterize the observation of the angular distribution. The β_{eff} can be expressed in the following equation[4,5]

$$\beta_{eff} = \beta^*[\frac{1+\omega^2\tau^2}{1+4\omega^2\tau^2}]$$

in which ω is the frequency of the parent HBr rotation, and the rotational frequency of the HBr molecule can be estimated with the classical mechanics. The β_{eff} value can be obtained from the fitting, and we assume that β_{eff} for N"=0 would be the same as β as the rotational

frequency for this rotational level is 0. By rearranging the equation above, the following equation can be obtained

$$\omega^2\tau^2 = \frac{1-\frac{\beta_{eff}}{\beta}}{4\frac{\beta_{eff}}{\beta}-1}$$

By working on a linear regression of $\frac{1-\frac{\beta_{eff}}{\beta}}{4\frac{\beta_{eff}}{\beta}-1}$ versus ω^2, along with the β_{eff} and β obtained from the $H(^2S)$ + $Br(^2P_{3/2})$ product translational energy distributions and the rotational frequencies for each rotational levels, the slope gives τ^2, then the dissociation time can be obtained to be ~ 50 to 60 fs for v"=1 and 70 to 80 fs for v"=2 (Figure 10.3 and 10.4). In this study, the photodissociation of internally excited HBr molecule is observed. Other than using the pump-probe delay and the PFY spectrum linewidth measurement, this method provides a different way to measure the dissociation time scale of the parent.

10.2 General Conclusions

Chapter 2 and 3 present the photodissociation dynamics of the OH radical via several rovibrational levels (v' = 2-4, J' = 0.5-2.5) in the $A^2\Sigma^+$ state and the sequential two-photon dissociation of OH. The photo-predissociation of OH in $A^2\Sigma^+$(v' = 2, 3, and 4, J' = 0.5-2.5) via the P_1, Q_1, and R_1 transitions are investigated. The $O(^3P_J)$ spin-orbit branching ratios are measured. The branching ratios change slightly with J' but significantly with v'. By comparing the experimental results with the full quantum calculations by Yarkony with co-work,[6] it is concluded that the predissociation of v' = 2 and 3 are mainly via the $1^4\Sigma^-$ state, while that of v' = 4 is via the $1^4\Sigma^-$, $1^2\Sigma^-$, and $1^4\Pi$ states with an interference among

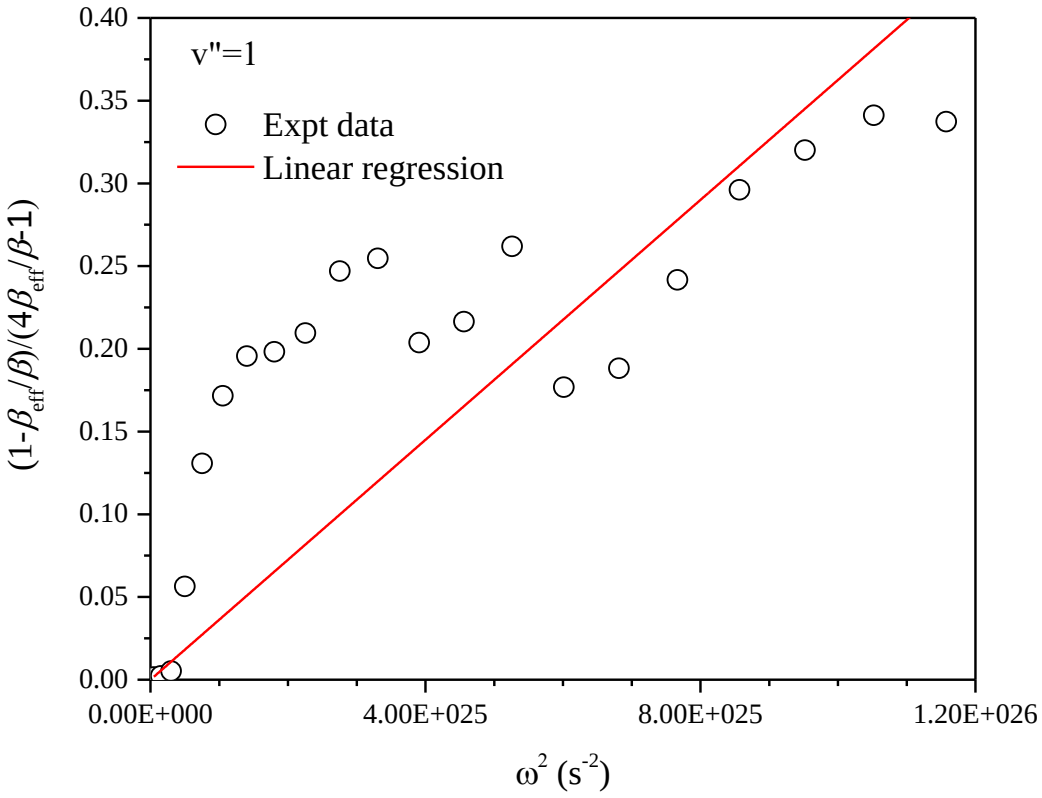

Figure 10.3. $\frac{1-\frac{\beta \mathrm{eff}}{\beta}}{4\frac{\beta \mathrm{eff}}{\beta}-1}$ versus ω^2 for the HBr parent with v'=1, N'= 1 to 21. From the slope, the dissociaiton time scale can be obtained.

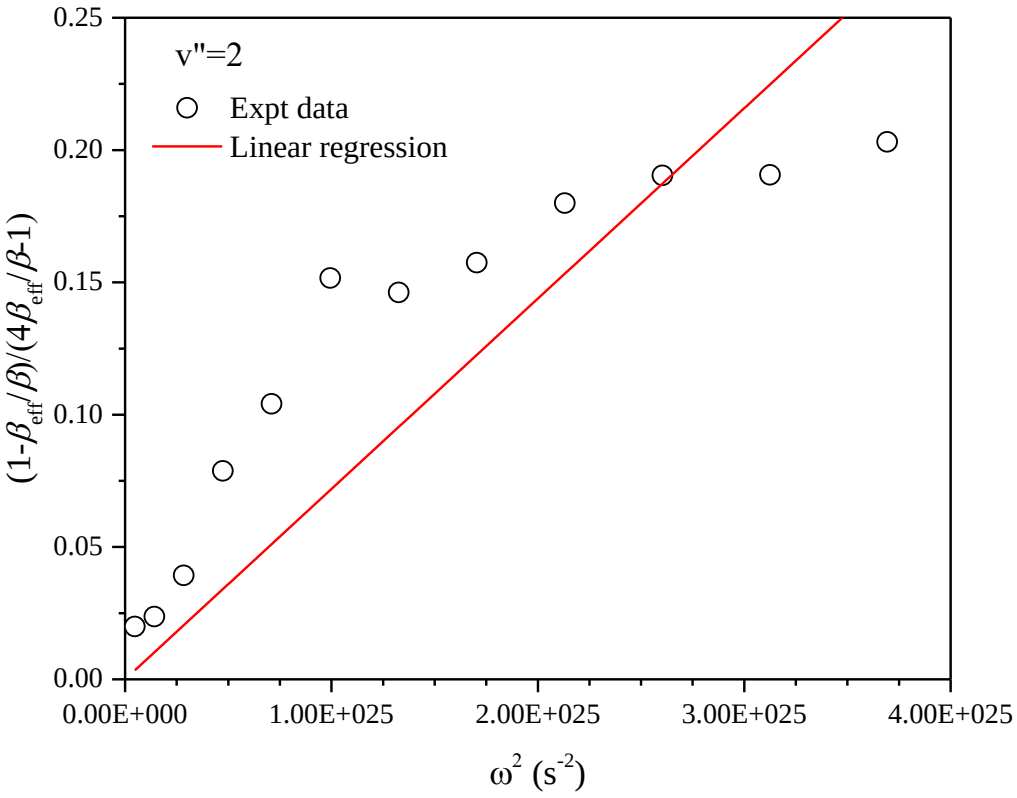

Figure 10.4. $\frac{1-\frac{\beta \mathrm{eff}}{\beta}}{4\frac{\beta \mathrm{eff}}{\beta}-1}$ versus ω^2 for the HBr parent with v'=2, N'= 1 to 12. From the slope, the dissociaiton time scale can be obtained.

them. The product angular distributions are measured. Due to the initial alignment of OH following the photo-excitation and the depolarization process, the product angular distributions show a strong dependent on the different P_1, Q_1, and R_1 transitions. Sequential two-photon excitations to the $2^2\Pi$ and $B^2\Sigma^+$ repulsive states were observed, and the dissociations on these states produce directly the H + O(^{1}D) and H + O(^{1}S) products, respectively. An accurate O-H bond dissociation energy was determined to be 35580 $\pm$ 15 cm^{-1}.

Chapter 4 to 6 show the photodissociation dynamics of several alkyl radicals, ethyl, *n*-butyls, *i*-butyl, *t*-butyl, and 1-pentyl, via the Rydberg states. The H-atom product translational energy distributions are bimodal. The main product channels for the alkyl radicals are (i) direct, prompt dissociation from the electronic excited state producing the product with a large translational energy release and anisotropic angular distributions (It is isotropic for *t*-butyl), and (ii) unimolecular dissociation after internal conversion from the electronic excited state to the ground state, with the modest translational energy release in the products and isotropic product angular distribution. In the dissociation of ethyl radical, the ethene product was observed with its vibrational mode excited from channel (i), and the C-C bond distance when the C-H bond is cleaved in the ethyl is determined to be 1.51 Å using the Franck-Condon modeling calculation.

Chapter 7 presents the UV photodissociation of the 2-propenyl radical. Similar to allyl and 1-propenyl,[7,8] the main H-atom photodissociation channel would be statistical dissociation on the ground electronic state after internal conversion from the excited electronic state and isomerization between the local minima are important during the

dissociation processes. The isotropic product angular distribution and small fraction of the total available energy released as the products' transitional energy are consistent with the statistical dissociation mechanism. QCT calculations yield the branching ratios for different dissociation product channels.

Chapter 8 investigates the photodissociation of vinoxy radical via the $\widetilde{B}^2A''$ state. The H + C_2H_2O product was observed with modest translational energy release with a slightly anisotropic angular distribution. The dynamics would be unimolecular dissociation of vinoxy after internal conversion from the $\widetilde{B}^2A''$ state to the electronic ground state ($\widetilde{X}^2A''$) and first electronic excited state ($\widetilde{A}^2A'$).

Chapter 9 presents the photodissociation dynamics of jet-cooled thiomethoxy radical (CH_3S) in the region of 216-225 nm. Several H-atom loss channels were determined. The CH_3S undergoes the repulsive dissociation producing the C-S stretch vibrationally excited $H_2CS(\widetilde{X}^1A_1)$ + H products, with a large translation energy release and an anisotropic product angular distribution. The Franck-Condon simulation indicated that the C-S bond distance was 1.75 Å for the excited state of CH_3S when the C-H bond cleaved. The D_0(H-CH_2S) bond dissociation energy was determined to be 48.8 $\pm$ 0.7 kcal/mol. The excited CH_3S could also undergo unimolecular dissociation after internal conversion from the electronic excited state to the ground electronic state, creating H + $H_2CS(\widetilde{X}^1A_1)$ products with a modest translational energy release and isotropic angular distribution. The $H_2CS(\widetilde{A}^1A_2)$ and $H_2CS(\tilde{a}^3A_2)$ product channels were observed as minor product channels.

Reference

1. A. G. Smolin, O. S. Vasyutinskii, G. G. Balint-Kurti, and A. Brown, *J. Phys. Chem. A* **110**, 5371 (2006).

2. R. N. Zare, *Mol. Photochem*. **4**, 1 (1972).

3. Webbook of Chemistry, National Institute of Standards and Technology, http://webbook.nist.gov/chemistry/, 2018.

4. C. Jonah, *J. Chem*. *Phys.* **55**, 1915 (1971).

5. G. E. Busch and K. R. Wilson, *J. Chem*. *Phys.* **56**, 3638 (1972).

6. G. Parlant and D. R. Yarkony, *J. Chem*. *Phys.* **110**, 363 (1999).

7. Y. Song, M. Lucas, M. Alcaraz, J. Zhang, and C. Brazier, *J. Phys. Chem*. *A* **119**, 12318 (2015).

8. M. Lucas, Y. Song, J. Zhang, C. Brazier, P. L. Houston, and J. M. Bowman, *J. Phys. Chem*. *A* **120**, 5248 (2016).